

# **Cavity-Ringdown Spectroscopy**



ACS SYMPOSIUM SERIES 720

# Cavity-Ringdown Spectroscopy

## An Ultratrace-Absorption Measurement Technique

**Kenneth W. Busch**, EDITOR  
*Baylor University*

**Marianna A. Busch**, EDITOR  
*Baylor University*



American Chemical Society, Washington, DC

In Cavity-Ringdown Spectroscopy; Busch, K., et al.;  
ACS Symposium Series; American Chemical Society: Washington, DC, 1999.



## Library of Congress Cataloging-in-Publication Data

Cavity-ringdown spectroscopy : an ultratrace-absorption measurement technique / Kenneth W. Busch, editor, Marianna A. Busch, editor.

p. cm. — (ACS symposium series, ISSN 0097-6156 : 720)

“Developed from a symposium sponsored by the Orange County Local Section of the American Chemical Society and the Society for Applied Spectroscopy, at the 33<sup>rd</sup> Western Regional Meeting of the American Chemical Society, Irvine, California, October 21-25, 1997”

Includes biographical references and index.

ISBN 0-8412-3600-3 (alk. paper)

1. Cavity-ringdown spectroscopy—Congresses.

I. Busch, Kenneth W. II. Busch, Marianna A. III. American Chemical Society. Orange County Local Section. IV. Society for Applied Spectroscopy. V. American Chemical Society. Western Regional Meeting (33<sup>rd</sup> : 1997 : Irvine, Calif.) VI. Series.

QD96.A2C38 1999  
543'.0858—dc21

98-32088  
CIP

The paper used in this publication meets the minimum requirements of American National Standard for Information Sciences—Permanence of Paper for Printer Library Materials, ANSI Z39.48-94 1984.

Copyright © 1999 American Chemical Society

Distributed by Oxford University Press

All Rights Reserved. Reprographic copying beyond that permitted by Sections 107 or 108 of the U.S. Copyright Act is allowed for internal use only, provided that a per-chapter fee of \$20.00 plus \$0.50 per page is paid to the Copyright Clearance Center, Inc., 222 Rosewood Drive, Danvers, MA 01923, USA. Republication or reproduction for sale of pages in this book is permitted only under license from ACS. Direct these and other permissions requests to ACS Copyright Office, Publications Division, 1155 16th Street, N.W., Washington, DC 20036.

The citation of trade names and/or names of manufacturers in this publication is not to be construed as an endorsement or as approval by ACS of the commercial products or services referenced herein; nor should the mere reference herein to any drawing, specification, chemical process, or other data be regarded as a license or as a conveyance of any right or permission to the holder, reader, or any other person or corporation, to manufacture, reproduce, use, or sell any patented invention or copyrighted work that may in any way be related thereto. Registered names, trademarks, etc., used in this publication, even without specific indication thereof, are not to be considered unprotected by law.

PRINTED IN THE UNITED STATES OF AMERICA



# Advisory Board

## ACS Symposium Series

**Mary E. Castellion**  
ChemEdit Company

**Arthur B. Ellis**  
University of Wisconsin at Madison

**Jeffrey S. Gaffney**  
Argonne National Laboratory

**Gunda I. Georg**  
University of Kansas

**Lawrence P. Klemann**  
Nabisco Foods Group

**Richard N. Loepky**  
University of Missouri

**Cynthia A. Maryanoff**  
R. W. Johnson Pharmaceutical  
Research Institute

**Roger A. Minear**  
University of Illinois  
at Urbana-Champaign

**Omikaram Nalamasu**  
AT&T Bell Laboratories

**Kinam Park**  
Purdue University

**Katherine R. Porter**  
Duke University

**Douglas A. Smith**  
The DAS Group, Inc.

**Martin R. Tant**  
Eastman Chemical Co.

**Michael D. Taylor**  
Parke-Davis Pharmaceutical  
Research

**Leroy B. Townsend**  
University of Michigan

**William C. Walker**  
DuPont Company



## Foreword

**T**HE ACS SYMPOSIUM SERIES was first published in 1974 to provide a mechanism for publishing symposia quickly in book form. The purpose of the series is to publish timely, comprehensive books developed from ACS sponsored symposia based on current scientific research. Occasionally, books are developed from symposia sponsored by other organizations when the topic is of keen interest to the chemistry audience.

Before agreeing to publish a book, the proposed table of contents is reviewed for appropriate and comprehensive coverage and for interest to the audience. Some papers may be excluded in order to better focus the book; others may be added to provide comprehensiveness. When appropriate, overview or introductory chapters are added. Drafts of chapters are peer-reviewed prior to final acceptance or rejection, and manuscripts are prepared in camera-ready format.

As a rule, only original research papers and original review papers are included in the volumes. Verbatim reproductions of previously published papers are not accepted.

ACS BOOKS DEPARTMENT

# Preface

This book deals with cavity-ringdown spectroscopy—a new method for making trace absorption measurements, particularly with gas-phase samples. Traditional absorption measurements involve the determination of two parameters: the incident power of a radiant beam on a sample ( $P_o$ ) and the radiant power of the beam after it has passed through the sample ( $P_i$ ). As the concentration of the absorbing species decreases, the value of  $P_i$  approaches  $P_o$ , and the detection limit is reached when the magnitudes of the two beams become indistinguishable statistically. By contrast, cavity-ringdown spectroscopy monitors the exponential decay of radiation in an optical cavity. For a given wavelength, the time associated with this exponential decay is related to the absorption coefficient of the gas contained within the cavity; the shorter the decay time, the higher the concentration of the sample. Improvements in the detection limit achieved with cavity-ringdown techniques can be on the order of  $10^3$  or more compared to traditional absorption methods. As discussed in the last chapter of this book, techniques related to cavity-ringdown spectroscopy may extend the detection limit even further.

The origins of cavity-ringdown spectroscopy can be traced to efforts in the 1980s to develop ways to measure the reflectivity of high reflectivity mirrors by arranging them to form optical cavities, known commercially as cavity lossmeters. In 1988, O'Keefe and Deacon demonstrated that the concept of a cavity lossmeter could be used to make absorption measurements with gas-phase samples. From this and subsequent work, it became clear that cavity-ringdown spectroscopy was capable of routinely measuring absorptions on the order of parts-per-million (ppm) per pass through the cavity.

We became interested in the analytical potential of cavity-ringdown spectroscopy after learning about it from two sources. The first source was a seminar presented at Baylor University by David Cedeño, a graduate student working with for Carlos Manzanares. The second source was a series of conversations with Richard Zare, held in March 1996, while he was visiting Baylor University to present the Gooch–Stephens Lectureship. When we were invited by the program chair of the 1997 Pacific Conference on Chemistry and Spectroscopy to organize a symposium for the meeting, we thought this would be a wonderful opportunity to hold a symposium on cavity-ringdown spectroscopy.

While we were organizing the conference symposium, a further thought occurred to us. It was clear, since the advent of cavity-ringdown spectroscopy in the late 1980s, that numerous papers on the topic had been published by research groups from around the world. In spite of the volume of published work, the concept of cavity-ringdown spectroscopy did not appear to be widely known outside a small circle of practitioners. Indeed, when we mentioned the subject of cavity-ringdown spectroscopy at dinner one evening to a former president of the American Chemical Society (ACS) who was visiting Baylor, he replied that he had never heard of the technique.

Because the basic principles of cavity-ringdown spectroscopy are not widely known, and the published work in this area is scattered among many specialist journals, we realized that a single reference source describing the technique and its applications could be extremely valuable to workers outside the immediate area. Aside from locating articles in the primary literature, another impediment for those wishing to gain an understanding of the technique is obtaining the necessary background in the behavior of optical cavities. For readers who are not familiar with some of the concepts associated with cavity-ringdown spectroscopy, Chapters 2–4 discuss stability criteria and mode formation in optical cavities. Because the participants in the symposium were the primary research groups currently working in the area, the publication of their contributions, preceded by introductory information that set forth the basic principles of the method, seemed a reasonable way to fill the need for a single reference source on cavity-ringdown spectroscopy.

Because absorption measurements are widely used in all areas of chemistry, it is anticipated that advances in cavity-ringdown spectroscopy will be of interest to broad segments of the analytical—and physical communities. This will include analytical chemists, spectroscopists, physical chemists doing laser spectroscopy and molecular beam work, combustion scientists, atmospheric chemists, and chemical engineers involved with process measurements—in fact, anyone involved in measuring trace components in gas-phase samples by absorption spectroscopy.

Having set forth the origins of this monograph, we would now like to thank those who helped make it possible. We would especially like to thank Michael L. Parsons of the DeVry Institute of Technology, Pomona, California, for inviting us to organize a symposium in the first place. We also thank the staff at ACS, including Cheryl Shanks, Anne Wilson, and Thayer Long, who worked with us on the acquisition and submission of the book. Finally, we especially thank Richard Saykally of the University of California, Berkeley, for the artwork on the cover of the volume.

Kenneth W. Busch  
Department of Chemistry  
Baylor University  
Waco, Texas 76798-7348

Marianna A. Busch  
Department of Chemistry  
Baylor University  
Waco, Texas 76798-7348

## Chapter 1

# Historical Overview of Spectral Studies: From Sunlight to Lasers

**B. A. Paldus and R. N. Zare**

**Department of Chemistry, Stanford University, Stanford, CA 94305-5080**

“The open society, the unrestricted access to knowledge, the unplanned and uninhibited association of men for its furtherance - these are what may make a vast, complex, ever growing, ever changing, ever more specialized and expert technological world, nevertheless a human community.” - J. Robert Oppenheimer, *Science and Common Understanding*, 1953.

Scientific development does not arise from a vacuum, but can be placed within an historical framework, in which new technologies both motivate and facilitate experiments. For example, cavity ring-down spectroscopy resulted from the advent of high reflectivity mirror, laser, and semiconductor technology breakthroughs. The introductory chapter that follows offers a cursory summary of historical events that led to the birth of linear absorption spectroscopy on which CRDS is based in particular, and to a history of spectral studies and associated technologies, in general.

### **Before the 16th Century: From Egypt to Italy.**

For millennia, sunlight and its refraction into colorful rainbows must have appealed to the mysticism of primitive man. Beautiful but untouchable and ephemeral, light was given supernatural significance by even the most sophisticated ancient civilizations. Ptolemy of Alexandria (A. D. 130), one of the early founders of optics and astronomy, was familiar with the measurement of angles of incidence and angles of refraction but failed to discover the simple laws of refraction. The study of light, color, and refraction, remained primarily limited by technology, all observations being made with the unaided human eye.

Glass was first discovered by the Phoenicians, but its use was confined to storage vessels and ornaments. It was not until the 14th century that the quality and clarity of glass improved to the extent that optical instruments could be built. In the 15th century, the discovery of the properties of convex glass led to the development of lenses, spectacles, and telescopes. Simultaneously, the Jesuit orders began promoting an "age of learning": they laid the foundation for scientific inquiry and empowered future scientists against the politics of the Church. Into this nascent scientific world were born Copernicus (1473-1543) and da Vinci (1452-1519). Copernicus used the power of glass to build telescopes and observe the stars. He proposed the first heliocentric theory, which ignited heresy trials of scientists by the Catholic Church that culminated in the sentencing of Galileo in 1633. It was for this reason that da Vinci shrouded his work in secrecy, which perhaps delayed significant advances in

the optical sciences for a few centuries. Da Vinci not only rediscovered the refraction of light but also discovered persistence of vision and the stereoscopic function of human eyes. He challenged the ancient belief that the eye was the source of illumination for objects perceived. More important, he postulated that both light and magnetism were wavelike in nature, and he reported the dispersion of white light into its spectrum of colors.

### **The 17th Century: The Age of Newton.**

Glass technology advanced significantly in the 17th century with the development of flint glass, a clear lead glass that could be ground into lenses. Thus, Hooke (1635-1703) and Leeuwenhoek (1632-1723) were able to build the first microscopes, while Kepler (1571-1630) improved the telescope. With better quality glass also came better measurements of refraction, which led to the formulation by Snell (1591-1626) that the sines of the angles of incidence and refraction have a constant ratio. Based on this work, humanity could observe both the vastness of space and the complexity of the microbial world.

But it was not until Newton (1642-1727) that the next step toward understanding the composite nature of white light was taken. In his treatises in the *Transactions of the Royal Society* (1672) and *Optiks* (1704), Newton described the first modern spectrometer that was capable of measuring the solar spectrum: when he used a slit with a lens placed in front of a prism, a series of differently colored images of the slit appeared on a screen in back of the prism. Had glass quality been somewhat better, it is possible that Newton would have observed Fraunhofer lines in his spectrum. Despite this great advance, he failed to realize that atoms and molecules absorb or emit only at characteristic wavelengths. By postulating that all flames were of the same nature because the light was produced by corpuscular vibrations, he delayed the understanding of spectra for at least another century.

Perhaps equal in importance to Newton's discoveries in optics, was the impact on science of the formation of scientific societies in Europe. Such bodies were established in England, France, and Germany. Not only did these bodies introduce peer review, they also disseminated results and elicited public interest (and royal funding) for the pursuit of science.

### **The 18th Century: The Age of Infrared and Ultraviolet Enlightenment.**

Globally, the 18th century was an epoch more of war and revolution than of scientific discovery. In the midst of the American War of Independence and the French Revolution, democracy was being born, while social change would begin to sweep Western society and lead to institutions of higher learning as we know them today. The military became a patron of research and development, appreciating that scientific discoveries and technological advances were intimately linked. Scientists of the time were often as much politicians and soldiers as they were researchers and philosophers.

Two such men were Dollond (1706-1761) and Franklin (1706-1790). Dollond, while working to improve the quality of telescopes for the navy, invented the achromatic lens. By using two glasses, crown glass and flint glass, which have different indices of refraction, he was able to correct for chromatic aberration. Franklin, the American ambassador to France and one of the founding fathers, established that electricity was both positive and negative. This early discovery stimulated further scientific inquiry, which led to the experiments of Faraday (1791-1867), Wheatstone (1802-1875), and Tesla (1856-1943), and which finally culminated in the formulation of electromagnetic theory by Maxwell (1831-1879). Without electricity, most spectroscopic instrumentation in use today would not function.

For a while, the only development that occurred in spectroscopic analysis was the first description of an emission spectrum; it was observed for a sodium flame in 1752. The important understanding that the optical spectrum is not limited to the visible was gained only at the end of the 18th century. Herschel (1738-1822), studied the distribution of heat from the sun with an array of thermometers, each placed at a different color of the dispersed visible spectrum. He thus discovered that most of the heat lay outside the visible spectrum, beyond the red: he had found the infrared. Almost simultaneously, Ritter (1776-1810) was studying the effectiveness of the dispersed visible spectrum in blackening silver chloride. Ritter observed that that the action was strongest beyond the violet: he had found the ultraviolet.

### **The 19th Century: Fraunhofer, Kirchhoff, and the Birth of Spectroscopy.**

Spectroscopy in the 19th century began almost furtively, with only qualitative observations of emissions from flames, sparks, arcs, and the sun. At this time, astronomy was the primary application of spectroscopy; several decades later, spectroscopic analysis would lead to the discovery of an element hitherto unknown on earth, helium, and to the formulation of the periodic table. Young (1773-1829) observed a distinctive yellow line in the spectrum of candles yet attributed this characteristic emission to interference effects. Wollaston (1766-1828) observed dark lines that interrupt otherwise continuous solar spectra but could not explain their origin. Countless others observed flame emission, but because their instruments were of poor quality or because the purity of their samples was inadequate, the fact that each atom and molecule has its own characteristic spectrum was not understood until the arrival of Fraunhofer and Kirchhoff.

Fraunhofer (1787-1826), initially an apprentice to a mirror maker, soon became the master optician of his time. In an attempt to define the color of light used in measuring the refractive index of glass in glass making, he constructed a theodolite telescope, which he placed behind a prism to view the images of a slit. In this manner he observed "an almost countless number of strong and weak (dark) vertical lines"<sup>1</sup>. Because he could quantify the angles in his experiment, he determined the relative line positions and developed a map of the solar spectrum. This map then served as a standard for the comparison of dispersion by different types and qualities of glasses. With all his measurements converted to "wavelengths," Fraunhofer established one of the first spectroscopic standards. Only with a wavelength standard could scientists directly compare results obtained using different optical devices and make spectroscopic advances.

Fraunhofer also developed the first objective prism; with it he observed the first stellar (Sirius) and planetary spectra. Furthermore, he discovered the transmission grating and thus observed the D-lines of sodium emission. Once he was able to manufacture transmission gratings of 3000 lines/cm with a diamond point and ruling machine, he measured the unresolved D-lines of sodium and found that the two yellow lines in sodium flames corresponded exactly in wavelength to the two dark lines in the solar spectrum.

The realization of a relation between emission and absorption spectra of light led to the formulation of a general law by Kirchhoff (1824-1887), the founder of spectral analysis: "The relation between the powers of emission and the powers of absorption for rays of the same wavelength is constant for all bodies at the same temperature"<sup>2</sup>. Kirchhoff was the first to articulate the significance of characteristic spectra emitted by different elements. He explained that the continuous nature of the solar spectrum was produced by emission from hot elements at the interior of the sun, while the dark lines were a result of absorption from this continuous emission spectrum by elements in the sun's cooler atmosphere. Not only did Kirchhoff completely map the solar spectrum, but with the aid of Bunsen (1811-1899) he also investigated many flame



and spark spectra of very pure elements<sup>†</sup> and discovered the existence of cesium and rubidium.

By the late 19th century, experimental spectroscopy exploded, with new discoveries and theoretical formulations appearing almost every year. Although a complete listing of all these historical developments lies beyond the scope of this brief overview, we summarize a few important steps taken by scientists. The 1830s and the 1840s saw the creation of photographic film by Talbot (1800-1877) and Daguerre (1789-1851), who developed a process to fix prints on paper soaked in silver nitrate. By 1870, Stokes (1819-1903) had discovered that quartz is transparent in the ultraviolet, and photographic plates made of dry gelatin were being used by spectroscopists such as Rowland (1848-1901) to measure ultraviolet spectra to 215 nm. Three decades later, Lyman (1874-1954) further extended the ultraviolet to 50 nm using a concave reflection grating of fluorite optics. In the 20th century, after numerous continual improvements in light sources, grating ruling, and optical mounting by Millikan (1868-1953) and Siegbahn (1918-), the ultraviolet limit was reduced to below 3 nm. Simultaneously, efforts were underway to extend spectroscopy to the infrared. By the 1880s, Abney (1843-1920) had developed photosensitive plates that could record spectra to 200  $\mu\text{m}$ , while Langley (1834-1906) invented the bolometer, a sensitive electrical resistance thermometer that could measure radiation to 180  $\mu\text{m}$ . Experimental spectroscopy, at this historical moment, seemed to have no boundaries.

But the general problem of the lack of suitable standards for spectra was not fully resolved until the 20th century. Of the many standards devised, most of which were based on tabulations of Fraunhofer lines, each carried its own flaws. Ångström (1814-1874) charted thousands of Fraunhofer lines, but his measurements were based on the Upsala meter, which was later shown to be inaccurate. Rowland (1848-1901) tabulated more accurate wavelength values by using a concave grating. Michelson (1852-1931) used interferometers to measure highly accurate line wavelengths. But it was not until 1907 that the first true spectroscopic standard was established by Fabry (1867-1945) and Pérot (1863-1925): their interferometric measurement of the red cadmium line at 643.84696 nm was accepted by the International Union for Cooperation in Solar Research. Secondary standards based on rare-gas spectra were only adopted only after World War I.

### Early 20th Century Spectroscopy.

In the early 20th century, spectroscopists were busily occupied using the newly created spectroscopes and higher powered telescopes. Balmer (1825-1898), Lyman (1874-1954), and Paschen (1865-1947) had discovered that specific series of hydrogen lines could be represented by a simple mathematical formula, first found empirically by Rydberg (1854-1919), while Zeeman (1865-1943) discovered the magnetic splitting of spectral lines. But physical societies were struggling over a strange new theory called quantum mechanics. In 1900, Planck (1858-1947) introduced the concept of quantized energy states leading to quantized transition energies. Five years later, Einstein (1879-1955) introduced the idea that under certain circumstances light can behave like particles, called photons. Quantization then began to take root: Bohr (1885-1962) used it to develop atomic theory and predict the energy levels of hydrogen. Born (1882-1970) applied it to the study of molecules, crystals, crystalline vibrations, and optical polarization.

---

<sup>†</sup> The Bunsen burner was originally developed for spectroscopic studies of flames to remove the interfering background from candle flames. It is another example of a spectroscopic spin-off now more famous as an inexpensive and ubiquitous heat source for studying chemical reactions.

Despite the vast tragedies of the First and Second World Wars, an entire generation of young physicists including Schrödinger (1887-1961), Heisenberg (1901-1976), deBroglie (1892-1987), Pauli (1900-1958), Goudsmit (1902-1978), Fermi (1901-1954), Condon (1902-1974), Dirac (1902-1984), Teller (1908-), and Hund (1896-1997) (to name just a few!) not only fully adopted the ideas of quantum mechanics, but furthered them. They devised a wave theory, formulated the particle-wave duality of electrons and photons, formalized the Schrödinger equation, and developed the mathematics needed to "solve" this equation for the energy levels of various simple physical systems. But these theoretical advances were not made without experimental measurements. In 1897, Thomson (1856-1940) discovered the electron; in 1912, Rutherford (1871-1937) scattered alpha particles from atoms to demonstrate that the atom consisted mainly of empty space; in the 1920s, Compton (1892-1962) showed that photons can behave like particles and carry momentum, when he scattered x-rays from carbon films and discovered that some of the x-rays had suffered 4% energy loss. By the end of the Second World War, both the theoretical and experimental stages were set for major advances in spectroscopy.

Raman (1888-1971) is most noted for his discovery of the Raman effect, the basis for present-day linear and nonlinear Raman spectroscopy, a powerful tool for the investigation of molecular vibrations. The advent of lasers has not only greatly enhanced the sensitivity of (spontaneous) Raman spectroscopy, but has led to new spectroscopic techniques based on the stimulated Raman effect, such as Coherent Anti-Stokes Raman Scattering (CARS). Lamb (1913-) is the father of saturation spectroscopy, which is based on the velocity-selective saturation of Doppler-broadened atomic and molecular transitions. The spectral resolution is then limited only by the much narrower width of the Lamb dip. He was thereby able to determine the fine structure of the hydrogen atom. Bloembergen (1920-) and Schawlow (1921-) are noteworthy for devising laser spectroscopy, on which many modern spectroscopic studies are based, while Townes (1915-), Basov (1922-) and Prokharov (1916-) are honored for inventing the maser, an important source in microwave spectroscopy and the forerunner of the laser. Herzberg (1904-) stands out for his work in determining the electronic structure and internal motions of molecules. His spectroscopic studies provided experimental results of prime importance to physical chemistry and helped stimulated a resurgence of interest in the detailed study of gas-phase chemical reactions.

Spectroscopy now covers a sizable fraction of the electromagnetic spectrum. A more elaborate discussion of modern quantitative linear absorption spectroscopy is presented in a later chapter. A plethora of other spectroscopies exist, but they are beyond the scope of this review. The reader is referred to the excellent treatments of Condon and Shortley<sup>3</sup> for atomic spectroscopy, of Herzberg<sup>4</sup> for molecular spectroscopy, of Schawlow and Townes<sup>5</sup> for microwave spectroscopy, and of Levenson<sup>6</sup> for nonlinear spectroscopy. A compendium of spectroscopic techniques can be found in Demtröder<sup>7</sup>.

## References

1. Ames, J.S.; *Prismatic and Diffraction Spectra*; Harper and Brothers, New York, 1898.
2. Kirchoff, G.R.; *Ann. d. Phys.* **1860**, *109*, 275.
3. Condon, E.U. & Shortley, G.H.; *The theory of atomic spectra*; Cambridge University Press, Cambridge, UK, 1951.

4. Herzberg, G.; *Molecular Spectra and Molecular Structure* ; VanNostrand and Reinhold, New York, 1950.
5. Townes, C.H. & Schawlow, A.L.; *Microwave Spectroscopy* ; New York, 1975.
6. Levenson, M.D. & Kano, S.S.; *Introduction to Nonlinear Laser Spectroscopy*. ; Academic Press Inc., Boston, MA, 1988.
7. Demtröder, W.; *Laser Spectroscopy* ; Springer Verlag, Berlin, 1996.

## Chapter 2

# Introduction to Cavity-Ringdown Spectroscopy

**Kenneth W. Busch and Marianna A. Busch**

**Department of Chemistry, Baylor University, Waco, TX 76798–7348**

Cavity-ringdown spectroscopy is an alternative way of measuring small fractional absorptions down to sub-ppm levels per pass in the cavity. In this chapter, the basic principles behind cavity-ringdown spectroscopy are discussed. The areas where ultra-sensitive absorption measurements in the gas phase are important are illustrated, and existing methods of making these measurements are presented. The experimental requirements for performing cavity-ringdown spectroscopy are discussed, and an expression for the detection limit in cavity-ringdown spectroscopy is derived from statistical considerations. Finally, future prospects for the technique are discussed.

Cavity-ringdown spectroscopy is an alternative way of making ultra-sensitive absorption measurements, particularly with gas-phase samples. This volume will discuss the research being conducted on cavity-ringdown spectroscopy by the leading research groups in the area. In the chapters that follow, various aspects of the cavity-ringdown experiment will be discussed and its applications described. Although the origins of the technique can be traced back to attempts to measure mirror reflectivities in the early 1980s (1-4), the spectroscopic application of the concept has only recently been reviewed (5,6) and is still not widely known to the general scientific community. Because the technique can provide the ability to measure small fractional absorptions (down to sub-ppm levels per pass), it should be of interest to broad segments of the analytical-, physical-, and engineering communities. This includes analytical chemists, spectroscopists, physical chemists doing laser spectroscopy and molecular beam work, combustion scientists, atmospheric chemists, and chemical engineers involved with process measurements—in fact, anyone involved with measuring trace components in gas-phase samples by absorption spectroscopy.

This chapter will provide a basic introduction to cavity-ringdown spectroscopy for the reader who is not familiar with the technique. The intent is to show the basic principles of the technique without introducing undue mathematical complexity at the outset. However, before describing the technique, it is worthwhile to review some of the areas where sensitive gas-phase absorption measurements are important.

## The Need for Gas-Phase Absorption Measurements

In addition to its use in purely theoretical spectroscopic investigations, gas-phase absorption spectrometric measurements are also of interest in a variety of applications ranging from pollution monitoring to process control. These gas-phase measurement situations include:

- Atmospheric modeling studies
- Pollution monitoring/control
- Remote sensing
- Battlefield detection of chemical warfare agents
- Trace analysis of high-purity gases such as those used in semiconductor fabrication
- Combustion studies
- Process control/optimization
- Detection of trace levels of illicit drugs or explosive agents in the atmosphere in the vicinity of baggage-handling areas in airports

While traditional absorption spectrometry has been applied to all of the above measurement situations, its sensitivity has frequently not been adequate for the task. Traditional absorption spectrometry requires the determination of two parameters—an incident intensity ( $I_0$ ), and a transmitted intensity ( $I_t$ ). Thus in order for a traditional absorption measurement to be successful, the signal-to-noise level must be adequate to distinguish the difference between  $I_0$  and  $I_t$ .

**Beer-Lambert Law.** In many respects, traditional absorption spectrometry has many desirable characteristics for the real-time determination of gaseous species. If the analyte is the only absorbing species in the beam of radiation at a particular wavelength, and if it is present in sufficient amount, its concentration can be determined directly with absorption spectrometry by means of the Beer-Lambert law,

$$I_t = I_0 \exp(-\sigma LN) \quad (1)$$

where  $I_t$  is the transmitted intensity,  $I_0$  is the incident intensity,  $\sigma$  is the cross section of the absorbing species at the wavelength of the measurement in  $\text{cm}^2$ ,  $L$  is the path length of the absorbing medium in cm, and  $N$  is the number density of the absorbing species in  $\text{cm}^{-3}$ . While the technique is robust and well developed theoretically, the primary difficulties encountered with the use of conventional absorption spectrometric measurements for the determination of gaseous species in challenging situations are insufficient sensitivity, and a certain lack of specificity in the UV/visible region because of the possibility of overlapping absorption bands from concomitants. It is clear from eq 1 that if the absorption being measured is very weak,  $I_t$  will be approximately equal to  $I_0$ . Thus the problem encountered in determining a very weak absorption band by traditional methods is the difficulty in measuring a small difference between two large

numbers, both of which are uncertain as a result of experimental and fundamental factors (i.e., noise). If the light source for the absorption measurements is a pulsed laser, the pulse-to-pulse variation in the intensity of the laser can easily mask a very weak absorption band, making the use of traditional methods unsatisfactory for this purpose.

**Long-Path Approaches.** In the laboratory, one obvious means to overcome the sensitivity problems of gas-phase absorption measurements is to increase the effective absorption path length of the absorbing medium by use of multi-pass absorption cells that can traverse the cell up to 48 times or more (7). In the area of pollution monitoring, the use of long path lengths has been effectively exploited in differential optical absorption spectroscopy (DOAS) (8-11), developed in 1980 by Platt and Perner (12). In DOAS, a high intensity source such as a xenon arc is collimated by a parabolic mirror and transmitted over a path length of typically 1 km in the atmosphere before being collected by a second parabolic mirror. The transmitted radiation is then analyzed with a spectrometer so that a complete spectrum of the source radiation, as modified by the atmosphere, is recorded. The transmitted spectrum is then ratioed to a stored spectrum, recorded over a very short optical path length to remove the spectrum of the source itself.

Other long-path spectroscopic methods that have been developed for gas-phase measurements include:

- Differential absorption lidar (DIAL) (13-19)
- Tunable diode laser absorption spectroscopy (TDLAS) (20-24)
- Open-path Fourier-transform spectroscopy (25)

**Alternative Techniques.** Because of the limitations of traditional absorption spectrometry, various alternative techniques have been developed in an attempt to improve the detection of gaseous species. These alternative methods of detecting trace levels of gaseous species include:

- Photoacoustic spectroscopy (26-30)
- Thermal lensing measurements (31-33)
- Laser-induced fluorescence (LIF) (34-36)
- Laser-induced photofragmentation/photoionization (37)
- (2 + 2) resonance-enhanced multiphoton ionization (REMPI) (38)
- Intercavity laser absorption spectroscopy (ICLAS) (39)

## Cavity-Ringdown Spectroscopy

In the discussion that follows, cavity-ringdown spectroscopy will be discussed on the basis of an intensity model. For a more detailed discussion of the topic based on cavity fields, the reader should see the chapters by Looney, *et al.*, and Lehmann.

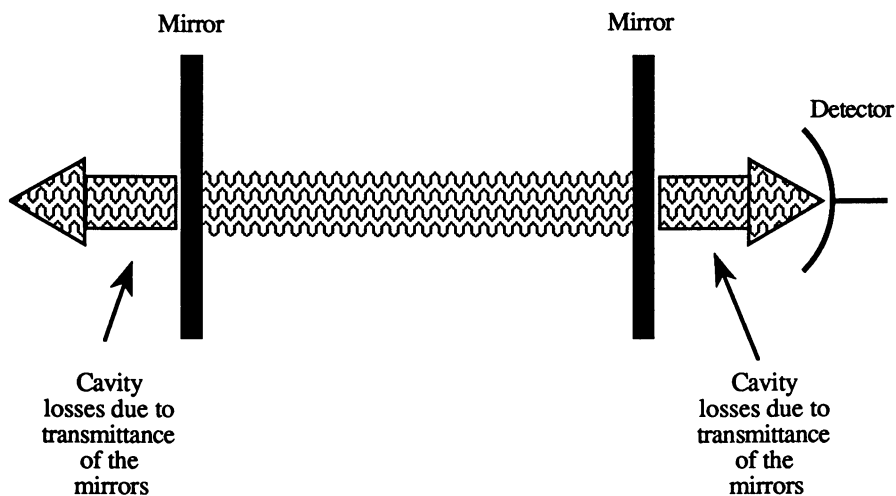


Figure 1. Schematic diagram of ringdown cavity.

**Basic Considerations.** Cavity-ringdown spectroscopy is an outgrowth of attempts to measure the reflectivity of high reflectance mirrors needed for missile guidance systems. (See chapters by O'Keefe, *et al.*, and Zare and Paldus for a discussion of the history of cavity-ringdown spectroscopy.) The technique makes use of an optical cavity composed of two or more mirrors. (See the next two chapters for a discussion of optical cavities.) Figure 1 shows a stable optical cavity composed of two mirrors. In the absence of any absorbing species in the volume between the two mirrors, the primary losses of the cavity will be from the small transmittance of the mirrors and diffraction losses. As a result, if a short pulse of light is injected into the cavity (whose coherence length is less than the length of the cavity), it will be reflected back and forth within the cavity, but its intensity will gradually decrease with time as energy leaks out of the cavity. A measure of the ratio of the energy stored in the cavity to that lost by the cavity is referred to as the  $Q$  (for quality) of the cavity. Thus, the intensity in a cavity with a high  $Q$  will take longer to decay than that in a cavity with a low  $Q$ . The exponential decay of the intensity with time resembles a ringing pattern (recall the gradual decay of sound from a resonant bell). As a result, the technique is referred to as cavity-ringdown spectroscopy to signify that the measured parameter is the exponential decay of the radiation in the cavity. Figure 2 shows a schematic representation of the ringdown pattern produced by a short laser pulse injected into the cavity.

If an absorbing species that obeys Beer's law is introduced into the cavity, its presence will increase the losses of the cavity and reduce its  $Q$ . As a result, the exponential decay (or ringdown curve) will take place over a shorter time frame than that observed with a cavity that does not contain the absorbing species.

In the case of an empty cavity composed of two mirrors with the same reflectivity  $R$ , the intensity within the cavity will decrease exponentially according to the following relationship:

$$i(t) = i_0 \exp \left[ - \left( \frac{\text{number of reflections}}{\text{round trip}} \right) \left( \frac{\text{loss}}{\text{reflection}} \right) (\text{number of round trips}) \right] \quad (2)$$

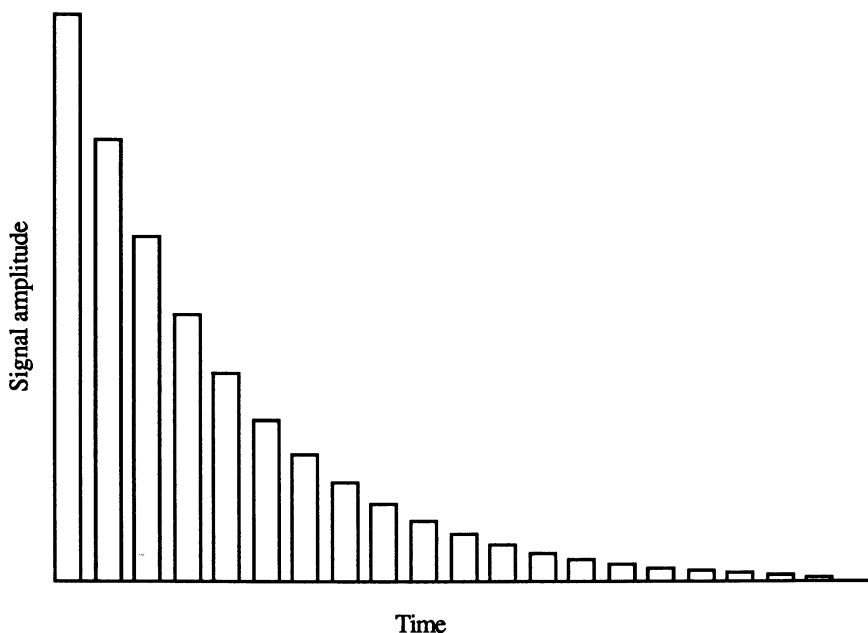


Figure 2. Schematic representation of the ringdown pattern produced by a short laser pulse injected into the cavity.

where  $i_0$  is the intensity of the initial pulse, and  $i(t)$  is the intensity after time  $t$ . For a cavity with two mirrors there are 2 reflections per round trip and the number of round trips in time  $t$  will be

$$\text{number of round trips after time } t = \frac{tc}{2L} \quad (3)$$

where  $c$  is the velocity of light. If the loss per reflection is taken as  $1 - R$ , where  $R$  is the reflectivity of the mirrors (recall from Kirchhoff's law that  $T + R = 1$ , where  $T$  is the transmission of the mirror), eq 2 can be rewritten as

$$i(t) = i_0 \exp \left[ - (1 - R) \frac{tc}{L} \right] \quad (4)$$



The time constant for this decay is the point where  $i(t) = i_0 e^{-1}$ . This will occur when  $t = \tau$  given by

$$\tau = \frac{t_r}{2(1-R)} \quad (5)$$

where  $\tau$  is the time constant for the decay, and  $t_r$  is the transit time for a round trip.

Consider now a cavity that contains a species that absorbs at the wavelength of the radiation injected into the cavity. For a round trip in the cavity, the loss due to absorption will be given by

$$\text{absorption loss} = \left( \frac{\text{loss}}{\text{round trip}} \right) (\text{number of round trips}) = (2\alpha L) \left( \frac{tc}{2L} \right) \quad (6)$$

where  $\alpha$  is the absorption coefficient given by  $\sigma N$  in eq 1. (Dimensionally,  $\alpha$  has units of reciprocal length, typically  $\text{cm}^{-1}$ ). The total loss in the cavity containing the absorbing species will now be

$$\text{total loss} = (1-R) \frac{tc}{L} + (\alpha L) \frac{tc}{L} = \left[ (1-R) + \alpha L \right] \frac{tc}{L} \quad (7)$$

and eq 4 can be rewritten as

$$i(t) = i_0 \exp \left\{ - \left[ (1-R) + \alpha L \right] \frac{tc}{L} \right\} \quad (8)$$

from which it follows that the time constant for the decay will be given by

$$\tau = \frac{t_r}{2 \left[ (1-R) + \alpha L \right]} \quad (9)$$

For a 0.50-m cavity,  $t_r/2$  will be  $1.7 \times 10^{-9}$  s. If both mirrors that make up the cavity have a reflectivity of 0.9999, the time constant for the empty cavity (eq 5) will be 17  $\mu\text{s}$ . If the cavity is filled with an absorbing species with an absorption coefficient of  $\alpha = 10^{-6} \text{ cm}^{-1}$ , the time constant for decay given by eq 9 will be 11  $\mu\text{s}$ . So by adding an absorbing species to the cavity, the time constant for the ringdown curve is reduced.

If eqs 5 and 9 are combined to eliminate  $R$ , the result can be written as

$$\alpha = \frac{1}{c} \left( \frac{1}{\tau_1} - \frac{1}{\tau_2} \right) \quad (10)$$

where  $\tau_1$  is the ringdown time for the cavity containing the absorbing species and  $\tau_2$  is the ringdown time for the empty cavity. Equation 10 shows that the absorption coefficient for the given wavelength can be determined if only the two ringdown times for the cavity are known.

In plotting the spectrum of an absorbing species [i.e.,  $\alpha(\lambda)$  versus  $\lambda$ ],  $\tau_2$  can be regarded as a constant background insofar as  $R(\lambda)$  is constant over the wavelength range of the measurements. The assumption that  $R(\lambda)$  is constant becomes problematic as  $\alpha(\lambda)$  becomes small because of the presence of small variations in the mirror reflectivity with wavelength.

**Experimental Implementation.** Throughout this volume, the reader will encounter various experimental arrangements for doing cavity-ringdown spectroscopy. As an introduction to the topic, we will consider a basic experimental setup shown in Figure 3. In this particular configuration, a tunable, pulsed laser source such as an excimer pumped dye laser could be used to inject light into the cavity. Such a laser might typically have a 15 ns pulse duration. The radiation from the laser would be introduced into the cavity with the appropriate mode-matching optics. A typical cavity might consist of two high reflectivity spherical mirrors ( $R = 0.999$  or better, radius of curvature, 6 m) separated by 50 cm to form a stable cavity. (See the following chapter for a discussion of stable cavities.) To minimize diffraction losses, the diameters of the

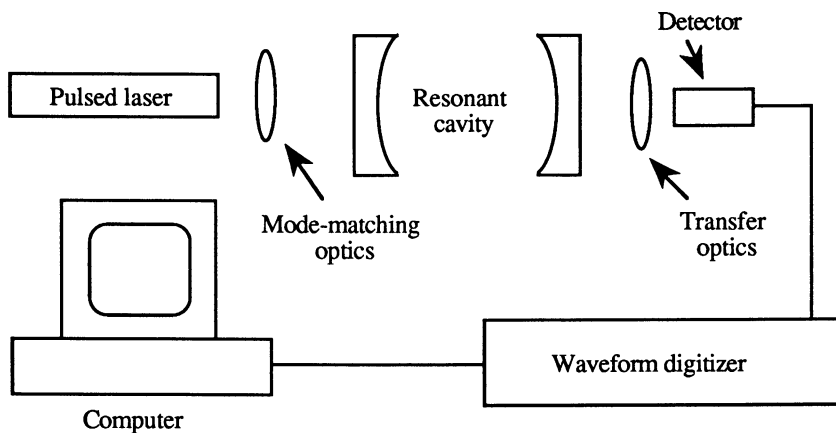


Figure 3. Schematic diagram of the cavity-ringdown experiment using a pulsed laser source.

mirrors would be chosen to be large with respect to the beam diameter at the mirrors. If the experiment is being conducted in the UV/visible region of the spectrum, a photomultiplier tube would be used to detect the light leaking out of the cavity through the output mirror. Once again some form of transfer optics may be required to collect the radiation emerging from the cavity and relay it to the detector. Since the intensity of the light emerging from the cavity is proportional to the intensity of the radiation trapped in the cavity, the signal produced by the photomultiplier will follow the ringdown curve of the radiation within the cavity. The ringdown signal from the photomultiplier (which may be on the order of 10  $\mu\text{s}$  or more) would then be captured by a waveform digitizer such as a digital oscilloscope with a sampling rate of 10 ns. The digitized signal would then be transferred to a computer, where the experimental points would be fitted to an exponential decay curve with a characteristic time constant  $\tau$ . Following curve fitting, the ringdown time can be determined. To get a better estimate of  $\alpha$ , the ringdown times ( $\tau$ ) obtained from several pulses of the laser can be averaged.

To determine the spectrum of an absorbing species, the traditional ringdown experiment is conducted at periodic wavelength intervals by adjusting the wavelength of the tunable dye laser. Each dye has a working range of approximately 40 nm, and it

typically takes 1-2 minutes to change the wavelength within this range. Scans over an extended range will require more than one dye. The wavelength range that can be accessed by the technique ranges from the ultraviolet to the infrared region of the spectrum. For a given experimental setup, the wavelength range that can be covered will depend on the dyes available with the laser and the reflectivity characteristics of the mirrors used in the cavity.

**Cavity Mirrors.** The mirrors used to form the cavity are an important factor in cavity-ringdown spectroscopy. In general, multilayer dielectric mirrors have a higher reflectance than the best metallic mirrors, which are made by vacuum deposition of a thin metallic layer on a suitable substrate. Figure 4 shows a schematic diagram of a cross-section of a multilayer dielectric mirror with 11 layers. Typical high reflectance mirrors may be composed of up to forty quarter-wavelength dielectric layers that alternate between a high and low index of refraction as shown in Figure 4 (40). This multilayer dielectric coating is deposited by evaporation on a transparent substrate, the back side of which is typically coated with an anti-reflection coating. Typical dielectric materials used to fabricate the layers that make up the reflecting sandwich of these

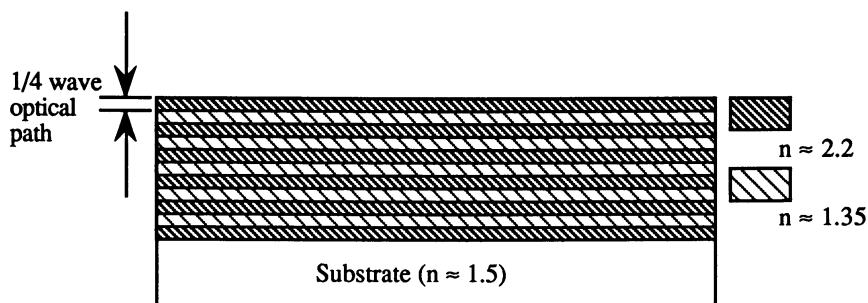


Figure 4. Schematic diagram of an 11-layer dielectric mirror composed of alternating layers of high and low refractive index materials. Each layer has an optical path (distance  $\times$  refractive index) of  $1/4$  wavelength, and  $n$  is the index of refraction.

mirrors include  $\text{SiO}_2$ ,  $\text{TiO}_2$ ,  $\text{ZrO}_2$ , and  $\text{ThF}_4$  (41). It was in the development and characterization of these high reflectivity mirrors that cavity approaches were first employed to measure mirror reflectivity (1-4). While multilayer dielectric mirrors are more durable than metallic mirrors, and can be fabricated for any desired reflectance, the high reflectance is only realized over a narrow wavelength range. In addition to resistance to abrasion, multilayer dielectric mirrors are resistant to chemical attack, a characteristic that makes them ideal for cavity-ringdown spectroscopy.

Scherer et al. (6) have discussed the characteristics of the mirrors required for cavity-ringdown spectroscopy. From eq 5, it is clear that very high reflectivity mirrors are needed to provide ringdown times that are convenient to measure. With a mirror reflectivity of 0.999, the ringdown time ( $\tau$ ) from eq 5 will be  $1.7 \mu\text{s}$  for a 0.50-m cavity. Over this time period ( $1\tau$ ), the pulse will make 1000 passes through the cavity (where a pass is one-half of a round trip). Under these circumstances, the effective path length for the absorption measurement is 500 m. If a mirror with a reflectivity of 0.9999 is employed with the same cavity, the ringdown time is  $17 \mu\text{s}$ , the number of passes through the cavity is 10,000, and the effective path length is 5 km.

While high reflectivity multi-layer dielectric mirrors are available commercially, the wavelength range over which this reflectivity is maintained is generally limited to

$\pm 15\%$  of the wavelength of maximum reflectivity as shown schematically in Figure 5 (6). For a mirror with a maximum reflectivity at 400 nm, this corresponds to  $\pm 60$  nm. So, to cover an extensive wavelength range with cavity-ringdown spectroscopy, a number of mirrors may be required in addition to different laser dyes for the pulsed dye laser. While the reflectivity profile shown in Figure 5 resembles a boxcar function with side lobes, the top of the boxcar is not completely constant and has a small ripple component. This ripple in the reflectivity profile of the top of the boxcar is not serious in most cases if the absorption coefficient is sufficiently large that variations in  $\tau_2(\lambda)$  are small compared with  $\tau_1(\lambda)$ . As the absorption coefficient in eq 10 becomes smaller and smaller, however, the variation in  $R$  with  $\lambda$  cannot be neglected, and  $\tau_2(\lambda)$  must be determined.

**Analog-to-Digital Conversion.** In general, it is desirable to monitor the ringdown decay of the intensity as a function of time rather than use a boxcar approach (which gives only two experimental points). By monitoring the entire ringdown curve, all of the experimental data collected may be used in a least-squares fitting routine. The selection of the appropriate analog-to-digital (A/D) converter for the cavity-ringdown experiment is a compromise between the number of data points collected (which is determined by the sampling rate of the A/D converter) and the precision of the measured

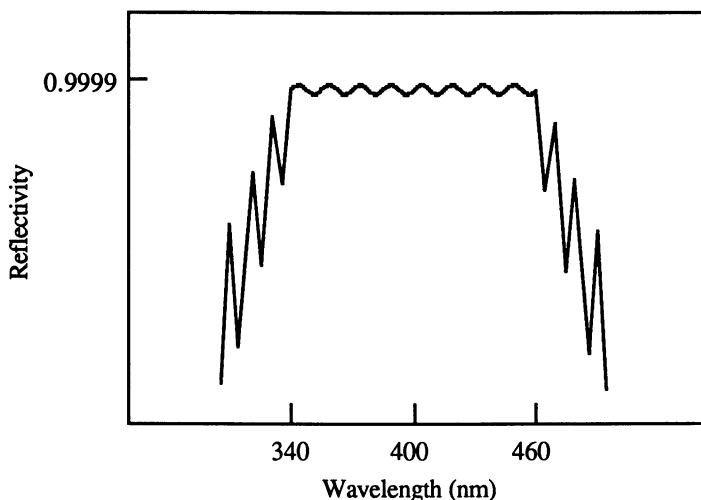


Figure 5. Schematic representation of mirror reflectivity for a multi-layer dielectric mirror as a function of wavelength. The ripple at the top of the reflectivity profile has been exaggerated to illustrate the effect.

value (which is determined by the resolution of the A/D converter). In general, the higher the sampling rate of the A/D converter, the lower the resolution available (i.e., the fewer bits associated with the measured quantity). For a hypothetical 0.50-m cavity composed of two mirrors with reflectivities of 0.9999, the ringdown time given by eq 5 is 17  $\mu$ s. With an 8-bit A/D converter with a sampling rate of 8 MHz, 1700 data points can be collected over  $1\tau$ . (If the intensity reaching the detector is large enough, the ringdown decay curve can be followed over several  $\tau$ , thereby allowing more points to be sampled). If a 12-bit A/D converter with a sampling rate of 20 MHz is employed, only 340 data points are collected over  $1\tau$  [one-fifth the number of points compared with the 100 MHz A/D converter]. While the number of data points collected is less, the

precision associated with each data point is more with the 12-bit A/D converter. Since the digitization error associated with the measurements is due to the uncertainty in the least significant bit associated with the measurement, the precision of the 8-bit measurement is good to only 1/256 (or 0.4%) compared with 1/4096 (or 0.02 %) with the 12-bit measurement. Clearly the choice of which converter to use will depend on the ringdown time being measured. For the situation described above, the 12-bit converter still collects sufficient data to permit a good least-squares fit of the experimental decay curve. However, if the experimental setup is altered in some way so that the ringdown time becomes shorter or the intensity reaching the detector is too low to follow for more than  $1\tau$ , a point will be reached where the slower A/D converter does not have a large enough sampling rate to collect enough points for a good measurement of the experimental decay curve.

**Experimental Considerations. Sensitivity.** Sensitivity in cavity-ringdown measurements is best reported in terms of the minimum detectable fractional absorption per pass through the cavity, where the fractional absorption per pass through the cavity is given by

$$\text{fractional absorption per pass} = \frac{I_0 - I_t}{I_0} = \alpha L = \sigma NL \quad (11)$$

The use of the minimum detectable fractional absorption per pass, which is typically reported in parts per million (ppm), is preferable to other means of expressing sensitivity because it is unitless. Ultimately, the fundamental sensitivity limit with cavity-ringdown spectroscopy is determined by the ability to distinguish  $\tau_1$  from  $\tau_2$  in eq 10 in a statistically significant manner (i.e., the minimum detectable fractional absorption per pass depends on the precision of the determination of the time constant from the ringdown curve).

Using statistical principles, it is possible to derive an expression to predict the minimum absorption coefficient that can be detected under a given set of experimental conditions. If we take  $\phi = 1/\tau$ , we can rewrite eq 10 as

$$\alpha = \frac{1}{c}(\overline{\phi}_1 - \overline{\phi}_2) = \frac{\Delta\overline{\phi}}{c} \quad (12)$$

where  $\overline{\phi}_1$  is the average value of  $\phi_1$ ,  $\overline{\phi}_2$  is the average value of  $\phi_2$ , and  $\alpha$  will be nonzero as long as  $\Delta\overline{\phi} \neq 0$ . Both  $\phi_1$  and  $\phi_2$  are characterized by standard deviations  $s_1$  and  $s_2$ , respectively. Now the minimum difference in  $\phi$  that is statistically significant will be given by

$$\Delta\overline{\phi} = t \sqrt{\frac{s_1^2}{n_1} + \frac{s_2^2}{n_2}} \quad (13)$$

where  $t$  is the value of the  $t$ -statistic and where  $n_1$  and  $n_2$  are the number of measurements in the average values for  $\phi_1$  and  $\phi_2$ , respectively. As we approach the detection limit,  $\phi_1$  approaches  $\phi_2$ , and we can take  $s_1 \equiv s_2 = s$ . For purposes of illustration, let us assume that  $n_1 = n_2 = n$ . Under these circumstances, eq 13 reduces to

$$\Delta\overline{\phi} = t s \sqrt{\frac{2}{n}} \quad (14)$$

From our definition of  $\phi$ ,

$$d\phi = -\frac{d\tau}{\tau} \quad (15)$$

Setting  $|d\phi| = s$  and symbolizing the relative precision of the time constant measurement by  $U_\tau = d\tau/\tau$ , we obtain

$$\alpha_{\min} = \frac{t U_\tau \sqrt{\frac{2}{n}}}{c \tau} \quad (16)$$

where  $\alpha_{\min}$  represents the minimum value of  $\alpha$  that can be measured by the cavity ringdown method for the given set of experimental conditions and  $t$  is the value of the  $t$ -statistic for  $n_1 + n_2 - 2$  ( $= 2n - 2$ ) degrees of freedom for the desired confidence level, and  $\tau = \tau_2$ , the ringdown time for the empty cavity.

For purposes of illustration, let us consider a 0.50-m cavity made up of two mirrors with  $R = 0.9999$ . We have seen with this cavity that the ringdown time is 17  $\mu\text{s}$  with no absorbing species present. For purposes of illustration, let us assume that  $n_1 = n_2 = 25$ . For the 95% confidence level with 48 degrees of freedom, the value of  $t$  is approximately 2. Finally, let us assume that we are able to measure  $\tau_2$  to a precision of  $\pm 1\%$ . Substituting these values into eq 16 gives a minimum detectable absorption coefficient of  $1.1 \times 10^{-8} \text{ cm}^{-1}$  or a fractional absorption ( $\alpha L$ ) of 0.6 ppm per pass. Naturally, the greater the precision associated with the measurement of  $\tau_2$  and the longer  $\tau_2$  is, the smaller the minimum detectable absorption coefficient. According to Scherer *et al.* (6), with state-of-the-art data collection, it is possible to determine a fractional absorption of 0.3 ppm per pass by cavity-ringdown methods from a single laser pulse, a value that is in qualitative agreement with the value calculated from eq 16.

**Dynamic Range.** The dynamic range of cavity-ringdown spectroscopy extends from the minimum value for the fractional absorption ( $\alpha L$ ) per pass of less than 1 ppm up to a value for  $\alpha L$  of a few percent. The upper limit for  $\alpha L$  is determined by the short decay time that results when a sample has a relatively high fractional absorption per pass through the cavity. Consider an absorbing species with a fractional absorption per pass of 1%. With our hypothetical 0.50-m cavity with mirrors with  $R = 0.9999$ , the expected ringdown time from eq 10 would be 0.17  $\mu\text{s}$ . With our 12-bit, 20 MHz A/D converter, we could collect only about 3 data points per time constant, which would not permit a satisfactory determination of the ringdown curve. Even with the 8-bit, 100 MHz A/D converter, only about 15 data points could be collected. Fortunately, however, it is not necessary to use cavity-ringdown methods for situations where the absorption is relatively strong as there are ample alternative methods that can be used in this situation.

## Future Prospects

It is clear from the foregoing discussion that cavity-ringdown spectroscopy is a sensitive means of measuring fractional absorptions in gas-phase samples from sub-ppm levels out to the  $10^3$  ppm range. To date the majority of studies with the technique have centered on theoretical spectroscopic investigations under ideal laboratory conditions. The primary advantages of the technique are high sensitivity and freedom from pulse-to-pulse variations of the laser. Potential problems that may degrade the performance of the technique in real-world environments include: 1) the effect of turbulence-induced

changes in refractive index on beam direction within the cavity; 2) the presence of particulate matter in the cavity that can result in scattering of the beam; 3) cavity alignment problems due to thermal lensing (42); and 4) transverse mode competition, that can lead to nonexponential ringdown curves. Most of these problems, however, can be avoided by careful design of the experiment. The most serious disadvantage from a routine analytical point of view is the expense associated with the pulsed laser source, which is typically an excimer-pumped dye laser system. For this reason, some of the later chapters in this book will discuss attempts to substitute more compact, less-expensive continuous-wave lasers for the pulsed sources typically used. The goal in much of the current research in cavity-ringdown spectroscopy is to develop measurement systems that are as inexpensive and compact as possible, which can reach the photon-shot noise limit of measurement.

### Literature Cited

1. Herbelin, J. M.; McKay, J. A.; Kwok, M. A.; Ueunten, R. H.; Urevig, D. S.; Spencer, D. J.; Benard, D. J. *Appl. Opt.* **1980**, *19*(1), 144.
2. Herbelin, J. M.; McKay, J. A. *Appl. Opt.* **1980**, *20*(19), 3341.
3. Kwok, M. A.; Herbelin, J. M.; Ueunten, R. H. *Opt. Eng.* **1982**, *21*, 979.
4. Anderson, D. Z.; Frisch, J. C.; Masser, C. S. *Appl. Opt.* **1984**, *23*(8), 1238.
5. Paul, J. B.; Saykally, R. J.; *Anal. Chem.* **1997**, *69*(9), 287A-292A.
6. Scherer, J. J.; Paul, J. B.; O'Keefe, A.; Saykally, R. J.; *Chem. Rev.* **1997**, *97*, 25-51.
7. Chambers, J. M. In *Encyclopedia of Analytical Science*, Vol. 4, Townshend, A. Ed.; Academic Press: London, 1995, p. 2178.
8. Plane, J. M. C.; Smith, N. *Adv. Spectrosc. (Chichester, U.K.)* **1995**, *24*, 223-62.
9. Martina, L.; Sladkovic, R.; Slemr, F.; Werle, P. *Proc. Annu. Meet.-Air Waste Manage. Assoc.* **1994**, *87*, 1-17, 94-RA106.01.
10. Conner, C. P. Air Monitoring by Differential Optical Absorption Spectrometry in Baytown, Texas. Report, EPA/600/R-95/002, Order No. PB95-183877. Avail. NTIS from: *Gov. Rep. Announce. Index (U.S.)* **1995**, *95*(11), Abstr. No. 527,732.
11. Camy-Peyret, C.; Berqvist, B.; Galle, B.; Carleer, M.; Clerbaux, C.; Colin, R.; Fayt, C.; Goutail, F.; Nunes-Pinharanda, M.; *et al*; *J. Atmos. Chem.* **1996**, *23*, 51-80.
12. Platt, U.; Perner, D. *J. Geophys. Res.* **1980**, *85*, 7453-7458.
13. Burreev, V. S.; Vartapetov, S. K.; Weselovskii, I. A.; Shablin, Y. S. *Kvantovaya Electron. (Moscow)* **1996**, *23*, 363-67.
14. Brenner, P.; Trickl, T.; Schaefer, K.; Weisensee, U.; Kalass, D. *Proc. SPIE-Int. Soc. Opt. Eng.* **1996**, *2883*, 114-8.
15. Toriumi, R.; Tai, H.; Takeuchi, N. *Opt. Eng. (Bellingham, Wash.)* **1996**, *35*, 2371-5.
16. Milton, M. J. T.; Woods, P. T.; Partridge, R. H.; Goody, B. A. *Proc. SPIE-Int. Soc. Opt. Eng.* **1995**, *2506*, 680-8.
17. Langford, A. O. *Appl. Opt.* **1995**, *34*, 8330-40.
18. Petrin, P. R.; Nelson, D. H.; Schmitt, M. J.; Quick, C. R.; Tiee, J. J.; Whitehead, M. *Proc. SPIE-Int. Soc. Opt. Eng.* **1996**, *2702*, 28-39.
19. Robinson, R. A.; Woods, P. T.; Milton, M. J. T. *Proc. SPIE-Int. Soc. Opt. Eng.* **1995**, *2506*, 140-9.
20. Brassington, D. J. *Adv. Spectrosc. (Chichester, U.K.)* **1995**, *24*, 85-148.
21. Wohle, P.; Muecke, R. *Proc. SPIE-Int. Soc. Opt. Eng.* **1995**, *2506*, 708-19.
22. Kolb, C.; McManus, J. B.; Nelson, D. D.; Wormhoudt, J. C.; Zahniser, M. S. *Opt. Photonics News* **1996**, *7*, 34-8.

23. Kita, D.; Schiff, H. I.; MacKay, G. I. *Proc. Annu. ISA Anal. Div. Symp.* **1996**, *29*, 249-58.
24. Feher, M.; Martin, P. A. *Spectrochim. Acta, Part A* **1995**, *51A*, 1579-99.
25. Todd, L. A. *Appl. Occup. Environ. Hyg.* **1996**, *11*, 1327-34.
26. Spillane, D. E. M. In *Encyclopedia of Analytical Science*, Vol. 7, Townshend, A. Ed.; Academic Press: London, **1995**, p. 3971-3976.
27. Pao, L. H., Ed. *Optoacoustic Spectroscopy and Detection*, Academic Press: New York, **1977**.
28. Rosencwaig, A. *Photoacoustics and Photoacoustic Spectroscopy*, Vol. 57 Chemical Analysis Series, Wiley Interscience: New York, **1980**.
29. Zaleskaya, G. A.; Yakovlev, D. L.; Baranovsky, D. I.; Khodin, M. V.; Sambor, E. G. *Proc. SPIE-Int. Soc. Opt. Eng.* **1996**, *2773*, 142-6.
30. Repond, P.; Sigrist, M. W. *Appl. Opt.* **1996**, *35*, 4065-85.
31. Imasaka, T. In *Encyclopedia of Analytical Science*, Vol. 9, Townshend, A. Ed.; Academic Press: London, **1995**, p. 5167-5173.
32. Harris, J. M. In *Analytical Application of Lasers*, Piepmeier, E. H., Ed., Wiley: New York, **1985**.
33. Imasaka, T.; Ishibashi, N. *Trends in Analytical Chemistry*, **1982**, *1*, 273-277.
34. Crosely, D. R. *Adv. Ser. Phys. Chem.* **1995**, *3*, 256-317.
35. Pfab, J. *Adv. Spectrosc. (Chichester, U.K.)* **1995**, *24*, 149-222.
36. Brune, W. H.; Stevens, P. S.; Mather, J. H. *Proc. Int. Sch. Phys. "Enrico Fermi"* **1995**, *124*, 135-51.
37. Sausa, R. C.; Simeonsson, J. B.; Memire, G. W.; Detection of NO<sub>x</sub> Compounds by Laser-Induced Photofragmentation/Photoionization Spectrometry. Report (ARL-TR-873) Order No. AD-A300 053, Avail. NTIS from: *Gov. Rep. Announce Index (U.S.)* **1996**, *96(7)*, Abstr. No. 07-00,374.
38. Pastel, R. J.; Sausa, R. C. *Appl. Opt.* **1996**, *35*, 4046-52.
39. Gurlit, W.; Burrows, J. P.; Burkhard, H.; Boehm, R.; Baev, V. M.; Toschek, P. E. *Infrared Phys. Technol.* **1996**, *37*, 95-8.
40. Siegman, A. E.; *Lasers*; University Science Books: Mill Valley, CA, 1986, p. 402.
41. Ready, J. F. In *Kirk-Othmer Encyclopedia of Chemical Technology*, 4th Ed., Kroschwitz, J. I.; Howe-Grant, M. Eds., Wiley: New York, **1995**, Vol. 15, p.5.
42. Meijer, G.; Boogaarts, M. G. H.; Jongma, R. T.; Parker, D. H.; Wodtke, A. M. *Chem. Phys. Lett.* **1994**, *217*, 112.



## Chapter 3

# Introduction to Optical Cavities

**Kenneth W. Busch, Aurélie Hennequin<sup>1</sup>, and Marianna A. Busch**

**Department of Chemistry, Baylor University, Waco, TX 76798–7348**

Geometric stability of optical cavity resonators is discussed in terms of ray matrix optics. The eigenvalues of the matrix representing one round trip in the cavity are used to establish the stability criteria for optical cavities. The theory of cavity stability is applied to both stable and unstable cavities. Various types of two-mirror optical cavities are discussed.

This volume describes the development, theory, and applications of a new method of making gas-phase absorption spectroscopic measurements, known as cavity-ringdown spectroscopy (1,2). For those readers who may be unfamiliar with optical cavities, this chapter will attempt to provide the background necessary to understand the discussion in the following chapters. Since a comprehensive discussion of cavity resonators is quite extensive, we will limit our attention in this chapter to a discussion of ray optics in periodic focusing systems.

Let us begin our discussion with the concept of resonance. For a physical system, resonance occurs when the frequency of a periodic driving force approaches the natural oscillation frequency of the system. In the case of an *LC*-tank circuit, for example, the electromagnetic energy stored in the circuit is periodically converted from an electric field stored by a capacitor to a magnetic field stored by a coil. Such an electrical resonator is referred to as a lumped resonator because the energy is stored in distinctly separate parts of the system (i.e., the coil or the capacitor).

In a general sense, a cavity resonator is an enclosure with a particular volume, which is capable of storing energy that oscillates between one form and another. By contrast with the lumped resonator, cavity resonators are classified as distributed resonators where the different forms of energy are distributed throughout the volume of the cavity. In the microwave region of the spectrum, electromagnetic resonant cavities consist of closed rectangular or cylindrical sections of a hollow conducting material, hollow conducting spheres, or other hollow symmetrical shapes fabricated from conducting material. Electromagnetic energy introduced into an electromagnetic

<sup>1</sup>Current address: École Supérieure d'Optique, Institut d'Optique Théorique et Appliquée, Centre Universitaire Bât 503-BP147-91403, Orsay Cedex, France

resonant cavity is stored in the form of oscillating magnetic and electric fields. By contrast with lumped resonators, which have a single resonance frequency, cavity resonators typically can support a large number of different electromagnetic oscillations. As the size of the resonant cavity decreases, the frequencies of the electromagnetic waves that can oscillate in the cavity increase.

In the optical region of the spectrum, it is impractical to use hollow conducting material for the cavity enclosure because the size of the cavity would be too small. Instead, optical cavities are usually produced by arranging two or more mirrors so that light will be reflected back and forth in the region between the mirrors. The simplest optical cavity can be formed by arranging two mirrors so that they face each other and are separated by some distance. By eliminating the side walls of the cavity, a large number of unwanted modes can be eliminated. Three possible optical arrangements are shown in Figure 1.

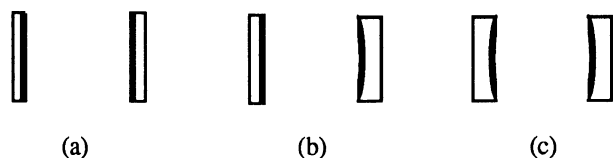


Figure 1. Optical cavities. Key: (a) plano-plano, (b) plano-concave, (c) concave-concave.

Optical cavities can be classified into two categories on the basis of losses. An optical cavity with two mirrors is said to be *stable* geometrically if a paraxial ray bundle is refocused within the cavity after successive reflections from the mirrors so that the optical energy is contained or trapped within the cavity. An optical cavity is said to be *unstable* geometrically if the ray bundle escapes the cavity after some number of reflections.

Optical cavities composed of two mirrors facing each other as shown in Figure 1 are referred to as linear- or standing-wave cavities. It is also possible to produce optical cavities known as ring- or traveling-wave cavities with three mirrors arranged in a triangular layout. In this chapter, we will confine our attention to linear cavities.

## Matrix Optics

The use of matrices as a means of performing calculations in Gaussian optics can be traced to the work of Sampson (3) in 1913. It was not until the 1960s, however, that the use of matrix methods in paraxial imaging became widely adopted (4–7). As early as 1966, Kogelnik and Li (8) published a paper in which they discuss the use of matrix optics to describe optical cavities in lasers. In this chapter, we will review the use of matrix methods to describe the properties of periodic focusing systems like optical cavities.

The most general approach to study the behavior of light in an optical cavity is based on diffraction integrals. However, if we limit our consideration to paraxial rays (i.e., rays whose deviations from the optical axis are small, i.e.  $\sin \alpha \approx \alpha$ ), simple geometric optics will suffice. Consider a generalized optical system as shown in Figure 2a, where the  $z$ -axis is the optical axis of the system. On this hypothetical two-dimensional plane, a ray will be characterized by its displacement  $r(z)$  from the  $z$ -axis and its slope, given by  $\tan \alpha(z)$ , where

$$\tan \alpha(z) = \frac{dr}{dz} \approx \alpha(z) \quad (1)$$

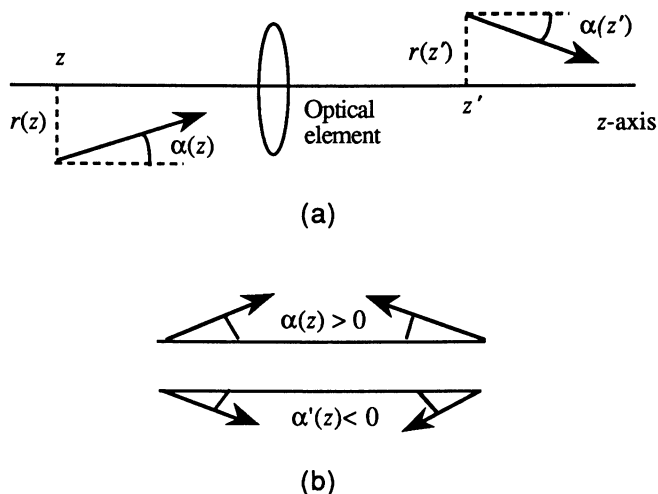


Figure 2. (a) Generalized optical system. (b) Sign convention

As shown in Figure 2a, after passing through an optical system, the ray will be characterized by a new set of parameters  $r(z')$  and  $\alpha(z')$ . The new parameters are related to the original parameters by the following matrix transformation:

$$\begin{bmatrix} r(z') \\ \alpha(z') \end{bmatrix} = \begin{bmatrix} A & B \\ C & D \end{bmatrix} \begin{bmatrix} r(z) \\ \alpha(z) \end{bmatrix} \quad (2)$$

where the  $ABCD$  matrix is the ray matrix that determines the ray parameters over the interval from  $z$  to  $z'$ . The planes passing through  $z$  and  $z'$  are reference planes and eq 2 gives the ray parameters at the output plane ( $z'$ ) in terms of the ray parameters at the input plane ( $z$ ).

At this point, it is worthwhile to discuss the sign conventions used in matrix optics. First of all, the positive direction for the  $z$ -axis is always the propagation direction of the beam. Secondly, in matrix optics, the radius of curvature of a concave mirror is positive regardless of whether the concave mirror is facing left or right. Conversely, the radius of curvature for a convex mirror is always negative. Finally, it is important to understand the sign convention for  $\alpha(z)$  in matrix optics. Regardless of whether a ray is propagating from left to right or from right to left, the sign of  $\alpha(z)$  is taken as positive if the displacement of the ray increases in the positive direction (i.e., up) along the direction of travel. In Figure 2b, the rays labeled  $\alpha(z)$  have  $\alpha$ 's that are both positive, while those labeled  $\alpha'(z)$  are both negative. These sign conventions are especially convenient in dealing with optical cavities because the ray matrix is the same regardless of whether the light is traveling from left to right or right to left.

In general, it can be shown (7) that the determinant of the ray transfer matrix will be equal to  $AD - BC = n/n'$ , where  $n$  is the refractive index of medium of the original ray and  $n'$  is the refractive index of medium for the transformed ray. If the medium is homogeneous and  $n = n'$ , the determinant of the ray transfer matrix will be equal to one.

Let us apply this concept to a ray propagating in a homogeneous medium over some distance  $d$  as shown in Figure 3. The initial parameters of the ray are  $r(z)$  and  $\alpha(z)$ . After propagating a distance  $d$ , the new parameters for the ray will be

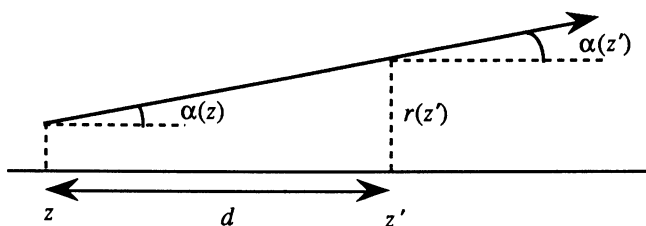


Figure 3. Ray propagating through a homogeneous medium.

$$r(z') = r(z) + \alpha(z)d \quad (3a)$$

$$\alpha(z') = \alpha(z) \quad (3b)$$

Because the medium is homogeneous, the ray is not deviated from its initial direction. In terms of the matrix notation in eq 2, eqs 3a and 3b can be represented by

$$\begin{bmatrix} r(z') \\ \alpha(z') \end{bmatrix} = \begin{bmatrix} 1 & d \\ 0 & 1 \end{bmatrix} \begin{bmatrix} r(z) \\ \alpha(z) \end{bmatrix} \quad (4)$$

It can be shown for a spherical concave mirror (5) that the ray transfer matrix is given by

$$\begin{bmatrix} A & B \\ C & D \end{bmatrix} = \begin{bmatrix} 1 & 0 \\ -\frac{2}{R} & 1 \end{bmatrix} \quad (5)$$

where  $R$  is the radius of curvature of the mirror.

With this background in mind, we are now ready to consider a simple two-mirror cavity. Consider an optical resonator composed of two spherical mirrors with radii of curvature  $R_1$  and  $R_2$ , separated by a distance  $L$ . Starting from the left-hand mirror (with a radius of curvature of  $R_1$ ), a ray propagates through a distance  $L$ , is reflected by the right-hand mirror (with a radius of curvature  $R_2$ ), returns through a distance  $L$ , and is reflected by the left-hand mirror.

One of the powerful features of matrix optics is that the matrix corresponding to several optical transformations is the product of the individual matrices for the optical system taken in reverse order to the propagation. As a result, the ray matrix corresponding to a round-trip in the cavity with the reference plane at the left-hand mirror can be represented by

$$\begin{bmatrix} A & B \\ C & D \end{bmatrix} = \begin{bmatrix} 1 & 0 \\ -\frac{2}{R_1} & 1 \end{bmatrix} \begin{bmatrix} 1 & L \\ 0 & 1 \end{bmatrix} \begin{bmatrix} 1 & 0 \\ -\frac{2}{R_2} & 1 \end{bmatrix} \begin{bmatrix} 1 & L \\ 0 & 1 \end{bmatrix} \quad (6a)$$

$$\begin{bmatrix} A & B \\ C & D \end{bmatrix} = \begin{bmatrix} 1 - \frac{2L}{R_2} & 2L - \frac{2L^2}{R_2} \\ \frac{4L}{R_1 R_2} - \frac{2}{R_1} - \frac{2}{R_2} & 1 - \frac{2L}{R_2} - \frac{4L}{R_1} + \frac{4L^2}{R_1 R_2} \end{bmatrix} \quad (6b)$$

where the trace of the matrix ( $T = A + D$ ) in eq 6b is

$$T = 4 \left( 1 - \frac{L}{R_1} \right) \left( 1 - \frac{L}{R_2} \right) - 2 \quad (7)$$

### Eigenvectors and Eigenvalues

Having determined the ray matrix  $\mathbf{M}$  (eq 6b) corresponding to a round trip through the cavity, we now desire to determine the effect of  $n$  round-trips. In terms of ray optics, for an optical cavity to be stable, it must be able to trap rays within the cavity so that they are unable to escape after multiple reflections. Thus, after  $n + 1$  round trips through the cavity, if  $|r_{n+1}| > |r_n| > \dots > |r_1| > |r_0|$  and  $|\alpha_{n+1}| > |\alpha_n| > \dots > |\alpha_1| > |\alpha_0|$ , the ray will eventually walk out of the cavity. If we express the ray parameters for the  $(n+1)$ th round-trip in terms of matrix notation, we obtain

$$\begin{bmatrix} r_{n+1} \\ \alpha_{n+1} \end{bmatrix} = \mathbf{M} \begin{bmatrix} r_n \\ \alpha_n \end{bmatrix} \quad (8)$$

If solutions to eq 8 can be found such that

$$\begin{bmatrix} r_{n+1} \\ \alpha_{n+1} \end{bmatrix} = \lambda \begin{bmatrix} r_n \\ \alpha_n \end{bmatrix} \quad (9)$$

where  $\lambda$  is a constant, the problem of stability will depend on the allowed values for  $\lambda$ . If we combine eqs 8 and 9, to give

$$\mathbf{M} \begin{bmatrix} r_n \\ \alpha_n \end{bmatrix} = \lambda \begin{bmatrix} r_n \\ \alpha_n \end{bmatrix} \quad (10)$$

we see that eq 10 is a classic algebraic eigenvalue problem. So to answer our question regarding cavity stability, we seek the eigenvalues that satisfy the equation

$$\mathbf{M} \mathbf{r} = \lambda \mathbf{r} \quad (11)$$

where  $\mathbf{M} = \begin{bmatrix} A & B \\ C & D \end{bmatrix}$ ,  $\mathbf{r} = \begin{bmatrix} r \\ \alpha \end{bmatrix}$  and  $\lambda$  is a scalar eigenvalue.

Equation 11 can be rewritten as

$$[\mathbf{M} - \lambda \mathbf{I}] \mathbf{r} = \begin{bmatrix} (A - \lambda) & B \\ C & (D - \lambda) \end{bmatrix} \begin{bmatrix} r \\ \alpha \end{bmatrix} = 0 \quad (12)$$

where  $\mathbf{I}$  is the identity matrix. According to Cramer's rule, nonzero solutions to eq 12 are possible only if the determinant of the  $2 \times 2$  matrix in eq 12 is zero.

$$\begin{vmatrix} (A - \lambda) & B \\ C & (D - \lambda) \end{vmatrix} = (A - \lambda)(D - \lambda) - BC = 0 \quad (13)$$

Realizing that  $AD - BC = 1$ , we obtain the characteristic equation for  $\lambda$  from eq 13.

$$\lambda^2 - T\lambda + 1 = 0 \quad (14)$$

where  $T = A + D$  is the trace of  $\mathbf{M}$ . Solving eq 14 gives two solutions for  $\lambda$ ,

$$\lambda_1 = \frac{T + \sqrt{T^2 - 4}}{2} \quad (15)$$

and

$$\lambda_2 = \frac{T - \sqrt{T^2 - 4}}{2} \quad (16)$$

where  $\lambda_1 \lambda_2 = 1$  and  $\lambda_1 + \lambda_2 = T$ .

Since there are two eigenvalues ( $\lambda_1$  and  $\lambda_2$ ), there are also two eigenvectors, which can be written as  $\mathbf{M} \mathbf{r}_1 = \lambda_1 \mathbf{r}_1$  and  $\mathbf{M} \mathbf{r}_2 = \lambda_2 \mathbf{r}_2$ . These eigenvectors can be obtained by expanding eq 11 to give  $Ar + B\alpha = \lambda r$  and  $Cr + D\alpha = \lambda \alpha$ . Solving these equations for  $r/\alpha$  gives

$$\frac{r}{\alpha} = \frac{(\lambda - D)}{C} \text{ or } \frac{B}{(\lambda - A)} \quad (17)$$

If we arbitrarily assume  $\alpha = C$  or  $r = B$ , we obtain the following eigenvectors

$$\mathbf{r}_1 = \begin{bmatrix} \lambda_1 - D \\ C \end{bmatrix} \text{ or } \begin{bmatrix} B \\ \lambda_1 - A \end{bmatrix} \quad (18)$$

and

$$\mathbf{r}_2 = \begin{bmatrix} \lambda_2 - D \\ C \end{bmatrix} \text{ or } \begin{bmatrix} B \\ \lambda_2 - A \end{bmatrix} \quad (19)$$

The eigenvectors  $\mathbf{r}_1$  and  $\mathbf{r}_2$  are linearly independent and form a basis set so that any arbitrary input ray,  $\mathbf{r}_0 = \begin{bmatrix} r_0 \\ \alpha_0 \end{bmatrix}$ , can be expressed as a linear combination of the two eigenvectors, given by

$$\mathbf{r}_0 = c_1 \mathbf{r}_1 + c_2 \mathbf{r}_2 \quad (20)$$

where  $c_1$  and  $c_2$  are appropriate coefficients that depend on the initial conditions ( $\mathbf{r}_0$ ). Finally, with this background in mind, we can determine  $\mathbf{r}_n$  after  $n$  round-trips through the cavity to be,

$$\mathbf{r}_n = \mathbf{M}^n \mathbf{r}_0 = \mathbf{M}^n (c_1 \mathbf{r}_1 + c_2 \mathbf{r}_2) = c_1 \lambda_1^n \mathbf{r}_1 + c_2 \lambda_2^n \mathbf{r}_2 \quad (21)$$

### Criteria for Cavity Stability

**Unstable Cavities.** We are now in a position to determine the stability of the cavity. If  $\left| \frac{T}{2} \right| > 1$ , the discriminants in eqs 15 and 16 are both positive, and both solutions are real. Since  $\lambda_1 \lambda_2 = 1$  and  $\lambda_1 + \lambda_2 = T$ , we can take the solutions for  $\lambda_1$  and  $\lambda_2$  to be  $e^b$  and  $e^{-b}$ , respectively, where  $b$  is equal to  $\cosh^{-1}(T/2)$ . For this case, the general solution according to eq 21 will be

$$\mathbf{r}_n = c_1 e^{nb} \mathbf{r}_1 + c_2 e^{-nb} \mathbf{r}_2 \quad (22)$$

where  $c_1$  and  $c_2$  are real and depend on the initial conditions. It is clear from eq 22 that as  $n \rightarrow \infty$ ,  $r_n$  also approaches infinity and the beam will leave the cavity. So, if  $|T| > 2$ , the cavity will be unstable.

**Stable Cavities.** If  $\left| \frac{T}{2} \right| < 1$ , the discriminants in eqs 15 and 16 will both be negative, and both solutions of eqs 15 and 16 will be complex. If  $T/2 = m$ , eqs 15 and 16 can be written as

$$\lambda_1, \lambda_2 = m \pm j \sqrt{1 - m^2} = \cos b \pm j \sin b = e^{\pm j b} \quad (23)$$

where  $j = \sqrt{-1}$ . Once again,  $\lambda_1 + \lambda_2 = T$ , so  $b$  is equal to  $\cos^{-1}(T/2)$ . From eq 21,  $\mathbf{r}_n$  will be given by

$$\mathbf{r}_n = c_1 e^{jnb} \mathbf{r}_1 + c_2 e^{-jnb} \mathbf{r}_2 \quad (24)$$

$$= c_1 (\cos nb + j \sin nb) \mathbf{r}_1 + c_2 (\cos nb - j \sin nb) \mathbf{r}_2 \quad (25)$$

$$= (c_1 \mathbf{r}_1 + c_2 \mathbf{r}_2) \cos nb + (c_1 \mathbf{r}_1 - c_2 \mathbf{r}_2) j \sin nb \quad (26)$$

$$\mathbf{r}_n = \cos nb \mathbf{r}_0 + \sin nb \mathbf{s}_0 \quad (27a)$$

where  $\mathbf{r}_0$  is given by eq 20, and

$$\mathbf{s}_0 = j (c_1 \mathbf{r}_1 - c_2 \mathbf{r}_2) \quad (27b)$$

In order for eq 27a to be valid physically, we require that the components of  $\mathbf{r}_n$  in eq 27a be real. As can be shown by substitution (eqs 22, 20 and 27b), this will be true if

$c_1 = c_2 = c$ ,  $\mathbf{r}_1 = \begin{bmatrix} B \\ e^{jb} - A \end{bmatrix}$  and  $\mathbf{r}_2 = \begin{bmatrix} B \\ e^{-jb} - A \end{bmatrix}$  (see eqs 18 and 19). After some algebraic manipulations it follows that

$$\mathbf{s}_0 = -2c \begin{bmatrix} 0 \\ \sin b \end{bmatrix} \quad (28)$$

and

$$\mathbf{r}_0 = 2c \begin{bmatrix} B \\ \cos b - A \end{bmatrix} \quad (29)$$

where the components of  $\mathbf{r}_0$  and  $\mathbf{s}_0$  are all real. Since eq 27 is bounded, the beam remains in the cavity as  $n \rightarrow \infty$ . So, if  $|T| < 2$ , the cavity will be stable.

**g-Parameters.** If the stability condition is interpreted in terms of eq 7, a two-mirror resonator cavity will be stable if

$$0 \leq g_1 g_2 \leq 1 \quad (30)$$

where

$$g_1 = \left(1 - \frac{L}{R_1}\right) \quad (31)$$

$$g_2 = \left(1 - \frac{L}{R_2}\right) \quad (32)$$

Equation 30 expresses the stability condition for the cavity in terms of the so-called *g*-parameters (eqs 31 and 32) of the cavity.

The stability condition given by eq 30 can be represented graphically by means of a stability diagram where  $g_2$  is plotted against  $g_1$  as shown in Figure 4. On this diagram, a point that falls in the shaded region corresponds to a stable periodic focusing system that is capable of trapping a Gaussian beam if the mirrors are large enough to prevent losses from diffraction. Points on the diagram that lie outside the shaded area correspond to unstable periodic focusing systems. In unstable systems, rays will steadily migrate across the mirrors upon successive reflections until they finally exit the cavity.

**Graphical Determination of Stability.** In addition to using the *g*-parameters, cavity stability can also be determined graphically by means of resonator circle diagrams (9-11). In this approach, a two-mirror resonator composed of two spherical mirrors with radii of curvature  $R_1$  and  $R_2$  are drawn so that they are separated by a distance  $L$ . Circles with diameters (not radii) equal to  $R_1$  and  $R_2$  are then drawn so that the respective circles are tangent to the concave surface of the respective mirrors. If the circles drawn in this fashion intersect, the cavity will be stable. A line connecting the



two intersection points will indicate the location of the narrowest part of the beam (the beam waist) in the cavity. Figure 5 shows the situation for three different mirror arrangements.

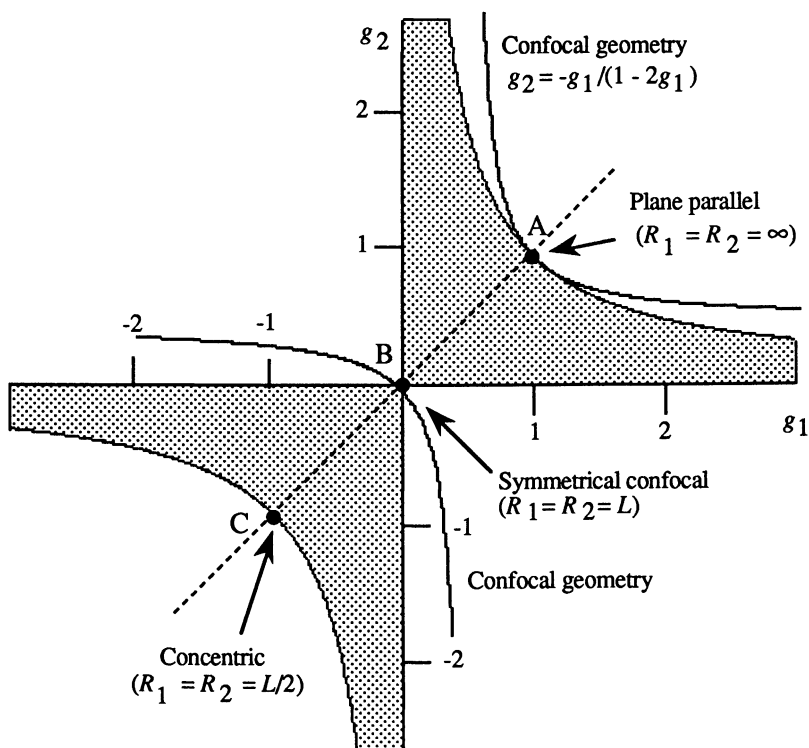


Figure 4. Stability diagram.

**Applications of Matrix Optics to Cavity Stability.** At this point, we are in a position to illustrate the properties of simple two-mirror cavities using the matrix optics approach to trace an initial ray through successive round-trips in the cavity. Consider a hypothetical cavity composed of two concave spherical mirrors whose radii of curvature are both equal to 6 m and whose separation  $L$  is 0.5 m. This cavity is typical of the type used in cavity ringdown spectroscopy ( $I$ ). From eqs 31 and 32, it is clear that  $g_1 = g_2 = 0.92$  for this cavity and the cavity satisfies the stability condition given in eq 30. From eq 6b, the  $M$  matrix for the cavity can be determined from the radii of curvature and the separation distance. If an arbitrary ray  $\mathbf{r}_0$ , originating from a reference plane at the vertex of the left-hand mirror, starts out 5 mm above the optical axis at an angle of 0.02 radians ( $1.15^\circ$ ), then  $\mathbf{r}_0 = \begin{bmatrix} 0.005 \\ 0.02 \end{bmatrix}$ , and we can now follow the path of this ray through successive reflections in the cavity. Table I gives the values for the ray vector  $\mathbf{r}_n$  after  $n$  successive round-trips through the cavity. If we plot the value of  $r$  (a scalar) versus the number of round-trips made by the initial ray through the cavity, a sinusoidal pattern is produced as shown in Figure 6. This sinusoidal behavior is predicted by eq 27 for a stable cavity.

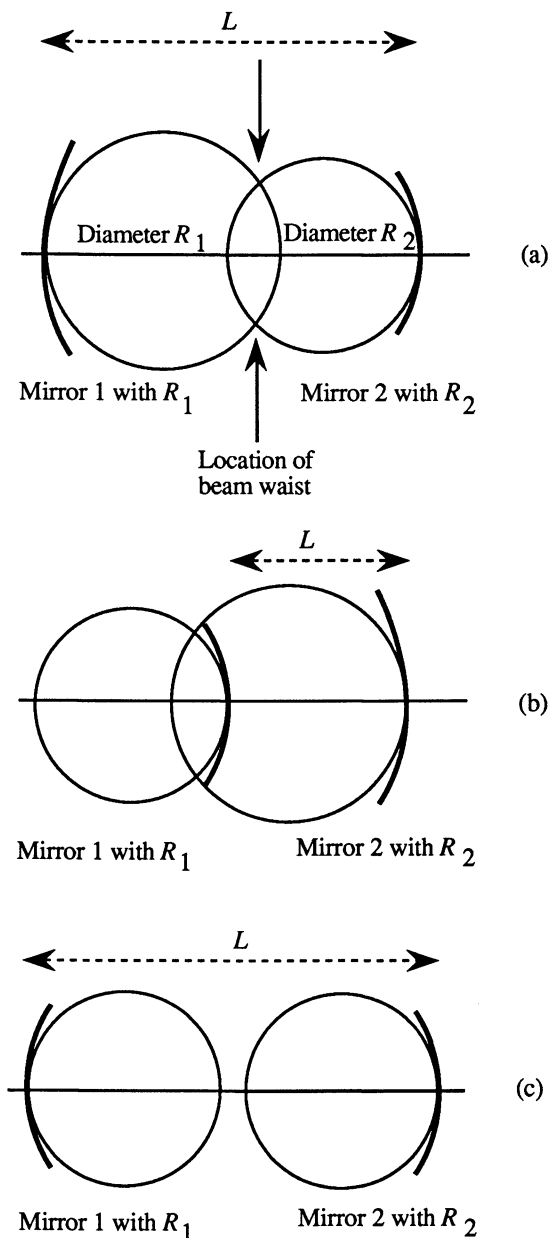


Figure 5. Resonator circle diagrams for three cavities composed of two mirrors with radii of curvature  $R_1$  and  $R_2$ . (a) Stable cavity composed of two concave mirrors; (b) Stable cavity composed of a convex mirror (1) and a concave mirror (2); (c) Unstable cavity composed of two concave mirrors. Note that  $R_1$  and  $R_2$  are also the diameters of the circles drawn tangent to the surfaces of the respective mirrors, and  $L$  is the distance between the two mirrors.

If we perform the same analysis for an unstable cavity consisting of two spherical mirrors with radii of curvature of 0.5 m separated by 1.1 m, we obtain the results shown in Table II for successive round-trips in the cavity for an arbitrary paraxial ray given by  $\mathbf{r}_0 = \begin{bmatrix} 0.00 \\ 0.02 \end{bmatrix}$ . Notice that in Table II, each successive value of  $|r_n|$  and  $|\alpha_n|$  is greater than the preceding values, a characteristic of an unstable cavity. If these results are represented diagrammatically in Figure 7, we see that even for a highly paraxial ray, successive reflections cause the ray to walk across the mirror and

**Table I. Ray Parameters after Successive Reflections in the Cavity**

<i>Number of round-trips within the cavity (n)</i>	<i>r<sub>n</sub> (mm)</i>	<i>α<sub>n</sub> (radians)</i>
1	22	0.007
2	26	-0.010
3	12	-0.021
4	-9	-0.019
5	-24	-0.004
6	-24	0.013
7	-9	0.021
8	12	0.017
9	26	0.001
10	23	-0.015

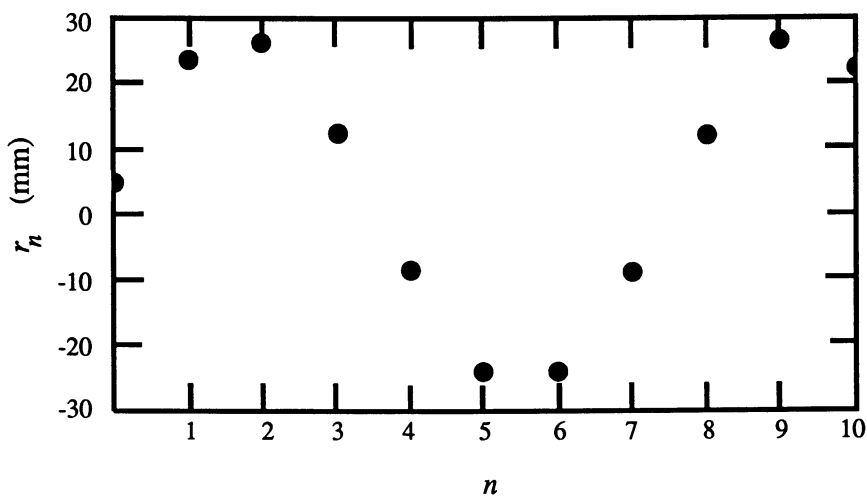


Figure 6. Transverse ray displacement,  $r_n$ , versus the number of round-trips,  $n$ , in the cavity.

**Table II. Ray Parameters after Successive Reflections in an Unstable Cavity**

<i>Number of round-trips within the cavity (n)</i>	<i>r<sub>n</sub> (mm)</i>	<i>α<sub>n</sub> (radians)</i>
1	-13	0.036
2	-50	0.13
3	-173	0.452

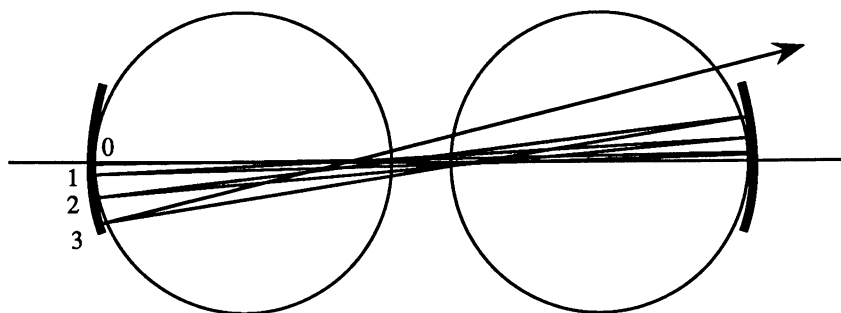


Figure 7. Hypothetical cavity showing two concave spherical mirrors (heavy lines) whose radii of curvature are both equal to 0.5 m and whose separation is 1.1 m. Since the resonator circles do not overlap, the cavity is unstable. Numbers indicate the number of round trips within the cavity.

eventually leave the cavity after only a few round-trips. Notice in Figure 7 that the resonator circles do not intersect, indicating that the cavity is unstable.

### Two-Mirror Cavities

A variety of two-mirror cavities can be produced using various combinations of mirrors as shown in Figure 8. These various cavities have different properties in terms of spot size and sensitivity with regard to misalignment. Spot size refers to the cross-sectional diameter of the beam that is trapped within the cavity, which determines the volume of the cavity that is capable of being probed by the beam. In terms of applicability to cavity ringdown spectroscopy, insensitivity toward misalignment is always desirable, while the desired spot size will depend on the application. Symmetrical cavities, where  $R_1 = R_2$ , fall on the line ABC in Figure 4. Point A in Figure 4 corresponds to a symmetrical cavity composed of two plane mirrors (a Fabry-Perot cavity) where  $R_1 = R_2 = \infty$  and  $g_1 = g_2 = 1$ . So-called long-radius resonators, which are a variation of the Fabry-Perot cavity, are produced when  $R_1 = R_2 \gg L$ , where  $L$  is the separation distance between the two mirrors. Point B in Figure 4 corresponds to the situation where  $R_1 = R_2 = L$ . This type of cavity is referred to as a symmetrical confocal cavity, since the focal points of both mirrors ( $R/2$ ) coincide halfway between the mirror separation. Since  $L = R$ ,  $g_1$  and  $g_2$  are both zero. When  $R_1 = R_2 = L/2$ , the cavity is referred to as a symmetrical concentric cavity, and  $g_1 = g_2 = -1$  (point C in Figure 4). A variation of the symmetric

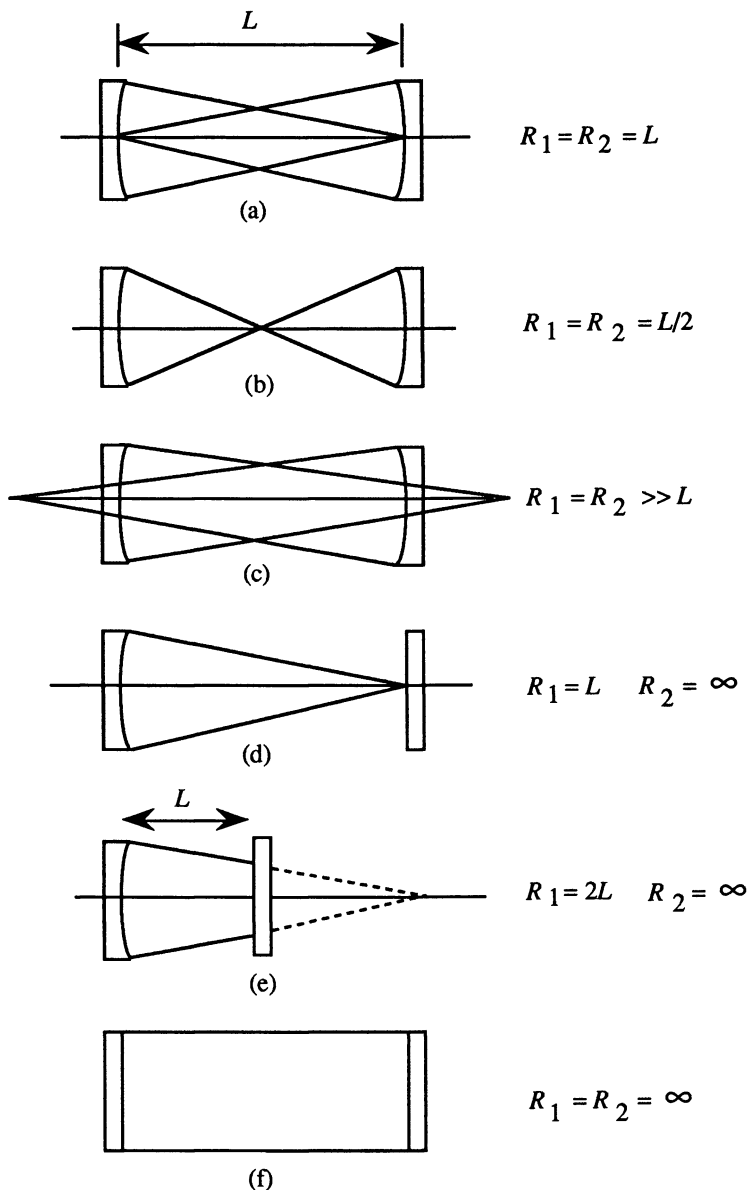


Figure 8. Two-mirror cavities. (a) confocal; (b) concentric; (c) long-radius; (d) hemispherical; (e) semi-confocal; (f) Fabry-Perot.

concentric cavity is the near concentric cavity where  $R_1 = R_2$  and  $R_1 + R_2$  is slightly less than  $L$ .

While the confocal cavity is relatively insensitive to misalignment, it suffers from a small spot size, which limits the volume of the cavity sampled by the beam. By contrast, long-radius resonators have a large spot size, but require careful alignment to remain stable.

### Acknowledgments

The authors would like to thank Baylor University for providing a summer fellowship to Aurélie Hennequin and the National Science Foundation for sponsoring the Summer Undergraduate Research Experience Program at Baylor University. The authors would also like to thank Prof. Nathalie Westbrook of École Supérieure d'Optique for her valuable comments on the manuscript.

### Literature Cited

1. Paul, J. B.; Saykally, R. J.; *Anal. Chem.* **1997**, *69*(9), 287A-292A.
2. Scherer, J. J.; Paul, J. B.; O'Keefe, A.; Saykally, R. J.; *Chem. Rev.* **1997**, *97*, 25-51.
3. Sampson, R. A.; *Phil. Trans. Roy. Soc.* **1913**, *212*, 149-185.
4. O'Neill, E. L. *Introduction to Statistical Optics*; Addison-Wesley: Reading, MA, 1963.
5. Brouwer, W. *Matrix Methods in Optical Instrument Design*; W. A. Benjamin: New York, NY, 1964.
6. Halbach, K.; *Amer. J. Phys.* **1964**, *32*, 90.
7. Gerrard, A.; Burch, J. M. *Introduction to Matrix Methods in Optics*; John Wiley: New York, NY, 1975.
8. Kogelnik, H.; Li, T.; *Appl. Optics* **1966**, *5*, 1550.
9. Deschamps, G. A.; Mast, P. E. In *Proceedings of the Symposium on Quasi-Optics*; Fox, J., Ed.; Brooklyn Polytechnic Press: New York, NY, 1964, p. 379.
10. Laures, P.; *Appl. Optics* **1967**, *6*, 747-755.
11. Siegman, A. E.; *Lasers*; University Science Books: Mill Valley, CA, 1986, p. 748.

## Chapter 4

# Mode Formation in Optical Cavities

**Kenneth W. Busch, Aurélie Hennequin<sup>1</sup>, and Marianna A. Busch**

**Department of Chemistry, Baylor University, Waco, TX 76798–7348**

Longitudinal mode formation in optical cavities is introduced with a discussion of the Fabry-Perot cavity. Transverse mode formation is discussed in terms of Hermite-Gaussian waves for cavities with rectangular cross-sectional symmetry and in terms of Laguerre-Gaussian waves for cavities with circular cross-sectional symmetry. Cavity resonance frequencies for both types of waves are discussed. Finally, the effect of the  $g$ -parameters on mode spacing is discussed.

We have seen in the previous chapter that an optical cavity, in the most general sense, is a volume of space with boundary conditions that depend upon the placement and characteristics of the optical elements that make up the cavity. Such a cavity may be stable or unstable depending on the values of the  $g$ -parameters ( $I$ ). In the previous discussion ( $I$ ), cavity behavior was discussed entirely from the point of view of geometrical optics, without regard for the wave character of the radiation. In this chapter, we will examine the development of resonant modes in optical cavities. To understand the development of resonant modes in optical cavities, we must consider the oscillating character of the light beam as it passes back and forth within the cavity. In our discussion, we will limit our attention to stable cavities where the energy is confined near the optical axis (paraxial conditions). For a mode to develop in such an optical cavity, the electric vector of the oscillating light wave must be zero at the boundaries of the cavity. The standing waves that develop within the cavity are known as cavity modes.

The role of mode formation in cavity-ringdown spectroscopy has been discussed extensively in the literature (2-6). When a pulsed laser with a very short pulse duration is used, the coherent wavetrain emitted during the pulse can be less than the length of the optical cavity. If this is true, mode formation is considered to be unimportant since the returning wave can never overlap the initial wave because the wavetrain is too short. Under these experimental conditions, the pulse is believed to behave like a "photon bullet" (6,7). While the photon bullet model is clearly applicable to the case where short duration pulses (~15 ns) from a pulsed laser source are used, experiments where continuous-wave lasers are used in cavity-ringdown spectroscopy may involve mode

<sup>1</sup>Current address: École Supérieure d'Optique, Institut d'Optique Théorique et Appliquée, Centre Universitaire Bât 503-BP147-91403, Orsay Cedex, France

formation. Moreover, since some authors (3,5) discuss the cavity-ringdown experiment in terms of mode formation, this chapter will attempt to provide the background material needed for understanding mode formation in optical cavities.

Modes in cavities are classified into two basic types. Longitudinal (or axial) modes determine the resonant oscillation frequencies that satisfy the wavelength requirements of the cavity along a given optical path (i.e., the electric vector is zero at the reflecting surface). Transverse modes, which travel over slightly different optical paths, determine the intensity pattern and divergence of the propagating beam. In other words, transverse modes determine the cross-sectional geometry of the beam. Each transverse mode, propagating along a unique direction, can have various allowed longitudinal modes associated with it.

### Fabry-Perot Cavity

Since one of the later contributions to this volume deals with the use of a Fabry-Perot (FP) cavity, we will begin our discussion of cavity modes with a brief introduction to the principles behind this type of cavity. In the previous chapter (1), we saw that a Fabry-Perot cavity consists of two plane mirrors facing each other and separated by some distance. Figure 1 shows a schematic diagram of an FP-cavity where the distance between the reflecting surfaces is  $L$  and the index of refraction of the medium between the mirrors is  $n$ . Outside the cavity, the index of refraction of the medium is taken as  $n'$ . Let us consider a hypothetical plane wave of infinite extent that strikes the cavity at an angle  $\theta'$  to the normal. The complex amplitude of the wave can be expressed as

$$u(t,z) = A(z) \exp \left[ -j(\omega t - n'kz + \phi) \right] \quad (1)$$

where  $j$  is  $\sqrt{-1}$ ,  $\omega$  is the angular frequency of the light wave,  $k$  is the propagation number given by  $k = 2\pi/\lambda$ ,  $\lambda$  is the vacuum wavelength, and  $\phi$  is a phase angle.  $A(z)$  is an amplitude factor that depends on distance  $z$  along the optical axis. As shown in Figure 1, a series of waves is reflected and transmitted by the cavity. To determine the transmission of the cavity, we must sum the amplitudes of the transmitted waves.

**Transmission of a Fabry-Perot Cavity.** We begin our discussion by considering the path difference between two successive partial waves. As shown in Figure 1, the path difference between two successive partial waves is given by

$$\delta = n(AB + BC) - n'(AD) \quad (2a)$$

$$= n \left( \frac{2L}{\cos \theta} \right) - n' \left( \frac{2L}{\cos \theta} \sin \theta \sin \theta' \right) \quad (2b)$$

where  $AB = BC = L/\cos \theta$ ,  $AC = 2L \tan \theta$ , and  $AD = AC \sin \theta'$ . Substituting Snell's law ( $n \sin \theta = n' \sin \theta'$ ) into eq 2b gives

$$\delta = n \left( \frac{2L}{\cos \theta} \right) - n \left( \frac{2L}{\cos \theta} \right) \sin^2 \theta = n \left( \frac{2L}{\cos \theta} \right) (1 - \sin^2 \theta) \quad (3a)$$

$$\delta = 2nL \cos \theta \quad (3b)$$



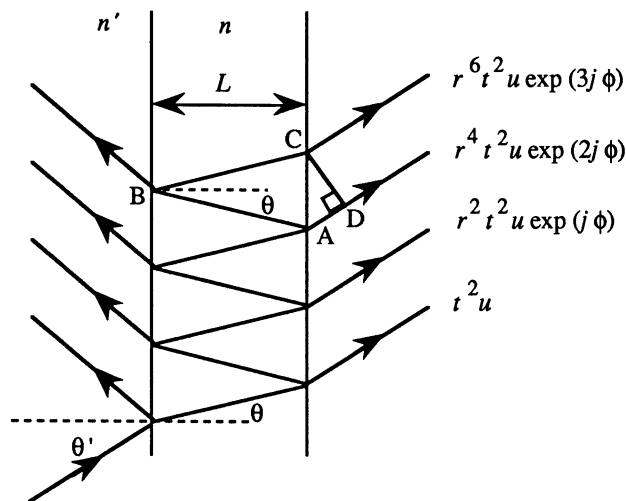


Figure 1. Propagation of an incident wave in a Fabry-Perot cavity

Since the corresponding phase delay is given by  $\phi = 2\pi\delta/\lambda$ , the path difference in eq 3b becomes

$$\phi = \frac{4\pi nL \cos \theta}{\lambda} = \frac{4\pi nLv \cos \theta}{c} \quad (4)$$

where  $\nu$  is the frequency of the light and  $c$  is the speed of light.

If we define  $r$  and  $t$  as the *amplitude* reflection and transmission coefficients, respectively, from  $n$  to  $n'$  or from  $n'$  to  $n$ , the corresponding reflectance and transmittance (in terms of intensity) will be given by  $R = r^2$  and  $T = t^2$ , respectively (recall that the intensity is the square of the amplitude). Figure 1 shows the situation for the transmitted amplitudes that result from an incident wave whose complex amplitude is given by  $U_0 = u \exp(-j\phi_0)$ , where  $\phi_0$  is the phase delay between the incident wave and the first transmitted wave. The total transmitted amplitude for the wave,  $A_t$ , will be given as the sum of the individual amplitudes

$$A_t = t^2 u + r^2 t^2 u \exp(j\phi) + r^4 t^2 u \exp(2j\phi) + r^6 t^2 u \exp(3j\phi) + \dots \quad (5a)$$

$$A_t = t^2 u \left[ 1 + r^2 \exp(j\phi) + r^4 \exp(2j\phi) + r^6 \exp(3j\phi) + \dots \right] \quad (5b)$$

$$A_t = \frac{t^2 u}{1 - r^2 \exp(j\phi)} = \frac{T u}{1 - R \exp(j\phi)} \quad (5c)$$

The magnitude of the transmitted intensity is given by

$$I_t = A_t A_t^* \quad (6)$$

where  $A_t^*$  is the complex conjugate of  $A_t$ . Evaluating eq 6 in terms of eq 5c gives

$$I_t = \frac{I_0 T^2}{(1-R)^2 + 4R \sin^2\left(\frac{\phi}{2}\right)} \quad (7)$$

where  $I_t$  is the transmitted intensity and  $I_0 = u^2$  is the incident intensity. Equation 7 could also be written in the form (8)

$$I_t = \frac{I_0 T^2}{(1-R)^2} \left[ 1 + \frac{4R}{(1-R)^2} \sin^2\left(\frac{\phi}{2}\right) \right]^{-1} \quad (8)$$

which is known as Airy's formula.

The transmission of the cavity will be a maximum wherever  $\phi$  is an integral multiple of  $2\pi$ . From eq 4, this corresponds to

$$p\lambda_{\max} = 2nL \cos \theta \quad (9)$$

or

$$\nu_{\max} = \frac{pc}{2nL \cos \theta} \quad (10)$$

where  $p$  is an integer known as the mode index,  $c$  is the speed of light,  $\lambda_{\max}$  is the wavelength corresponding to a transmission maximum of the cavity, and  $\nu_{\max}$  is the frequency corresponding to a transmission maximum of the cavity.

Figure 2 shows a plot of the transmission of a Fabry-Perot cavity using eq 7 for the case where there is no absorption by the medium in the cavity (i.e.,  $R + T = 1$ ).

**Properties of a Fabry-Perot Cavity.** Consider a cavity where  $\theta$  is zero,  $p$  is one, and the reflection coefficient  $R$  in eq 7 is close to one. According to eq 9, for this case, a beam will be transmitted through the cavity as long as the separation between the reflecting surfaces of the mirrors is some integral multiple of half the wavelength of the light. As a result, an FP-cavity can be used to scan a certain spectral range by varying the value of  $L$ . If the spacing between the mirrors is fixed, the cavity is known as a Fabry-Perot etalon.

**Free Spectral Range.** The free spectral range of an FP-cavity can be defined in terms of the frequency separation between two successive transmission frequencies (or resonant modes). According to eq 10, at normal incidence ( $\cos \theta = 1$ ) this frequency separation will be

$$\Delta\nu_{\text{fsr}} = \nu_{p+1} - \nu_p \quad (11a)$$

$$\Delta\nu_{\text{fsr}} = \frac{c}{2nL} \quad (11b)$$

**Full Width at Half Maximum.** Let us consider the full width of a transmission band at half the peak value. The transmission profile as a function of frequency can be obtained from eqs 4 and 7. If we substitute a value of 0.5 for  $I_t/I_0$  in eq 7, and evaluate the expression for  $\phi/2$ , we obtain

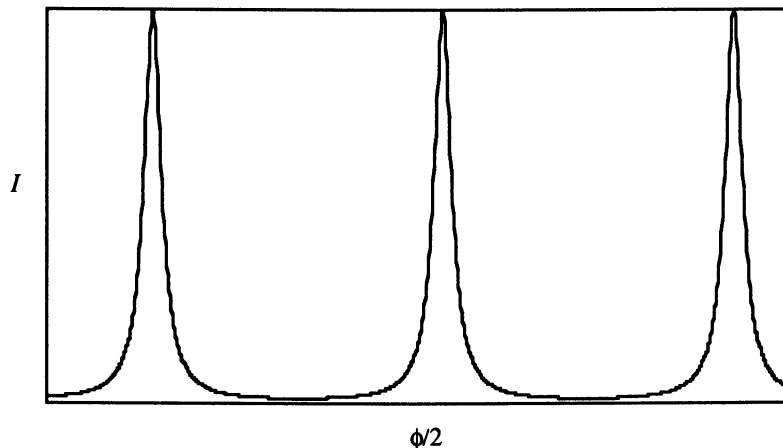


Figure 2. Transmittance of an FP-cavity versus  $\phi/2$  for  $R = 0.80$

$$\frac{\phi}{2} = \frac{1-R}{2\sqrt{R}} \quad (12)$$

If we then substitute eq 4 for  $\phi$  into eq 12 and double the result to get the full width at half maximum, we obtain the following expression:

$$\Delta\nu_{1/2} = \frac{c}{2\pi nL \cos \theta} \left( \frac{1-R}{\sqrt{R}} \right) \quad (13)$$

Equation 13 indicates that the width of the transmission bands obtained with the Fabry-Perot cavity become progressively narrower as  $R$  approaches 1.

**Finesse.** The finesse of an FP-etalon is a measure that characterizes the quality of the resolution obtained with the cavity and is given by the ratio of the free spectral range (eq 11b) to the full width at half the maximum of a transmission band. Thus,

$$F = \frac{\Delta\nu_{\text{fsr}}}{\Delta\nu_{1/2}} \quad (14)$$

For  $\theta = 0$ ,  $F$  is equal to

$$F = \pi \frac{\sqrt{R}}{1-R} \quad (15)$$

**Practical Considerations.** In order for the resonance condition given by eq 10 to be valid for the entire surface of a large mirror, the surface quality of the mirror becomes an important factor. For example, if  $R$  is 0.90,  $F$  is 30, and the surface defects in the mirror must be less than  $\lambda/60$ .

## Longitudinal Modes

Longitudinal modes determine the frequencies of radiation that satisfy the wavelength requirements of the cavity (i.e., the fact that the electric vector of the light wave must be zero at the reflective surfaces of the mirrors). In the previous discussion of FP-cavities, we have seen that in order for a given longitudinal mode to be resonant, the phase delay of a wave corresponding to a round-trip within the cavity must be equal to  $2p\pi$ , where  $p$  is the longitudinal mode index. Equation 10 gives the frequencies of maximum transmission expected for a plane wave in an FP-cavity. In general, for a cavity where the wavefront is not strictly planar, the allowed oscillation frequencies for longitudinal modes will be given by

$$\nu_p = \frac{c}{2L} \left( p - \frac{\alpha}{2\pi} \right) \quad (16)$$

where  $\nu_p$  is the frequency of the radiation,  $c$  is the speed of light,  $L$  is the length of the cavity,  $p$  is the longitudinal mode index (an integer), and  $\alpha$  is a corrective term to account for the fact that the wave is not planar. From eq 16, the spacing between two adjacent longitudinal modes will be

$$\Delta\nu = \frac{c}{2L} \quad (17)$$

## Transverse Modes

In addition to longitudinal modes or axial modes, various types of transverse modes, which determine the cross-sectional profile of the beam, can develop in cavities. Let us begin by considering the transverse profile of the amplitude of the electric field for a light wave, given by  $u(x,y,z)$ . For a mode to develop, this transverse profile must be the same after one round-trip. If  $\tau$  is an operator that characterizes a round-trip within the cavity, we can write  $\tau[u_{\text{mode}}(x,y,z)] = u_{\text{mode}}(x,y,z)$ . From this we can see that  $u_{\text{mode}}(x,y,z)$  is an eigenvector of the transformation  $\tau(\mathcal{O})$ . For a given cavity, there are many eigenvectors, and each represents a transverse mode, characterized by a particular transverse amplitude distribution. These modes are referred to as TEM (transverse electromagnetic modes) because the electric field and the magnetic field are quasi-perpendicular to the propagation direction. The lowest order transverse mode, or fundamental mode (TEM<sub>00</sub>), has a gaussian cross-sectional profile, while higher order modes are broken up into an array of sub-beams.

For a given transverse mode, there are an infinite number of longitudinal modes associated with it, separated by  $\Delta\nu$ . Since different transverse modes require different geometrical distributions of energy, the phase delay for a round-trip through the cavity will typically differ slightly for different transverse modes. In general, the frequency spacing between two successive transverse modes is usually much smaller than the spacing between two successive longitudinal modes (eq 17), and depends on the characteristics of the cavity (length, mirror radii).

**Quantitative Aspects of Transverse Modes.** To treat the transverse modes, we must determine  $u(x,y,z)$ , which is the transverse profile for the complex amplitude of the electromagnetic field given by

$$E(x,y,z,t) = u(x,y,z)e^{j\omega t} \quad (18)$$

where  $\omega$  is the angular frequency of the light wave. We can obtain  $u(x,y,z)$  by solving the propagation equation,

$$\nabla^2 E(x,y,z) + k^2 E(x,y,z) = 0 \quad (19a)$$

where  $k$  is the propagation number, given by  $2\pi/\lambda$ ,  $\lambda$  is the wavelength of the light, and

$$\nabla^2 = \frac{\partial^2}{\partial x^2} + \frac{\partial^2}{\partial y^2} + \frac{\partial^2}{\partial z^2} \quad (19b)$$

**TEM Modes.** The appropriate solution to equation 19a depends on the cross-sectional geometry of the cavity. For cavities with rectangular cross-sections, the appropriate solutions involve the use of Hermite polynomials and are therefore known as Hermite-Gaussian waves. For cavities with cylindrical cross-sections, the appropriate solutions involve the use of Laguerre polynomials and the resulting waves are known as Laguerre-Gaussian waves. Regardless of the cross-sectional geometry of the cavity, all modes are characterized by three indices (one to characterize the longitudinal mode and two to characterize the transverse mode).

**Rectangular Symmetry.** For a cavity with a rectangular cross-section, the complex transverse amplitude of the electromagnetic field will be given by

$$u(x,y,z) = u_0 \frac{w_0}{w(z)} N_{mn} H_m \left[ \frac{\sqrt{2}x}{w(z)} \right] H_n \left[ \frac{\sqrt{2}y}{w(z)} \right] \times \exp \left\{ -j \left[ kz - (m+n+1)\phi(z) \right] \right\} \exp \left( -jk \frac{x^2 + y^2}{2R(z)} \right) \exp \left( -\frac{x^2 + y^2}{w^2(z)} \right) \quad (20)$$

where  $j = \sqrt{-1}$ ,  $u_0$  is a constant amplitude factor,  $w_0$  is width of the beam at the beam waist (i.e., the width of the beam at  $z = 0$ ),  $\lambda$  is the wavelength of the light, and

$$N_{mn} = \left( \frac{2}{2^{m+n} m! n! \pi} \right)^{1/2} \quad (21)$$

$$H_f = (-1)^f \exp(x^2) \frac{\partial^f}{\partial x^f} \exp(-x^2) \quad (22)$$

$$\phi(z) = \tan^{-1} \left( \frac{z}{z_R} \right) \quad (23)$$

$$z_R = \frac{\pi w_0^2}{\lambda} \quad (24)$$

$$R(z) = z \left\{ 1 + \left( \frac{z_R}{z} \right)^2 \right\} \quad (25)$$

$$w^2(z) = w_0^2 \left\{ 1 + \left( \frac{z}{z_R} \right)^2 \right\} \quad (26)$$

In eq 20,  $H_m$  and  $H_n$  are Hermite polynomials of order  $m$  and  $n$ , and are given by eq 22. According to eq 22, the first four Hermite polynomials are given by:  $H_0(x) = 1$ ,  $H_1(x) = 2x$ ,  $H_2(x) = 4x^2 - 2$ , and  $H_3(x) = 8x^3 - 12x$ . The subscripts  $m$  and  $n$ , which are the order of the Hermite polynomials, are also referred to as the node numbers in the notation  $\text{TEM}_{mn}$ . The value of  $m$  determines the number of nodes in the  $x$ -direction (horizontal axis) while the value of  $n$  determines the number of nodes in the  $y$ -direction (vertical axis).

Figure 3 shows a sectional view of a cavity resonator. The parameter  $z_R$ , which is known as the Rayleigh distance, represents the distance from  $z = 0$  to  $z = z_R$ , at which point the beam radius has increased by  $\sqrt{2}$  over the smallest radius (or waist)  $w_0$  that occurs at  $z = 0$ . The function  $R(z)$  gives curvature of the wavefront as a function of  $z$ . At the waist ( $z = 0$ ),  $R(0)$  is infinity and the wavefront is planar. As the beam propagates outward, the wavefront gradually becomes more curved. For distances  $z > z_R$ ,  $R(z) \cong z$  and the wavefront becomes essentially spherical with its center at  $z = 0$ . In order for a wave to be reflected back on itself, the curvature of the mirror surface should match the curvature of the wavefront. The function  $\phi(z)$  is a phase shift relative to an ideal plane wave whose phase shift would be  $kz$ .

Equation 20 gives the complex transverse amplitude of the electromagnetic field in the cavity. To convert this amplitude into an intensity, we must multiply equation 20 by its complex conjugate. When this is done, we get

$$I_{mn}(x,y,z) = I_0 \frac{1}{w(z)} H_m^2 \left[ \frac{\sqrt{2} x}{w(z)} \right] H_n^2 \left[ \frac{\sqrt{2} y}{w(z)} \right] \exp \left( -2 \frac{x^2 + y^2}{w^2(z)} \right) \quad (27)$$

where  $I_{mn}(x,y,z)$  represents the intensity distribution for the given mode ( $mn$ ) as a function of the coordinates  $x$ ,  $y$ , and  $z$ . For the lowest order mode ( $\text{TEM}_{00}$ ), it is clear from equation 27 that the cross-sectional intensity distribution is Gaussian, where  $w_0$  corresponds to the point where the intensity has dropped to  $I_0 e^{-2}$ . Figure 4 shows the beam profiles for the first four Hermite polynomials. From the figure, it is clear that the number of nodes in the intensity profile is equal to the order number of the Hermite polynomial. Figure 5 shows the beam cross-sections for various transverse Hermite-Gaussian modes.

**Cylindrical Symmetry.** For cavities with a circular cross-section like those employed in cavity-ringdown spectroscopy, the complex transverse amplitude of the electromagnetic field will be given in terms of Laguerre polynomials and expressed in terms of cylindrical coordinates ( $r$ ,  $\theta$ ,  $z$ ).

$$u(r, \theta, z) = u_0 M_{L\mathcal{P}} \frac{w_0}{w(z)} \left( \frac{\sqrt{2} r}{w(z)} \right)^{\mathcal{L}} L_{\mathcal{P}}^{\mathcal{L}} \left( \frac{2r^2}{w(z)^2} \right) \exp \left\{ j(2\mathcal{P} + \mathcal{L} + 1) \phi(z) \right\} \times \exp \left\{ -jk \frac{r^2}{2R(z)} \right\} \exp(j\mathcal{L}\theta) \exp \left( \frac{-r^2}{w(z)^2} \right) \quad (28)$$

where  $M_{L\mathcal{P}}$  is a rather uninteresting scaling factor that depends on  $\mathcal{L}$  and  $\mathcal{P}$ , but is independent of  $r$ ,  $\theta$ , and  $z$ , and  $L_{\mathcal{P}}^{\mathcal{L}}$  are the generalized Laguerre polynomials given by

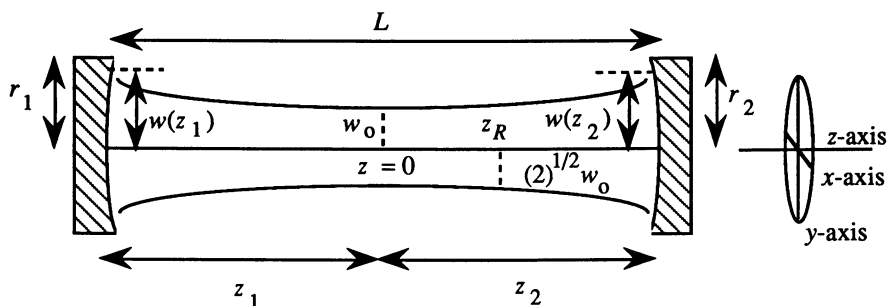


Figure 3. Sectional view of a resonator.

$$L_{\mathcal{P}}^{\mathcal{L}}(x) = \frac{e^{-x}}{x} \frac{d^{\mathcal{P}}}{dx^{\mathcal{P}}} \left( e^{-x} x^{\mathcal{P}+\mathcal{L}} \right) \quad (29)$$

and the other terms have been defined previously. Examples of some Laguerre polynomials for different values of the mode indices  $\mathcal{P}$  and  $\mathcal{L}$  are:

$$\begin{aligned} L_0^{\mathcal{L}}(x) &= 1 \\ L_1^{\mathcal{L}}(x) &= \mathcal{L} + 1 - x \\ L_2^{\mathcal{L}}(x) &= \frac{1}{2}(\mathcal{L} + 1)(\mathcal{L} + 2) - (\mathcal{L} + 2)x + \frac{1}{2}x^2 \end{aligned} \quad (30)$$

By contrast to Hermite-Gaussian waves, which have rectangular symmetry (see Figure 5), Laguerre-Gaussian waves have cylindrical symmetry. Figure 6 shows the beam cross sections for several transverse modes typical of cavities with circular cross sections. In Figure 6, the modes are specified as  $\text{TEM}_{\mathcal{P}\mathcal{L}}$  where  $\mathcal{P}$  refers to the number of nodes in the  $r$ -coordinate and  $\mathcal{L}$  refers to the number of nodes in the  $\theta$ -coordinate over an angle of  $\pi$ .

### Cavity Resonance Frequencies

**Hermite-Gaussian Waves.** We have seen previously in our discussion of the Fabry-Perot cavity that the condition for resonance is the formation of a standing wave within the cavity, where the phase shift  $\phi$  corresponding to a round-trip within the cavity must be an integral multiple of  $2\pi$ . For a Hermite-Gaussian wave, the total phase shift that occurs when going from one end of the cavity to the other (half of a round trip) is given by

$$\Phi = kL - (n + m + 1)\phi(z) = p\pi \quad (31)$$

where  $\Phi$  is the total phase shift,  $k$  is the propagation number given by  $2\pi/\lambda$ ,  $L$  is the length of the cavity,  $n$  and  $m$  are the Hermitian mode indices in eq 20,  $\phi(z)$  is defined by eq 23, and  $p$  is an integer (the longitudinal mode index). Because the total phase shift for the Hermite-Gaussian wave is a function of the Hermitian mode indices, higher order modes in a stable cavity will have slightly different oscillation frequencies.

It can be shown (10) that  $\phi(z)$  is given by

$$\phi(z) = \cos^{-1} \left( \pm \sqrt{g_1 g_2} \right) \quad (32)$$

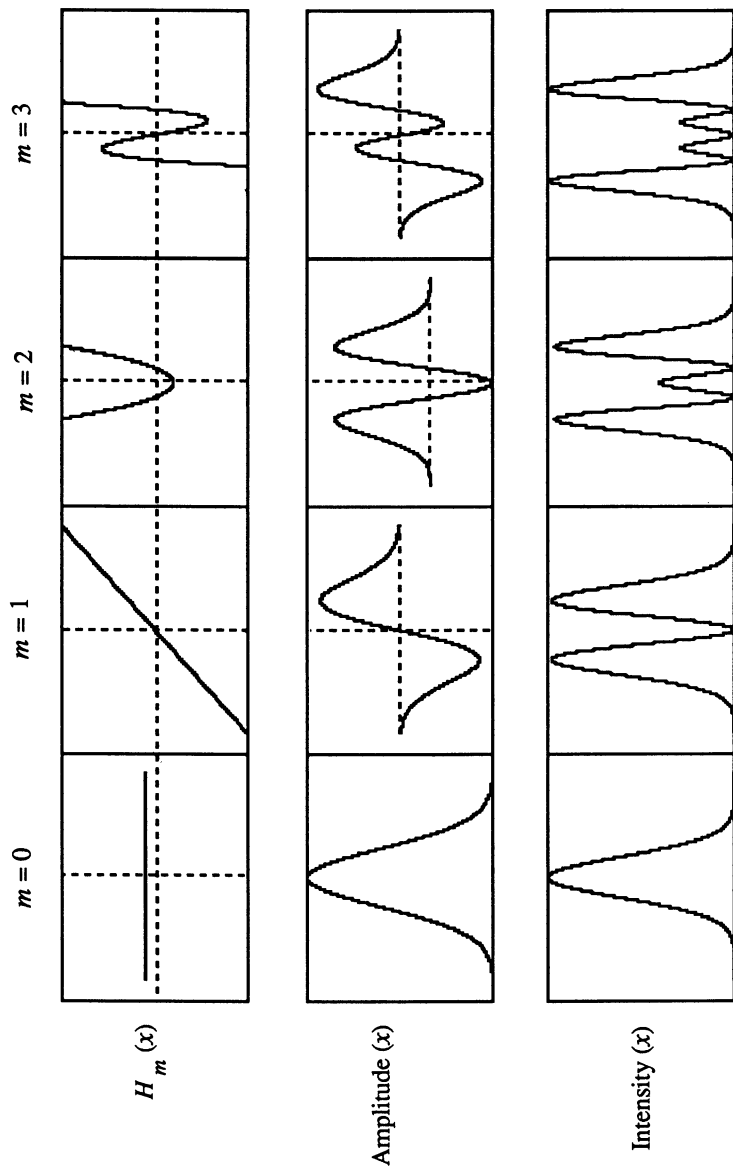


Figure 4. Beam profiles for the first four Hermitean polynomials as a function of  $x$ .



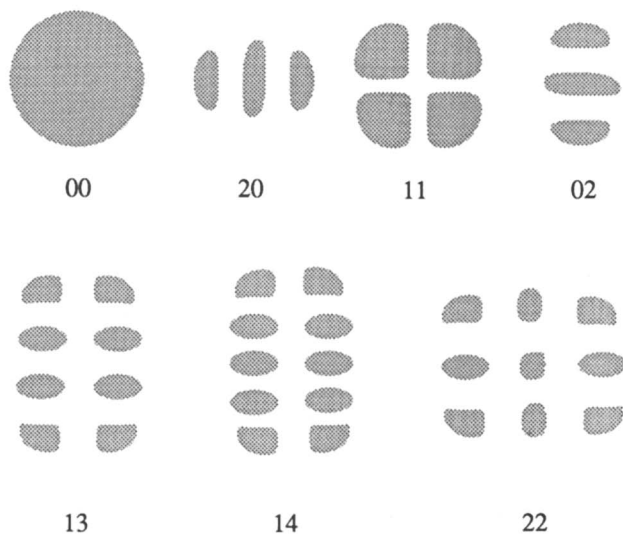


Figure 5. Schematic representation of the cross-sectional intensity patterns for various Hermite-Gaussian modes.

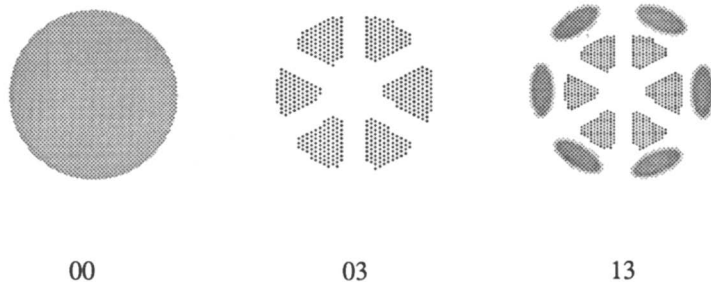


Figure 6. Schematic representation of the cross-sectional intensity patterns for three Laguerre-Gaussian modes.

where  $g_1$  and  $g_2$  are the  $g$ -parameters introduced previously ( $I$ ) and the plus sign applies to  $g_1$  and  $g_2 > 0$ . The negative sign applies to  $g_1$  and  $g_2 < 0$ . If we substitute eq 32 into eq 31 and solve for  $kL$ , we obtain

$$kL = \frac{2\pi L\nu}{c} p_{mn} = p\pi + (n + m + 1) \cos^{-1} \left( \pm \sqrt{g_1 g_2} \right) \quad (33)$$

Solving eq 33 for  $v_{pmn}$  gives

$$v_{pmn} = \frac{c}{2L} \left\{ p + (n + m + 1) \frac{\cos^{-1}(\pm \sqrt{g_1 g_2})}{\pi} \right\} \quad (34)$$

Equation 34 gives the cavity resonance frequencies in terms of the longitudinal mode index  $p$ , the two Hermitian mode indices  $m$  and  $n$ , and the  $g$ -parameters of the cavity.

**Laguerre-Gaussian Waves.** In the case of Laguerre-Gaussian waves, the total phase shift that occurs when going from one end of the cavity to the other is given by

$$\Phi = kL - (\mathcal{L} + 2\mathcal{P} + 1)\phi(z) = p\pi \quad (35)$$

where  $\Phi$  is the total phase shift,  $L$  is the length of the cavity,  $\mathcal{L}$  and  $\mathcal{P}$  are the Laguerre mode indices,  $\phi(z)$  is defined by eq 23, and  $p$  is the longitudinal mode index. If eq 32 is substituted into eq 35 and the result solved for the cavity resonance frequencies, the following expression is obtained:

$$v_{p\mathcal{L}\mathcal{P}} = \frac{c}{2L} \left[ p + (\mathcal{L} + 2\mathcal{P} + 1) \frac{\cos^{-1}(\pm \sqrt{g_1 g_2})}{\pi} \right] \quad (36)$$

### Mode Spacing

Equations 34 and 36 give the resonant frequencies of the cavity in terms of the three mode indices required for the particular type of cavity symmetry and the cavity parameters given by  $g_1$  and  $g_2$ . For the Hermite-Gaussian case, eq 34 predicts that the longitudinal mode separation should be given by

$$\Delta v_{\text{longitudinal}} = v_{p+1, mn} - v_{p, mn} = \frac{c}{2L} \quad (37)$$

where  $c$  is the speed of light and  $L$  is the length of the cavity. Similarly, the mode spacing predicted by eq 34 for the transverse modes is

$$\Delta v_{\text{transverse}} = v_{p, m+n+1} - v_{p, m+n} = \frac{c}{2L} \left\{ \frac{\cos^{-1}(\pm \sqrt{g_1 g_2})}{\pi} \right\} \quad (38)$$

In the previous chapter we discussed three stable resonators: the Fabry-Perot and symmetrical concentric resonators, where the product of  $g_1 g_2$  was close to 1; and the symmetrical confocal resonator, where  $g_1 g_2$  was equal to zero. For the Fabry-Perot resonator, where  $\sqrt{g_1 g_2}$  is taken as being close to +1, eq 38 predicts that the transverse mode spacing should be small compared with the longitudinal mode spacing as shown in Figure 7. For the confocal resonator, where  $g_1 g_2$  is equal to zero, eq 38 predicts that

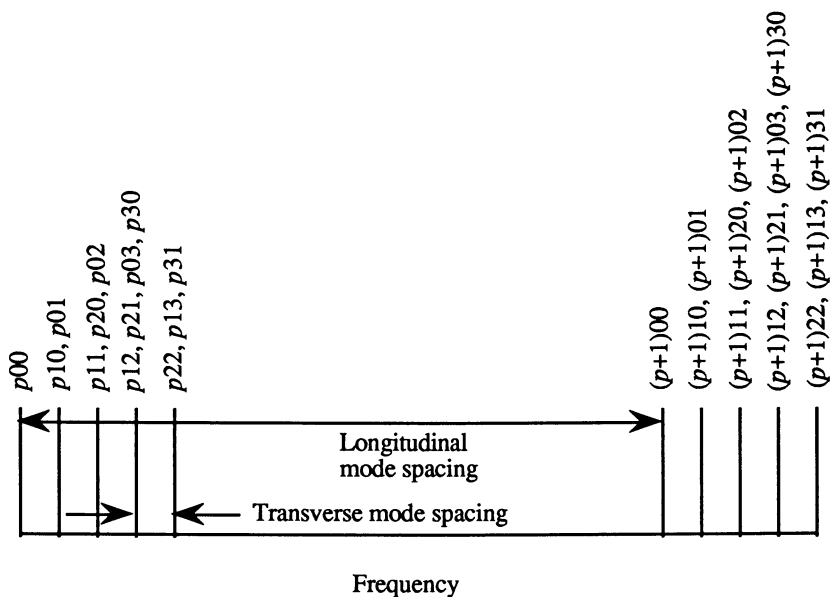


Figure 7. Resonant frequencies for a resonator where  $\sqrt{g_1 g_2}$  is close to +1. All transverse modes, where  $n + m$  is the same, are degenerate and oscillate at the same frequency.

the transverse mode spacing should be exactly half of the longitudinal mode spacing as shown in Figure 8. Finally, for the symmetrical concentric resonator, where  $\sqrt{g_1 g_2}$  is taken as being close to -1, eq 38 predicts that the transverse mode spacing should be exactly equal to the longitudinal mode spacing.

### Mode Formation and Cavity-Ringdown Spectroscopy

The effect of mode formation on cavity-ringdown spectroscopy has been discussed by Zalicki and Zare (5), who discuss the topic in terms of the relationship between the pulse duration ( $t_p$ ), the round-trip transit time ( $t_r$ ), and the relaxation time of the absorbing species ( $T_2$ ).

**Case I.**  $T_2 \ll t_p$ . If the pulse duration is much longer than the relaxation time of the absorbing species ( $T_2 \ll t_p$ ), the absorbing species sees quasi-continuous-wave light. If  $t_r > t_p \gg T_2$ , mode formation cannot occur, and the absorbing species sees a "photon bullet" of quasi-continuous-wave light that is not affected by the mode structure of the cavity. On the other hand, if the pulse duration is longer than the round-trip transit time ( $t_p > t_r$ ), cavity modes will develop due to interference between pulse fragments propagating in the same direction. Under these conditions, absorption will occur when an absorption line of the absorbing species coincides with one or more of the cavity modes. Therefore under these conditions ( $T_2 \ll t_p > t_r$ ), *to avoid missing spectral features in the spectrum with cavity-ringdown spectroscopy, the linewidth of the absorbing species must be greater than the spacing between the cavity modes.*

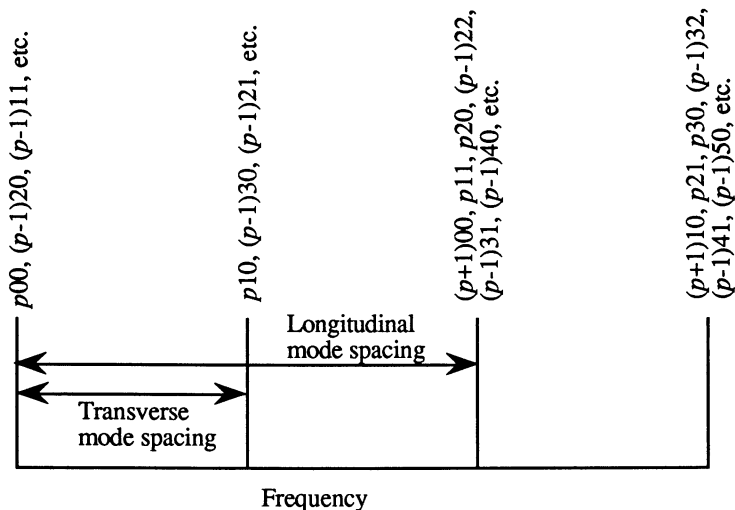


Figure 8. Resonant frequencies for a confocal resonator. The transverse mode spacing is exactly half of the longitudinal mode spacing. All modes where  $2p+m+n$  is the same are degenerate and oscillate at the same frequency.

**Case II.**  $T_2 \gg t_p$ . When the relaxation time of the absorbing species is greater than the pulse duration, the absorbing species interact with a series of light pulses during their lifetime. In this situation, the absorption spectrum of the absorbing species can be obtained from a Fourier transform of the time-domain variation of the field intensity inside the cavity (6). The result of this analysis shows that absorption is enhanced for transitions that are resonant with the cavity modes while it is suppressed for non-resonant transitions. Again, the conclusion is the same as for Case I: to avoid missing spectral features in the spectrum with cavity-ringdown spectroscopy, the linewidth of the absorbing species must be greater than the spacing between cavity modes.

**Mode Spacing in a Typical Cavity.** Since cavity mode spacing is a potentially important factor in cavity-ringdown spectroscopy, it is worthwhile to examine the mode spacing in a typical cavity-ringdown experiment. Consider a near-planar resonator composed of two mirrors whose radii of curvature are both equal to 6 m and whose separation is 0.5 m. For this cavity,  $g_1 = g_2 = 0.92$ . From eq 37, the longitudinal mode spacing for this cavity will be 300 MHz. According to eq 38, the transverse mode spacing will be 39 MHz. If higher order transverse modes are allowed to form in the cavity, they will fill in the gaps between the longitudinal modes as shown in Figure 7. For the cavity under consideration, the gaps between the longitudinal modes will be completely filled in if transverse modes up to  $mn = 33$  are allowed (i.e., 01, 10, 11, 02, 20, 12, 21, 03, 30, 22, 23, 32, and 33). If this condition can be met, the mode spacing of the cavity will resemble a Dirac comb (11) with a spacing of approximately 40 MHz. If we realize that the mode profiles are not Dirac delta functions, but have some finite full width at half maximum (FWHM) based on the finesse of the cavity, we realize that the mode structure begins to take on the appearance of a quasi-continuum. Meijer et al. (3) demonstrated this experimentally by measuring the transmission of a confocal cavity as it was detuned from the confocal separation distance. Thus, by careful design of the cavity (3), it is possible to establish a quasi-continuum of cavity modes that will guarantee the presence of several cavity modes under the linewidth of any spectral transition. In this way, it is possible to couple even a narrowband laser into the cavity.

## Literature Cited

1. Busch, K. W.; Hennequin, A.; Busch, M. A. In *Cavity Ringdown Spectroscopy—A New Technique for Trace Absorption Measurements*, Busch, K. W.; Busch, M. A. Eds.; American Chemical Society: Washington, DC, 1998.
2. Romanini, D.; Lehmann, K. *J. Chem. Phys.* **1993**, *99*, 6287-6301.
3. Meijer, G.; Boogaarts, M. G. H.; Jongma, R. T.; Parker, D. H.; Wodtke, A. M. *Chem. Phys. Lett.* **1994**, *217*, 112-16.
4. Scherer, J. J.; Voelkel, D.; Rakestraw, D. J.; Paul, J. B.; Collier, C. P.; Saykally, R. J.; O'Keefe, A. O. *Chem. Phys. Lett.* **1995**, *245*, 273-80.
5. Zalicki, P.; Zare, R. N. *J. Chem. Phys.* **1995**, *102*, 2708-17.
6. Scherer, J. J.; Paul, J. B.; O'Keefe, A.; Saykally, R. J. *Chem. Rev.* **1997**, *97*, 25-51.
7. Paul, J. B.; Saykally, R. J. *Anal. Chem.* **1997**, *69*(9), 287A-292A.
8. Busch, K. W.; Busch, M. A. *Multielement Detection Systems for Spectrochemical Analysis*; Wiley Interscience: New York, 1990, pp. 248-52.
9. Kreyszig, E. *Advanced Engineering Mathematics*, 4th Ed.; Wiley: New York, 1979, p. 350.
10. Seigman, A. E. *Lasers*; University Science Books: Mill Valley, CA, 1986, p. 761.
11. Busch, K. W.; Busch, M. A. *Multielement Detection Systems for Spectrochemical Analysis*; Wiley Interscience: New York, 1990, p. 312.

## Chapter 5

# Absorption Spectroscopies: From Early Beginnings to Cavity-Ringdown Spectroscopy

B. A. Paldus and R. N. Zare

Department of Chemistry, Stanford University, Stanford, CA 94305-5080

Spectroscopy is defined by the *Encyclopaedia Britannica* as "the study of the absorption and emission of light and other radiation by matter, as related to the dependence of these processes on the wavelength of the radiation." Linear absorption spectroscopy has several requirements common to other spectroscopies:

- a sample that is confined to a predetermined volume with a specific pathlength,
- a source of excitation (incoherent or coherent electromagnetic radiation) used to generate a characteristic response from the sample,
- a means to resolve the sample response in wavelength,
- a detector used to sense the transmission through or emission from the sample.

Absorption spectroscopy measures the loss of electromagnetic energy after the radiation passes through a cell containing the sample under study. Atoms, ions, or molecules absorb radiation at a wavelength,  $\lambda_{ik}$ , that excite them from a lower energy state,  $E_i$ , to an upper energy state,  $E_k$ :

$$\lambda_{ik} = hc/(E_k - E_i) \quad (1)$$

Consequently, radiation at this absorbed wavelength is attenuated at the exit of the sample cell. If the energy states are both bound levels, the spectrum produced consists of discrete lines. If the upper energy state is above the dissociation limit or the ionization threshold of the sample, the absorption spectrum becomes continuous. Similarly, absorption within a continuous band is also possible wherever a high density of broadened lines exist in a given spectral region, such as commonly observed in liquids and solids.

Because atoms and molecules have unique and identifiable energy levels, a measurement of the attenuated wavelengths allows identification of the species present. According to the Beer-Lambert law, the transmitted intensity,  $I_{\text{trans}}(\lambda)$ , at the wavelength  $\lambda$  is related to the incident intensity  $I_0(\lambda)$  by

$$I_{\text{trans}}(\lambda) = I_0(\lambda) \exp(-\alpha(\lambda)l_{\text{eff}}), \quad (2)$$

where  $\alpha(\lambda)$  is the absorption coefficient, and  $l_{\text{eff}}$  is the effective pathlength of the sample. For weak absorption, the first-order Taylor expansion of  $\exp(-\alpha(\lambda)l_{\text{eff}})$  yields  $1 - \alpha(\lambda)l_{\text{eff}}$ , so that the absorption coefficient can be computed from

$$\alpha(\lambda) = \frac{I_0(\lambda) - I_{\text{trans}}(\lambda)}{I_0(\lambda)l_{\text{eff}}} = \frac{\Delta I(\lambda)}{I_0(\lambda)l_{\text{eff}}} \quad (3)$$

Clearly, the minimum detectable concentration of absorbers for a specific absorption transition is inversely proportional to the effective sample pathlength and directly proportional to the minimum intensity fluctuation of the system.

Before discussing different absorption techniques, we need a common way of expressing the sensitivity that can be achieved. For this purpose, we introduce the following definitions. The absorption signal is denoted by  $S$ . We denote by  $\langle \dots \rangle_{av}$  the average over the duration of an absorption measurement, which we call a shot and denote by  $\Delta t_{shot}$ . Thus, the mean absorption signal  $S_{mean}$  is  $\langle S \rangle_{av}$ , and the standard deviation of the signal is found from  $\sigma_s^2 = \langle (S - S_{mean})^2 \rangle_{av}$ . The minimum detectable fractional signal per shot is  $MDFS_{shot} = \sigma_s / S_{mean}$ . It follows that the minimum detectable absorption loss per shot is  $MDAL_{shot} = MDFS_{shot} / l_{eff}$ , where the physical sample length  $l_{sample}$  is less than or equal to  $l_{eff}$ , which is the total distance the radiation traverses in the sample.  $MDAL_{shot}$  has units of  $cm^{-1}$ . By repeated absorption measurements at a specific wavelength the minimum detectable absorption loss decreases as the square root of the number of measurements, assuming that the measurement error is only statistical. If  $N$  replicate measurements (shots) are acquired, then the minimum detectable absorption loss becomes

$$MDAL(N) = MDAL_{shot} / \sqrt{N}. \quad (4)$$

For a measurement repetition rate of  $f$  shots per second ( $f$  Hz), which may differ from but not exceed  $1/\Delta t_{shot}$ , the sensitivity is defined as

$$Sy = MDAL(f). \quad (5)$$

Sy has units of  $cm^{-1} Hz^{-1/2}$ .

### Laser Spectroscopy.

In a conventional absorption spectrometer using a broadband, incoherent radiation source, the wavelength resolution is determined by the resolving power of the spectrometer. Laser spectroscopy uses coherent light sources, whose linewidths can be made extremely narrow and whose spectral densities can be made many orders of magnitude larger than those of incoherent sources. Laser spectroscopy can achieve higher sensitivity for narrow spectral absorption features than conventional dispersive spectroscopy. The origin of this effect is that a dispersive instrument with low resolution typically averages the absorbance over a wavelength interval wider than the feature, which diminishes the observed fractional absorbance. By using a laser having a linewidth narrower than the absorption linewidth, the maximum fractional absorption can be observed (at line center), thereby increasing the absorption signal, and consequently the signal to noise ratio, of the measurement.

The advantages of laser spectroscopy can be enumerated as follows:

- For laser linewidths narrower than the absorption feature, the absorption spectrum can be directly obtained by scanning the laser through the desired feature; a monochromator is no longer necessary.
- Spectral resolution is higher than in conventional spectroscopy owing to the narrow linewidths, and spectral profiles can be determined with great accuracy.
- Detector noise becomes negligible for sufficiently large spectral power densities.
- Methods can be devised to suppress laser intensity fluctuations; such suppression increases the signal-to-noise ratio and improves sensitivity.
- That laser light, being coherent, can be collimated, which allows the use of long pathlength absorption cells and results in increased sensitivity.
- The laser frequency can be locked to the center of an absorption line in order to measure the linecenter wavelength with unprecedented accuracy (1 part in  $10^{14}$ ).

Laser spectroscopy is therefore ideally suited for the spectroscopy of weak transitions and for measurements of ultralow concentrations. Because laser sources are becoming more reliable, less expensive, and more compact, the potential of laser spectroscopy for practical applications in industry and medicine continues to increase.

## Part I. Ultrasensitive Laser Absorption Spectroscopies.

**Ratiometric Dual-Path Absorption Spectroscopy.** Traditional single-path absorption spectroscopy is limited by excess noise, spurious modulation, and power drift in the laser light source, which can exceed the shot noise by 50 dB. Precise optical measurement techniques often apply modulation to the laser beam to avoid most of these low frequency noise problems, or use optical feedback stabilization for the laser source. Of all the possible eliminations techniques, only frequency modulated spectroscopy using heterodyne detection can actually achieve the shot noise limit.

Were it possible to eliminate or “divide out” the noisy fluctuations electronically (i.e., perform all electronic noise cancellation) by splitting the initial laser beam into sample and reference beams, direct absorption sensitivity could be dramatically improved. Several straightforward dual-detector circuit schemes relying on the near-ideal properties of photodiodes and bipolar junction transistors have been proposed by Hobbs<sup>1</sup> and applied by others<sup>2,3</sup> for the detection of NO<sub>2</sub>, H<sub>2</sub>O and O<sub>2</sub> using diode lasers. Hobbs noise cancellation circuits can suppress excess laser noise by as much as 60 dB from DC to tens of MHz, leading to MDAL<sub>shot</sub> of 10<sup>-8</sup> cm<sup>-1</sup> Hz<sup>-1/2</sup> for a 10 cm sample length.

**Long Path Differential Absorption Spectroscopy.** Long path absorption spectroscopy is based on the fact that detection sensitivity can be improved by increasing the pathlength through the sample. Although LPAS is not particularly practical for studying species placed in artificial sample cells, it has found applications in atmospheric chemistry studies, where no sample cell is necessary. In typical tropospheric studies, a radiation source is fixed at an elevated location, such as on a mountain top or hillside, and the detector is placed in a nearby valley<sup>4</sup>, or even mine<sup>5</sup>, creating a line-of-sight path that is up to several tens of kilometers long. LPAS has successfully performed real-time, quantitative spectroscopy of both naturally occurring, and man-made atmospheric molecules<sup>6</sup>.

Initially, LPAS made use of incoherent light sources (e.g., Xe arc lamps), primarily emitting in the ultraviolet and visible spectral ranges<sup>7</sup>. Incoherent sources limited LPAS sensitivity by their strong divergence (determined from the lamp area and focal length) and low luminous intensity. In this case, increasing the detection path did not necessarily improve sensitivity, because longer absorption paths resulted in decreased signal intensities, which in turn decreased the signal-to-noise ratio. Moreover, the spectral resolution depended on the spectrograph used for detection, rather than the linewidth of the light source. LPAS using incoherent light sources achieved a typical MDAL of 10<sup>-7</sup> - 10<sup>-8</sup> cm<sup>-1</sup>·<sup>16,7</sup>. The advent of laser sources reduced the source divergence, increased the amount of light power available for detection, allowed the use of longer path lengths, and improved spectral resolution. Tunable laser sources have resulted in differential LPAS, where the ratio of absorbance on and off a spectral feature is measured almost simultaneously, in order to eliminate background effects. Differential LPAS using laser sources now routinely achieves MDAL of 10<sup>-9</sup> - 10<sup>-10</sup> cm<sup>-18</sup>.

The primary limitation of LPAS, apart from its need for vast amounts of real estate, is the environment probed. More specifically, the atmosphere not only produces broadband absorption, but scatters the probe light by the Mie (droplets and particulates) and Rayleigh (molecules) mechanisms, often limiting the pathlength to under 10 km. Air turbulence produced by winds often limits sensitivity by randomizing the scattering and absorption losses on time scales much smaller than even the differential LPAS measurement times. These scattering effects can be circumvented by using a technique analogous to LPAS, called LIDAR (Light



Detection And Ranging), which was originally developed to measure wind velocity and turbulence.

In LIDAR, a short laser pulse is sent out into the atmosphere through an expanding telescope. The fraction of the laser pulse that undergoes backscattering and is collected by the telescope is measured as a function of time and wavelength. For each wavelength, the time-dependence of the signal provides information on both scattering and absorption as a function of distance from the original source<sup>9</sup>. Differential LIDAR, where the time-dependence of two signals, one on and the other off the absorption feature, is measured, can even yield species concentrations as a function of distance from the laser source. Moreover, the source and detector are placed in the same area, so that LIDAR neither has the real estate requirements of LPAS, nor required the source/detector pair to remain stationary (e.g., LIDAR can be performed from flying planes<sup>10</sup>). LIDAR remains limited by laser source output pulse power, and the ambient atmospheric conditions<sup>11</sup>.

**Multipass Absorption Spectroscopy.** Multipass absorption spectroscopy is based on the fact that detection sensitivity can be improved by increasing the *effective* pathlength through the sample. For a fixed volume, the light path can be folded around the input and output surfaces many times, thereby yielding an effective path through the sample cell that is many times the sample length. Multipass absorption spectroscopy typically can achieve  $MDAL_{shot}$  on the order of  $10^{-5}$  to  $10^{-7}$   $\text{cm}^{-1}$  with direct detection<sup>12</sup>.

Multipass cells (cf. figure 1a) that increase pathlength by a factor of 10 to 100 are commercially available. It is even possible to obtain multipass cells a meter in length that have effective pathlengths up to a kilometer, but these special cells are expensive and require very stable operating temperatures to ensure that mirror shape and separation do not change. Two commonly used cells are White cells<sup>13</sup>, where the beam is refocused to the same spot size on each roundtrip and light enters at one end and leaves at the other, and Herriot cells<sup>14</sup>, where the beam circulates in a near-concentric optical cavity and light enters and leaves through the same hole in one of the mirrors.

The temperature stability requirement arises from the fact that most multipass cells have large mirror surfaces to maximize cell throughput (i.e., the mirrors have a small ratio of focal length to aperture) and are placed so that the optical cavity formed is at the stability boundary. Hence any change in cavity length will perturb the ability of the cell to refocus the beam at each pass, leading to a diverging beam and a loss in cell throughput. Furthermore, maintaining the geometry of each mirror is important, as the number of beam spots on the mirror determines the effective pathlength, and any fluctuations in effective wavelength will translate into measurement noise of effective absorbance and reduce the system sensitivity. In all multipass cells, mirror reflectivity affects the maximum pathlength achievable because light is lost at each reflection, and mirror size affects the overall path length achievable because each beam spot must be spatially resolved from all others along the beam path to prevent interference effects. Even with this gain in pathlength, multipass absorption spectroscopy still suffers from intensity fluctuations in the light source, which limits  $MDAL_{shot}$ .

**Frequency Modulation Spectroscopies.** Even in direct absorption spectroscopy, it is well known that sensitivity can be improved by amplitude modulation of the CW light source and by lock-in detection at the modulation frequency. Lock-in detection effectively filters the signal at the modulation frequency with a narrow bandpass and therefore eliminates excess noise in the system. This technique was furthered with the advent of frequency modulation (FM) spectroscopy, which is a rapid and sensitive technique for detecting both absorption and dispersion features of species.

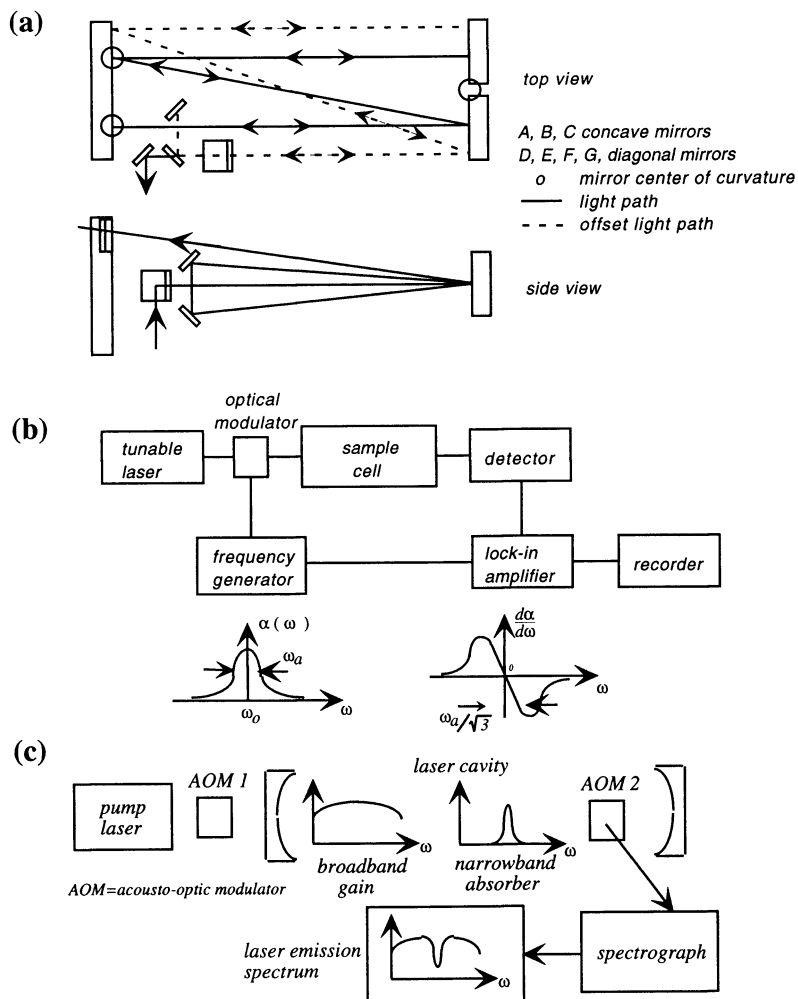


Figure 1. Experimental setups for (a) multipass cell spectroscopy, (b) FM modulation spectroscopy, and (c) intracavity laser absorption spectroscopy.

In FM spectroscopy<sup>15</sup>, a single-mode laser oscillating at optical frequency  $\omega_c$  is sinusoidally modulated at a frequency  $\omega_m$  and amplitude  $\Omega$  (see figure 1b). This modulation is produced either externally with a phase modulator to achieve large frequency shifts (MHz to GHz) or internally with a transducer (e.g., a piezoelectric transducer for a solid-state laser or an input current modulation for a laser diode) for lower frequency shifts (kHz to MHz). This setup produces a pure FM optical output consisting of a strong carrier at  $\omega_c$  and two weak sidebands at  $\omega_c \pm \omega_m$ ; the output is then passed through a sample cell. It can be shown<sup>16</sup> that for the laser light with frequency  $\omega_L = \omega_c + \Omega \sin(\omega_m t)$ , the Taylor expansion of the light intensity transmitted through a sample cell containing an absorber with absorbance coefficient,  $\alpha(\omega)$  yields a lock-in signal of:

$$S(\Omega) = -\Omega L \frac{d\alpha(\omega)}{d\omega} \sin(\Omega t) \quad (6)$$

for lock-in detection at frequency  $\Omega$ , where it was assumed that the single pass loss and the modulation amplitude are both very small, i.e.,  $\alpha L \ll 1$  and  $\Omega/\omega_c \ll 1$ . Similar expressions can be obtained for higher derivatives of the absorption coefficient. In general, the transmitted intensity can be detected on a square law detector and demodulated using standard RF heterodyne techniques. Both the phase and the dispersion associated with a the spectral feature can be measured by simultaneously monitoring the amplitude and the phase of the heterodyne signal as the laser frequency is swept through the absorption feature.

FM spectroscopy achieves sensitivity improvements through noise reduction in several ways. Heterodyne and lock-in detection filter the frequency response to a narrow interval around the modulation frequency, which reduces the total signal noise. Any background noise, such as from cell window absorption, laser intensity fluctuations, or sample concentration variations, is also reduced. Increasing the modulation frequency can minimize technical noise in the signal, such as  $1/f$  noise. Furthermore, choosing a modulation frequency that is large compared to laser linewidth reduces noise inherent to the laser light, and choosing the modulation frequency to be larger than the spectral feature of interest maintains the spectral resolution of the original laser source. Thus the total noise may be limited to the quantum-noise limit of the statistical fluctuations in the number of detected photons: the shot-noise limit.

Typical  $MDAL_{\text{shot}}$  values that can be detected using FM spectroscopy lie in the range from  $10^{-6}$  to  $10^{-7} \text{ cm}^{-1}$ . FM spectroscopy has been performed with many types of lasers, including semiconductor<sup>17, 18</sup> and lead-salt diode lasers<sup>19</sup>. Combinations of multipass cells and frequency modulation spectroscopy can achieve  $MDAL_{\text{shot}}$  values as small as  $10^{-10} \text{ cm}^{-1}$ ; most of that effort is concentrated on removing the noise in the detection electronics. Unfortunately, FM spectroscopy cannot directly yield absolute concentrations of species unless precalibration is performed.

**Intracavity Laser Absorption Spectroscopy (ICLAS).** As its name implies, intracavity laser absorption spectroscopy is performed by placing a narrow-line absorber into the cavity of a laser. If the laser is single-mode, the laser gain is narrow-band as well, and lasing action can be strongly affected by the sample absorption. Therefore, in order to obtain a reasonable sensitivity enhancement over a passive sample cell, the laser medium pump must be kept close to threshold with a constant pump power. Minor changes in intracavity losses may result in major changes in the laser output. It can be shown that the effective pathlength,  $l_{\text{eff}}$ , is given by<sup>16</sup>

$$l_{\text{eff}} = \frac{g_0}{\gamma(g_0 - \gamma)} \quad (7)$$

where  $\gamma$  is the total passive intracavity losses per round trip and  $g_0$  is the unsaturated laser gain. This approach is limited by the increasing instability of laser output as threshold is approached, and by a spontaneous emission background from the laser above threshold.

By using the homogeneously broadened gain of a multimode laser that is much broader than the absorption features of interest, the laser gain will be affected only by broadband losses such as cavity mirror loss. Then, the gain will be determined by the smallest loss among oscillating modes. The absorption spectrum is obtained by switching on an acousto-optic modulator to direct the laser output onto a spectrograph (see figure 1c). The emission and hence absorption spectra are resolved on a detector array.

In this case, the sensitivity gain occurs because light inside the laser cavity travels through the absorber many times, so that the laser cavity functions as a very effective multipass cell. Pathlength enhancements from 0.5 to 30,000 m have thus been achieved<sup>12, 20</sup>. The ultimate sensitivity of the emission spectrum of a multimode laser to intracavity absorbers is limited by the laser pulse duration and nonlinear mode coupling. The photon number distribution  $M_0$  produced during the cavity buildup process develops in time as  $M(t_g)$ <sup>21</sup>:

$$M(t_g) = M_0 \frac{\sqrt{t_g}}{M_{\text{norm}}} \exp \left[ - \left( \frac{q - q_0}{Q} \right)^2 \gamma t_g \right] \exp(-\alpha c t_g) \quad (8)$$

where  $M_{\text{norm}}$  is a normalizing factor,  $t_g$  is the emission spectrum generation time, The rate of stimulated emission into a mode  $q$  has half-width half-maximum  $Q$ ,  $\gamma$  is the cavity broadband loss rate, and  $c$  is the speed of light. The effective pathlength is then given by<sup>21</sup>:

$$l_{\text{eff}} = c t_g. \quad (9)$$

By optimizing the ICLAS system, quantum noise limited detection is achieved<sup>22</sup>.

Many different multimode lasers have been applied to intracavity spectroscopy: dye lasers<sup>20, 23</sup>, Ti:sapphire lasers<sup>21, 24, 25</sup>, fiber laser<sup>26</sup>, color center lasers<sup>27</sup>, and diode lasers<sup>28</sup>. MDAL<sub>shot</sub> values vary widely, from  $10^{-6} \text{ cm}^{-1}$  for diode lasers to  $10^{-11} \text{ cm}^{-1}$  for dye and Ti:sapphire lasers<sup>20, 21, 24</sup>.

The primary advantage of ICLAS is its “multiplex factor”, which allows about  $15 \text{ cm}^{-1}$  of spectrum (with  $0.01 \text{ cm}^{-1}$  resolution) to be obtained in a single measurement, a few seconds in duration. Recently,  $3 \times 10^9 \text{ cm}^{-1}$  MDAL in  $400 \mu\text{s}$  long single-shot measurements has been demonstrated<sup>29</sup>. ICLAS also allows the use of sample cells having “dirty” windows (up to several percent losses) to be placed inside the laser cavity without affecting the sensitivity. Because the laser beam in ICLAS is spatially confined inside the laser cavity, it is possible to perform spatially resolved spectroscopies of complex environments such as supersonic slit jets and flame fronts. Furthermore, ICLAS can yield absolute absorption coefficients<sup>21, 30</sup> with quantum noise limited detection, even for poor quality detectors, owing to its effective unity quantum efficiency<sup>21</sup>.

However, ICLAS is not without its disadvantages. It requires specialized, often expensive equipment, in particular a broadband laser, and a spectrograph. Difficulties can arise in determining the baseline losses with good accuracy. ICLAS measurements also demonstrate a relatively low dynamic range, compared to multipass or cavity ring-down spectroscopies. Finally, the spectral range (i.e. 300 to 1600 nm) of ICLAS remains limited by the availability of good quality broadband laser gain media. Perhaps this spectral range limitation has been the greatest drawback in the applicability of ICLAS to detect trace pollutants.

**Cavity Ring-down Spectroscopy.** In actual cavity ring-down spectroscopy (CRDS) (see figures 2 and 3), a pulsed laser source is injected into a cavity having high reflectivity mirrors, and the exponentially decaying output pulse train is measured on a photodetector. Signal processing is then performed on the electrical decay waveform  $I_{\text{ringdown}}(t)$  (with initial amplitude  $I_0$ ) to extract its ring-down time,  $\tau$ :

$$I_{\text{ringdown}}(t) = I_0 e^{-t/\tau} \quad (10)$$

The reciprocal of  $\tau$  gives the ring-down rate. This signal processing can be done either by digitizing the waveform on an oscilloscope and then fitting the set of data points numerically or by integrating the two portions of the waveform and taking their ratio, as is done with a boxcar integrator. The ring-down rate is obtained at different wavelengths for both an empty cavity and a cavity containing the desired sample. The quantitative spectrum of the sample obtained by subtracting the empty cavity rate (i.e., the baseline) from that of the sample-containing cavity rate can be directly converted into an absolute concentration.

There are several advantages to this approach:

- The measurement of an absorption spectrum depends only on the ring-down rate of light inside the cavity, not on the intensity of the transmitted light.
- CRDS uses a low-loss optical resonator to enhance its pathlength up to several tens of kilometers.
- The baseline losses of the cavity can be measured by simply evacuating it and taking a spectral scan. When these losses are subtracted from the sample spectral scan, absolute absorbance values for the sample are directly and simply obtained.
- Pulsed CRDS is a very simple technique to implement.

In contrast to direct absorption measurements, CRDS is insensitive to intensity fluctuations of the laser source. In contrast to multipass cells, these optical resonators are stable and hence much less sensitive to length changes or temperature fluctuations. For any given absorptive transition, CRDS can be used to quantify either extinction coefficients when concentrations are known or concentrations when extinction coefficients are known. Unlike FM spectroscopy or intracavity laser absorption spectroscopy, CRDS is a self-calibrated, absolute measurement technique. For simple setups involving a laser source, some mode-matching optics, a detector, and signal processing equipment, nominal MDAL of  $10^{-7}$  to  $10^{-8} \text{ cm}^{-1}$  can easily be measured. For these detection levels the setup will be relatively insensitive to mechanical, acoustic, or thermal noise. Most CRDS experiments have employed pulsed laser sources; however, as will be discussed below, continuous-wave laser sources allow much lower MDAL values.

We close this section by presenting in table 1 a comparison of various absorption spectroscopies. Which type of absorption spectroscopy is most suitable depends on factors such as cost, complexity, and sensitivity needed. In what follows, we restrict our discussion to CRDS.

Absorption Spectroscopy	Characteristic MDAL ( $\text{cm}^{-1}$ )	Sensitivity (molecules/ $\text{cm}^3$ )	Cost	Complexity
Single-Pass	$10^{-4}$	$10^{19}$	cheap	simple
Multipass	$10^{-6}$	$10^{17}$	moderate	straightforward
Intracavity Laser	$10^{-6} - 10^{-11}$	$10^{17} - 10^{12}$	expensive	difficult
Absorption Frequency Modulation	$10^{-6} - 10^{-8}$	$10^{17} - 10^{15}$	moderate	moderate-difficult
P-CRDS	$10^{-6} - 10^{-10}$	$10^{17} - 10^{13}$	moderate	simple
CW-CRDS	$10^{-10} - 10^{-12}$	$10^{13} - 10^{11}$	moderate	simple-difficult

Table 1. Comparison of several ultrasensitive detection techniques. In the calculation of sensitivity, an extinction coefficient  $\epsilon = 6.0 \text{ cm}^2/\text{mole}$  has been assumed.

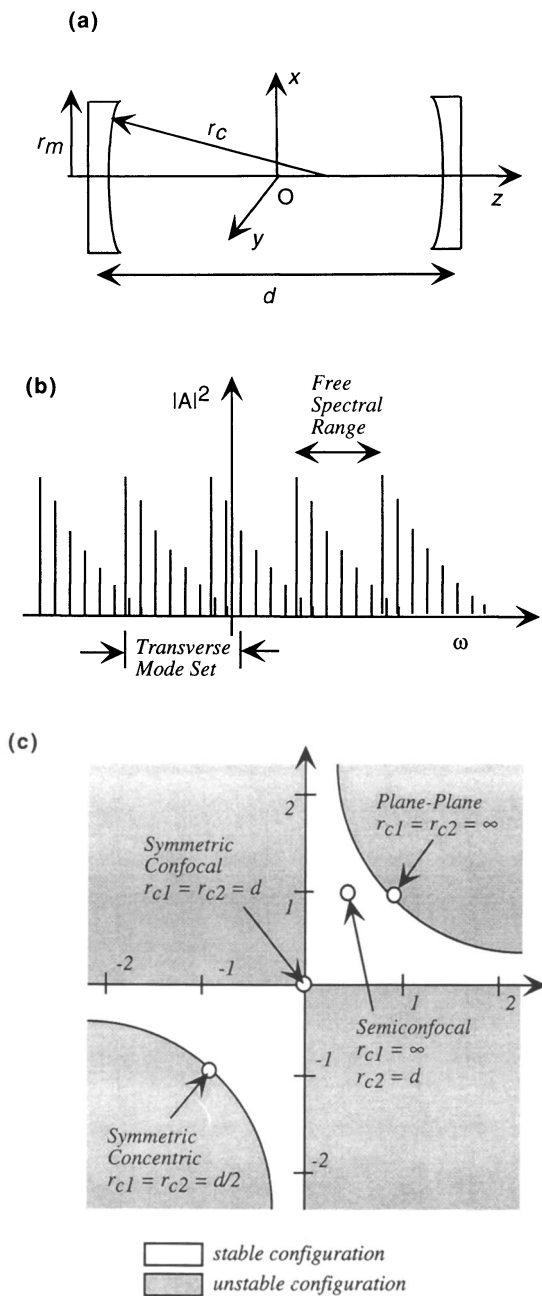


Figure 2. (a) Linear optical resonator formed by two identical circular mirrors, having spherical curvature. These mirrors are characterized by their radius  $r_m$ , radius of curvature,  $r_c$ , and separation  $d$ . (b) Mode structure of linear optical resonator. (c) Stability diagram for optical resonator.

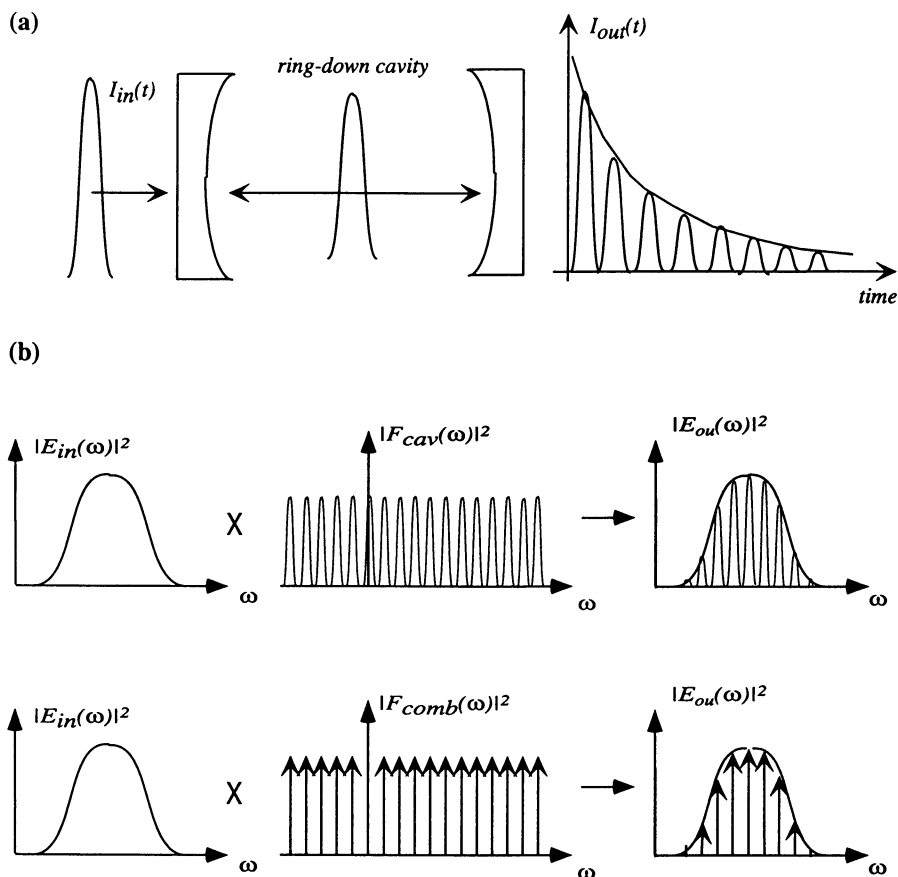


Figure 3. (a) Ping-pong model of pulsed CRDS. (b) Frequency domain model of pulsed CRDS for Dirac delta function comb and Airy function comb .

## Part II. Overview of CRDS

**Theory.** In what follows, we outline the basic theory for CRDS. CRDS and its fundamental limitations can be understood only if the response of an optical resonator, i.e., the ring-down cavity, is well known. Excellent, detailed treatments of resonator theory can be found in books by Siegman<sup>31</sup>, Demtröder<sup>16</sup>, and Yariv<sup>32</sup>. The reader is referred to the work of Hodges, Looney, and van Zee<sup>33</sup>, Lehmann and Romanini<sup>34</sup>, and Zalicki and Zare<sup>35</sup> for more rigorous treatments of cavity ring-down spectroscopy theory than will be presented here.

**A Simplistic View: The Ping-Pong Model.** Pulsed CRDS (P-CRDS) is based on the injection of a light pulse into an optical resonator, called the ring-down cavity (RDC), that is either empty or encloses the sample of interest (see figure 3). From a "ping-pong" viewpoint, the pulse of light inside the cavity bounces back and forth between the mirrors, and at each mirror a small fraction is transmitted. Thus,

the envelope of the intensity of the pulses exiting the cavity decays exponentially in time at a rate dependent on the total cavity losses. These losses comprise the loss from finite reflectivity of the mirrors, from diffraction, and from any absorption within the cavity. If  $I_{\text{out}}$  is the intensity of light pulses monitored at the output of the cavity,  $I_{\text{in}}$  is the initial pulse intensity,  $t_{\text{rt}}=(2L)/c$  is the round trip time of the cavity, and the pulse duration is assumed to be much shorter than  $t_{\text{rt}}$ , then the output intensity after  $n$  round trips is

$$I_{\text{out}}(nt_{\text{rt}}) = T^2 (1-A_{\text{abs}}-A_{\text{cav}})^{2n+1} I_{\text{in}}, \quad (11)$$

where  $T$  is the mirror transmission and total cavity losses are  $A = \alpha L = A_{\text{abs}} + A_{\text{cav}}$  in the presence of absorber loss. If the losses are small ( $A \ll 1$ ), then the output pulse intensity can be rewritten such that it decays exponentially

$$I_{\text{out}}(nt_{\text{rt}}) = T^2 e^{-(2n+1)(A_{\text{abs}} + A_{\text{cav}})} \quad (12)$$

and the envelope of this signal as observed using a detector too slow to resolve individual pulses is

$$\text{Env}(t) \approx e^{-2(A_{\text{abs}} + A_{\text{cav}})t / \tau}. \quad (13)$$

Thus the decay rate of the cavity depends on cavity losses and on absorption losses of a sample present inside the resonator. This exponential decay caused by absorption is exactly a restatement of the Beer-Lambert law when  $\alpha_{\text{abs}} = \epsilon cL$ , where  $\epsilon$  is the extinction coefficient and  $c$  is concentration. If  $\epsilon$  is known for a specific wavelength and species, then the concentration of the species present can be obtained by measuring the absorption losses.

**A More Sophisticated View: RDC Transfer Functions.** However straightforward and appealing the ping-pong model may seem, it is too simple. Although it explains why an exponentially decaying envelope is usually observed in ring-down experiments, it fails to account for the fact that only light having frequencies near a cavity mode will be allowed inside the resonator. Only a set of allowed frequencies, called “modes” can propagate inside the resonator. The resonator modes are determined by boundary conditions on the light that are established from geometrical considerations. This fact, and a few others needed later to illustrate the advantage of CW-CRDS, can be explained by considering the physics of CRDS in the frequency domain and deriving the RDC transfer function<sup>34</sup>

$$F_{\text{cav}}(\omega) = (Te^{-i\omega L/c}) / (1 - Re^{-i\omega L/c}), \quad (14)$$

where  $T$  and  $R$  are the intensity transmission and reflection coefficients for the RDC mirrors, respectively.

The transfer function of the cavity for the input light *field* cannot be simply squared to obtain the transfer function for light *intensity* if more than one mode is excited in the cavity. If only a single mode is excited, the Fourier transform (FT) of the ring-down waveform, can be directly obtained by squaring  $F_{\text{cav}}$ , and multiplying it by the FT of the input light intensity and by the detector intensity response. It should be noted that this transfer function for the cavity is independent of phase noise in the input signal, of the duration of the input signal, of the carrier frequency of the input signal, and of the effective bandwidth of the input signal. Thus the cavity response is unaffected by the coherence length of the input pulse.

The RDC transfer function is a series of sharp, identical resonance peaks (see figure 2b), each having an Airy lineshape and separated by the free spectral range (FSR). The halfwidth of the RDC transfer function resonances in frequency space,  $\Delta\nu$ , can be shown to be given  $\Delta\nu = (\text{FSR})/F^*$ , where  $F^*$  is the cavity finesse. As the reflectivity of the mirrors increases ( $R \rightarrow 1$ ), the RDC halfwidth decreases while the FSR, dependent on RDC geometry, remains unchanged. The RDC finesse increases with increasing mirror reflectivity, but less of the total input light can enter and consequently exit the cavity. This tradeoff between cavity throughput and finesse is of fundamental importance to CRDS. It will be discussed further in the context of



CW-CRDS. For now, we note only that increasing the finesse increases the RDC decay time, which increases CRDS sensitivity, but decreasing the throughput increases the noise levels in the detected waveform (it is harder to detect less light), which decreases CRDS sensitivity.

If multiple modes are excited inside the RDC, the output field of the RDC will consist of the weighted sum of exponentially decaying fields, each having a different time constant. If the frequency difference between two such modes is comparable to the rate of decay and the output light of the cavity is not completely collected, then sinusoidal beating will be observed and can preclude the accurate determination of the ring-down rate. This phenomenon has been experimentally demonstrated by Martin *et al.*<sup>36</sup> Note that the excitation of multiple longitudinal modes will result in a similar mode beating. Because the beating frequency equals the cavity FSR (typically > 100 MHz), this effect will occur too quickly to be observed with most detectors, although it will appear as excess noise on the exponential-like decay waveform. This beating phenomenon is a fundamental limitation of P-CRDS when more than a single mode in the resonator is excited, as has been the case in almost all P-CRDS experiments. This limitation, however, is not significant for many of the purposes for which P-CRDS is used.

To calculate the total field for multimode excitation, the response of the cavity for each mode must be computed, and the field responses summed, before the square of the magnitude is taken. The cross terms in this squared sum will produce mode-beating effects if all the light is not collected. Such calculations can rapidly become complex. Once again, if all the light is collected at the detector (which is rarely the case in real-world experiments), mode interference is completely eliminated and each mode can be treated independently. Nonetheless, the superposition of many exponential decays, each having a slightly different decay, makes multiple transverse mode excitation clearly undesirable for the most accurate measurements. Thus, the quality of the CRDS experimental results usually depends on the effort made to mode match the laser source to a single transverse mode of the cavity.

**CRDS Sensitivity.** CRDS sensitivity can be defined as:

$$S_y = \sqrt{2} \frac{MDAL_{shot}}{\sqrt{fN_{phot}}} \quad (15)$$

where the signal for  $MDAL_{shot}$  is the ring-down time,  $\tau(t)$ ,  $N_{phot}$  is the number of photons impinging on the photodetector, and  $f$  is the measurement repetition rate. The sensitivity can be improved by decreasing  $MDAL_{shot}$ , and by increasing the cavity throughput. It is clear that under ideal conditions, with no noise introduced by detection electronics, shot-noise-limited experiments only restricted by cavity throughput could be performed. Presently, the state-of-the-art electronics, especially the detectors and digitizers used to render decay waveforms for mathematical fitting on a personal computer, introduce noise that exceeds the shot noise of the light. Cavity throughput will always remain a limitation of P-CRDS, but can be minimized by the use of narrowband, externally modulated continuous-wave (CW) laser sources. The best pulsed source  $MDAL_{shot}$  is about 0.2%<sup>37</sup>, whereas the best CW source is  $MDAL_{shot}$  0.05%<sup>38</sup>. The best CRDS  $MDAL$  achieved to date is on the order of  $10^{-10} \text{ cm}^{-1}$ <sup>39</sup>, but is expected to decrease as detection systems improve. In fact, by using slightly more complex detection schemes such as heterodyning the ring-down signal with a local oscillator, almost shot-noise-limited measurements have now been enabled<sup>38</sup>.

**Overview of CRDS: Experimental History.** In what follows, we outline the basic experimental genesis of CRDS, starting from the first attempts to measure low loss mirror reflectivities, and culminating in shot-noise-limited CW-CRDS detection schemes.

**Precursors of CRDS: Mirror Reflectometers.** The evolution of optical science took a giant leap in the second half of the 20th century with the advent of the laser, the silicon-based semiconductor transistor and integrated circuit, the compound semiconductor optoelectronic photodiode and diode laser, the optical fiber, and a new generation of thin film optical coatings. Without these technological advances, cavity ring-down spectroscopy would not be possible today. Ironically, the advances in optical coating technology, and a lack of suitable measurement techniques for highly reflecting mirrors, brought about the birth of cavity ring-down spectroscopy.

As high reflectivity mirrors became more important for many applications and optical instruments (such as high power lasers, gyroscopes, optical frequency standards), considerable efforts were made by the commercial manufacturers. Over the last decade, significant progress was achieved in the development of superpolished, high purity substrates (surface roughness less than  $\lambda/10,000$ ), as well as in the growth of extremely low-loss thin-film dielectric coatings. Mirrors with losses on the order of parts per million (ppm) are readily available in the visible and nearinfrared. Mirrors with several tens of ppm are available in the midinfrared, and are expected to become available in the near future for the ultraviolet. Record reflectivities for these "supermirrors" are 0.999994, corresponding to losses of  $6 \times 10^{-6}$ , or 6.0 ppm<sup>40</sup>.

Although the transmission,  $T$ , through these high reflectors could be measured by very precise and expensive power meters having a large dynamic range, little information could be obtained about the mirror reflectivity,  $R$ , and mirror scattering and absorption losses,  $S$  (where  $T+R+S = 1$ ). Two competing techniques were developed to measure reflectivity based on the decay constant of a linear cavity Fabry-Perot resonator formed by two plano-concave mirrors: measurement of the light-intensity decay constant when the excitation source is abruptly terminated<sup>41, 42</sup> and measurement of the phase shift accrued by amplitude-modulated light as it traverses the resonator<sup>43-45</sup>.

In 1980, Herbelin *et al.*<sup>44</sup> were the first to propose measuring the decay lifetime of photons injected into an optical resonator to measure mirror reflectivity (see figure 4a). In 1985, Elleaume *et al.*<sup>43</sup> used the phase-shift method to measure the reflectivity of high reflectors used in a free-electron laser and to determine the mechanisms of UV-induced degradation on the dielectric stacks. In both approaches, a CW laser beam is amplitude-modulated with an external electro-optic modulator (frequency  $f$ ), which produces a linearly polarized, sinusoidally varying photon beam. Once this modulated beam passes through the linear optical resonator of interest, it becomes shifted in phase by angle  $\alpha$ , which is directly related to the cavity intensity decay time,  $\tau$ , by <sup>45</sup>  $\tan(\alpha) = 4\pi f\tau$ . Phase shift  $\alpha$  is determined by standard lock-in detection, as shown in figure 4a: the phase of the light is measured before and after the resonator, and these two phases are subtracted to yield  $\alpha$ ; or  $\tan(\alpha)$  can be directly measured using two lock-in amplifiers with a relative phase shift of 90 degrees. Herbelin also remarked that "Many other applications are envisioned, including very sensitive gas-phase absorption studies and the study of optically transparent materials under high electric or magnetic fields or both." Meijer *et al.*<sup>46</sup> realized this prediction sixteen years later.

In 1985, Anderson *et al.*<sup>41</sup> were the first to use cavity decay time measurements to measure mirror reflectivity (see figure 4b). The output of a CW He-Ne laser was directed to the input of a linear optical resonator through a Pockels cell and mode-matching lenses. When sufficient light was built up inside and transmitted

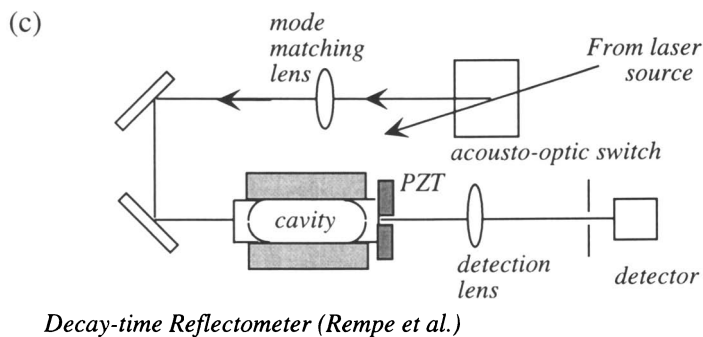
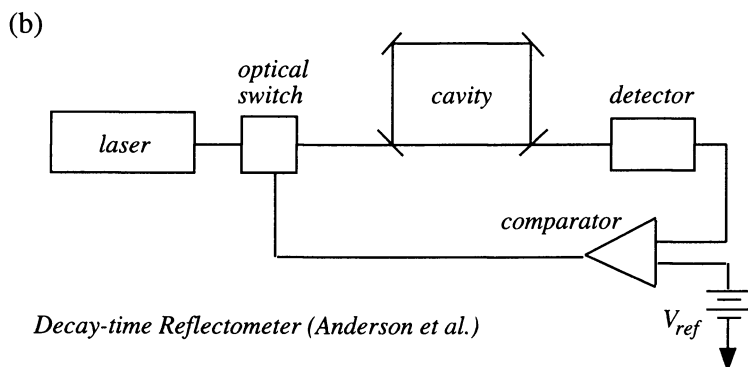
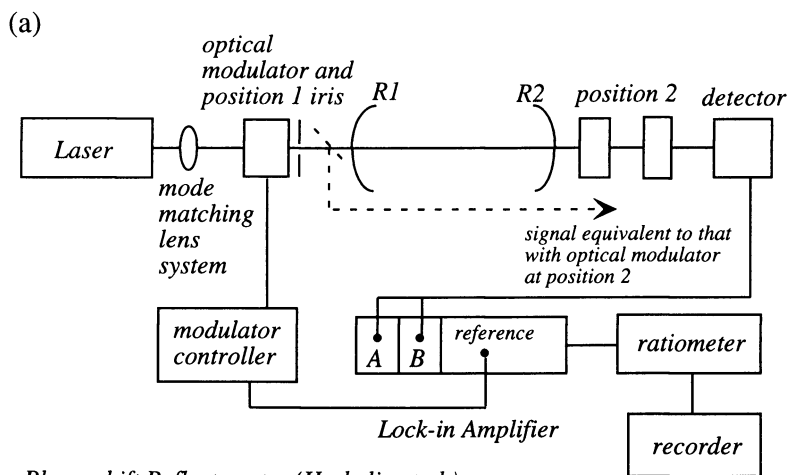


Figure 4. Reflectometry setups by (a) phase shift detection, (b) Anderson et al. decay-time detection, and (c) quasi-CW decay-time detection.

by the optical resonator onto a photodetector, the laser light was terminated by the Pockels cell. The decay of light inside the resonator was then monitored using the photodetector, and decay time,  $\tau$ , was measured using a counting circuit. Frequency overlap between the cavity and laser were incidental. The mirror reflectivity,  $R$ , was then computed from the decay lifetime,  $\tau$ :  $R \approx \tau_r/\tau$ .

Rempe *et al.*<sup>42</sup> used a similar approach in 1992 to measure the reflectivity of 1.6 ppm loss supermirrors (see figure 4c). In contrast to Anderson, Rempe mounted one of the cavity supermirrors onto a piezoelectric actuator, so that the cavity length could be scanned across the test laser linewidth to build up light inside the resonator. When a sufficient light level was obtained, the CW laser light was deflected from the cavity with an acousto-optic modulator. The light-intensity decay waveform was digitized and then numerically fit. This approach was adopted four years later by Romanini *et al.*<sup>47, 48</sup> to perform the first CW laser cavity ring-down spectroscopy experiments.

Anderson's time-domain approach, rather than the phase-shift technique, was later adopted by most supermirror manufacturers<sup>42</sup> and was even commercialized. It is interesting to note a remark by Anderson<sup>41</sup>: "The cavity optical path was evacuated: we have made tests in open air cavities but found our results depended on the ambient Pasadena air quality." Anderson *et al.* had measured molecular absorption losses, but they did not pursue the spectroscopic avenue. Three years passed before the first pulsed laser cavity ring-down spectroscopic application was fully documented by O'Keefe and Deacon<sup>49</sup>.

**Pulsed Cavity Ring-Down Spectroscopy.** The first incarnation of P-CRDS appeared in the literature in 1988, in a paper by O'Keefe and Deacon<sup>49</sup>, where a nitrogen-laser-pumped pulsed (15 ns) dye laser emitting at 690 nm and mode-matched to the TEM<sub>00</sub> mode of the RDC was used to investigate the  $b\Sigma_g^+ \rightarrow x^3\Sigma_g^+$  overtone transitions of molecular oxygen. Ring-down waveforms were digitized using an oscilloscope, and the decay constant was extracted from a linear fit of the logarithm of the waveform (after baseline subtraction). For mirrors having  $R > 99.99\%$  and a cavity length of 25 cm, the first minimum detectable losses reported were on the order of  $2 \times 10^{-8} \text{ cm}^{-1}$ . After this seminal paper in P-CRDS<sup>49</sup>, O'Keefe began a collaboration with Saykally at the University of California at Berkeley, which has endured to this day.

The first application of CRDS appeared in 1990<sup>50</sup>: the UC Berkeley group used P-CRDS with a nitrogen-laser-pumped dye laser (450 nm, 15 ns, 10-100 Hz repetition rate) to investigate the spectroscopic constants of jet-cooled metal clusters in a molecular beam. They used a 55 cm long linear cavity with  $R \approx 99.99\%$  reflectors and obtained a spectral resolution of about  $1 \text{ cm}^{-1}$ . This approach proved very fruitful, and a great deal of work was performed on metal clusters over the next six years<sup>51</sup>. Extensive spectroscopic investigations of silver silicides<sup>52</sup>, aluminum silicides<sup>53</sup>, gold silicides<sup>54</sup>, platinum silicides<sup>55</sup>, and copper silicides<sup>56</sup> have been published. These later P-CRDS experiments applied an excimer-pumped dye laser emitting in the ultraviolet (365 nm for silver, 405-413 nm for aluminum, and 400 nm for copper), with 0.3 to 0.04  $\text{cm}^{-1}$  spectral resolution. The RDCs used were about 25 cm in length (primarily limited by the size of the molecular beam reactor) and had 99.99% reflectivity mirrors. Waveforms detected using a photomultiplier (PMT) were acquired by a 12-bit, 20 MHz digitizer. A linear fit of the waveform logarithm (after baseline subtraction) was the preferred means for extracting the decay constant. MDAL on the order of  $10^{-8} \text{ cm}^{-1}$  were achieved and allowed extensive vibrational analysis both of vibronic isotope shifts and rotational bands of the cluster spectra. Recently, P-CRDS has been extended into the mid-infrared (using a Raman shifter cell) to study spectra of stable organic molecules and water clusters<sup>57, 58</sup>.

From 1993 to 1996, applications of CRDS were extended to detailed spectroscopic studies of line intensities, transition wavelengths, and coupling effects in vibrational and rotational spectra of gas-phase species by Lehmann and Romanini at Princeton University<sup>59</sup>. When spectroscopic information from rotational structure of HCN and its isotopomers, H<sup>13</sup>CN, and H<sup>15</sup>CN<sup>60</sup>, was compared to *ab initio* calculations, Coriolis coupling in one band, and Herman-Wallis effect (R and P branch asymmetry) in several bands were observed. Furthermore the standard computational techniques used to model vibrational overtone transitions for HCN were shown to produce inaccurate results when compared to experimental measurements, and CRDS enabled the Princeton group to improve on existing models<sup>61, 62</sup>. In the CRDS experiments, a XeCl excimer-pumped dye laser (30 Hz repetition rate) operating between 480 and 580 nm with 0.04 to 0.08 cm<sup>-1</sup> resolution was employed. Mode-matching optics were not fully deployed, resulting in intensity fluctuations of the output decay waveforms up to 50%<sup>59-62</sup>. However, owing to the good-quality reflectors used (R > 99.99%), the 1.3 m cavity length, and detection using a PMT, which provided almost shot-noise ring-down measurements, sensitivities (S<sub>y</sub>) as low as 7 × 10<sup>-10</sup> cm<sup>-1</sup>Hz<sup>-1/2</sup> were achieved. It is interesting to note that Romanini and Lehmann<sup>59</sup> did not digitize the ring-down waveforms but used a two-channel boxcar integrator to directly yield the sample absorbance. In fact, it was shown<sup>59</sup> that this detection scheme is inherently as accurate as waveform digitization followed by a linear fit and reduced shot-to-shot fluctuations (MDFS) to the order of 0.5%.

The Meijer group at the University of Nijmegen has been another source of innovations in P-CRDS. In 1994, Meijer *et al.*<sup>63</sup> introduced the concept of using short cavities having a dense transverse mode structure (and collecting all the modes to avoid mode beating) to improve the potential resolution of P-CRDS. By using a 10 cm, off-confocal RDC, they were able to obtain a 10 MHz transverse mode spacing and hence perform spectroscopy on the OH radical in a flame at 298 nm (doubled Nd:YAG pumped dye laser). In all their P-CRDS studies, the Nijmegen group digitize the ring-down waveform on an oscilloscope and use a linear fit to obtain the ring-down constant, in the spirit of the original O'Keefe and Deacon paper. In addition to performing detailed spectroscopic studies of oxygen<sup>64, 65</sup> for comparison with detailed theoretical *ab initio* calculations and applying P-CRDS to the study of laser-desorbed, jet-cooled organics (diphenylamine)<sup>66</sup>, the Nijmegen group was the first to demonstrate the utility of P-CRDS in the UV for trace gas detection. Using a pulsed Nd:YAG pumped dye laser followed by a KDP and/or BBO doubler to obtain radiation at 300 nm, the Nijmegen group showed P-CRDS sensitivities of 10 parts per billion to ammonia, and 1 part per trillion to elemental mercury in air<sup>67</sup>. The Nijmegen group was also the first to point out laser bandwidth effects in P-CRDS that result in multiexponential decays if the laser line is broader than the absorption feature. They were also the first to demonstrate P-CRDS in the far infrared using a free-electron laser tuned between 10 and 11 μm to measure vibrational transitions of ethylene<sup>68</sup>. In the past two years, three other important P-CRDS innovations have appeared thanks to the Nijmegen group: phase-shift CW-CRDS (discussed in the previous section)<sup>46</sup>, Fourier-transform P-CRDS<sup>69</sup>, and polarization-dependent P-CRDS<sup>70</sup>. Briefly, Fourier-transform P-CRDS combines the multiplex and resolution advantage of a Fourier-transform spectrometer with the sensitivity of P-CRDS: time-resolved FT scans are taken at the output of the RDC excited with a broadband source, so that the inversion of the interferogram yields the time-dependent ring-down waveform at all excitation frequencies, i.e., it yields the entire decay constant spectrum. In polarization-dependent P-CRDS, the sample is exposed to the presence of a magnetic field, the polarization of the excitation source is set to be a mixture of orthogonally polarized light components, and the spectral splittings are observed by simultaneously collecting and then subtracting ring-down spectra at the two orthogonal polarizations.

From 1995 to the present, Zare and co-workers<sup>71-74</sup> at Stanford University have been applying P-CRDS in the ultraviolet (216 nm) for the detection of methyl radicals in a hot-filament reactor used for chemical vapor deposition of diamond films. P-CRDS was demonstrated to be a much more sensitive absorption detection technique than multipass direct absorption spectroscopy<sup>71</sup> and to have sufficient spatial resolution (along the axis perpendicular to the RDC) to facilitate spatially resolved concentration profile measurements in the reactor<sup>72, 74</sup>. Thus the methyl radical concentration could be measured as a function of distance from the hot filament, and the implications of this concentration on the chemistry of diamond film growth rates could be deduced<sup>73, 74</sup>. There has been much confusion in the literature as to what conditions are necessary for the ring-down waveform to exhibit exponential decay in P-CRDS. The Stanford group<sup>36</sup> was the first to show, using an Nd:YAG-pumped, Fourier-transform-limited optical parametric oscillator (OPO) laser source, that multimode cavity excitation results in mode effects that can severely distort the ring-down waveform. Thus, they were able to eliminate mode beating in further experiments involving this laser source. The Stanford group<sup>75</sup> also recently applied P-CRDS in the visible to obtain spectra of ground-state species in hostile environments. The spectra of overtone rovibrational transitions of water vapor generated by combustion at atmospheric pressures, methane-air flat-flame were obtained, as a function of distance from the burner surface<sup>75</sup>. From these spectra, the temperature and concentration profiles of water vapor were computed. Baseline degradation caused by nonuniform optical densities and emission from the flame medium were shown to be acceptable. MDAL values on the order of  $2 \times 10^{-8} \text{ cm}^{-1}$  are repeated for these hostile environments.

In 1996, Hodges, Looney and van Zee at the National Institute of Standards and Technology were the first group to dedicate experiments to the actual physics of P-CRDS. Their efforts have successfully resulted in two very detailed studies of laser source effects on the noise and sensitivity of P-CRDS. In particular, the NIST group<sup>76</sup> was able to demonstrate the limitations of using laser sources that are broadband when compared to the absorption features of interest. They showed that it is possible to overcome these limitations by using cavities where only a single mode is excited (so that the RDC and not the laser linewidth determines P-CRDS resolution). Furthermore, the NIST group<sup>33</sup> performed very careful P-CRDS experiments to determine the effects of mode beating and multimode excitation on noise in the ring-down waveforms and on the consequent reduction in detection sensitivity. By eliminating these effects, they have recently obtained shot-to-shot noise statistics on the order of 0.2%, a significant improvement over most P-CRDS systems.

Scherer and Rakestraw at Sandia National Laboratories furthered P-CRDS into the mid-infrared<sup>77</sup> in 1996: an OPO was used to obtain the first P-CRDS spectra of acetylene at 1.6  $\mu\text{m}$ , and of methane at 3.3  $\mu\text{m}$ . In this case, the OPO output consisted of almost-Fourier-transform-limited pulses (2-4 ns), which provide a resolution of  $0.0025 \text{ cm}^{-1}$ . Minimum observable losses on the order of  $10^{-7} \text{ cm}^{-1}$  were obtained in the mid-infrared. The Sandia group has also recently demonstrated the effectiveness of P-CRDS for spectroscopy in harsh environments<sup>78-80</sup>: the rovibrational spectra of methyl radicals were measured in a low-pressure laminar-flow methane-air flame around 3  $\mu\text{m}$ , and data were compared to flame chemistry simulations under various flame stoichiometric conditions<sup>79</sup>. Similarly, the Sandia group employed P-CRDS for the detection of formyl radicals in a low-pressure  $\text{CH}_4\text{-N}_2\text{-O}_2$  flame<sup>78</sup> using ultraviolet radiation, demonstrating sensitivities comparable to intracavity laser absorption spectroscopy.

Over the last two years, P-CRDS has become increasingly popular among spectroscopists, and its utility to chemists in general seems to grow by the day. Recent applications of P-CRDS to hostile environments include detection of  $\text{C}_6\text{H}$  radicals in a hollow cathode discharge by Maier and coworkers<sup>81</sup> and spectroscopy of

NaH in flames by Hering and co-workers<sup>82</sup>. Application of P-CRDS to predissociation dynamics include studies of the  $\bar{A}^1A$  state of HNO<sup>83</sup> and the  $A^2\Sigma^+\nu = 1$  state of SH radicals by Ashfold and co-workers<sup>84</sup> in the visible and ultraviolet, respectively, and studies of photolysis products of ethyl nitrate<sup>85</sup> and glyoxal<sup>86</sup> in the ultraviolet by Ding and Zhu. Kinetic studies of aromatic radical reactions rate have been performed by Lin and coworkers<sup>87</sup>. Other spectroscopic applications of P-CRDS include studies of acetylene spectra at 1064 nm using ultrahigh finesse cavities by Nakagawa *et al.*<sup>88</sup>, measurements of the radiative lifetime of the  $a^1\Delta_g$  state of molecular oxygen by Miller *et al.*<sup>89</sup>, detection of ultra-slow mirror velocities by Feld and co-workers<sup>90</sup>, and evanescent-wave cavity ring-down spectroscopy for liquids based on total internal reflections by Pipino *et al.*<sup>91</sup>. It can be stated with confidence that over the next decade P-CRDS, from the deep ultraviolet to the far infrared, will gain acceptance as a standard spectroscopic tool, with applications ranging from reaction dynamics to detailed spectroscopic studies of complex molecules.

**Continuous-Wave Cavity Ring-down Spectroscopy (CW-CRDS).** The use of pulsed lasers imposes several limitations on P-CRDS. Unless care is specifically taken to mode-match the laser to only a single mode of the RDC<sup>33</sup>, and allow the cavity to synchronously follow the laser, P-CRDS typically suffers from excess noise caused by multi-mode excitation, and is limited in resolution (for dense mode RDCs) by the laser linewidth. Analysis of the behavior for multi-mode systems can prove to be tedious<sup>33, 34</sup>. For pulsed lasers, even when Fourier-transform-limited, the laser linewidth typically exceeds several hundred MHz (resolution  $\approx 0.002\text{cm}^{-1}$ ). Data acquisition rates have been limited in the past by slow repetition rates of pulsed lasers, although OPOs having kHz repetition rates are presently becoming available. Most importantly, the intensity of the light coupled into and out of the cavity is small in P-CRDS as a consequence of the high cavity mirror reflectivity. To overcome these problems, Lehmann<sup>92</sup> proposed the use of continuous wave (CW) laser sources. Single-mode, CW lasers modulated externally not only have higher duty cycles allowing kHz repetition rates (limited only by the buildup time of light inside the RDC), but also have narrower linewidths (typically  $< 100$  MHz). The resulting increased overlap between the laser and RDC linewidth results in actual energy buildup inside the RDC<sup>31</sup>. Higher light levels at the cavity output imply improved signal-to-noise ratios on the decay waveforms, improved waveform fitting accuracy, and better detection sensitivity. Furthermore, the ability to use CW laser sources enables the exploitation of relatively inexpensive laser sources: laser diodes.

In an approach similar to that first presented by Herbelin *et al.*<sup>44, 45</sup>, the Nijmegen group<sup>46</sup> was to first to measure phase-shifts accrued by a sinusoidally modulated CW laser beam after it passes through a cavity, and to deduce from the phase shift losses caused by the RDC and an absorber. Spectra of O<sub>2</sub> transitions were obtained around 635 nm using a single-mode, argon-ion-pumped dye laser. The Nijmegen group demonstrated that acquisition rates of kHz were compatible with high-resolution CRDS, and that narrowband laser throughput could be made possible (though by no means optimized) by using resonators having a dense transverse mode structure. However, multi-mode excitation within the RDC produced excess noise in the decay constant, leading to MDAL values on the order of  $10^{-6}\text{cm}^{-1}$ .

Initially, efforts to use a LD in CRDS were directed at optically locking a LD to a high-finesse cavity<sup>47</sup>. This approach was precluded, however, by a lack of long-term stability (caused by thermal drift) in locking the laser to the same cavity mode. Later on, Romanini *et al.*<sup>39, 48, 93</sup> at the Centre National de Recherche Scientifique and Université Joseph Fourier (the CNRS-UJF group) avoided this optical locking problem altogether by sweeping one resonant mode of their ring-down cavity through the CW laser linewidth. When sufficient buildup of light within the cavity was

detected, the input laser beam was deflected with an acousto-optic modulator (AOM), and the cavity ring-down decay was recorded. Extensive mode-matching was carried out to guarantee that only TEM<sub>00</sub> modes would be excited in the cavity, although excess baseline noise was initially reported when actual spectral scans were performed, with shot-to-shot variation in the decay time of several percent. Using this technique and an external cavity diode laser, the CNRS-UJF group<sup>39</sup> achieved acquisition rates of several hundred Hz, greatly reduced baseline noise, and obtained MDAL on the order of 10<sup>-10</sup> cm<sup>-1</sup>. The stability of this CW-CRDS system provided the reproducibility necessary to obtain absolute measurements of continua<sup>93</sup>.

Most of the laser sources previously described in CRDS experiments are not only large, and relatively complicated to operate, but expensive. Although solid state lasers (such as OPOs, Ti:Sapphire lasers) are slowly replacing more traditional dye lasers with their increased reliability, ease of operation, mode quality, and tuning range, they are no less expensive. Laser diodes (LDs), on the other hand, have been decreasing in cost thanks to the continuous growth of the telecommunications and data storage industries. Today, laser diodes have sufficient power (> 1 mW), wavelength coverage (UV to mid-infrared) and reliability to be used as experimental light sources. Owing to their compactness, high wallplug efficiency, and low cost, LDs seem to be an ideal source for implementing practical CW-CRDS systems. The CNRS-UJF group was the first to employ external cavity diode lasers (ECDLs) in CW-CRDS<sup>39</sup> to measure high quality NO<sub>2</sub> spectra in a supersonic slit jet, with a residual Doppler width of about 250 MHz. Efforts are also underway by Lehmann to implement the swept cavity scheme using simpler distributed feedback (DFB) LDs for trace water vapor detection.

The use of edge-emitting LDs (no external grating as in DFBs) with linear cavities was first demonstrated by the Stanford group<sup>94</sup>. The problem of "external cavity" formation between the LD back facet and externally placed optics (the output facet has a low reflectivity to maximize output power), affects both the phase and gain relations of LD and makes the LD output highly dependent on the uncontrollable external cavity length. This problem was eliminated by placing an acousto-optic modulator (AOM) inside the "external cavity" formed by the LD and the RDC input mirror. In this approach, only low optical isolation is required for the LD to achieve stable behavior and reproducible coupling into the RDC. A dense cavity transverse mode structure was used that limited MDAL (by multi-mode excitation) to 10<sup>-8</sup> cm<sup>-1</sup>.

In order to minimize multimode coupling into the cavity and improve sensitivity, the Stanford group demonstrated that it is possible to frequency lock the RDC to the laser source<sup>95</sup>. A ring resonator consisting of two flat mirrors and a plano-concave mirror was exploited for its nondegeneracy between p- and s-polarizations. Thus, the RDC is effectively two resonators: a lower finesse RDC for p-polarized light, and a high finesse RDC for s-polarized light. The laser beam was split into two arms: the p-polarized arm was used to lock the cavity to the laser, while the s-polarized light was used for CRDS. Thus, the locking arm could remain uninterrupted during the spectral scan, ensuring a continuous overlap between the laser line and TEM<sub>00</sub> mode of the RDC. It is noted that the s- and p-polarized TEM<sub>00</sub> modes are shifted in frequency relative to one another. By using the Pound-Drever-Hall electronic locking technique, not only were intensity fluctuations between ring-down decays reduced to several percent, but the shot-to-shot fluctuations were reduced to 0.5%, comparable to P-CRDS. This cavity-locked approach ensured that only a single transverse mode was excited and eliminated spurious oscillations in the spectral background. However, owing to the substantial linewidth of the ECDL (several MHz), cavity throughput for the high-finesse remained limited, so that detector noise, and poor quality mirrors (R=99.93%) limited the MDAL to the order of 5 x 10<sup>-9</sup> cm<sup>-1</sup>.

The two-arm locking scheme with large p-arm cavity throughput, and limited s-arm throughput where the two beams are frequency-shifted relative to one another has enabled heterodyne detection to be performed at the cavity output. This detection



scheme, developed by Levenson *et al.*<sup>96</sup>, improved the signal-to-noise ratio in the ECDL system by 31 dB, leading to digitization-limited shot-to-shot noise of 0.2%. Recent efforts by the Stanford group to perform true shot-noise-limited CW-CRDS measurements using low-noise detectors<sup>38</sup> and a narrowband laser source (nonplanar ring oscillator Nd:YAG) frequency-locked to the ring-down cavity have been successful. MDAL<sub>shot</sub> of  $10^{-8}$  cm<sup>-1</sup> have been achieved for 900 ns decays. Efforts using locked supercavities (R > 99.995%) are expected to significantly improve single-shot sensitivity, while faster signal processing electronics are expected to provide real-time averaging of single shot decays at kHz rates.

Shot-noise-limited detection of decay waveforms from supercavities is expected to improve single-shot CRDS sensitivity to  $10^{-14}$  cm<sup>-1</sup>Hz<sup>-1/2</sup>, assuming that about 50 mW of laser light exits the cavity, and heterodyne detection is performed with averaging of 100 waveforms at 100 Hz. This level of sensitivity would allow detection of about 10 molecules in the volume of the probe beam inside the optical cavity for strong infrared transitions and about 1 molecule for strong visible transitions. The results of this calculation are very encouraging about the ultimate sensitivity of CW-CRDS. The reader is warned, however, that other factors may come into play if such extreme limits are pursued. For example, in this calculation it has been assumed that the transition relaxation rate is faster than a cavity round-trip, which is generally not the case in the mid-infrared.

We foresee that CRDS will play an increasing role in absorption measurements. Presently, absorption spectroscopy is a workhorse for spectrochemical analysis. We believe that P-CRDS offers the possibility of transforming this venerable Clydesdale draft horse into a quarter horse for robust, practical applications; moreover, CW-CRDS might spawn an Arabian thoroughbred racehorse for ultrahigh sensitivity applications, with outstanding limits of detection.

## Bibliography

1. Hobbs, P.C.D.; *Appl. Opt.* **1997**, *36*, 903.
2. Allen, M.G., *et al.*; *Appl. Opt.* **1995**, *34*, 3240.
3. Sonnenfroh, D.M. & Allen, M.G.; *Appl. Opt.* **1996**, *35*, 4053.
4. Harris, G.W., Winer, A.M., Pitts, J.N., Platt, U. & Perner, D. in *Optical and Laser Remote Sensing* (eds. Killinger, D.K. & Mooradian, A.) 106 (Springer-Verlag, Berlin, 1983).
5. Harder, J.W., Williams, E.J., Baumann, K. & Fehsenfeld, F.C.; *J. Geophys. Res.* **1997**, *102*, 6227.
6. Stutz, J. & Platt, U.; *Appl. Opt.* **1997**, *36*, 1105.
7. Platt, U. & Perner, D. in *Optical and Laser Remote Sensing* 97 (Springer-Verlag, Berlin, 1983).
8. Brauers, T., Hausmann, M., Brandenburger, U. & Dorn, H.-P.; *Appl. Opt.* **1995**, *34*, 4472.
9. Bufton, J.L., Itabe, T. & Grolemond, D.A. in *Optical and Laser Remote Sensing* (eds. Killinger, D.K. & Mooradian, A.) 2 (Springer-Verlag, Berlin, 1983).
10. Bilbro, J. in *Optical and Laser Remote Sensing* (eds. Killinger, D.K. & Mooradian, A.) 356 (Springer-Verlag, Berlin, 1983).
11. Rothe, K.W., Walther, H. & Werner, J. in *Optical and Laser Remote Sensing* (eds. Killinger, D.K. & Mooradian, A.) 10 (Springer-Verlag, Berlin, 1983).
12. Cherrier, P.P. & Reid, J.; *Nucl. Inst. Meth. Phys. Res.* **1987**, *A257*, 412.
13. White, J.U.; *J. Opt. Soc. Amer.* **1976**, *66*, 411.
14. Herriot, D.; *Appl. Opt.* **1964**, *3*, 523.
15. Bjorklund, G.C., Levenson, M.D., Length, W. & Ortiz, C.; *Appl. Phys. B* **1983**, *32*, 145.
16. Demtröder, W.; *Laser Spectroscopy*; Springer Verlag, Berlin, 1996.

17. Riris, H., Carlisle, C.B., Cooper, D.E., Martinelli, R.U. & Menna, R.J.; *Appl. Opt.* **1994**, *33*, 7059.
18. Silver, J.A. & Hovde, D.C.; *Rev. Sci. Instr.* **1994**, *65*, 1691.
19. Cooper, D.E. & Warren, R.E.; *Appl. Opt.* **1987**, *26*, 3726.
20. Vinogradov, S.E., Kachanov, A.A., Kovalenko, S.A. & Sviridenkov, E.A.; *JETP Lett.* **1992**, *55*, 581.
21. Kachanov, A., Charvat, A. & Stoeckel, F.; *J. OSA B* **1994**, *11*, 2412.
22. Kachanov, A.A., Mironenko, V.R. & Pashkovich, I.K.; *Sov. J. Quant. Electron.* **1989**, *19*, 95.
23. Singh, K. & O'Brien, J.J.; *J. Mol. Spec.* **1994**, *167*, 99.
24. Kachanov, A., Charvat, A. & Stoeckel, F.; *J. OSA B* **1995**, *12*, 970.
25. Gilmore, D.A., Vujkovic-Cvijin, P. & Atkinson, G.H.; *Opt. Comm.* **1990**, *77*, 385.
26. Böhm, R., Stephani, A., Baev, V.M. & Toschek, P.E.; *Opt. Lett.* **1993**, *18*, 1955.
27. Baev, V.M., *et al.*; *Sov. J. Quantum. Electron.* **1979**, *9*, 51.
28. Baev, V.M., Eschner, J., Paeth, E., Schüler, R. & Toschek, P.E.; *Appl. Phys. B* **1992**, *B55*, 463.
29. Kachanov, A.A., Romanini, D., Chavrat, A., Abel & Kovalenko.; *Pers. Comm.* **1997**.
30. Stoeckel, F., Melieres, M.-A. & Chenevier, M.; *J. Chem. Phys.* **1982**, *76*, 2192.
31. Siegman, A.E.; *Lasers*; University Science Books, Mill Valley, CA, 1986.
32. Yariv, A.; *Quantum Electronics*; John Wiley and Sons, New York, 1989.
33. Hodges, J.T., Looney, J.P. & Zee, R.D.v.; *J. Chem. Phys.* **1996**, *105*, 10278.
34. Lehmann, K.K. & Romanini, D.; *J. Chem. Phys.* **1996**, *105*, 10263.
35. Zalicki, P. & Zare, R.N.; *J. Chem. Phys.* **1995**, *102*, 2708.
36. Martin, J., *et al.*; *Chem. Phys. Lett.* **1996**, *258*, 63.
37. Hodges, J.T., Looney, J.P. & Zee, R.D.v. (1997).
38. Spence, T.G., *et al.* (1997).
39. Romanini, D., Kachanov, A.A. & Stoeckel, F.; *Chem. Phys. Lett.* **1997**, *270*, 538.
40. De Riva, A.M., *et al.*; *Rev. Sci. Instrum.* **1996**, *67*, 2680.
41. Anderson, D.Z., Frisch, J.C. & Masser, C.S.; *Appl. Opt.* **1984**, *23*, 1238.
42. Rempe, G., Thompson, R.J., Kimble, H.J. & Lalezari, R.; *Opt. Lett.* **1992**, *17*, 363.
43. Elleaume, P., Velghe, M., Billardon, M. & Ortega, J.M.; *Appl. Opt.* **1985**, *24*, 2762.
44. Herbelin, J.M., *et al.*; *Appl. Opt.* **1980**, *19*, 144.
45. Herbelin, J.M. & McKay, J.A.; *Appl. Opt.* **1981**, *20*, 3341.
46. Engeln, R. & Meijer, G.; *Chem. Phys. Lett.* **1996**, *262*, 105.
47. Romanini, D., Gambogi, J. & Lehmann, K.K. in *50th International Symposium on Molecular Spectroscopy* (ed. Miller, T.A.) (ACS, Ohio State University, Columbus, OH, 1995).
48. Romanini, D., Kachanov, A.A., Sadeghi, N. & Stoeckel, R.; *Chem. Phys. Lett.* **1997**, *264*, 316.
49. O'Keefe, A. & Deacon, D.A.G.; *Rev. Sci. Instr.* **1988**, *59*, 2544.
50. O'Keefe, A., *et al.*; *Chem. Phys. Lett.* **1990**, *172*, 214.
51. Scherer, J.J., Paul, J.B., Collier, C.P. & Saykally, R.J.; *Chem. Rev.* **1997**, *97*, 25.
52. Scherer, J.J., Paul, J.B., Collier, C.P. & Saykally, R.J.; *J. Chem. Phys.* **1995**, *103*, 113.
53. Scherer, J.J., Paul, J.B. & Saykally, R.J.; *Chem. Phys. Lett.* **1995**, *242*, 395.
54. Scherer, J.J., Paul, J.B., Collier, C.P., O'Keefe, A. & Saykally, R.J.; *J. Chem. Phys.* **1995**, *103*, 9187.
55. Paul, J.B., Scherer, J.J., Collier, C.P. & Saykally, R.J.; *J. Chem Phys.* **1996**, *104*, 2782.

56. Scherer, J.J., Paul, J.B., Collier, C.P. & Saykally, R.J.; *J. Chem. Phys.* **1995**, *102*, 5190.
57. Paul, J.B., *et al.* in *CLEO '96 51* (Anaheim, CA, 1996).
58. Paul, J.B., Collier, C.P., Saykally, R.J., Scherer, J.J. & O'Keefe, A.; *J. Phys. Chem. A* **1997**, *101*, 5211.
59. Romanini, D. & Lehmann, K.K.; *J. Chem. Phys.* **1993**, *99*, 6287.
60. Romanini, D. & Lehmann, K.K.; *J. Chem. Phys.* **1995**, *102*, 633.
61. Romanini, D. & Lehmann, K.K.; *J. Chem. Phys.* **1996**, *105*, 68.
62. Romanini, D. & Lehmann, K.K.; *J. Chem. Phys.* **1996**, *105*, 81.
63. Meijer, G., Boogaarts, M.G.H. & Wodtke, A.M.; *Chem. Phys. Lett.* **1994**, *217*, 112.
64. Huestis, D.L., *et al.*; *Can. J. Phys.* **1994**, *72*, 1109.
65. Slanger, T.G., Huestis, D.L., Cosby, P.C., Naus, H. & Meijer, G.; *J. Chem. Phys.* **1996**, *105*, 9393.
66. Boogaarts, M.G.H. & Meijer, G.; *J. Chem. Phys.* **1995**, *102*, 5269.
67. Jongma, R.T., Boogaarts, M.G.H., Holleman, I. & Meijer, G.; *Rev. Sci. Inst.* **1995**, *66*, 2821.
68. Engeln, R., *et al.*; *Chem. Phys. Lett.* **1997**, *269*, 293.
69. Engeln, R. & Meijer, G.; *Rev. Sci. Inst.* **1996**, *67*, 2708.
70. Engeln, R., Bierden, G., Berg, E.v.d. & Meijer, G.; *J. Chem. Phys.* **1997**, *107*, 4458.
71. Zalicki, P., *et al.*; *Chem. Phys. Lett.* **1995**, *234*, 269.
72. Zalicki, P., *et al.*; *Appl. Phys. Lett.* **1995**, *67*, 144.
73. Wahl, E.H., *et al.*; *Diam. Rel. Mat.* **1996**, *5*, 373.
74. Wahl, E.H., *et al.*; *Diam. Rel. Mat.* **1997**, *6*, 476.
75. Xie, J., *et al.*; *Chem. Phys. Lett.* **1997**, *accepted Nov.*
76. Hodges, J.T., Looney, J.P. & Zee, R.D.v.; *Appl. Opt.* **1996**, *35*, 4112.
77. Scherer, J.J., *et al.*; *Chem. Phys. Lett.* **1995**, *245*, 273.
78. Scherer, J.J. & Rakestraw, D.J.; *Chem. Phys. Lett.* **1997**, *265*, 169.
79. Scherer, J.J. & Rakestraw, D.J.; *J. Chem. Phys.* **1997**, *107*, 6196.
80. Scherer, J.J., Voelkel, D. & Rakestraw, D.J.; *App. Phys. B (Lasers and Optics)* **1997**, *B64*, 699.
81. Kotterer, M. & Maier, J.P.; *Chem. Phys. Lett.* **1997**, *266*, 342.
82. Lehr, L. & Hering, P.; *IEEE J. Quant. Elec.* **1997**, *33*, 1465.
83. Pearson, J., Orr-Ewing, A.J., Ashfold, M.N.R. & Dixon, R.N.; *J. Chem. Phys.* **1997**, *106*, 5850.
84. Wheeler, M.D., Orr-Ewing, A.J., Ashfold, M.N.R. & Ishiwato, T.; *Chem. Phys. Lett.* **1997**, *268*, 421.
85. Zhu, L. & Ding, C.F.; *Chem. Phys. Lett.* **1997**, *265*, 177.
86. Zhu, L. & Ding, C.F.; *Chem. Phys. Lett.* **1996**, *257*, 487.
87. Yu, T. & Lin, M.C.; *J. Amer. Chem. Soc.* **1993**, *115*, 4371.
88. Nakagawa, K., Katsude, T., Shelkovnikov, A.S., Labachellerie, M.d. & Ohtsu, M.; *Opt. Comm.* **1994**, *107*, 369.
89. Miller, H.C., McCord, J.E., Choy, J. & Hager, G.D. in *1996 Conference on Lasers (OSA, Portland, OR, 1996)*.
90. An, K., Yang, C., Desary, R.R. & Feld, M.S.; *Opt. Lett.* **1995**, *20*, 1068.
91. Pipino, A.C.R., Hudgens, J.W. & Húie, R.E.; *Rev. Sci. Inst.* **1997**, *68*, 2978.
92. Lehmann, K.K. (Princeton University, U. S., 1996).
93. Romanini, D., Kachanov, A.A. & Stoeckel, R.; *Chem. Phys. Lett.* **1997**, *270*, 546.
94. Paldus, B.A., Martin, J., Xie, J., Harris, J.S. & Zare, R.N.; *J. Appl. Phys.* **1997**, *82*, 3199.
95. Paldus, B.A., *et al.*; *J. Appl. Phys.* **1997**, *accepted Dec.*
96. Levenson, M.D., *et al.*; *Opt. Lett.* **1997**, *submitted Dec.*

## Chapter 6

# Cavity-Ringdown Laser Spectroscopy History, Development, and Applications

A. O'Keefe<sup>1</sup>, J. J. Scherer<sup>1</sup>, J. B. Paul<sup>2</sup>, and R. J. Saykally<sup>2</sup>

<sup>1</sup>Los Gatos Research, 67 East Evelyn Avenue, Mountain View, CA 94041

<sup>2</sup>Department of Chemistry, University of California, Berkeley, CA 94720

Cavity Ringdown Spectroscopy has become a widely used technique in the optical absorption analysis of atoms, molecules, and optical components. The technique allows the determination of total optical losses within a closed cavity comprised of two or more mirrors, and can be made arbitrarily more sensitive by improvements in the cavity mirror reflectivity. Part of the great attraction that Cavity Ringdown has, in addition to its' great sensitivity, is the simplicity of its' use. The required equipment is modest, and the theory of operation is easily grasped by students of modest training. In fact, the technique is used at a growing number of universities as an undergraduate laboratory demonstration. This article presents a review of the development of the Cavity Ringdown technique from its' roots as an unstable and difficult to use method of measuring mirror reflectivities, to the development of the high sensitivity pulsed and continuous adaptations which are in current use.

### Original Driving Forces: Ring Gyroscopes and Interferometers

The fundamental concept behind the Cavity Ringdown technique can be traced back to several efforts in the early 1980's which were aimed at characterizing the reflectivity of HR mirror surfaces for several different applications. The development of the optical ring gyroscope operating at the HeNe laser wavelength, 6328 Å, was having an enormous impact upon both civilian and military aviation systems. The accuracy of the navigational gyro was determined, in part, by the optical residence time within the ring cavity. Increasing the reflectivity of the mirror coatings was the obvious solution to this problem. The development of mirrors with reflectivities exceeding 99.9% was of great interest to the optics community as well as such coatings were of great value in interferometric

applications. The problem confronting both communities was the lack of precision in the characterization of the mirror coatings which was unreliable below 0.1% change. This made it impossible to make the incremental improvements in coating quality.

In 1980, Herbelin et al. (1) demonstrated a novel Phase Shift method which could accurately measure the averaged reflectivity of a pair of mirrors in a cavity to 0.01%. This was followed by the work of Anderson et al. (2) in 1984 which utilized a shuttered laser injection of an optical cavity and could determine the reflectivity of a mirror pair to an accuracy of 0.0005%.

In this adaption of the measurement scheme, the output of a single mode Argon ion laser was passed through a pockels cell shutter, a polarizer, and a pair of mode matching lenses, into a closed, aligned ring cavity. A pair of mode matching lenses are used to optimize the injection coupling and to minimize the coupling and build up of multiple cavity spatial modes. The cavity can, in principle, be of any geometry as long as it is aligned. The use of a ring cavity rather than a two mirror linear cavity is advantageous in applications employing a continuous laser as this geometry largely eliminates optical feedback into the laser. Such feedback could result in laser instabilities.

The laser cavity and the sample cavity are not locked to each other and so the laser cavity modes drift relative to the sample cavity modes. When the laser output frequency accidentally coincides with a sample cavity mode frequency, energy is efficiently coupled into the cavity. The build up of intra-cavity power is accompanied by an increased transmission out of the cavity in the “forward” direction, which is directed onto a photodetector. If left to drift independently, The photodetector would see a random sequence of transmission spikes of varying amplitude, reflecting the random temporal duration of the mode overlap. In Anderson’s adaption, a power level trigger senses when the intra-cavity power reaches a set level and signals the Pockels cell to shut off further laser injection. At this point the monitor detector records the transient response, or “ringdown” of the cavity.

Assuming that the switching time of the Pockels cell is short relative to the cavity decay time, the measured output of the cavity decays exponentially according to the first order expression

$$I(t) = I_0 \times \exp^{-t/\tau} \quad (1)$$

where  $\tau$  is the ringdown decay time constant of the cavity. If the cavity loss is purely due to the transmission of the cavity mirrors, and assuming that the mirror transmission,  $T$ , is given by

$$T \approx 1 - R \quad (2)$$

then the cavity output decay time can be related to  $R$  via

$$\tau = L/c \times [\sqrt{R}/(1-\sqrt{R})] \quad (3)$$

where  $L$  is the mirror separation,  $c$  is the speed of light, and  $R = R_1R_2$  is the reflectance for a two mirror configuration. While this approach demonstrated very good sensitivity, it suffered from temporal instability in that there was no precise method by which to control the onset of the measurement. Because the frequency coincidence of the laser and sample cavities was a random occurrence, it was impossible to synchronize to external experiments. Other factors contributed to the measured system sensitivity, however it was clear that with some effort the ultimate sensitivity could be improved. More important, from the standpoint of spectroscopic analysis, was the difficulty in frequency tuning a single mode laser over any usable or interesting range. While the approach of Anderson et al. (2) would be of value in testing mirror reflectivities at fixed frequencies, it was not yet ready for general spectroscopic use.

### **Development of Pulsed Cavity Ringdown**

We adapted the approach of Anderson et al. (2) by substituting a tunable wavelength pulsed laser for the single mode fixed frequency laser. The first wavelength tunable cavity decay rate instruments were developed at Deacon Research for characterization of mirror reflectivities in an effort to help develop higher reflectivity mirrors for the early Free Electron Laser program. As mirrors of higher reflectivity were developed, it became clear that spectroscopic sensors based upon this technique would provide significant improvements over existing approaches, especially if mirror technology continued to improve. Deacon Research produced and sold dozens of mirror testing instruments based upon this technology under the commercial name *Cavity Lossmeter*. Most of these systems were sold to aerospace technology companies and several national laboratories for optic analysis, however some were adapted for spectroscopic use as the applications became apparent.

The modifications made to the approach used by Anderson et al. (2) allowed us to overcome two problems. First, by using a pulsed laser with a short coherence length, light is coupled into the sample cavity with a constant efficiency (efficiency =  $1 - R$ , where  $R$  is the input mirror reflectivity). Under transient impulsive excitation, the cavity can accept the full spectral range of the input pulse and does not exhibit the narrow frequency acceptance of a classic etalon under continuous irradiation.

The use of a pulsed dye laser source provided other advantages as well. The injection pulse could also be tuned in wavelength over the entire range of the dye laser. This is typically at least as wide as the bandwidth of the mirrors used in the cavity. This allowed not only the measurement of the mirror reflectivity at a single wavelength, but to map out the *reflectivity curve* of the coating. This information, along with the absolute value of the reflectivity, was important feedback to the coating manufacturers, and permitted a significant increase in coating reflectivity in only a few years. Using the Cavity Lossmeter to characterize and perfect new coatings helped produce a 100 fold increase in coating reflectivity

in this period. This remarkable improvement in mirror coating reflectivity set the stage for the advent of Cavity Ringdown spectroscopy.

During 1987 and 1988 a series of internal experiments was initiated at Deacon Research using a modified Lossmeter system to make total loss measurement of gas samples. Using a modest resolution pulsed dye laser (bandwidth  $\sim 1 \text{ cm}^{-1}$ ) system we began a series of experiments aimed at demonstrating the sensitivity of the approach for a range of applications including static gas samples, gas phase reaction product analysis, and transient species detection. These tests utilized a large set of mirrors which spanned the spectral region from 295 nm to 1600 nm in regular intervals, with each mirror set having maximum reflectivities of  $\sim 99.99\%$  or better.

### **General Theory of Operation**

The theory of operation behind the pulsed Cavity Ringdown technique is quite simple (3-5). The basic theory is a special case of that developed by Anderson et al. (2) for the case of continuous wave excitation of a cavity, which is somewhat more complicated because in the continuous wave case the energy within the cavity builds up in time with the same time constant as the cavity decay (as long as the two cavity modes remain locked). When the source injection light is shut off rapidly relative to the cavity buildup or decay time, the resulting decay can be shown to be exponential. Within the constraints of pulsed excitation it is easy to demonstrate why this is so. The technique can be schematically illustrated as in Figure 1.

The output of a tunable pulsed laser is spatially mode matched and injected into an optical cavity made of two or more mirrors with reflectivity  $R$ . The mirrors which make up the cavity must be dielectric multilayer reflectors as it is necessary to allow for a small amount of transmission through the optic. Optical injection is accomplished by aligning the laser beam with the cavity axis and onto one of the cavity mirrors such that the laser beam is reflected back onto itself. The small amount of mirror transmission allows for the pulse injection. The light that enters the cavity is a replica of the incident pulse in spectral content, as the input mirror can only attenuate the field amplitude and cannot spectrally filter the light.

For the case of a laser pulse shorter than the cavity it is easy to envision the injected pulse bouncing between the two cavity mirrors, each reflection resulting in a small transmitted pulse being emitted from the cavity. Each transmitted pulse is related in amplitude to the trapped circulating pulse by the cavity transmission factor,  $T$ , where in the absence of mirror scatter or absorption losses is simply  $1-R$ . The rate of loss from the cavity is given by

$$dI/dt = I \times T \times c/2L \quad (4)$$

where  $c$  is the speed of light and  $L$  is the mirror separation. The solution to this equation is

$$I = I_0 \times \exp^{[-Ttc/2L]} \quad (5)$$

We can rearrange this expression to yield the total round trip loss,  $\Gamma$ , from the cavity

$$\Gamma = 1 - \exp^{[-2L/c\tau]} \quad (6)$$

where  $\tau$  is the  $1/e$  decay time of this signal. As long as there are no other loss mechanisms the measured loss will simply map out the transmission curve of the mirrors used for the cavity. If at some wavelength within the high reflective range of the mirrors there is some additional loss mechanism, such as resonant molecular absorption, then the rate of decay increases. If the baseline mirror loss rate is known then the additional loss can be easily related to the absorption coefficient of the absorbing species.

Because the approach is a direct absorption measurement, it is easy to make quantitative absorption determinations, as long as standard absorption measurement procedures are followed. The bandwidth of the source laser (i.e. the bandwidth of the intra-cavity light) should match or be narrower than the absorbing species, especially if the absorption is strong compared to the mirror losses.

### Static Cell Absorption Measurements

The first series of experiments targeted weak absorbers in the visible region including the doubly forbidden molecular oxygen  $b^1\Sigma_{v=0,1,2} - X^3\Sigma_{v=0}$  absorption system and a series of molecular vibration overtone systems. The weak molecular oxygen absorptions in the red spectral region, with bandheads at 6276.6 Å and 6867.2 Å result from the  $b^1\Sigma_{v=2} - X^3\Sigma_{v=0}$  and  $b^1\Sigma_{v=1} - X^3\Sigma_{v=0}$  transitions respectively. These band systems provide an interesting test case with which to evaluate the sensitivity of the Cavity Ringdown approach. A portion of the (1-0) band is shown in Figure 2. This band system of oxygen is very weak as the symmetry of the electronic states involved,  $\Sigma_g^+ - \Sigma_g^-$  does not permit electric dipole radiation and so the transition must occur through a magnetic dipole interaction. Further, the transition violates the selection rule for electronic spin conservation. The transition probability for this system is reported (3) to be

$$A_{bx} = 0.07 \text{ sec}^{-1}. \quad (7)$$

Rotational component resolved absorption strengths are known for this transition (4) and by making some simple extrapolations we were able to calculate a predicted absorption strength which was within 30% of the measured value. This agreement was considered excellent given the accuracy with which we knew the laser bandwidth and the oxygen linewidth. The first paper describing this technique, along with some of the results obtained with the oxygen absorption spectra was published in 1988 in the Review of Scientific Instruments (3). Subsequently, additional experiments of static gases, looking at weak vibrational



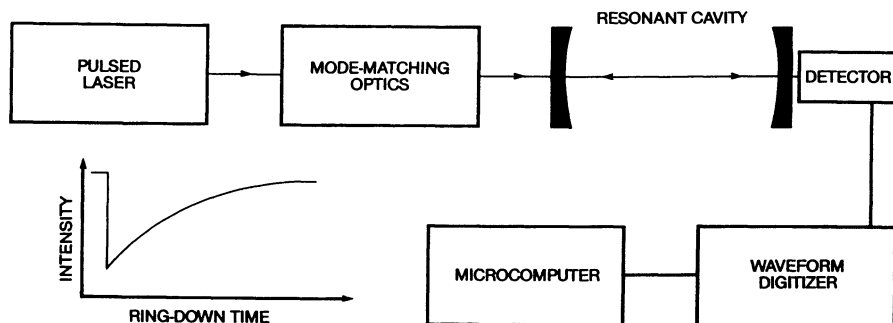


**Figure 1.** Schematic illustration of the Cavity Ringdown process.

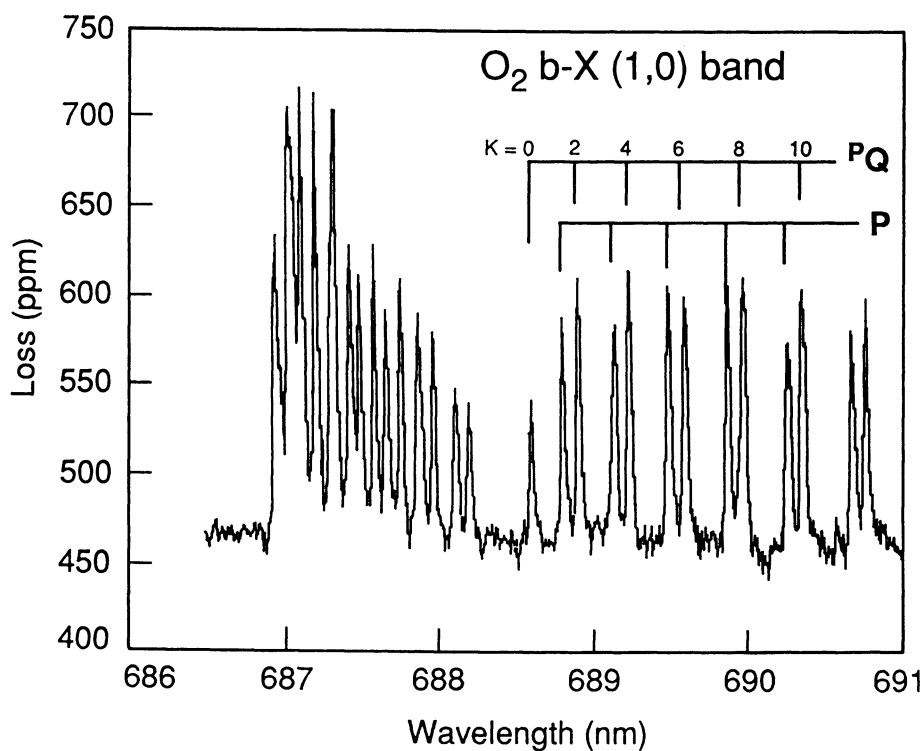


**Figure 2.** Cavity Ringdown spectrum of the molecular oxygen b( $\nu=1$ ) - X( $\nu=0$ ) band taken with a nominal 1 wavenumber bandwidth laser. This spectrum was taken in room air using a 60 cm cavity length.

overtones of water, methane, propane and other simple gas species were carried out and some of the results relating to trace analytical detection methods presented in 1989 (4). A typical set of water overtone transitions is shown in Figure 3 for the combination overtone bands near 593 nm and 650 nm. These spectra are plotted in units of ppm, representing parts-per-million loss.

### **Trace Species Detection**

One of the most promising analytical applications of the Cavity Ringdown technique was clearly in the field of trace species detection, particularly for gas samples (4). Shortly after our first publication introducing the technique, work began on a series of measurements targeting species of interest for air pollution analysis such as nitrogen dioxide and sulphur dioxide. Nitrogen dioxide, NO<sub>2</sub>, has a broad electronic absorption spread over much of the visible spectrum with a number of broad bandhead like features. Again, using room air as the sample, we recorded spectra of NO<sub>2</sub> in the spectral range 425 nm - 460 nm with a nominal 1 wavenumber resolution. The spectra we obtained are shown in Figure 4, where the increasing loss at shorter wavelengths is due to the increased mirror loss baseline.

It is possible to use the measured absorption strength to estimate the concentration of NO<sub>2</sub> in the air at the time of the measurement. The baseline mirror losses at 448 nm were measured to be 100 ppm, and the cavity pathlength is 100 cm.. The absorption strength at 448 nm from Figure 4 is about 20 parts-per-million, resulting in an absorption coefficient,  $k_a=2 \times 10^{-7} \text{ cm}^{-1}$ . Taking the absorption cross section from the feature at 448 nm to be (6) approximately  $\sigma = 5 \times 10^{-19} \text{ cm}^2$ , we calculate:

$$[\text{NO}_2] = k_a/\sigma = 4 \times 10^{11} \text{ molecules cm}^{-3} \quad (8)$$

or about 16 parts-per-billion in air.

It is interesting to note that this absorption system of NO<sub>2</sub> extends far to the red and has a considerable absorption strength at 514 nm. In the early work of Anderson et al. (2) it was noted that tests made at that wavelength in the open "Pasadena air" produced varying results depending upon the local air quality. Thus, it may be that the first spectroscopic measurement made using Cavity Ringdown was made in 1983 by that group!

### **Measurements of Reaction Products**

The next series of tests were made looking at various reactive environments to see if it would be possible to detect transient species and reaction products. A flow reactor cell was constructed into which different species could be introduced in a controlled manner. The cavity mirrors were used as windows for the cell, and were mounted so that the relative angles could be varied for alignment. One gas inlet path of the cell was through a d.c. electric discharge to that we could make atoms

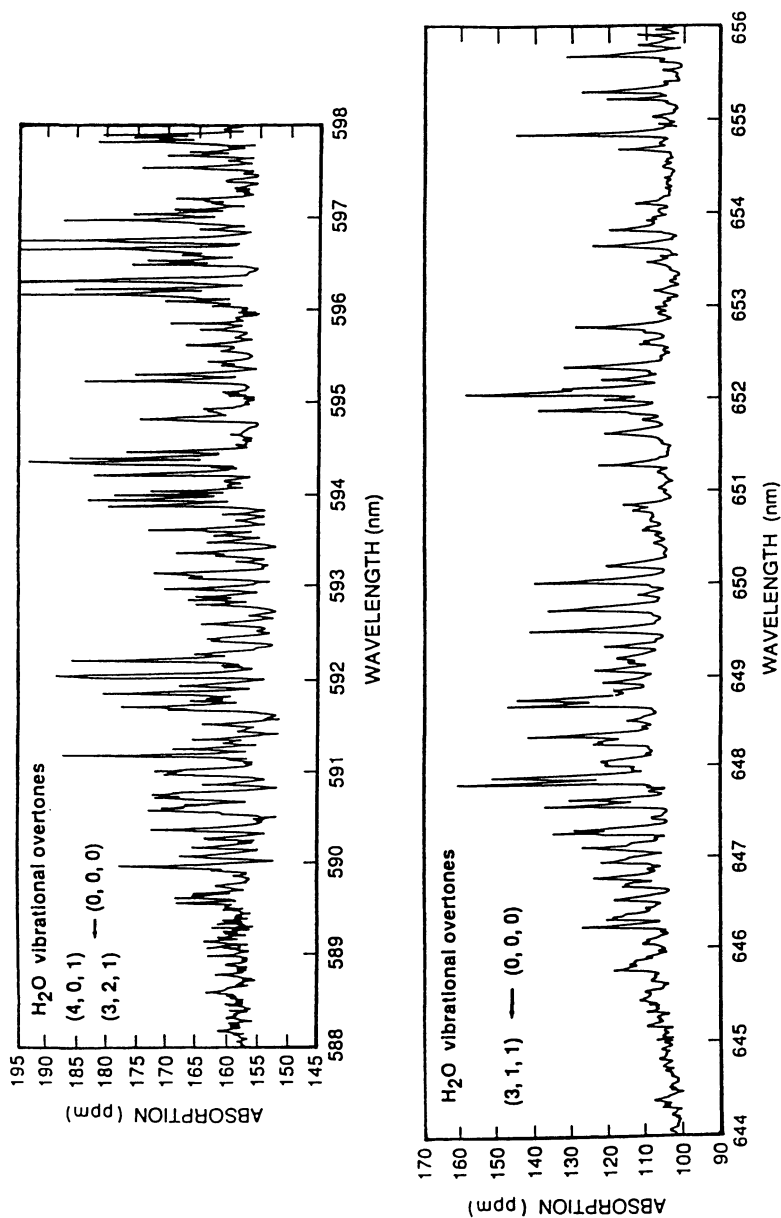


**Figure 3. Overtone and combination band systems of water vapor in air centered at 593 nm and 650 nm. The baseline losses of the mirrors used have not been subtracted.**

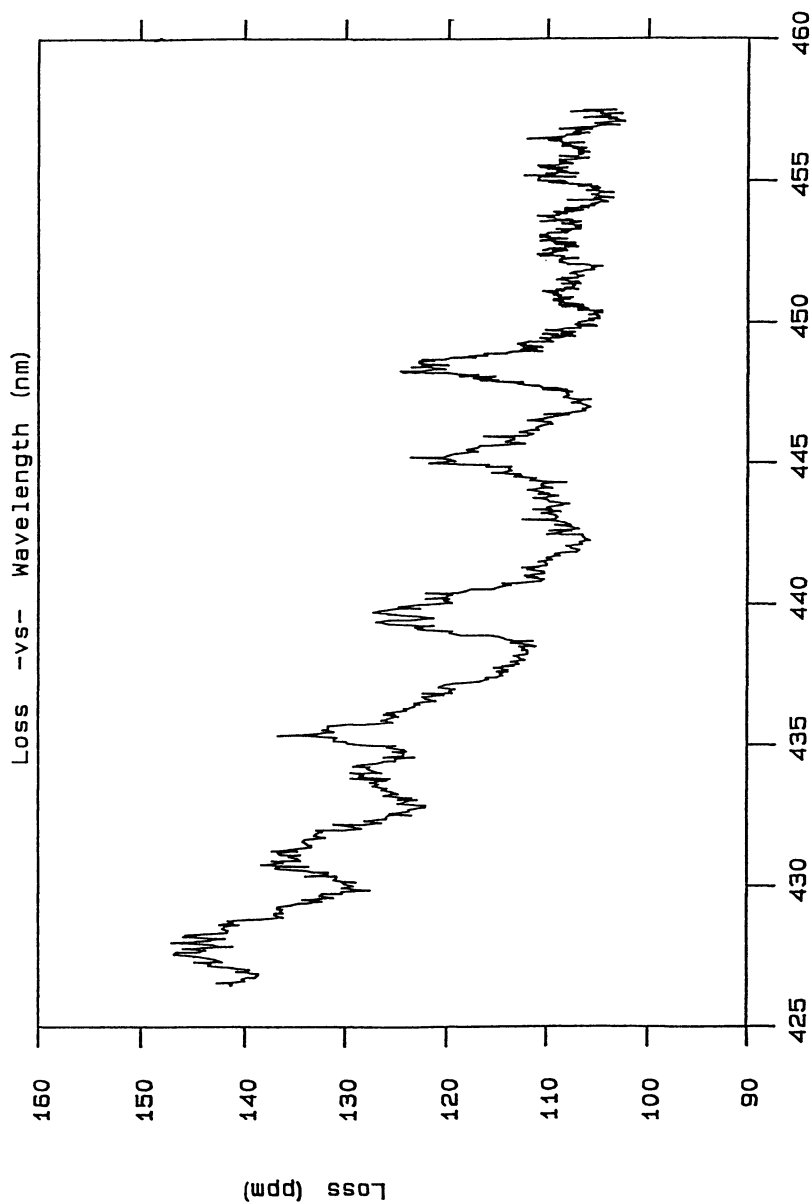


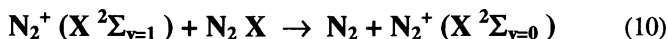
**Figure 4. Cavity Ringdown spectra of NO<sub>2</sub> in room air taken at 0.1 Å steps with a 8 laser shot per point acquisition rate. The increasing loss at shorter wavelength is due to the increasing mirror losses, as the mirror reflectivity maximum is centered at 460 nm.**

or radicals either as target species or as reactive precursors. In one set of tests a purified air mixture was passed through a weak discharge producing some  $\text{NO}_2$  product. Scanning the instrument over the same spectral range as above produced the spectrum shown in Figure 5.

The same broad absorption features seen in Figure 4 are seen in Figure 5. Using the same approach to estimating the concentration of  $\text{NO}_2$  in the cell results in an averaged line of sight density of

$$[\text{NO}_2] = k_a/\sigma = 2.4 \times 10^{11} \text{ molecules cm}^{-3} \quad (9)$$

Other experiments were carried out with the discharge located within the optical cavity. By varying the discharge conditions, such as the voltage, current, and gas pressure, it was possible to change the plasma chemistry so as to favor the formation of significant quantities of different species. A discharge of 300 Vdc in a 5 Torr slow flow of pure nitrogen produced a complex absorption spectrum around 662 nm, probably due to the  $\text{B}^3\Pi_{v=6} - \text{A}^3\Sigma_{v=3}$  excited nitrogen First Positive System. Changing the discharge conditions and chemistry produced significant changes. Using a gas mixture of 90% helium and 10% nitrogen at a total pressure of 0.8 Torr and a 500 Vdc discharge resulted in the production of a larger positive ion concentration. A representative spectrum recorded in 1988 is shown in Figure 6. Some of the lines are identified by their N quantum numbers, and it appears that the level of greatest strength is either  $N''=6$  or 8. Using the  $\text{X}^2\Sigma_{v=1}$  rotational constant for the first vibrational level,  $B''=1.9 \text{ cm}^{-1}$ , the predicted maximum line would occur for  $N''=7$  (the odd-even intensity alternation is the result of spin statistics) for a 300 K sample, which is consistent with our observations. This fact and the line positions and spacings make this identification essentially certain. It is very difficult to estimate the concentration of the  $\text{N}_2^+$  in the discharge because we do not know a) the spatial distribution, b) the vibrational distribution, or c) the line width (which could be broadened in the plasma). We can infer that the population in the  $\text{X}_{v=1}$  level is only a small fraction because it has been shown (7) that this vibrational level of this ion undergoes rapid charge-transfer vibrational relaxation:



This reaction has been shown to occur on nearly every collision (7). These results represent the first Cavity Ringdown absorption spectra of gas phase ionic species and demonstrate the sensitivity of the approach.

While the studies described above were interesting and helped demonstrate the sensitivity of the Cavity Ringdown technique, they did not take advantage of the temporal resolution provided by the technique. Many aspects of chemistry and physics which are of spectroscopic interest require precise temporal control to be studied. Because the approach used pulsed laser light sources it was possible to synchronize the ringdown probe with a dynamic target. The possible applications included pulsed laser induced plasmas, shock tunnels, and pulsed supersonic expansions.

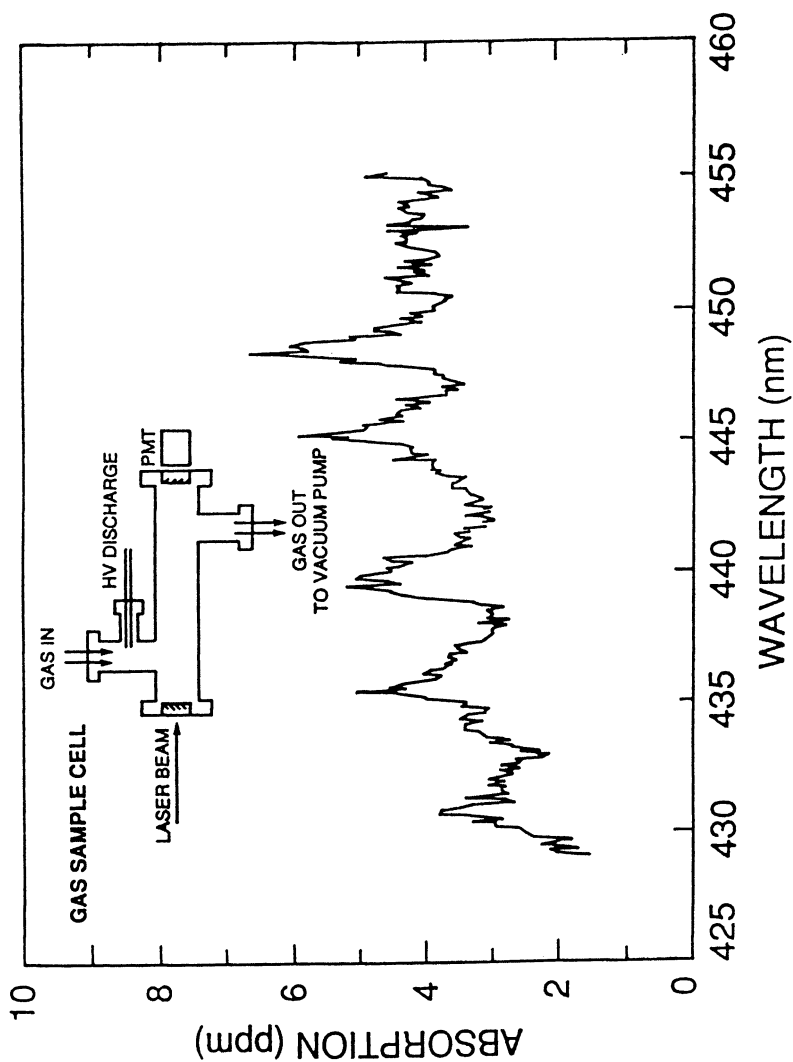


**Figure 5.** Absorption spectra of  $\text{NO}_2$  formed in a d.c. discharge of air at a total pressure of 0.5 Torr. The baseline losses have been subtracted. The spectra were recorded using a 30 laser pulse per point averaging.

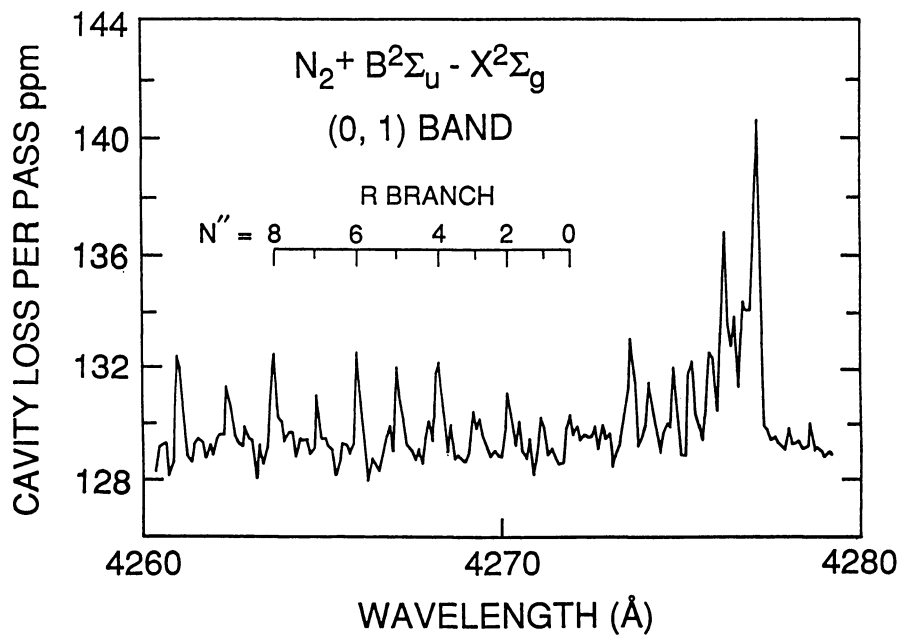


**Figure 6. Cavity Ringdown absorption spectrum of the  $N_2^+$   $B^2\Sigma_{v=0} - X^2\Sigma_{v=1}$  band around 427 nm. The characteristic P-branch bandhead for this transition is at 4278 Å.**

## Going Supersonic

We began a collaboration with Prof. Richard Saykally in early 1990, after many discussions regarding the potential for success. The goal was to use the approach to measure the absorption spectra of metal clusters produced in a laser vaporization pulsed supersonic expansion. The scientific goal was to be able to measure true absorption spectra rather than the only demonstrated alternate methods of laser induced fluorescence (LIF) and resonant two photon ionization (R2PI). It was suspected that many of the metal clusters with high electronic level densities would display rapid excited state deactivation either through internal conversion or predissociation. If so, then many excited states would be invisible to these techniques. A direct absorption measurement would, in contrast, see all of these transitions, making it a much more valuable approach. The technical concerns and risks were significant. It was not clear whether the Cavity Ringdown technique could provide the needed sensitivity. Estimates of the metal cluster densities in the laser vaporization expansions varied over several orders of magnitude, and the species partitioning was unknown. Of equal or greater concern was whether the mirror reflectivity would be rapidly degraded in the vaporization/expansion chamber.

A commercial Cavity Lossmeter was adapted for use with one of the Berkeley laser vaporization pulsed supersonic expansion chambers. This system employed the comparatively low resolution pulsed dye laser used in the studies described above. Within two weeks of the initial set up the collaboration had produced recorded the spectra of several supersonic cooled metal oxides and had yielded several new band systems for the copper clusters,  $\text{Cu}_2$  and  $\text{Cu}_3$ , which had not been observed in prior studies. The absorption spectrum of the copper trimer is shown in Figure 7 over the spectral range 530 nm to 543 nm.

The peaks labeled 2,4,5,6, and 7 were seen in earlier R2PI experiments (8) although with significantly different relative intensities. In the R2PI study the peak labeled 7 had only ~2% of the relative intensity of that labeled 2 in Figure 7. Similarly, the intensity of peak 5 was much weaker in the R2PI work. The feature labeled 7' in Figure 7 was not even seen in the earlier study. In our first paper on the absorption studies of metal clusters (5) we identified this feature as being due to an absorption from the higher energy Jahn-Teller component of the ground state to the same upper level as in peak 7. The peaks labeled 7 and 7' have the same relationship as those labeled 5 and 4 in Figure 7. The energy splitting between them is identical, supporting this assignment.

Following these first experiments, the Berkeley group built a dedicated metal cluster - Cavity Ringdown apparatus equipped with a narrowband excimer pumped dye laser with a bandwidth of  $\sim 0.04 \text{ cm}^{-1}$ ; and later, accompanied by a parallel R2PI detection system to aid in identifying the absorbing species. The copper dimer and trimer spectra were re-visited once this system was operational.

The rotational structure of the  $\text{Cu}_2$  C-X, B-X, and A-X band systems could be resolved given the low rotational temperature of the species in the pulsed supersonic expansion and the 0.04 bandwidth of the tunable dye laser. The



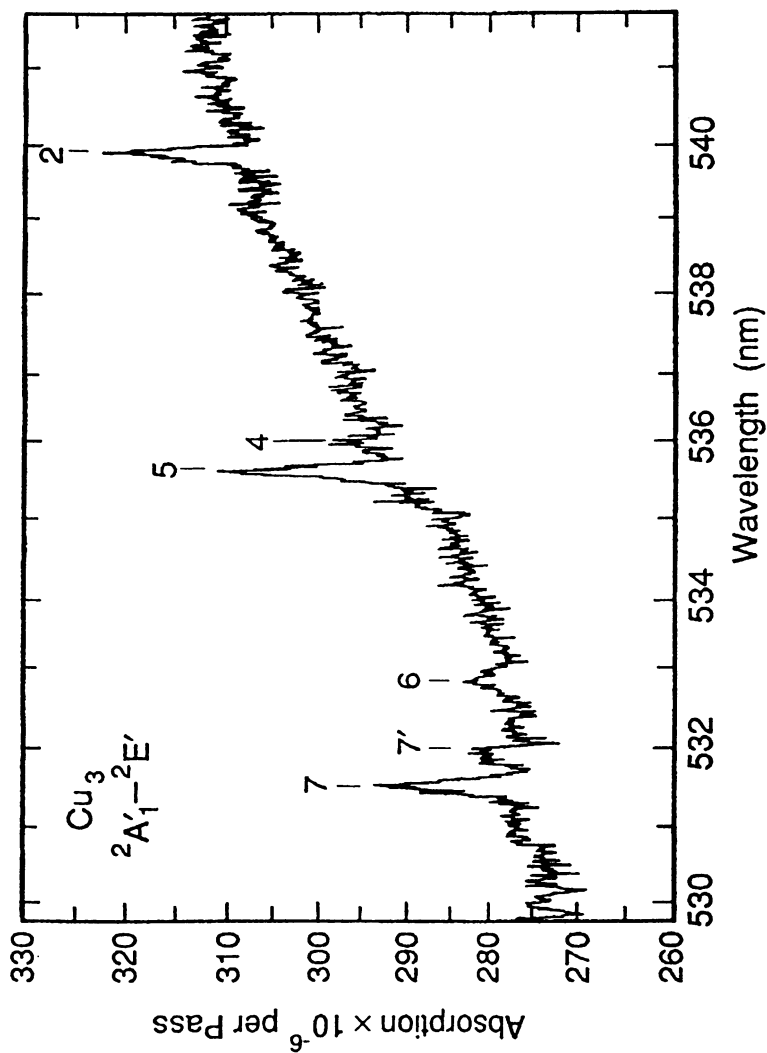


Figure 7. Cavity Ringdown absorption spectrum of the copper trimer,  $\text{Cu}_3$ , obtained by probing a laser vaporization supersonic gas expansion with a 1 wavenumber bandwidth dye laser. The peak labeling is discussed in the text.

rotational structure of the B-X and A-X systems had been resolved by LIF experiments(9,10) however that of the C-X had not. The resolved structure of the Cu<sub>2</sub> B-X and C-X transitions are shown in Figures 8 and 9 respectively. In Figure 8 we note that in our experiments it is possible to resolve even the isotope splittings at high J (inset in Figure) which clearly show the contributions of the <sup>63</sup>Cu<sub>2</sub> (47%), <sup>63</sup>Cu<sup>65</sup>Cu (43%), and the <sup>65</sup>Cu<sub>2</sub> (10%) isotope pairs. The isotope ratios are folded together with the intensity alternation resulting from the nuclear spins.

The resolved spectrum of the Cu<sub>2</sub> C-X system seen in Figure 9 helps to identify the symmetry of the C state. The dimer ground state is known to be a <sup>1</sup>Σ<sub>g</sub> and the configurations possible in the combination of one ground state <sup>2</sup>S<sub>1/2</sub> copper atom with an excited <sup>2</sup>D<sub>3/2</sub> or <sup>2</sup>D<sub>5/2</sub> copper atom can produce twelve possible Σ, Π, and Δ states, of which only the singlet spin states will have any appreciable transition intensity with the ground state. The clear presence of a strong Q-branch in Figure 9 demonstrates that the C state is likely to be a <sup>1</sup>Π<sub>u</sub> state.

A high resolution spectrum of the Cu trimer is shown in Figure 10 where the transition origin band at 5397 Å (peak 2 in Figure 8) is shown. The P,Q, and R branch structure is evident in this spectrum. With the significant improvements in signal levels realized in perfecting the cluster supersonic source and improving the laser bandwidth the copper cluster transition intensity has increased by a factor of 20 over what was first seen. This has allowed the identification of several additional bands in this system. The summary of the observed trimer bands is presented in Table I.

TABLE I  
Vibronic bands and assignments for Cu<sub>3</sub>

Band #	Wavelength <sup>a</sup> (Å)	Assignment <sup>b</sup>
1	5422.5	<sup>2</sup> A <sub>1</sub> - 1ω <sub>1</sub> <sup>2</sup> E'
2	5398.5	<sup>2</sup> A <sub>1</sub> - <sup>2</sup> E' (origin)
4	5360.0	<sup>1</sup> υ <sub>1</sub> - A' (c)
5	5356.0	1υ <sub>1</sub> - <sup>2</sup> E' (origin)
6	5328.2	1υ <sub>2</sub> - <sup>2</sup> E' (origin)
7'	5318.5	<sup>2</sup> υ <sub>1</sub> - A' (c)
7	5314.4	<sup>2</sup> υ <sub>1</sub> - <sup>2</sup> E' (origin)
8	5290.5	1υ <sub>1</sub> 1υ <sub>2</sub> - 2E' (origin)
9	5278.5	<sup>3</sup> υ <sub>1</sub> - A' (c)
10	5275.0	<sup>3</sup> υ <sub>2</sub> - <sup>2</sup> E' (origin)

a) Wavelengths are band centers +/- 0.5 Å

b) Upper state designations for bands 2-10 use the normal mode nomenclature of Ref. 8

c) A' designates the higher energy ground state Jahn-Teller component which is estimated to be 14 cm<sup>-1</sup> above the lowest E' level.

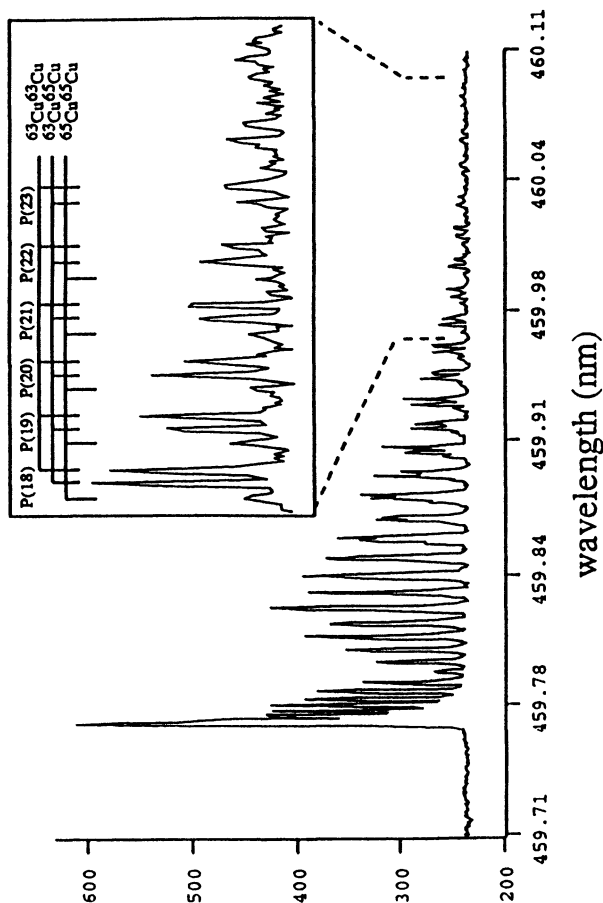


**Figure 8.** Cavity Ringdown absorption spectrum of the copper dimer B-X system around 459.8 nm. The inset shows the isotopic splitting at high J.

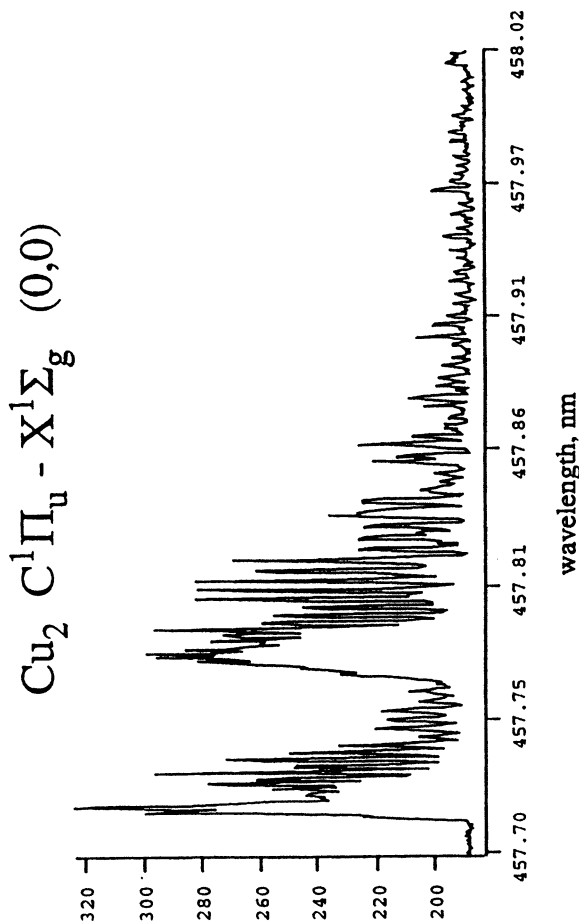


**Figure 9. Cavity Ringdown absorption spectrum of the copper dimer C-X system around 457.7 nm. This was the first rotationally resolved analysis of this system.**

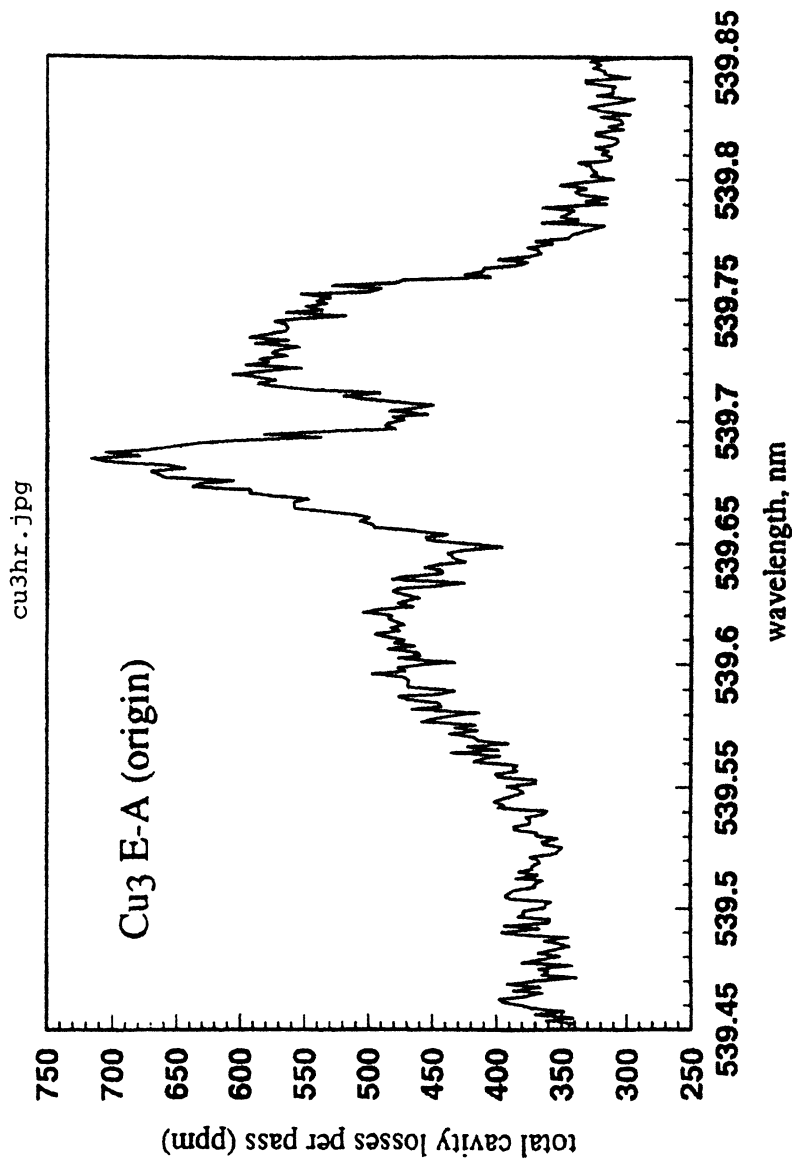


Figure 10. High resolution Cavity Ringdown spectra of the origin band of the copper trimer at 539.7 nm. The single band seen in Figure 7 (peak 2) is now clearly comprised of distinct rotational branches.

The summary of work done in this paper is a very condensed review of what was done in our labs and at U.C. Berkeley when the technique of Cavity Ringdown was in the early stages of development. While our own work progressed, a number of other workers contributed greatly to the field. While some of these contributions are detailed in this ACS compilation, many others are not due to the constraints of space. In an effort to provide a fair perspective of the first decade of work in Cavity Ringdown, we present a summary list of atomic and molecular species which have been studied using the technique during this period in Table II (11-47). Recent reviews of the field are presented in references 48 and 49.

**TABLE II**

Compilation of the different atomic and molecular species which have been studied to date using the technique of Cavity Ringdown Spectroscopy. Table gives the species, wavelength range of study, authors, and published reference number.

<b>Species</b>	<b>wavelength</b>	<b>Authors</b>	<b>pub. ref.</b>
O <sub>2</sub>	626-693 nm	O'Keefe and Deacon	Ref. 3 (1988)
H <sub>2</sub> O	1.102 micron	Ramponi et al.	Ref. 11 (1988)
H <sub>2</sub> O	588-656nm	O'Keefe and Lee	Ref. 4 (1989)
NO <sub>2</sub>	425-460 nm	O'Keefe and Lee	Ref. 4 (1989)
N <sub>2</sub> <sup>+</sup>	426-428 nm	O'Keefe	Ref. 12 (1989)
Cu <sub>2</sub>	452-454 nm	O'Keefe et al.	Ref. 5 (1991)
Cu <sub>3</sub>	530-550 nm	O'Keefe et al.	Ref. 5 (1991)
BiF	471 nm	Bernard and Winker	Ref. 13 (1991)
AlAr	395 nm	Scherer et al.	Ref. 14 (1992)
C <sub>6</sub> H <sub>5</sub>	505 nm	Yu and Lin	Ref. 15 (1993)
HCN	435-571 nm	Romanini and Lehmann	Ref. 16 (1993)
OH	308 nm	Meijer et al.	Ref 17 (1994)
I <sub>2</sub>	637 nm	Meijer et al.	Ref.17 (1994)
CO	206 nm	Jongma et al.	Ref. 18 (1994)
O <sub>2</sub>	243 nm	Huestis et al.	Ref. 19 (1994)
C <sub>6</sub> H <sub>5</sub> O <sub>2</sub>	510 nm	Yu and Lin	Ref. 20 (1994)
NH <sub>2</sub>	537 nm	Diau et al.	Ref. 21 (1994)
CuSi	380-410 nm	Scherer et al.	Ref. 22 (1995)

continued on next page

**TABLE II (continued)**

<b>Species</b>	<b>wavelength</b>	<b>Authors</b>	<b>pub. ref.</b>
NH <sub>3</sub>	204 nm	Rienk et al.	Ref. 23 (1995)
Hg	254 nm	Rienk et al.	Ref. 23 (1995)
AgSi	364-380 nm	Scherer et al.	Ref. 24 (1995)
Al <sub>2</sub>	411-413	Scherer et al.	Ref. 25 (1995)
[C <sub>6</sub> H <sub>5</sub> ] <sub>2</sub> NH	307 nm	Boogaarts and Meijer	Ref. 26 (1995)
C <sub>2</sub> H <sub>2</sub>	1.548 micron	Scherer et al.	Ref. 27 (1995)
CH <sub>4</sub>	3.313 micron	Scherer et al.	Ref. 27 (1995)
CH <sub>3</sub>	216 nm	Zalicki et al.	Ref. 28 (1995)
AuSi	342-352 nm	Scherer et al.	Ref. 29 (1995)
CH <sub>2</sub> CHO	330-350 nm	Zhu and Johnston	Ref. 30 (1995)
PtSi	342-357 nm	Paul et al.	Ref. 31 (1996)
N <sub>2</sub> <sup>+</sup>	505 nm	Kotterer et al.	Ref. 32 (1996)
HNO	750 nm	Pearson et al.	Ref. 33 (1996)
CHO	613-618 nm	Zhu et al.	Ref. 34 (1996)
O <sub>2</sub>	765 nm	Hodges et al.	Ref. 35 (1996)
O <sub>2</sub>	243 nm	Slanger, et al.	Ref. 36 (1996)
O <sub>2</sub>	628 nm	Engeln and Meijer	Ref. 37 (1996)
C <sub>2</sub> H <sub>2</sub>	569 nm cw	Romanini et al.	Ref. 38 (1997)
CHO	614-617 nm	Scherer and Rakestraw	Ref. 39 (1997)
C <sub>6</sub> H	526 nm	Kotterer et al.	Ref. 40 (1997)
C <sub>2</sub> H <sub>4</sub>	10.5 micron	Engeln et al.	Ref. 41 (1997)
OH	1.5 micron	Scherer et al.	Ref. 42 (1997)
NO <sub>2</sub>	776 nm cw	Romanini et al.	Ref. 43 (1997)
OH	308 nm	Spaanjaars et al.	Ref. 44 (1997)
O <sub>2</sub>	628 nm	Engeln et al.	Ref. 45 (1997)
CH <sub>3</sub>	3.3 micron	Scherer et al.	Ref. 46 (1997)
(H <sub>2</sub> O) <sub>n</sub>	3 micron	Paul et al.	Ref. 47 (1997)

### References

- 1) Herbelin, J.M., McKay, J.A., Kwok, M.A., Uenten, R.H., Urevig, D.S., Spencer, D.J., Bernard, D.J., *Appl. Opt.* **1980**, *19*, 144
- 2) Anderson, D.Z., Frisch, J.C., Masser, C.S., *Appl. Opt.*, **1984**, *23*, 1238
- 3) O'Keefe, A., Deacon, D.A.G., *Rev. Sci. Instrum.*, **1988**, *59*, 2544
- 4) O'Keefe, A., Lee, O., *American Laboratory*, **1989**, December, 19
- 5) O'Keefe, A., Scherer, J.J., Cooksy, A.L., Sheeks, R., Heath, J., Saykally, R.J., *Chem. Phys. Lett.*, **1990**, *172*, 214

- 6) Takeuche, N., Shimizu, H., Okuda, M., *Appl. Opt.*, **1978**, 17, 2734
- 7) Mahan, B.H., Martner, C., O'Keefe, A., *J. Chem. Phys.*, **1982**, 76, 4433
- 8) Morse, M.D., Hopkins, J.B., Langridge-Smith, P.R.R., Smalley, R.E., *J. Chem. Phys.*, **1983**, 79, 5316
- 9) Powers, D.E., Hansen, S.G., Geusic, M.E., Pulu, A.C., Hopkins, J.B., Dietz, T.G., Duncan, M.A., Langridge-Smith, P.R.R., Smalley, R.E., *J. Chem. Phys.*, **1982**, 86 2556
- 10) Page, R.H., Gudemann, S.C., *J. Chem. Phys.*, **1991**, 94, 39
- 11) Ramponi, A.J., Milanovich, F.P., Kan, T., Deacon, D., *Appl. Opt.*, **1988**, 27, 4606
- 12) O'Keefe, *Rocky Mtn. Conf. Anal Chem.*, **1989**, also sub. to *Chem. Phys. Lett.*
- 13) Bernard, D.J., Winker, B.K., *J. Appl. Phys.*, **1991**, 69, 2805
- 14) Scherer, J.J., Paul, J., Saykally, R.J., *Ohio State Symp Mol. Spec.*, **1992**
- 15) Yu, T., Lin, M.C., *J. Am. Chem. Soc.*, **1993**, 115, 4371
- 16) Romanini, D., Lehmann, K.K., *J. Chem. Phys.*, **1993**, 99, 6287
- 17) Meijer, G., Boogaarts, M.G.H., Jongma, R.T., Parker, D.H., Wodtke, A.M., *Chem. Phys. Lett.*, **1994**, 217, 112
- 18) Jongma, R.T., Boogaarts, M.G.H., Meijer, G., *J. Mol. Spectrosc.*, **1994**, 165, 303
- 19) Huestis, R.A., Copeland, R.A., Knutsen, T.G., Slanger, R.T., Jongma, R.T., Boogaarts, M.G.H., and Meijer, G., *Can. J. Phys.*, **1994**, 72, 1109
- 20) Yu, T., Lin, M.C., *J. Phys. Chem.*, **1994**, 98, 9697
- 21) Diau, E.W., Yu, T., Wagner, M.A.G., Lin, M.C., *J. Phys. Chem.*, **1994**, 98, 4034
- 22) Scherer, J.J., Paul, J.B., Collier, C.P., Saykally, R.J., *J. Chem. Phys.*, **1995**, 102, 5190
- 23) Jongma, R.T., Boogaarts, M.G.H., Holleman, I., Miejer, G., *Rev. Sci. Instrum.*, **1995**, 66, 2821
- 24) Scherer J.J., Paul, J.B., Collier, C.P., Saykally, R.J., *J. Chem. Phys.*, **1995**, 103, 113
- 25) Scherer, J.J., Paul, J.B., Saykally, R.J., *Chem. Phys. Lett.*, **1995**, 242, 395
- 26) Boogaarts, M.G.H., Meijer, G., *J. Chem. Phys.*, **1995**, 103, 5269
- 27) Scherer, J.J., Voelkel, D., Rakestraw, D.J., Paul, J.B., Collier, C.P., Saykally, R.J., O'Keefe, A., *Chem. Phys. Lett.*, **1995**, 245, 273
- 28) Zalicki, P., Ma, Y., Zare, R.N., Wahl, E.H., Owano, T.G., Harris, J.S., Kruger, C.H., *Chem. Phys. Lett.*, **1995**, 234, 269
- 29) Scherer, J.J., Paul, J.B., Collier, C.P., O'Keefe, A., Saykally, R.J., *J. Chem. Phys.*, **1995**, 103, 9187
- 30) Zhu, L., Johnston, G., *J. Phys. Chem.*, **1995**, 99, 15114
- 31) Paul, J.B., Scherer, J.J., Collier, C.P., Saykally, R.J., *J. Chem. Phys.*, **1996**, 104, 2782
- 32) Kotterer, M., Conceicao, J., Maier, J.P., *Chem. Phys., Lett.*, **1996**, 259, 233
- 33) Pearson, J., Orr-Ewing, A.J., Ashford, M.N.R., Dixon, R.N., *J. Chem. Soc. Faraday Trans.*, **1996**, 92, 1283
- 34) Zhu, L., Kellis, D., Ding, C.F., *Chem. Phys. Lett.*, **1996**, 257, 487
- 35) Hodges, J.T., Looney, J.P., vanZee, R.D., *Appl. Opt.*, **1996**, 35, 4112
- 36) Slanger, T.G., Huestis, D.L., Cosby, P.C., Naus, H., and Meijer, G., *J. Chem. Phys.*, **1996**, 105, 9393
- 37) Engeln, R., and Meijer, G., *Rev. Sci. Instrum.*, **1996**, 67, 2708
- 38) Romanini, D., Kachanov, A.A., Sadeghi, N., Stoeckel, F., *Chem. Phys., Lett.*, **1997**, 264, 316
- 39) Scherer, J.J., Rakestraw, D.J., *Chem. Phys. Lett.*, **1997**, 265, 169
- 40) Kotterer, M., Maier, J.P., *Chem. Phys. Lett.*, **1997**, 266, 342



- 41) Engeln, R., van den Berg, E., Meijer, G., Lin, L., Knippels, G.M.H., van der Meer, A.F.G., *Chem. Phys. Lett.*, **1997**, 269, 293
- 42) Scherer, J.J., Voelkel, D., Rakestraw, D.J., *Appl. Phys. B*, **1997**, 64, 699
- 43) Romanini, D., Kachanov, A.A., Stoeckel, F., *Chem. Phys., Lett.*, **1997**
- 44) Spaanjaars, J.J.L., ter Meulen, J.J., Meijer, G., *J. Chem. Phys.*, **1997**, 107, 2242
- 45) Engeln, R., Berden, G., vander Berg, E., Meijer, G., *J. Chem. Phys.*, **1997**, 107, 4458
- 46) Scherer, J.J., Cernansky, N.P., Aniolek, K., Rakestraw, D.J., *J. Chem. Phys.*, **1997**, 107, 6196
- 47) Paul, J.B., Collier, C.P., Saykally, R.J., Scherer, J.J., and O'Keefe, A., *J. Phys. Chem. A*, **1997** 101, 5211
- 48) Scherer, J.J., Paul, J.B., O'Keefe, A., and Saykally, R.J., *Chem. Rev.*, **1997**, 97, 25
- 49) Paul, J.B., Scherer, J.J., O'Keefe, A., and Saykally, R.J., *Laser Focus World*, **1997**, March, 71

## Chapter 7

# Quantitative Absorption Measurements Using Cavity-Ringdown Spectroscopy with Pulsed Lasers

J. Patrick Looney, Joseph T. Hodges, and Roger D. van Zee

Chemistry Science and Technology Laboratory, National Institute of Standards and Technology, Gaithersburg, MD 20899

The theory and implementation of quantitative gas phase absorption measurements based on cavity-ringdown spectroscopy with pulsed lasers is discussed. The response of ringdown cavities is modeled using an eigenmode description of the cavity fields, and expressions for a number of measurable quantities are given in terms of experimental parameters. Results for long and short ringdown cavities are presented and compared, and it is shown that absolute, high-resolution absorption line shapes can be obtained using a pulsed laser and a short cavity.

Cavity-ringdown spectroscopy (CRDS) is a relatively new absorption spectroscopy that promises sensitive and accurate absorption measurements. The power of CRDS for trace gas monitoring and quantitative absorption measurements was recognized from the earliest measurements by O'Keefe and Deacon (1). Absorptivity measurements of  $<10^{-9}$   $\text{cm}^{-1}$  have been reported (2), and the shot-noise detection limit is  $<10^{-13}$   $\text{cm}^{-1}$ .

A conventional implementation (3) of CRDS uses a pulsed laser to excite a linear cavity formed from two highly reflective, spherical mirrors. Usually the cavity design is not particularly special, (*i.e.* not confocal or otherwise degenerate), and the cavity is not length stabilized. In such an arrangement, a cavity can store the optical field for durations as long as  $10^{-4}$  s, during which time the intensity decays exponentially in time with a time constant called the ringdown time. This decay is measured at the exit of the cavity, the signal is digitized, and the ringdown time is extracted from the digitized signal. For a cavity filled with an absorbing gas under conditions when the Beer-Lambert law is valid, the ring-down time is extracted using the relationship,

$$\tau(\omega) = \frac{\ell}{c \cdot [(1 - R) + \alpha(\omega)\ell]}, \quad (1)$$

where  $\ell$  is the cavity length,  $R$  is the intensity reflectivity of the mirror,  $\alpha(\omega)$  is the frequency dependent absorption coefficient, and  $c$  is the speed of light.

Making measurements with the best sensitivity and the highest accuracy is one objective of our ongoing research. In this chapter, we explore how such measurements can best be made. Below, we review the theoretical underpinning of the method, provide predictive formulae for some of the observable signals, and discuss alternative measurement strategies and present corresponding data.

### Theoretical Model of Cavity-Ringdown Spectroscopy.

This section discusses the theory behind ringdown signals using a field-based description of ringdown signals. Detailed derivations for the starting formulae used below have been given before (4,5) and are not repeated here. Expressions for the signal as a function of time, the peak power levels, the transmitted energy, and ultimate detection limits are derived below.

**Field-based Derivation of Cavity-Ringdown Signals.** The response of a ringdown cavity to the incident excitation field is embodied by the eigenmodes of the cavity (4-7). The net field exiting a ringdown cavity is simply a weighted sum of all of the excited cavity eigenmodes, where the weighting of each mode depends on the overlap of the excitation field spectrum with the cavity eigenfrequency structure, and on the spatial overlap of the transverse profile of the incident field with the spatial structure of the cavity eigenmodes. The overall measured signal is proportional to the modulus squared of the total field exiting the cavity.

**The Excitation Field.** For a transform-limited, Gaussian pulse centered at frequency  $\omega_c$ , the input field to the cavity can be written as

$$\tilde{E}_i(x,y,z,\omega) = \tilde{e}_i(\omega)u_i(x,y,z) = E_0 \frac{\sqrt{\pi}}{\sigma_\omega} e^{-(\omega-\omega_c)^2/4\sigma_\omega^2} u_i(x,y,z). \quad (2)$$

In this expression,  $u_i(x,y,z)$  specifies the transverse profile of the incident field along the  $z$  axis, and  $\tilde{e}_i(\omega)$  the spectrum of the field. The spectral width of this incident field,  $\sigma_\omega$ , is related to the temporal duration of the pulse,  $\sigma_p$ , through the relation  $\sigma_\omega = (2\sigma_p)^{-1}$ . Of course, the width of the associated power spectrum is  $2^{-3/2}$  as wide as the field spectrum, since it is proportional to the square of the field spectrum.

**The Cavity.** The ringdown cavity discussed here is a Fabry-Pérot resonator, and its eigenfrequency structure is a series of narrow resonances, each centered at a cavity eigenfrequency. The spacing of the cavity eigenfrequencies is determined from the geometry of the cavity and the index of the medium filling the cavity. For a symmetric cavity formed from two reflectors with radius of curvature,  $r$ , and separated by a length,  $\ell$ , such that  $\ell < 2r$  and filled with a medium with index of refraction  $n(\omega)$ , the resonance frequencies are given by (8)

$$v_{qmn} = \frac{\omega_{qmn}}{2\pi} = \frac{c}{2 \cdot \ell \cdot n(\omega_{qmn})} \left\{ q + \frac{1}{\pi} (m+n+1) \cos^{-1} [1 - (\ell/r)] \right\}. \quad (3)$$

The three indices  $\{q,m,n\}$  uniquely label each mode. The index  $q$  designates the longitudinal mode and the indices  $\{m,n\}$  the transverse mode. Only cavities of specific lengths are degenerate, that is, have a transverse mode spacing  $[\Delta q=0, \Delta(m+n)=1]$  that is a rationally related ratio of the longitudinal mode spacing  $[\Delta q=1, \Delta(m+n)=0]$  which is also referred to as the free spectral range,  $\Delta\omega_f$ . For nondegenerate cavities, there can be a mode at essentially any arbitrary frequency, though the transverse mode indices may be large.

When a Fabry-Pérot resonator is irradiated, only certain components of the incident field spectrum are efficiently transmitted. The ratio of the transmitted field to the incident field is described by a frequency dependent function referred to as the cavity response function. This function is commonly known as Airy's formula when the cavity is empty (9). When the mirror reflectivities are near unity, as it is for a ringdown cavity, Airy's formula can be approximated as a superposition of isolated Lorentzians centered at the cavity resonances or eigenfrequencies. This structure simply reflects the fact that only light centered at the cavity eigenfrequencies can resonate within the cavity because of the boundary conditions imposed by the mirrors (5).

If the cavity is filled with an absorber, two things happen to the cavity response function. First, the resonance frequencies are shifted, though by such small amounts that these shifts are ignored here. Second, each of the resonances in the vicinity of a spectral absorption feature is broadened and its peak is decreased. In the limit of Beer-Lambert law absorption, the cavity response function associated with mode  $\{q,m,n\}$  is given by

$$\tilde{\mathcal{H}}_{qmn}(\omega) \approx \left[ \frac{1-R}{1-Re^{-\alpha(\omega)\ell}} \right] \frac{\Gamma_{qmn} e^{-\alpha(\omega)\ell/2}}{(\Gamma_{qmn} - i(\omega - \omega_{qmn}))} \quad (4)$$

where the mode width is given by

$$\Gamma_{qmn} = \frac{1}{2\tau_{qmn}} = \frac{1 - Re^{-\alpha(\omega_{qmn})\ell}}{t_r} \equiv \frac{T_{eff}(\omega_{qmn})}{t_r} \quad (5)$$

and where  $T_{eff}$  is an effective single pass intensity transmittance and  $\tau_{qmn}$  is the intensity ringdown time for the specified mode. Note that in the limit,  $\alpha(\omega) \rightarrow 0$  and for the specified resonance, Equation 4 reduces to the Lorentzian approximation of Airy's formula (5).

**The Cavity Excitation.** For pulsed excitation, the frequency spectrum of the excitation field is composed of many frequencies. As discussed above, the field spectrum of mode  $\{q,m,n\}$  exiting the cavity  $\tilde{e}_{qmn}(\omega)$  is the product of the cavity response function and the incident field spectrum,

$$\tilde{e}_{qmn}(\omega) = \tilde{\mathcal{H}}_{qmn}(\omega) \tilde{e}_i(\omega). \quad (6)$$

The number of cavity modes excited depends upon the spacing of these cavity modes relative to the bandwidth of the excitation laser. It is useful then to define a characteristic dimensionless parameter,  $\eta = 2\sigma_\omega/\omega_f$ . A pictorial representation of the

cavity excitation in the frequency domain is given in Figure 1. The cavity response function is plotted versus frequency. Superimposed on this figure is the excitation spectrum of the incident laser field. As the cavity resonances are quite narrow, they appear as spikes. The two cases depicted in this figure correspond to a cavity mode spacing that is much larger than the excitation bandwidth, or  $\eta \ll 1$  (Figure 1a) and to a mode spacing that is small compared to the laser bandwidth, or  $\eta > 1$  (Figure 1c). These two cases are designated as the short- and long-cavity limits, respectively. In the long-cavity limit,  $\eta$  represents the number of cavity modes that is excited.

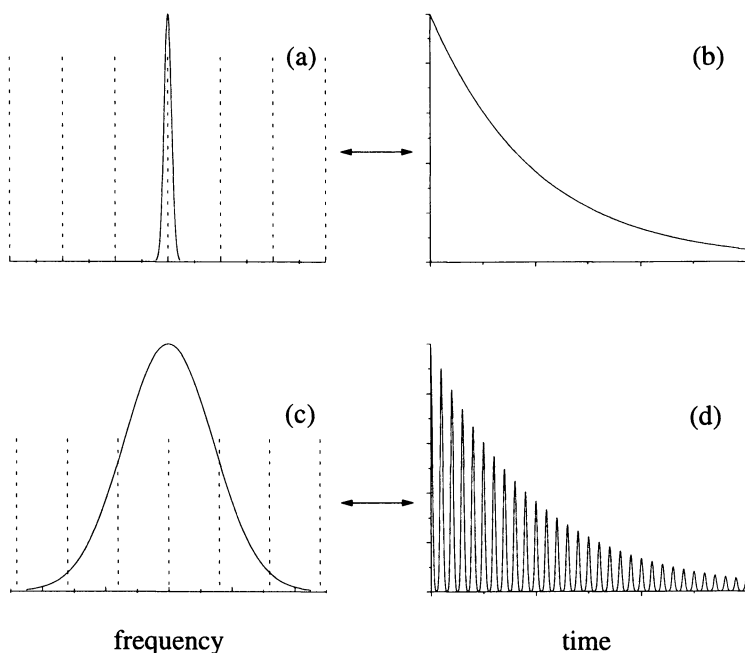


Figure 1: This figure illustrates excitation of a ringdown cavity by a transform-limited, Gaussian pulse. On the left, the longitudinal mode structure and excitation field spectrum are shown for a short (a) and a long (c) ringdown cavity. On the right, the corresponding ringdown signals are shown.

The excitation of cavity modes also depends upon the spatial coupling of the light into the cavity. The spatial overlap factor  $C_{mn}$  is given by the projection of the incident field,  $u_i(x,y,z)$ , onto the transverse mode functions of the cavity (4,5),

$$C_{mn} = \int_{-\infty}^{\infty} \int_{-\infty}^{\infty} u_i(x,y,-l/2) \Psi_{mn}^*(x,y,-l/2) dx dy. \quad (7)$$

Here,  $\Psi_{mn}(x,y,z)$  are the Gauss-Hermite polynomials. The spatial partitioning of the laser input energy among the different cavity transverse modes is given by  $f_{mn} = |C_{mn}|^2 / \sum |C_{mn}|^2$ .

For perfect mode matching into a single transverse mode there is only one non-zero  $f_{mn}$  which, in this case, must be unity. Multiple transverse modes may be excited if the incident wavefront is not matched to a single cavity mode. It is worth noting that the intensity coupling is proportional to the square of these coefficients. In practice, good mode matching is not readily achieved without spatial filtering of the input beam, a judicious choice of the coupling optics, careful alignment of the cavity, and monitoring of the transverse profile of the light exiting the cavity.

**CRDS Signals.** The net field exiting the cavity at frequency  $\omega$  is simply the weighted sum of all of the excited eigenmodes of the cavity. This is given by (5)

$$\vec{E}(x, y, \ell/2, \omega) = \sum_q \sum_{mn} C_{mn} \Psi_{mn}(x, y, \ell/2) \vec{e}_{qmn}(\omega) . \quad (8)$$

Fourier transformation yields the time evolution. Spatial integration of the resulting intensity then yields the radiant power, which is the quantity measured in the laboratory.

For the excitation field described in Equation 4 with a pulse energy  $\mathcal{E}_p$ , the total power radiated from a given excited transverse mode as measured at the exit of the cavity is (5)

$$\begin{aligned} \dot{\mathcal{E}}_{mn}(t) = & \sqrt{2\pi} \mathcal{E}_p \left[ \frac{T^2}{\sigma_\omega t_r^2} \right] f_{mn} \left\{ \sum_{q=1}^{\infty} e^{-\alpha(\omega_{qmn})\ell} e^{-(\omega_{qmn}-\omega_c)^2/2\sigma_\omega^2} e^{-2\Gamma_{qmn}t} \right. \\ & + 2 \sum_{q=1}^{\infty} \sum_{q'=q+1}^{\infty} e^{-\alpha(\omega_{q'mn})\ell/2} e^{-\alpha(\omega_{qmn})\ell/2} e^{-(\omega_{qmn}-\omega_c)^2/4\sigma_\omega^2} e^{-(\omega_{q'mn}-\omega_c)^2/4\sigma_\omega^2} \\ & \left. e^{-(\Gamma_{qmn}+\Gamma_{q'mn})t} \cdot \cos[(\omega_{qmn}-\omega_{q'mn})t] \right\} . \quad (9) \end{aligned}$$

This expression is in general valid for times that are larger than the laser's pulse duration. The single summation describes the envelope of the ringdown signal and is the weighted sum of exponential decays from the excitation of multiple longitudinal modes. Each term in this sum has a decay time based on the optical losses in the cavity at the corresponding eigenfrequency, with each weighting factor being dependent upon the spectral overlap of the excitation spectrum with the cavity eigenfrequency. If the line widths of the excited modes are constant with mode index, which is to say all modes have the same losses, then the envelope of the decay will be purely exponential. The double summation in Equation 9 contains the interference terms arising from the beating of different excited longitudinal modes. These exponentially decaying terms sinusoidally modulate the envelope signal. Since the mode-beating terms contain negligible energy, the net transmitted energy is essentially all contained within the envelope of the decay given by the single summation in Equation 9. If more than one transverse mode of the cavity is excited, then the total measured signal is the sum over all of the excited transverse modes. Transverse mode beating can give rise to additional complexities (4,5).

Assuming the excitation of a single transverse mode, in the short-cavity limit only one longitudinal mode contributes to the total signal and the optical decay is a simple

exponential decay (Figure 1b). In the long-cavity limit, many longitudinal modes contribute to the signal and the observed optical decay signal is a series of “pulses” of decaying amplitude, each separated by the round-trip time in the cavity (Figure 1d). In the intermediate cavity case, a few cavity modes are excited and the observed decays will show modulations with the depth of modulation dependent on  $\omega_c$ . If the dispersion within the cavity cannot be neglected, then the cavity eigenmodes will no longer be equally spaced and the mode-beating will no longer be strictly periodic (4). This effect, in turn, will alter the shape of the pulses leaving the cavity.

**Signal Power Levels and the Energy Transmitted by the Cavity.** Evaluated at  $t=0$ , the single summation in Equation 9 gives the peak power radiated by a single cavity mode. The total transmitted energy is determined by integrating Equation 9 over all time. Table I gives expressions for these quantities in the long- and short-cavity cases and summarizes some of the other properties of ringdown cavities that have been discussed above. It is interesting to note that the peak power levels in the cavity at the end mirror will be a factor of  $\sqrt{2/\pi\eta^2}$  greater in the short-cavity limit when compared to the peak power for the long cavity excited by the same pulse. For incident pulse energies of  $\sim 1$  mJ, the intra-cavity power levels for a short cavity can be sufficient to make absorption rates exceed relaxation and dephasing rates for strong transitions. This may lead to saturation phenomena such as hole burning (10) and to non-exponential ringdown signals. Coupled with the very high spectral resolution of single-cavity mode spectroscopy, this regime may provide an area of future interest in CRDS measurements.

### Statistical Uncertainties in CRDS-based Absorption Measurements.

Since absorption measurements in CRDS are made by measuring on-resonance losses and subtracting the empty cavity losses, the overall uncertainty in the absorption coefficient depends upon the uncertainty in the mean ringdown time of both the on- and off-resonance measurements. Therefore, the minimum measurable absorption coefficient for many independent measurements is (2)

$$\alpha_{\min} = \sqrt{2} \frac{\sigma_{\tau_{\text{empty}}} / \bar{\tau}_{\text{empty}}}{c \bar{\tau}_{\text{empty}}}, \quad (10)$$

where  $\sigma_{\tau_{\text{empty}}}$  is the uncertainty (typically expressed as a standard deviation) in the mean value of the empty cavity ringdown time  $\bar{\tau}_{\text{empty}}$ . In the shot noise limit, the ratio  $\sigma_{\tau_{\text{empty}}} / \bar{\tau}_{\text{empty}}$  is the reciprocal of the square root of the number of detected photons. However, in practice, this ratio is determined by an appropriate statistical analysis of the ensemble of time constant measurements, and this measured value may very well be larger than the shot-noise limited value. In Table I, expressions for  $\alpha_{\min}$  are given for the long- and short-cavity cases assuming shot-noise limited detection. Shot-noise limited values of  $\alpha_{\min}$  range from  $10^{-9}$  –  $10^{-13}$   $\text{cm}^{-1}$  for realistic parameters. The midpoint of these absorptivity limits corresponds to number densities of  $\sim 10^{16}$   $\text{m}^{-3}$  in the case of a very weak absorption band, such as the  $b(v=0) - X(v=0)$  electronic transitions of molecular oxygen or  $\sim 10^{11}$   $\text{m}^{-3}$  for a strong absorber, such as the (00011) – (00001) vibrational band of carbon dioxide.

Table I. Comparison of Short and Long Cavity Properties to Pulsed Gaussian Excitation.

	<i>Short</i> ( $\eta \ll 1$ )	<i>Long</i> ( $\eta > 1$ )
Signal	Single Exponential Decay	Series of Recurring "Pulses"
Peak Power in Ring-Down Signal (e.g. Watts)	$\mathcal{E}_p \frac{\sqrt{2\pi} T^2}{\sigma_\omega t_r^2} f_{mn} e^{-(\omega_{qmn} - \omega_c)^2 / 2\sigma_\omega^2}$	$\mathcal{E}_p \frac{T^2}{t_r} f_{mn}$
Energy Transmitted (e.g. Joules)	$\mathcal{E}_p \frac{\sqrt{\pi/2} T^2}{\sigma_\omega t_r^2 \Gamma_{qmn}} f_{mn} e^{-(\omega_{qmn} - \omega_c)^2 / 2\sigma_\omega^2}$	$\mathcal{E}_p \frac{\sqrt{\pi/2} T^2}{\sigma_\omega t_r} f_{mn} \sum_{q=1}^{\infty} \frac{e^{-(\omega_{qmn} - \omega_c)^2 / 2\sigma_\omega^2}}{1 - R e^{-\alpha(\omega_{qmn} - \omega_0)\ell}}$
Shot-Noise Limited Absorptivity ( $\alpha_{\min}$ ) (e.g. cm <sup>-1</sup> )	$\frac{2}{\ell} \sqrt{\frac{h\nu}{\mathcal{E}_p \beta}} \frac{\eta}{\sqrt{2/\pi}} \frac{T}{N_s}$	$\frac{2}{\ell} \sqrt{\frac{h\nu}{\mathcal{E}_p \beta}} \frac{T}{N_s}$
$\eta$	$= 2\sigma_\omega / \Delta\omega_f$ = ratio of excitation spectral linewidth to cavity free spectral range.	
$\sigma_\omega$	$= e^{-1/2}$ width of power spectrum of incident laser pulse.	
$\Delta\omega_f$	$= \pi c / \ell$ = cavity free spectral range ( $c$ = speed of light, $\ell$ = cavity length).	
$\omega_{qmn} - \omega_c$	$=$ detuning of mode $\{q, m, n\}$ from laser central frequency.	
$\omega_{qmn} - \omega_0$	$=$ detuning of mode $\{q, m, n\}$ from absorption line center.	
$f_{mn}$	$=$ fraction of incident light coupled into the $\{m, n\}$ transverse mode.	
$t_r$	$= 2\ell / c$ = cavity round-trip time.	
$T$	$= 1 - R$ = intensity transmittance of cavity mirrors ( $R$ = intensity reflectivity).	
$\Gamma_{qmn}$	$= (2^* \tau_{qmn})^{-1}$ = linewidth of cavity mode $\{q, m, n\}$ ( $\tau_{qmn}$ = ringdown time).	
	$\mathcal{E}_p$ = incident laser pulse energy.	
	$h\nu$ = photon energy.	
	$\beta$ = detector quantum efficiency.	
	$N_s$ = number of shots.	
	$\ddagger$ = reduces to $\mathcal{E}_p f_{mn} T/2$ for an empty cavity.	



The best estimation of the ringdown time is determined from a weighted, least-squares regression to the natural logarithm of the ringdown signal (11). Our current approach is to identify the dominant noise sources and estimate noise levels to obtain the weighting factors. To account for baseline effects, the average value of the digitized baseline signal that precedes each exponential decay is determined, and this level is subtracted from the ringdown signal. The time constant is then simply the reciprocal of the best-fit slope.

The weighting factors are equal to the reciprocal of the overall signal variance. The signal variance due to shot noise can be estimated in terms of the measured signal level, detector responsivity, and the system bandwidth. The digitizer noise is based on the vertical resolution of the oscilloscope, and the detector's technical noise is given by the measured variance in the baseline signal. All three variances are summed to give the total variance. When the data are weighted in this manner, the ringdown signals have a reduced- $\chi^2$  near unity, indicating a good fit (11). In fact, the reduced- $\chi^2$  was found to be a very sensitive measure of the quality of our ringdown curves.

### **Quantitative Absorption Measurements.**

Above, the shape of ringdown signals was considered in the long- and short-cavity limits. It was seen that in the long-cavity limit, a ringdown signal consists of a series of decaying "pulses" that result from beating between the longitudinal modes that are excited by the incident light. If longitudinal modes with different transverse indices ( $m$  and  $n$ ) are excited, and if, as is typical in real experiments, complete orthogonality between the transverse modes cannot be maintained, then additional mode beats will occur (4,5). This transverse mode beating only further complicates the observed signals. Consequently, the accuracy of absorptivity measurements determined from such ringdown curves can be expected to be compromised because of the difficulty associated in extracting the decay constant from complex signals. Furthermore, even if only a single transverse mode is excited (perfect mode matching), under certain circumstances the ringdown signal will not be purely exponential. Specifically, for a long cavity and if the line width of the absorbing feature is comparable to the spectral width of the incident light, the overall decay will actually be a superposition of many exponentials. Thus, as predicted by Equations 5 & 9, the signal comprises multiple modes each decaying at a different rate. For this case, some type of backcorrection to the signals will be required to obtain  $\alpha(\omega)$  (6).

In the limit of a short cavity, on the other hand, a single mode excitation can be more simply realized. Thus, to the extent that a single transverse mode is dominant, the ringdown signals can be expected to be single exponentials. Because each mode of a ringdown cavity is extremely narrow, the absorptivity over an essentially infinitesimal frequency interval is measured, so that no backcorrection is required. It would therefore be expected that the most accurate absorptivity measurements could be made in this short-cavity limit.

Below, data are presented for both a conventional, long-cavity and short-cavity implementation of CRDS.

**Conventional CRDS Measurements.** To investigate the accuracy of the ringdown technique, we have previously reported CRDS measurements of Doppler-broadened transitions of the  $b(v=0) - X(v=0)$  band of  $^{16}\text{O}_2$  using a conventional CRDS setup (12). The cavity was 1.2 m long and nondegenerate, and was excited by a single-mode  $\text{Ti:Al}_2\text{O}_3$  laser with an effective spectral bandwidth of  $\sim 250$  MHz. Based on the single-shot laser bandwidth,  $\eta \sim 1.0$  for this experiment. Neither the length of the ringdown cavity nor the laser frequency was stabilized, and multiple transverse modes were intentionally excited by off-axis injection of the laser (4,5,13). Multiple ringdown signals were averaged, and the time averaged spectrum of the laser was simultaneously recorded. The electronic bandwidth of the detection system was 30 MHz. Data obtained on resonance were modeled using the integral formulation (Equation 1 of Reference 12) for the decay signals to extract the line strengths of the rotational transitions.

To illustrate the results, we show in Figure 2a a 25-shot average of the optical decay measured on the peak of the 'R(9) line at a total  $\text{O}_2$  pressure of 1330 Pa and temperature of 296 K. The decay in this case is exponential within signal-to-noise limits. However, the decay time constant derived from the fit of a single exponential to the data results in an estimated absorptive peak loss of 8038 ppm/pass. This is  $\sim 8\%$  low of the expected peak value of 9251 ppm/pass (14). Peak absorptive losses of 9110 ppm/pass, or only about 1.5% low of the expected value are obtained by using the integral formulation to the observed decays and the measured laser spectrum. Although the agreement with published values is good, the accuracy of these data was limited by several factors common to most CRDS experiments. These include uncertainties in the time-averaged laser bandwidth, variations in the laser/cavity mode detuning, and transverse mode beating in the decay signals. A spectrum of the  $\text{O}_2$  'R(9) line was obtained by determining the losses from a simple exponential fit as the laser was scanned over the transition. This result, given in Figure 2b illustrates that failure to deconvolute bandwidth effects yields a line shape that is broadened relative to the expected nearly Doppler-limited profile.

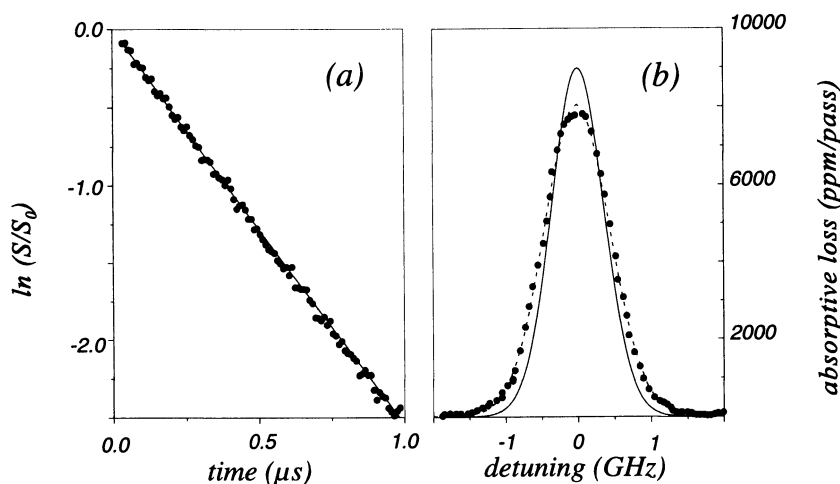


Figure 2: A ringdown signal (a) and rovibronic line profile (b) of the 'R(9) transition of the  $^{16}\text{O}_2$  A-band measured using a conventional implementation of CRDS.

**Measurements Using Short Cavities.** To improve on the measurements discussed above, we designed an experimental system to optimize the quantitative measurement capability of CRDS. The approach we chose was predicated on the assumption that the most accurate CRDS measurements would be made with single mode excitation. This also required using a frequency-stabilized laser and a length-stabilized ringdown cavity.

Light for these measurements was generated with an injection-seeded, pulsed optical parametric oscillator (OPO) that was frequency stabilized against a transfer cavity. The resulting frequency stability was estimated to be better than 3 MHz. In seeded operation and when pumped with a fluence of  $\sim 2 \text{ J/cm}^2$ , the OPO generated  $\sim 1 \text{ mJ}$  of signal light, in a pulse  $\sim 4 \text{ ns}$  long with a bandwidth of  $\sim 115 \text{ MHz}$ . Length stabilization was achieved by constructing a chamber from invar and housing the entire assembly in a temperature regulated enclosure. A pair of 20 cm radius of curvature dielectric mirrors separated by 10.4 cm formed the ringdown cavity. For this setup,  $\eta \sim 0.067$ . The output mirror was mounted on a tubular piezoelectric element to permit scanning of the ringdown cavity length and hence the cavity resonant frequency. A commercial Si-PIN photodiode package was used to measure the ringdown signals. The amplifier output was terminated into  $50 \Omega$  at the input of a 10-bit digital oscilloscope. The electronic bandwidth was 15 MHz. The digitized ringdown decay signals were transferred to a computer and processed on a shot-by-shot basis.

To minimize coupling into higher order transverse modes, the OPO beam was spatially filtered and imaged into the ringdown cavity. About three quarters of the transmitted light could be coupled into  $TEM_{00}$ , and no mode with a transverse mode index sum ( $m+n$ ) greater than two was appreciably excited. Ringdown signals from different transverse modes were readily observed and compared. It is interesting to note that the empty cavity ringdown losses were found to increase by  $\sim 5 \text{ ppm}$  per unit change in the transverse mode index sum. Such large differences cannot be explained by transverse-mode-dependent diffraction losses or the frequency dependence of the mirror reflectivity. These variations perhaps arise from nonidealities in cavity alignment, such as a tilt of the mirror, or nonidealities in the mirrors themselves, such as astigmatism, spatial variations in the surface smoothness, or imperfections in the dielectric stack.

A typical ringdown signal and the associated residuals from a weighted-least-squares fit are shown in Figure 3. This empty cavity signal has a ringdown time of  $13.18 \mu\text{s}$ , corresponding to a mirror loss per pass of 26.33 ppm/pass. The fractional uncertainty in the measured time constant, also extracted from this fit, is 0.03%. A better measure of the uncertainty in the ringdown time is the standard deviation of an ensemble of time constants that is obtained by repeated measurements. It was found that such a distribution typically had a larger standard deviation (0.2–0.4%) than that extracted from a single-shot. This larger number sets the detection limit of this experiment.

To demonstrate the quantitative potential of this ringdown system, the line shape of the  $^{\text{P}}\text{P}(9)$  rotational transition of  $^{16}\text{O}_2$  was measured at a pressure of 1.29 kPa and temperature of 296.0 K. In this experiment, the OPO frequency was scanned in 50 MHz steps, and at each step the OPO and ringdown cavity were brought in to resonance. Ten shots per step were acquired, with each shot processed to yield an average ringdown time,  $\bar{\tau}$ . At each frequency step,  $\bar{\tau}$  and the associated variance in the set of ten measured time constants were calculated. Near the line center, the standard deviation of the ten measured

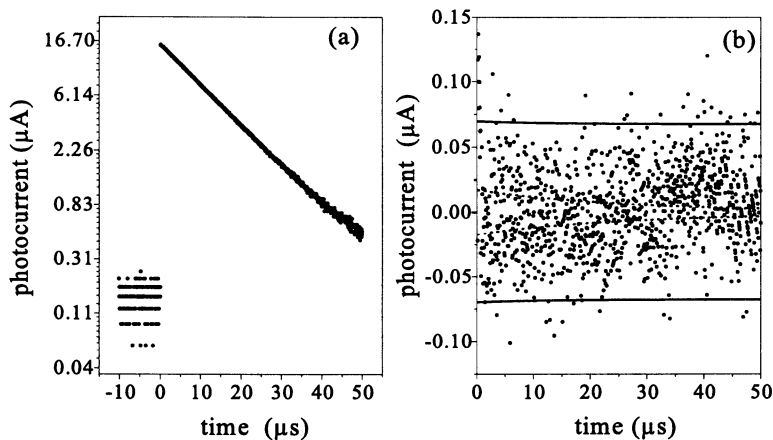


Figure 3: Panel (a) shows a ringdown signal measured using a single mode, pulsed excitation of a short cavity. Panel (b) shows the residuals to a fit of the measured curve. The solid line shows the  $2\sigma$  uncertainty associated with technical detector noise, and the dashed line is the shot-noise associated with the flux exiting the cavity.

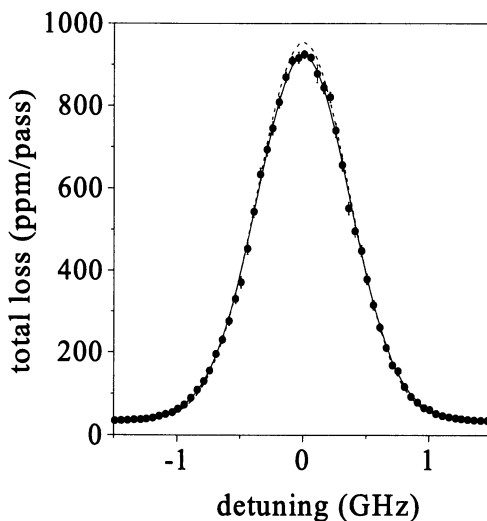


Figure 4: A line profile of the  ${}^9\text{P}(9)$  transition of the  ${}^{16}\text{O}_2$  A-band measured using the short cavity. The  $2\sigma$  uncertainty at each step is also shown. The solid line is a fit using a Galatry line shape, and the dashed line is a Doppler profile.

time constants increased by a factor of about four compared to the empty cavity, as there are about fifteen times fewer points in the ringdown curves. The results are shown in Figure 4.

These data were fit to two line shape models. First, they were fit using a Galatry line shape and the broadening and narrowing coefficients reported by Ritter and Wilkerson as constants (14). The off-resonance ringdown cavity loss and the transition line strength were varied. For each datum, the weighting coefficient was taken to be the reciprocal of the sum of the measured variance in cavity loss and the variance associated with the uncertainty in the frequency axis, which was estimated to be 10 MHz. Except in the far wings and near the line center, the maximum contribution to the uncertainty in each datum is associated with the imprecision in the frequency axis. This fit gives a line strength of  $8.56 \cdot 10^{-24} \text{ cm}^2 \text{ cm}^{-1}/\text{molecule}$ , about 0.9% larger than that reported by Ritter and Wilkerson. The fit to the line profile is quite good and yields a  $\chi^2 = 0.81$ . Figure 4 also shows a best-fit Doppler profile. The line strength extracted from this fit is  $\sim 0.5\%$  larger than the Ritter and Wilkerson value; however, the quality of this fit is inferior ( $\chi^2 = 31$ ). The discrepancies between the measured profile and best-fit Doppler profile are most notable near line center. The best-fit Doppler profile gave empty-cavity losses of  $\sim 34$  ppm/pass,  $\sim 10\%$  larger than the measured value of  $31 \pm 0.1$  ppm/pass. The ability to distinguish between line shapes demonstrates that the inherent frequency selectivity of optically short cavities can be used to make sensitive and accurate measurements.

## Conclusion.

This paper has extended the field-based description of ringdown signals (5) to include the case when the cavity is filled with a sample that absorbs in the Beer-Lambert law limit. Expressions for the peak power exiting the cavity, transmitted energy and shot-noise limited absorptivity were derived for the short- and long-cavity limits. It was argued that quantitative absorptivity measurements are best made in the short-cavity limit, and data were presented for both a short- and a conventional, long-cavity implementation of CRDS. The experimental results bolster the conjecture that the most sensitive measurements can be made in the short-cavity case, and also suggest that single mode, pulsed cavity-ringdown spectroscopy can be used for measurements requiring high spectral resolution, such as the measurement of line shapes or saturation spectroscopies.

## Literature Cited.

- (1) O'Keefe, A.; Deacon, D. A. *G. Rev. Sci. Instrum.* **1988**, *59*, 2544.
- (2) Romanini, D.; Lehmann K. K. *J. Chem. Phys.* **1993**, *99*, 6287.
- (3) Scherer, J. J.; Paul, J. B.; Collier, C. P.; Saykally, R. J. *J. Chem. Phys.* **1995**, *102*, 5190.
- (4) Romanini, D.; Lehmann K. K. *J. Chem. Phys.* **1996**, *105*, 10263.
- (5) Hodges, J. T.; Looney, J. P.; van Zee, R. D. *J. Chem. Phys.* **1996**, *105*, 10278.
- (6) Zalicki, P.; Zare, R.N. *J. Chem. Phys.* **1995**, *102*, 2708.
- (7) Martin, J.; Paldus, B.A.; Zalicki, P.; Wahl, E.H.; Owano, T. G.; Harris Jr., J. S.; Kruger, C.H.; Zare, R. N. *Chem. Phys. Lett.* **1996**, *258*, 63.
- (8) Kogelnik, H.; Li, T. *Proc. IEEE* **1966**, *54*, 1312.
- (9) Born, M.; Wolf, E. *Principles of Optics*; Pergamon Press: New York, NY, 1980; p 325.

- (10) *High-Resolution Spectroscopy*; Shimoda, K., Ed.; Topics in Applied Physics; Springer-Verlag: Heidelberg, Germany, 1976; vol. 13.
- (11) Bevington, P. R. *Data Reduction and Error Analysis for the Physical Sciences*, McGraw-Hill: New York, NY, 1969.
- (12) Hodges, J. T.; Looney, J. P.; van Zee, R. D. *Appl. Opt.* **1996**, 35, 4112.
- (13) Meijer, G.; Boogaarts, M. G. H.; Jongma, R. T.; Parker, D. H.; Wodtke, A. M. *Chem. Phys. Lett.* **1994**, 217, 112.
- (14) Ritter, K. J.; Wilkerson, T. D. *J. Mol. Spectro.* **1987**, 121, 1.

## Chapter 8

# Dispersion and Cavity-Ringdown Spectroscopy

Kevin K. Lehmann

Department of Chemistry, Princeton University, Princeton, NJ 08544

Cavity Ring Down Spectroscopy has become an important method in gas phase spectroscopy and its uses promise to expand. While previous investigators have considered the decay of the stored energy in the cavity ring down cell following short pulsed excitation, this paper considers the effects of pulse reshaping during cavity ring down. It is found that in order to properly model these effects, one must consider not only the mode dependent loss of the ring down cavity, but also dispersion that shifts the resonant modes of the cavity. Only by considering the latter effect does one get a "causal" result where the free induction decay signal of the absorber occurs *after* the excitation pulse. It is demonstrated that in the limit that the cavity round trip time is long compared to both the  $T_2$  time of the intracavity absorber and the temporal width of the excitation pulse, the reshaping of the  $n$ 'th pulse out of the ring down cavity is the same as the reshaping produced by free space propagation over a distance of  $(2n + 1)L$  where  $L$  is the separation of the mirrors in the cell. However, when the absorber  $T_2$  becomes comparable to or longer than the cavity round trip time, then discrete modes of the ring down cavity become important. A general expression for the output is given for the important case of a weak absorber, and changes in the output are computed for a single absorption line as a function of the ratio of  $T_2$  to the cavity round trip time for several values of the optical thickness of the sample. Lastly, it is suggested that monitoring changes in the pulse shape of the cavity ring down signal provides a way to characterize an absorption spectrum on a frequency scale of the laser bandwidth down to the cavity free spectral range.

Cavity ring down spectroscopy (CRDS) has become an important method for obtaining highly sensitive absolute absorption spectra of weak transitions or rarefied species (1-8). Very briefly, CRDS uses pulsed laser excitation of a stable optical cavity formed by two or more highly reflective mirrors. One observes absorption by molecules contained between the mirrors by an increase in the decay rate of photons trapped in the cavity. The absorption spectrum is obtained by measurement of the cavity decay time versus the excitation wavelength. Absorption equivalent noise as low as  $\sim 3 \cdot 10^{-10}/\text{cm} \sqrt{\text{Hz}}$  has been demonstrated, and in principle several orders of magnitude further improvement is possible (3,6).

The theoretical underpinnings of the method have been the subject of recent controversy. O'Keefe (a co-inventor of the method) and his collaborators have favored a "particle" picture of CRDS where one considers the photons injected into the cavity as bouncing incoherently between the cavity mirrors (1,12). Meijer *et al.* (5) noted that a ring down cavity (RDC) is in fact a very high finesse etalon ( $\sim 10^5$  is typical), and considered the effect of the discrete cavity modes on a spectrum observed by CRDS. They pointed out that for a mode matched cavity, one can get distortions in the absorption spectrum due to the filtering produced by the cavity modes of the cell. Zalicki and Zare (9) reach the same conclusion. Meijer *et al.* also pointed out that it is possible to "fill in" the cavity mode spectrum by excitation of high order transverse modes, which are in general shifted in frequency from the TEM<sub>00</sub> modes. However, O'Keefe and collaborators (7) have attacked this conclusion and argued that the complete spectrum of the input pulse enters the ring down cavity when its coherence time is less than the cavity round trip time. They claimed that for short coherence length excitation, CRDS can be completely interpreted by the particle model and that no distortion of the absorption spectrum will occur, regardless of the relative values of the absorption sample's coherence dephasing time  $T_2$  and the cavity round trip time ( $t_r$ ).

This controversy motivated Lehmann and Romanini (10) and Hodges, Looney, and van Zee (11) to develop rigorous theories for the output signal in a CRDS experiment. The only assumptions in these analyses were the most fundamental principles of optics and that of linear absorption by the sample. Further, it was shown that for the important case of a high finesse cavity, the output can be described as a convolution of the input electric field with a Green's function expressed as a sum over all cavity modes, with each cavity mode consisting of a damped exponential times an excitation amplitude that depends upon the spatial properties of the input beam. These results demonstrated that CRDS is only sensitive to sample absorption at the resonant frequencies of excited cavity modes of the RDC, in direct contradiction to the conclusions of Scherer *et al.* (7).

The present paper builds upon that analysis. When the input pulse is shorter than the cavity round trip time, one will always excite more than one cavity mode. Beating of these modes is responsible for the localized traveling wave that moves in the cavity according to the particle model of CRDS. Here we consider changes in the pulse shape as the cavity rings down. If the input radiation pulse width is less than the time it takes light to make one round trip of the cavity but long compared the dephasing time,  $T_2$ , of the absorber, the excitation will create a well defined intracavity pulse that will experience an overall decay in amplitude but otherwise retain the shape of the input pulse. This is the limit where the particle model of CRDS



is appropriate. However, if the sample  $T_2$  is not short compared to the laser coherence time, then the pulse will change shape as it propagates inside the cell, as is well known for the case of free space propagation (13). Such an effect cannot be described by a particle picture since it arises from the selective attenuation and dispersion of the spectral components that make up the intracavity wavepacket. The purpose of this paper is to demonstrate that the mode theory developed by Lehmann and Romanini (10) provides a natural description of this effect. It will be demonstrated that in the limit of a cavity round trip time that is long compared to  $T_2$ , the output of the RDC consists of a series of pulses, each of which is the exactly the same as for free space propagation, such as was previously described by Crisp (13). Comparisons will be made between the free space results and numerical calculations for the case of finite values for the round trip time.

It is important to emphasize that the results presented in this paper are based upon linear response theory and as such are only applicable in the limit of negligible saturation of the sample by the intracavity pulse. The case of intracavity saturation is an important situation since this should allow for sub-Doppler spectroscopy by observation of Lamb Dips when the forward and reverse going pulses interact with the same molecules.

### The Effect of Dispersion on a Mode Matched Ring Down Cavity

Consider a ring down cavity formed by two mirrors with radius of curvature  $R_c$ , separated by a distance  $L$  [which must be  $< 2R_c$  to have a stable cavity (14)]. We define  $t_r = 2L/n_0c$ , the round trip time of the cell, where  $c$  is the speed of light in vacuum and  $n_0$  is the nonresonant index of refraction in the medium between the mirrors. For simplicity, we will assume that the mirrors have identical electric field reflectivity  $\mathcal{R}$  (defined from the substrate side of the mirror, the sign is opposite for reflection from the other side) and transmittivity  $\mathcal{T}$ . The more familiar intensity reflectivity and transmittivity are given by  $R = |\mathcal{R}|^2$  and  $T = |\mathcal{T}|^2$ . Further, we will initially assume that we can treat  $\mathcal{R}$  and  $\mathcal{T}$  as constants over the bandwidth of input radiation to the RDC.

We will assume that the input field is mode matched to the  $TEM_{00}$  transverse mode of the cavity. This is done primarily for mathematical simplicity in that it effectively reduces the problem from three dimensional to one dimensional. Using the general three dimensional results from Ref. (10), the present results can easily be generalized. However, in applications of these results, it is likely that one will want to carefully mode match the radiation. This is because the effects of excitation of multiple transverse modes is to produce a time dependent shape of the cavity output in the plane transverse to the optic axis, due to transverse mode beating. Such effects would likely complicate attempts to study the changes in the pulse shape along the optic axis due to pulse reshaping by the sample. In the ideal case where diffraction losses can be neglected and one detects all the output radiation, there is no interference between different transverse modes due to their orthogonality. In this case, one can just average the cavity output calculated for each set of longitudinal modes associated with fixed transverse mode numbers  $TEM_{mn}$ . In a detailed calculation, one must consider the overlap of the excitation radiation with different  $TEM_{mn}$  modes (10) as well as the shift in resonance frequency with transverse mode numbers.

As demonstrated in Ref. (10) [Eq. (11)], the output of the RDC subjected to arbitrary excitation can be written in terms of a Green's function as:

$$E_o(t) = \int G(t-t')E_i(t')dt' \quad , \quad (1)$$

where  $E_i(t')$  is the electric field of the input radiation, as measured at the input mirror, and  $E_o(t)$  is the electric field of the output radiation, measured at the output mirror. Physically,  $G(t-t')$  gives the output of the cell following a delta function input at time  $t'$ . This simple form of the output is a consequence of the RDC cell being a linear optical system with time independent properties. Under the conditions appropriate for CRDS experiments [see Ref. (10) for details],  $G(t)$  takes the following simple form:

$$G(t) = \frac{1}{\sqrt{2\pi}} \sum_q A(\omega_q) \exp\left(-\frac{t-t_r/2}{2t_d(\omega_q)}\right) \exp[i\omega(t-t_r/2)] \Theta(t-t_r/2) \quad , \quad (2)$$

where  $\omega_q$  and  $A(\omega_q)$  are the angular frequency and excitation amplitude of the  $q$ 'th cavity resonance mode;  $t_d(\omega_q)$  is the ring down time of the  $q$ 'th mode;  $\Theta(t)$  is the unit step function that equals zero for  $t < 0$  and one for  $t \geq 0$ .  $G(t)$  can be calculated from the cavity parameters, the index of refraction,  $n(\omega)$ , and absorption spectrum,  $\alpha(\omega)$ , of the sample inside the cavity by the following relationships:

$$A(\omega_q) = \sqrt{2\pi} \frac{\mathcal{T}^2 e^{-\alpha(\omega)L/2}}{t_r R_{eff}(\omega)} \quad (3a)$$

$$R_{eff}(\omega) = R(\omega) e^{-\alpha(\omega)L} \quad (3b)$$

$$t_d(\omega_q) = \frac{t_r R_{eff}(\omega)}{2[1 - R_{eff}(\omega)]} \quad . \quad (3c)$$

The resonance condition for the  $q$ 'th mode is give by:

$$k(\omega_q)L = \pi q + \theta \quad (4)$$

with  $k(\omega) = n(\omega)\omega/c$  the wavenumber of the radiation and  $\theta = \arg(-\mathcal{R})$  the phase shift per reflection from the mirrors. Equation (4) neglects a phase shift due to diffraction (14), which can easily be incorporated into  $\theta$ .

Consider that the RDC is filled with a sample that has a broad band (nonresonant) index of refraction  $n_0$ , and a resonant susceptibility  $\chi(\omega) = \chi' - i\chi''$ , where the sample has a macroscopic polarization defined by  $P(\omega) = \chi(\omega)E(\omega)$ . Since

for a gas the response is isotropic,  $P \parallel E$ , the medium will not change the polarization state of the electric field and we need not consider the vector character of the radiation field. In the presence of an external field, the sample will be anisotropic and the treatment will need to be slightly modified (15). Recently, Meijer's group has reported measurements and theory for polarization selective cavity ring down spectroscopy (16). The field radiated by this polarization leads to both absorption ( $\chi''$ ) and dispersion ( $\chi'$ ). Following Yariv (14) [Eq. (8.2-4)], we can write the index of refraction for small  $|\chi|$  as:

$$n(\omega) = n_0 \left[ 1 + \frac{\chi'(\omega)}{2n_0^2} \right] - i \frac{\chi''(\omega)}{2n_0} \quad (5)$$

From this we see that the absorption coefficient (which describes the exponential decay of the intensity) is given by:

$$\alpha(\omega) = \frac{\omega \chi''(\omega)}{cn_0} \quad (6)$$

The real and imaginary components of  $\chi$  are related by the principle of causality, which insures that the inverse Fourier Transform of  $\chi$  [which gives the Green's function that describes time dependent polarization produced by an impulse  $E(t) = \delta(t)$ ] be zero for all  $t < 0$ . This is traditionally expressed by the Kramers-Kronig relationships, a pair of integral equations relating  $\chi'$  and  $\chi''$ . The traditional derivation of these relationships, which is based upon closing a contour to evaluate the integrals (14) is not valid for a Doppler broadened line, but the classic text by Frohlich (17) presents an alternative derivation that does not have this limitation. Peterson and Knight (18) have presented an efficient Fast Fourier Transform (FFT) method for calculation of the real from the imaginary susceptibility or visa versa.

In order to calculate the cavity resonant frequencies in the presence of the molecular resonance, we substitute Eq. (4) into Eq. (5). Using the fact that  $\chi$  is small, we can write:

$$\omega_q = \omega_q^0 \left[ 1 - \frac{\chi'(\omega_q)}{2n_0^2} \right] \quad (7)$$

where

$$\omega_q^0 = \frac{2}{t_r} (\pi q + \theta) = \frac{c}{n_0 L} (\pi q + \theta) \quad (8)$$

is the cavity mode condition without sample dispersion. In normal situations, the shift in cavity resonance frequency due to dispersion will be very small. The peak value for  $|\omega_q - \omega_q^0|$  will be about  $\pm 0.3 c \alpha(\omega_0)$  where  $\omega_0$  is the peak of the absorption line (19). Since in CRDS one typically deals with samples where the peak  $\alpha(\omega)$  is  $10^{-5} \text{ cm}^{-1}$  or less, the corresponding shift in resonance modes will be  $|\omega_q - \omega_q^0| < 2\pi \times 10^4 \text{ s}^{-1}$ .

This small shift will be much less than the width of any resonances (20), and thus one can safely replace  $\chi(\omega_q)$  by  $\chi(\omega_q^0)$  in the right hand side of Eqs. (6) and (7). In a traditional CRDS experiment, one filters out all but the slow decay of the light energy in the cell. In this case, since dispersion causes a negligible change in decay rates,  $t_d$ , it has no effect on the CRDS signal, as predicted earlier by Zalicki and Zare (9).

One may wonder if such a small shift could be important at all. Without the contribution from  $\chi$ , the beating of different cavity modes is strictly periodic with period  $t_r$ . The small dispersion contributions cause this periodicity to be lost, and this affects the shape of the pulses leaving the cavity. For example, after a ring down time of  $3.3\mu\text{s}$ , with  $\alpha(\omega_0) = 10^{-5} \text{ cm}^{-1}$ , light would have traveled one Beer's length through the sample (1 km). Cavity beating terms can be phase shifted by as much as  $\pm 0.5$  radian. This is enough that one may expect to observe significant distortion in the shape of the signal. As the sample becomes even more optically thick, the phase shifts grow proportionally.

Substituting Eqs. (7) and (6) into Eq. (2), and exploiting the approximation that  $R_{\text{eff}} \approx 1$  that was used in the derivation of this equation, it is possible to derive the following expression:

$$G(t) = \frac{\mathcal{T}^2}{t_r} R_{\text{eff}}^{\frac{t}{t_r} - \frac{1}{2}} \sum_q e^{i\omega_q^0(t-t_r/2)} \exp\left[-i \frac{\omega_q^0}{2n_0^2} \chi(\omega_q^0)(t-t_r/2)\right] \theta(t-t_r/2) \quad (9)$$

From this equation, using the relationship  $\sum_q \exp(2\pi i q x) = \sum_N \delta(x - N)$ , it is straightforward to show that

$$\lim_{\chi \rightarrow 0} G(t) = \sum_{N=0}^{\infty} \mathcal{T}^2 \mathcal{R}^{2N} \delta(t - t_N) \quad (10)$$

where  $t_N = (N + 1/2) t_r$ , which is the time that the  $N$ 'th pulse would leave the cavity without dispersion. This last result can be derived directly by considering the sum of paths through the cell and thus serves as a check of the present results. Based upon this limit, we expect that even with modest dispersion  $G(t)$  will consist of spikes at times near  $t_N$ , where the different terms in the sum over modes will constructively interfere.

We define a dimensionless time  $\tau = (t - 1/2 t_r)/t_r$ . It is also convenient to add and subtract one to the exponential term in the sum on the right hand side of Eq.(9), since this allows the  $\delta$  function singularity to be treated analytically. This allows the Green's function to be rewritten in the following form:

$$G(t) = \frac{\mathcal{T}^2 \mathcal{R}^{2\tau}}{t_r} \left[ \sum_{N=0}^{\infty} \delta(\tau - N) - \sum_q e^{2\pi i q \tau} \left( 1 - \exp\left[-i \frac{\pi q + \theta}{n_0^2} \chi(\omega_q^0)(\tau + 1/2)\right] \right) \theta(\tau) \right] \quad (11)$$

The physical interpretation is that, in the limit of a very short optical pulse used to excite the cavity, the sum of  $\delta$  functions is just the external field injected into the RDC, while the second sum represents the field radiated by the absorbers, i.e., the free induction decay (FID) of the sample. For the more realistic case of cavity excitation by a pulse of finite duration, the output is given by the convolution of the input pulse with  $G(\tau)$ . Note that the FID term is in the form a discrete Fourier Transform, and thus the sum can be numerically calculated by a FFT routine (21). If one is considering very short response times, then the assumption of constant  $\mathcal{R}$  and  $\mathcal{T}$  will break down. However, one can generalize the above expressions by explicitly writing  $\mathcal{R}(\omega_q^0)$  and  $\mathcal{T}(\omega_q^0)$  and moving these factors inside the sum over  $q$ .

For a general input electric field, we can use Eq. (1) to calculate the output electric field. However, for the case of an "impulsive" excitation, where the input field is confined to a time much less than the ring down times for the excited modes, this integral becomes a Fourier integral. We are left with the following expression for the output:

$$E_0(\tau) = \mathcal{T}^2 \mathcal{R}^{2\tau} \left[ \sum_{N=0}^{\infty} E_i((\tau - N)t_r) - \frac{\sqrt{2\pi}}{t_r} \sum_q e^{2\pi i q r} \left( 1 - \exp \left[ -i \frac{\pi q + \theta}{n_0^2} \chi(\omega_q^0)(\tau + 1/2) \right] \right) \tilde{E}_i(\omega_q^0) \Theta(\tau) \right] \quad (12)$$

where  $\tilde{E}_i(\omega_q^0)$  is the Fourier component of the input wave  $\tilde{E}_i(t)$  at the  $q$ 'th resonance frequency of the cavity. As above, the second sum in the above expression can be efficiently evaluated using an FFT routine.

Let us now consider the special case where the spacing between cavity modes ( $\omega_q^0$ ) is small enough that  $\chi(\omega)$  changes negligibly between modes. This corresponds physically to the situation for which the dephasing time,  $T_2$ , is short compared to the cavity round trip time,  $t_r$ . We expect that the Green's function will be significant only for a few  $T_2$  after the times  $(N + 1/2)t_r$ , i.e.,  $\tau = N$ . In this 'long cell' limit, the sum over modes in Eq. (9) can be replaced by an integral over ( $\omega_q^0$ ), which will just be written as  $\omega$ . Under the approximation that  $R_{\text{eff}} \approx 1$ , this integral expression for  $G(t)$  can be simplified to:

$$G(t) = \sum_N \frac{\mathcal{T}^2 \mathcal{R}^{2N}}{2\pi} \int d\omega e^{i\omega t} \exp \left[ -i\omega \frac{\chi(\omega)}{2n_0^2} t_N \right] \Theta(t - t_r / 2) . \quad (13)$$

Each term in this sum has a natural physical interpretation. Except for the factor reflecting two transmissions and  $2N$  reflections off the cavity mirrors, each term is the Green's function that one gets for free space propagation of the input pulse through the same intracavity medium over a pathlength corresponding to  $(N + 1/2)$  round trips of the cavity (13). Thus in the situation that the absorption dephasing time is short compared to the cavity round trip time (which means that the sample will coherently interact with only one intracavity pulse at a time), the  $N$ 'th output pulse of

the RDC provides a faithful measurement of what the same input pulse would do if it experienced free space propagation over a length  $(2N + 1)L$ .

### Cavity Field with Lorentzian Absorber

An interesting question is how large the ratio  $t_r/T_2$  needs to be for the “long cell” limit to provide an adequate description of the ring down cell output. In this section, we will compare calculated ring down outputs computed for different values of this ratio.

Let us assume that the RDC is filled with a two level Lorentzian absorber, with resonant angular frequency given by  $\omega_0$ , with number density  $N_0$ , and with transition dipole moment given by  $\mu_0$ . We will further assume that all the population is in the lower state of the transition. In this case (14):

$$\chi(\omega) = -\frac{\mu_0^2 N_0}{\epsilon_0 \hbar} \frac{1}{(\omega - \omega_0) - i/T_2} \quad (14)$$

This sample will have a resonance with frequency full width at half maximum (FWHM) given by  $\Delta\nu = (\pi T_2)^{-1}$  and peak absorption coefficient,  $\alpha(\omega_0)$ , given by:

$$\alpha_0 = \frac{\omega_0 \mu_0^2 T_2 N_0}{c n_0 \epsilon_0 \hbar} \quad (15)$$

We will now assume that the ring down cavity is excited with a pulse much shorter than  $T_2$ ; we approximate the excitation by a delta function input. In this case, the Green's function directly gives the output signal of the RDC, assuming that  $t = 0$  is defined by the time of cavity excitation. For early times in the ring down ( $\alpha_0 c t \ll 1$ ), the sample will be optically thin for all frequencies. In the long cell limit, we can use Eq. (13) to show that the output is:

$$G(t) = \sum_N \mathcal{T}^2 \mathcal{R}^{2N} \left[ \delta(t - t_N) \frac{c \alpha_0 t_N}{2 n_0 T_2} \exp((i\omega_0 - 1/T_2)(t - t_N)) \Theta(t - t_N) \right] \quad (16)$$

Note that an exponential FID follows each exciting pulse, is out of phase, and builds up in amplitude. For finite values of  $c \alpha_0 t$ , we must consider the effect of the FID acting back on the sample. From the result presented by Crisp (13), it is possible to write an analytic result for this case as well:

$$G(t) = \sum_N \mathcal{T}^2 \mathcal{R}^{2N} \left[ \delta(t - t_N) - \sqrt{\frac{c \alpha_0 t_N}{2 n_0 T_2 (t - t_N)}} J_1 \left[ 2 \sqrt{\frac{c \alpha_0 t_N (t - t_N)}{2 n_0 T_2}} \right] \exp((i\omega_0 - 1/T_2)(t - t_N)) \Theta(t - t_N) \right] \quad (17)$$

where  $J_1$  is a Bessel function.

We now consider the opposite limit, that of a “short” RDC with  $t_r \ll T_2$ . In this case, at most one cavity mode will strongly overlap the resonant response of the sample. We must now consider the relative position of the resonance frequency and the cavity modes. First, we will consider the case where one of the cavity modes is centered on the resonance,  $\omega_0$ . Referring to Eq. (11), it is clear that the FID will be dominated by the term where  $\omega_q = \omega_0$ . If we only include this term in the sum, the Green’s function can be written as:

$$G(t) = \left[ \sum_N \mathcal{T}^2 \mathcal{R}^{2N} \delta(t - t_N) \right] - \frac{\mathcal{T}^2 |\mathcal{R}|^{2\tau}}{t_r} e^{i\omega_0(t-t_r/2)} \left[ 1 - \exp\left(-\frac{c\alpha_0}{2n_0} t\right) \right] \Theta(t - t_r/2) \quad (18)$$

$$\xrightarrow{\alpha_0 c t_r \ll 1} \left[ \sum_N \mathcal{T}^2 \mathcal{R}^{2N} \delta(t - t_N) \right] - \mathcal{T}^2 |\mathcal{R}|^{2\tau} \frac{c\alpha_0}{2n_0} (\tau + 1/2) e^{i\omega_0(t-t_r/2)}$$

Thus the FID consists of a pure wave at angular frequency  $\omega_0$  whose amplitude starts growing linearly but then saturates. The frequency domain interpretation of this result is as follows: The radiation admitted into the RDC consists of a picket fence of frequencies, only one of which is absorbed by the sample. By the superposition principle, this can be expressed as the picket fence minus a pure wave at  $\omega_0$ . The picket fence corresponds, in the time domain, to a train of delta functions while the pure wave is the FID. This FID saturates once the net wave at the resonance has been completely eliminated. In the time domain approach, we see that having a cavity resonance coincide with the sample resonance insures that the train of delta functions coherently excite the sample, thus the sample coherence and FID grows linearly at first. However, this FID acts to de-excite the sample (since it is out of phase), and we approach a steady state where the two sources of excitation exactly cancel, producing no net absorption. This is related to the area theorem as discussed by Crisp (13).

Now let us consider the case where the sample resonance is exactly half-way between cavity modes  $\omega_q$  and  $\omega_{q+1}$ , while still taking  $t_r \ll T_2$ . The response will be dominated by  $\chi$  at these modes, which will be  $\approx 3$  times larger than for the modes  $\omega_{q-1}$  and  $\omega_{q+2}$ , and thus we make the approximation that only these two modes need be considered. With this approximation, we get:

$$G(t) = \left[ \sum_N \mathcal{T}^2 \mathcal{R}^{2N} \delta(t - t_N) \right] - 2 \frac{\mathcal{T}^2 |\mathcal{R}|^{2\tau}}{t_r} \left[ \cos(\pi\tau) - \cos\left(\left(\pi + \frac{c\alpha_0 t_r^2}{2\pi n_0^3 T_2}\right)\tau\right) \right] e^{i\omega_0(t-t_r/2)} \quad (19)$$

$$\xrightarrow{\frac{\alpha_0 c t_r^2}{\pi T_2} \ll 1} \left[ \sum_N \mathcal{T}^2 \mathcal{R}^{2N} \delta(t - t_N) \right] + \mathcal{T}^2 |\mathcal{R}|^{2\tau} \frac{c\alpha_0 t_r^2}{2n_0^3 \pi T_2} (\tau + 1/2) \left[ \cos(\pi\tau) - \frac{t_r}{\pi T_2} \sin(\pi\tau) \right] e^{i\omega_0(t-t_r/2)} \quad (20)$$

We thus see that we get an FID wave that is modulated at the cavity free spectral range and has an amplitude that is  $\approx (2t_r/\pi T_2)$  smaller at early times. Including modes further from the resonance line will add higher Fourier components to the FID. Because of smaller  $\chi$  at the cavity modes, the linear approximation works for correspondingly longer times. The leading term, down by one power of the ratio  $t_r/\pi T_2$ , comes from the dispersion contribution to the signal, while the term proportional to  $(t_r/\pi T_2)^2$  arises from the absorption term.

The case of  $t_r \approx T_2$  requires numerical calculation. Figure 1(a) presents the FID amplitude calculated by Eq. (17) for the case of free space propagation at four values of the on-resonance optical depth of the sample,  $(c \alpha_0 t_N)/n_0 = 0.1, 1, 10, 100$ .

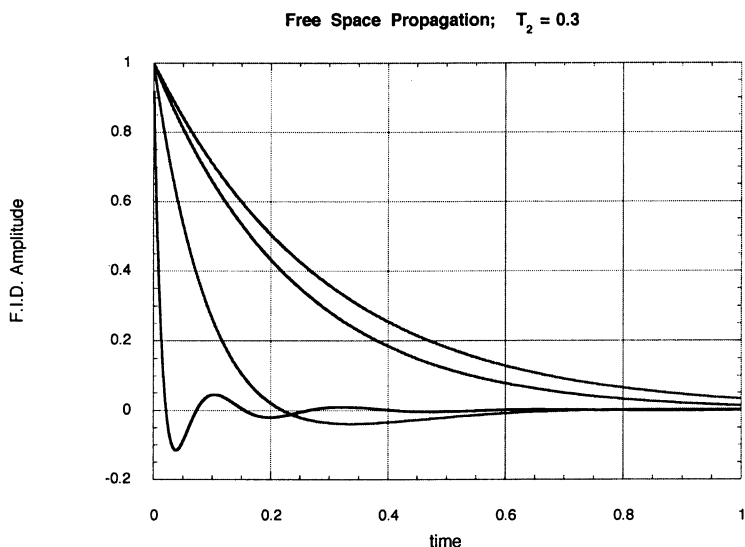


Figure 1a. Normalized Free Induction decay amplitude produced by Free Space Propagation of a  $\delta$  function through a sample with  $T_2 = 0.3t_r$ , where  $t_r$  is the unit of time used in the graph. Calculated by Eq. (17). The Four curves, in order of increasing initial decay rates, are for propagation through a sample with  $\alpha_0 L = 0.1, 1, 10,$  and  $100$ , respectively.

The results depend only on the ratio of  $t$  to  $T_2$ , but in order to compare free space and cavity propagation, we have arbitrarily used  $t_r$  as the unit of time for this plot and assumed  $T_2 = 0.3t_r$ . Figure 1(b) presents the FID for the case of a cavity ring down experiment, calculated from Eq. (11), where we have again taken the time unit to be the cavity round trip time  $t_r$ , and the origin equal to  $t_N$ , the output time of the input pulse that travels  $(2N + 1)$  passes of the cavity. The same four values for the on-resonance optical depth are given. The cavity modes were phased so that one mode was exactly resonant with the transition frequency. Despite the fact that the cavity mode spacing is slightly greater than the FWHM of the absorption line, the FID is almost quantitatively the same as for free space propagation over the same path length. The apparent noise near the discontinuity of the FID is an artifact due to the



abrupt cut-off of the high frequency components of the FID, known as the Gibbs' phenomenon (22). These calculations were done using  $2^{10}$  cavity modes with the  $2^9$ 'th mode resonant with the optical transition.

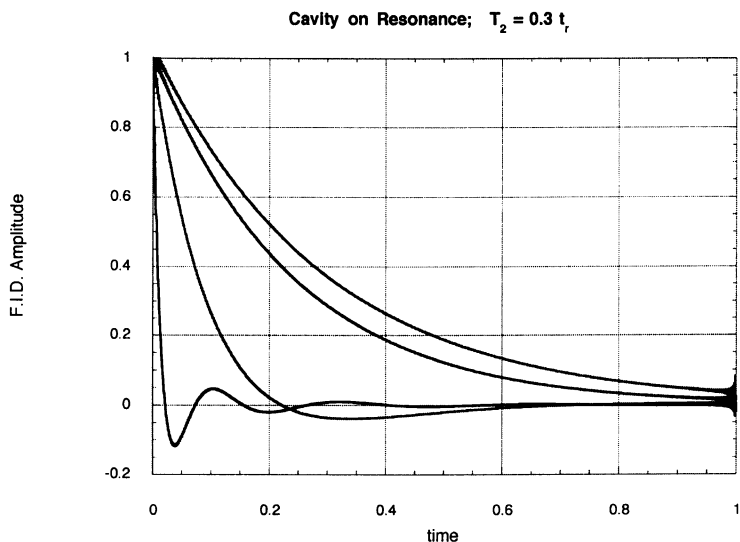


Figure 1b. Normalized Free Induction decay amplitude produced by Cavity Propagation of a  $\delta$  function input through a sample with  $T_2 = 0.3 t_r$ . The time axis is in units of  $t_r$ . The cavity has a resonant mode at the same frequency as the center of the sample absorption line. Calculated by Eq. (11). The Four curves, in order of increasing initial decay rates, are for propagation through a sample with  $\alpha_0 t_N = 0.1, 1., 10.,$  and  $100,$  respectively.

Figure 1(c) shows the results of the same calculation, but with the optical resonance midway between the  $2^9$ 'th and  $2^9+1$ 'th cavity modes. For high optical depth, the curves are almost identical to the on-resonance case, but for lower optical depths one observes a faster decay and then the FID amplitude goes negative. Figures 2(a-c) presents the results of the same calculation of the free space, on-resonance, and off-resonance calculations, but now with  $T_2 = t_r$ . In this case, the cavity mode spacing is  $\pi$  times greater than the FWHM of the absorption line, and significant deviation from the free space propagation results are evident. What is perhaps remarkable is how similar the on resonance FID remains given the fact that the absorption line is being so dramatically under sampled by the discrete modes of the ring down cavity.

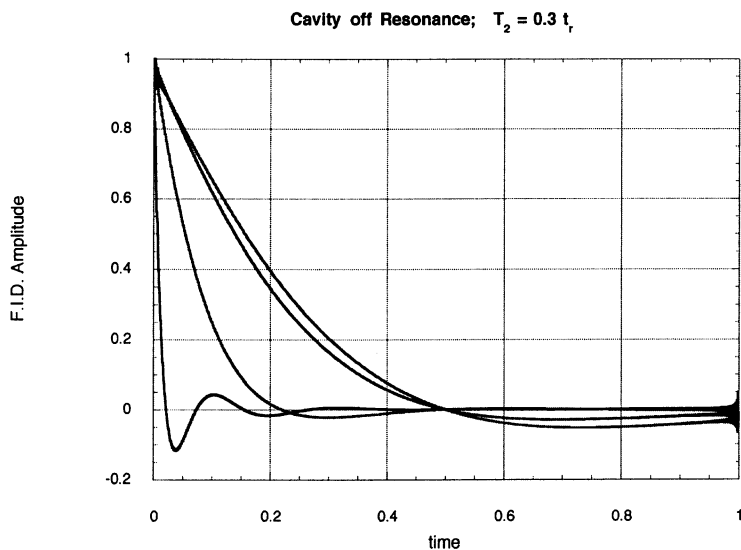


Figure 1c. Same as Fig. 1b except the center of the sample absorption line is exactly half way between two cavity modes.

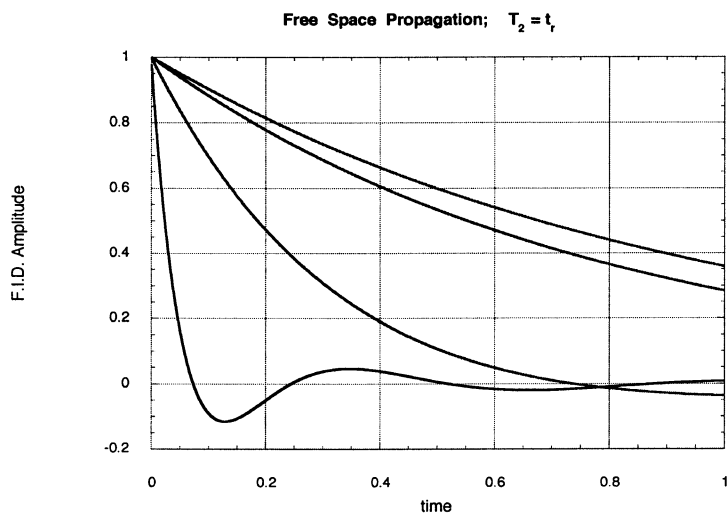


Figure 2a. Same as Fig. 1a, except with  $T_2 = t_r$ , where  $t_r$  is the unit of time used for the graph.

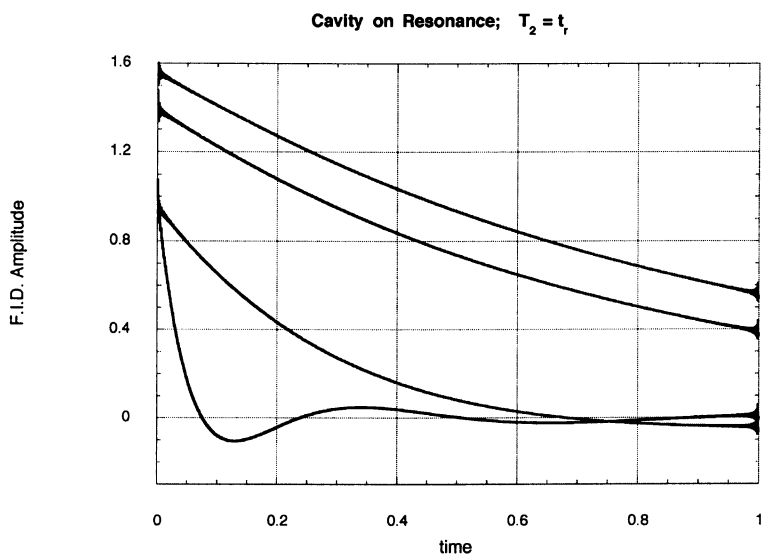


Figure 2b. Same as Fig. 1b, expect with  $T_2 = t_r$ .

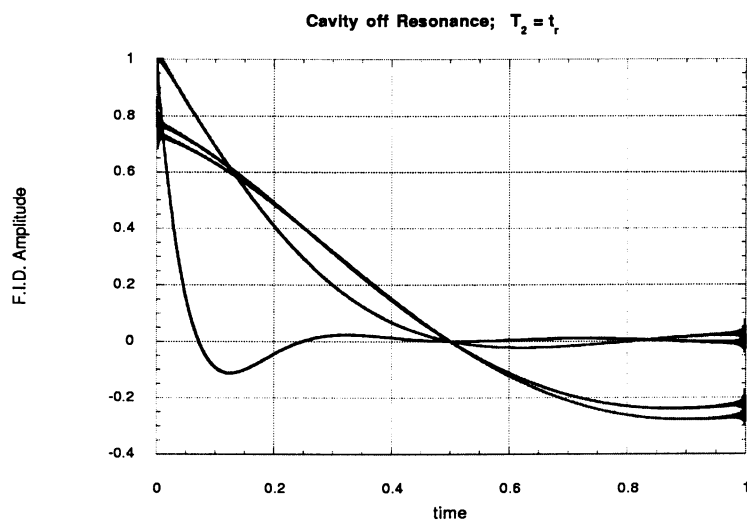


Figure 2c. Same as Fig. 1b, expect with  $T_2 = t_r$  and the center of the sample absorption line is exactly half way between two cavity modes.

## Cavity Field with Gaussian Absorber

The results presented in the previous section are applicable to the case of a gas phase absorption line with homogeneous width large compared to the Doppler width. For transitions at low to modest pressure, one must include the Doppler broadening of the spectroscopic transitions. The most straightforward way to include Doppler broadening is to convolve the time dependent susceptibility for a Lorentzian line with the inverse FT of the Doppler profile. This assumes that the  $T_2$  time is independent of Doppler shift and also neglects Dicke narrowing effects. This convolution can be evaluated analytically and results in the following expression for the susceptibility:

$$\chi(t) = -i \frac{\sqrt{2\pi} \mu^2 N_0}{\epsilon_0 \hbar} \exp\left(i\omega_0 \cdot t - t / T_2 - \frac{1}{2} \sigma_\omega^2 \cdot t^2\right) \quad (21)$$

where  $\sigma_\omega$  is the standard deviation of the Gaussian Doppler line and is given by:

$$\sigma_\omega = \sqrt{\frac{k_B T}{M}} \frac{\omega_0}{c} \quad (22)$$

In the above expression,  $k_B$  is the Boltzmann constant,  $T$  the sample temperature, and  $M$  the mass of the absorber. Fourier transformation of  $\chi(t)$  gives  $\chi(\omega)$ . The imaginary part of  $\chi(\omega)$  is the Voigt line shape. The real part gives the dispersion of the Voigt line shape. Figure 3 shows the normalized dispersion curve for a line with negligible Lorentzian component. It has the same qualitative shape as for a Lorentzian line shape. Far above and below resonance, it goes to zero as  $\sim 1/(\omega_0 - \omega)$ . It has a minimum and maximum of  $\pm 0.6$  at  $\omega - \omega_0 = \pm 1.3 \sigma_\omega$ . In the wings of the line, the ratio of the dispersive to absorptive line shape is much greater for a Gaussian than for a Lorentzian line shape.

Since in CRDS calculations we are only interested in  $\chi(\omega)$  at the cavity mode frequencies, we can also calculate these by the FFT method. If we wish to calculate modes  $\omega_q$  through  $\omega_{q+N-1}$ , we should compute the FFT of the function  $\exp(-i\omega_q t)\chi(t)$  evaluated at the points  $t_k = k \cdot t/N$  with  $k = 0, 1, \dots, N-1$ . Substitution of the resulting  $\chi(\omega_q)$  into Eq. (11) and evaluation by inverse FFT gives the FID decay signal following a delta function input. For a more general input field, the output can be found by substitution of  $\chi(\omega_q)$  into Eq. (12).

## Towards a Time Domain Cavity Ring Down Spectroscopy?

The results of this paper demonstrate that pulse reshaping is a general phenomenon in CRDS whenever the input pulse coherence time is shorter than the dephasing time of the absorbing gas in the cavity. Previous CRDS experiments have not had to consider this effect because the cavity output was strongly filtered to eliminate all but the lowest frequency components of the output intensity. However, we hope the present paper will motivate increased attention to the shorter time characteristics of the output signal since these are sensitive to the sample spectrum over the resolution

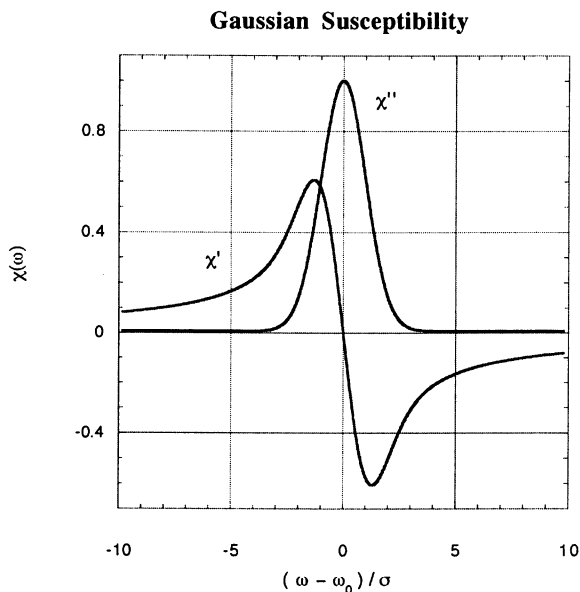


Figure 3. Normalized Real ( $\chi'$ ) and negative Imaginary ( $\chi''$ ) Susceptibility for a Doppler Broadened Transition. Calculated by the Fast Fourier Transform of Eq. (21) with a time step of  $(64\sigma_\omega)^{-1}$  and a total of  $2^{14}$  time steps.

interval between the laser bandwidth and the free spectral range of the RDC. The effect of the resonant modes of the RDC is to replace the continuous Fourier Transform relationship between time and frequency domain response by a discrete Fourier Transform, due to the output field being nearly periodic in time. We have demonstrated that the detailed output pulse shape can be easily calculated from the absorption and dispersion spectra of the sample in the cavity by use of a fast Fourier Transform approach.

These results suggest that it is possible to do CRDS spectroscopy in the “time domain.” We will now demonstrate that such experiments are, at least in principle, practical. To make the discussion more concrete, we will assume that the experiment is designed to detect the concentration and temperature of a molecular oxygen using the A band (i.e., the  $b^1\Sigma_g^+ - X^3\Sigma_u^-$  transition) at  $7620 \text{ \AA}$ . If the sample is assumed to be at room temperature and atmospheric pressure, the individual rotational lines of this band will be pressure broadened to a width of  $\approx 0.1 \text{ cm}^{-1}$  FWHM, which implies  $T_2 \approx 100 \text{ ps}$  (23). Under these conditions, the strong rotational lines have a peak absorption strength of  $\alpha_0 \approx 1 \cdot 10^{-3} \text{ cm}^{-1} \cdot \text{atm}^{-1} \cdot P(\text{O}_2)$ , where  $P(\text{O}_2)$  is the partial pressure of molecular oxygen (23).

Consider the proposed experimental design shown schematically in Fig. 4. A mode locked Ti:sapphire laser with nearly Fourier Transform limited output of  $\Delta t = 5 \text{ ps}$  with repetition period  $\tau_1 \approx 10 \text{ ns}$  is used. With an average power of  $1 \text{ W}$ , this laser will produce output pulses of  $\approx 10 \text{ nW}$  and peak power of  $\approx 2 \text{ kW}$ . Part of this output is amplified in a Regenerative Amplifier, which will be assumed to produce

an output pulse energy  $J \approx 50 \mu\text{J}$ . The output of the amplifier will be mode matched and coupled into a RDC with a nominal length of 1.5 meters, producing a cavity round trip time,  $t_r$  only slightly shifted from that of the Ti:sapphire laser. We will further assume that the mirrors of the ring down cavity have  $T = 1 - R = 10^{-4}$ . These conditions that  $\delta t \ll T_2 \ll t_r$  allow one to treat the excitation of the sample as impulsive (i.e., the FID is just proportional to the Green's function), and the "long cell" limit where the FID's from different cavity passes do not overlap significantly. In this limit, up to a time where  $A = c \alpha_0 t_n / n_0 \approx 1$ , the intensity of the FID wave leaving the cavity will be:

$$I_{\text{FID}}(t) \approx T^2 R^{2N} A^2 \left( \frac{J \Delta t}{4 T_2^2} \right) \exp[-(t - t_n) / 2 T_2]. \quad (23)$$

$A$  is just the on-resonance absorption of the sample for a pathlength equal to that the light traveled in time  $t_n$ . For  $A \approx 1$ , the output power  $I_{\text{FID}} = 60 \mu\text{W}$  that is 240 photons/ps.

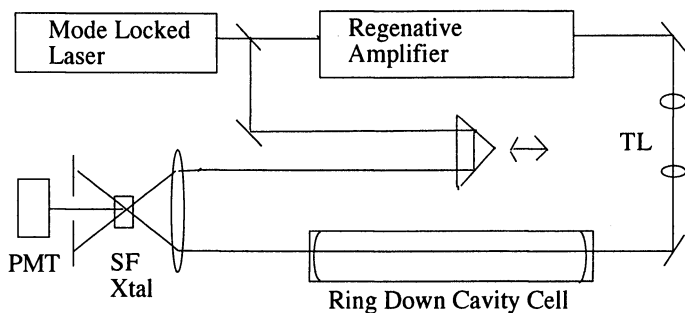


Figure 4. Schematic diagram of experimental apparatus for detection of time resolved Cavity Ring Down Spectroscopy.

This FID intensity will be time resolved by the method of sum frequency generation (SFG), using the light from the oscillator. The FID and pump beam will be assumed to cross at an angle of 0.1 rad, which will allow the sum frequency beam to be easily physically separated from the much stronger beam produced by the second harmonic of the pump. We will also assume that we will use Lithium Iodate as the nonlinear crystal. Since the two pulse trains have almost the same frequency, one will "stroboscopically" sweep out the FID, advancing  $\tau_1 - t_r$  each  $\tau_1 \approx 10$  ns. Each such pulse can be resolved and digitized using electronics with a few ns time resolution. If we assume  $\tau_1 - t_r = 10$  ps, we get a time resolution of the FID of 10 ps and we sweep out one cycle of the FID curve every 10  $\mu\text{s}$ . Based upon the expressions given by Shah (24), one can calculate a conversion efficiency of  $\approx 0.05$ , thus implying that the peak of the FID will produce  $\approx 300$  SFG photons per oscillator pulse. This is will allow the FID to be obtained with moderate signal to noise even from a single cavity excitation pulse. It should be pointed out that for constant input pulse intensity, the

estimated number of photons scales with the square of the excitation pulse duration ( $\Delta t$ ). Thus, to optimize the FID signal, one should not use an excitation pulse shorter than is needed to resolve the FID signal.

An important practical issue that we have not yet considered is the effect of the finite reflectivity bandwidth of the RDC mirrors. To achieve the shortest possible pulses, one must use specially designed mirrors that have "chirped" coatings (25). The mirrors used in RDCS are designed for maximum reflectivity, which is typically high over a bandwidth of 5–10%. In the red part of the spectrum, these mirrors are made of alternating 1/4 wave layers with indexes of 2.1 and 1.49 (26). Using the transfer matrix method (27), one can calculate the  $\mathcal{R}(\omega)$ . The time dependent output of an impulsively excited RDC cell after  $2n+1$  passes of the cell can be calculated by the Fourier Transform of  $\mathcal{R}(\omega)^{2N}$ . In Fig. 5 is given the calculated output intensity after 10,000 reflections off of a dielectric mirror of 15 pairs of layers, quarter wave at 760 nm. Such a mirror is calculated to have a peak reflectivity of 99.99%.

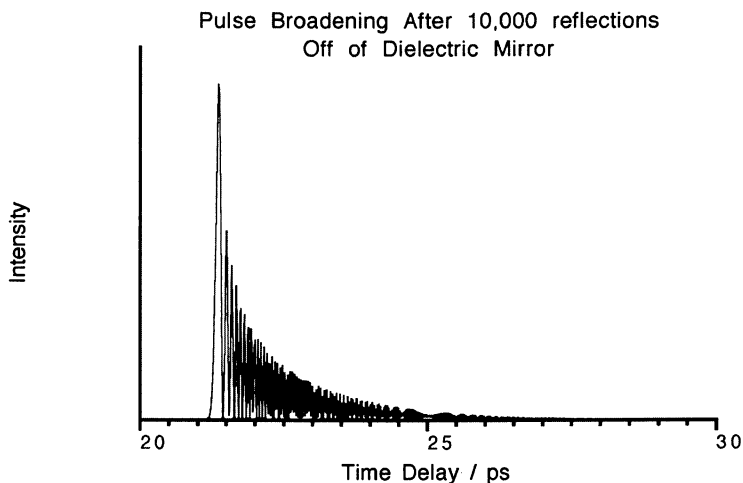


Figure 5. Calculated time dependent intensity of short light pulse after 10,000 reflections off of a high reflectivity dielectric mirror, coated with alternating layers of index 2.1 and 1.49, quarter wave at 800 nm.

The shift in the pulse by  $\approx 22.5$  ps reflects the penetration of the coating by the light, which leads to a slight time delay per reflection, which can be viewed as the cell having a slightly longer effective length. The highly structured decay, with a width of  $\approx 2$  ps reflects the finite bandwidth of the light, filtered by 10,000 reflections. It is thus seen that the finite bandwidth of such a high reflectivity coating will limit one to a time resolution of a few ps.

One must naturally ask if there is any advantage to such a time domain approach to CRDS? In principle, such experiments will not give any information that cannot be obtained by scanning a narrow bandwidth laser over the same spectral region and observing the more traditional frequency domain version of CRDS. The

same objection can be raised against many gas phase, short pulse experiments, and the author acknowledges that he has often found such experiments to be just a needlessly difficult and low signal to noise way of obtaining spectroscopic data. If for no other reason than the current fashion that erroneously views "time domain" experiments as more "direct" than the equivalent frequency domain experiments, the present results will likely find experimental application. Further, there are situations where the time domain approach would offer some practical advantages. The width of a transition can be determined on a single pulse and thus one has a multiplex advantage. This could be useful if one is studying a sample that has an unstable concentration, so that significant noise is observed if a transition is slowly scanned. Another possibility is the study of small spectral widths and splittings, where relatively long FID's could be created and detected with inexpensive lasers and detection equipment, while the equivalent frequency domain experiment may require a highly sophisticated laser to realize the needed resolution. Of course, one must be mindful that the cavity be long enough that the mode filtering not excessively distort the spectral features, but this will be obvious from the observed FID. By off-axis excitation of a cell with a spacing that satisfies the conditions of a Herriott Cell (28), the effective  $t_i$  can be increased to observe even longer FID's.

We conclude that time resolved CRDS, where one observes changes in the intracavity pulse shape as it travels through the sample, is likely to find application in future experiments. The present paper presents the theory needed to interpret and model such experiments.

## Acknowledgments

The author wishes to thank Dr. Daniele Romanini for a careful reading of this manuscript. I would also like to thank John E. Bertie for pointing out reference 17 and its proof that the Kramers-Kronig relations do hold for a Gaussian line shape. The present work was supported by grants from the New Jersey Commission on Science and Technology and the Petroleum Research Fund, administered by the American Chemical Society. Lastly, I would like to thank the staff of the JILA Scientific Reports Office, who converted my Latex document to a format that is compatible with the ACS choices.

## Literature Cited

- [1] O'Keefe, A.; Deacon, D.A.G. *Rev. Sci. Instrum.* **1988**, *59*, 2544.
- [2] O'Keefe, A.; Scherer, J. J.; Cooksy, A. L.; Sheeks, R.; Heath, J.; Saykally, R. *J. Chem. Phys. Lett.* **1990**, *172*, 214.
- [3] Romanini, D.; Lehmann, K. K. *J. Chem. Phys.* **1993**, *99*, 6287.
- [4] Yu, T.; Lin, M. C. *J. Am. Chem. Soc.* **1993**, *115*, 4371.
- [5] Meijer, G.; Boogaarts, M. G. H.; Jongma, R. T.; Parker, D. H.; Wodtke, A. M. *Chem. Phys. Lett.* **1994**, *217*, 112.
- [6] Romanin, D.; Lehmann, K. K. *J. Chem. Phys.* **1995**, *102*, 633.
- [7] Scherer, J. J.; Voelkel, D.; Rakestraw, D. J.; Collier, J. B. P. C. P.; Saykally, R. J.; O'Keefe, A. *Chem. Phys. Lett.* **1995**, *245*, 273.



- [8] Zalicki, P.; Ma, Y.; Zare, R. N.; Wahl, E. H.; Dadamio, J.; Owano, T. G.; Kruger, C. H. *Chem. Phys. Lett.* **1995**, 234, 269.
- [9] Zalicki, P.; Zare, R. N. *J. Chem. Phys.* **1995**, 102, 2708.
- [10] Lehmann, K.; Romanini, D. *J. Chem. Phys.* **1996**, 105, 10263.
- [11] Hodges, J. T.; Looney, J. P.; van Zee, R. E. *J. Chem. Phys.* **1996**, 105, 10278.
- [12] Scherer, J. J.; Paul, J. B.; O'Keefe, A.; Saykally, R. J. in *Advances in Metal and Semiconductor Clusters*, **1995**, 3, 149.
- [13] Crisp, M. D. *Phys. Rev. A* **1970**, 1, 1604.
- [14] Yariv, A. *Quantum Electronics*, 3rd ed. (John Wiley, New York, 1989).
- [15] Lehmann, K. K., unpublished.
- [16] Engeln, R.; Berden, G.; van den Berg, E.; Meijer, G. *J. Chem. Phys.* **1997**, 82, 3199.
- [17] Fröhlich, H. *Theory of Dielectrics*, (Oxford, London 1949), section I.2.
- [18] Peterson, C. W.; Knight, B. W. *J. Opt. Soc. Am.* **1973**, 63, 1238.
- [19] For a Gaussian line, the peak value for  $\chi'$  is  $\pm 0.6\chi''$  as shown in section IV. This combined with Eqs (5) and (7) results in this limit.
- [20] Even if there are no other broadening mechanisms, the finite time of flight of a molecule through the TEM<sub>00</sub> beam will result in a broadening of several hundred kHz for typical RDC parameters.
- [21] Press, W. H.; Flannery, B. P.; Teukolsky, S. A.; Vetterling, W. T. *Numerical Recipes* (Cambridge University Press, Cambridge, 1989).
- [22] Gibbs, J. W. *Nature*, **1899**, 59, 606.
- [23] Ritter, K. J.; Wilkerson, T. D. *J. Mol. Spectrosc.* **1987**, 121, 1.
- [24] Shah, J. *IEEE J. Quantum Electronics* **1988**, 24, 276, Eq. (14).
- [25] Mayer, E. J.; J. Möbius, J.; Euteneuer, A.; Rühle, W. W.; Szipőcs, R. *Opt. Lett.* **1997**, 22, 528.
- [26] Lalezari, R. *Research Electro--Optic*, private communication.
- [27] Fowles, G. R. *Introduction to Modern Optics*, 2nd ed. (Dover, New York 1975). See in particular Eq. (4.30).
- [28] Herriott, D.; Kogelnik, H.; Kompfner, R. *Appl. Opt.* **1964**, 3, 523.

## Chapter 9

# Cavity-Ringdown Spectroscopy versus Intra-Cavity Laser Absorption

Daniele Romanini

Laboratoire de Spectrométrie Physique–CNRS UMR 5588, Université  
J. Fourier de Grenoble, B. P. 87–38402 Saint Martin d’Hères Cedex, France

Cavity ring down spectroscopy (CRDS) and intra cavity laser absorption spectroscopy (ICLAS) are among the most powerful quantitative absorption methods. In view of the growing interest they attract, we will give a detailed comparative description of their most relevant features. We will try considering all recent developments, for example the use of continuous lasers or of single mode pulsed lasers in CRDS, and the single-pulse ICLAS by correlated double sampling. These are rather complementary methods, and the choice of the most appropriate will vary with the applications. Among these, most promising are trace detection and high resolution spectroscopy of transient species in plasmas or supersonic jets.

In spectroscopy, high sensitivity absorption is used extensively for the characterization of extremely weak transitions. For example, the investigation of highly excited vibrational (overtone) states has contributed to much of the current understanding of molecular dynamics. In astrophysics, weak transitions characterize the solar spectrum filtered through the atmospheres of the sun and of the earth, and for more distant stars, their spectra may collect information about diffuse interstellar clouds. This precious information about very remote environments can be decoded only after identification and spectral characterization of the carriers of those weak transitions in controlled laboratory conditions.

In the future, compact spectroscopic devices allowing ultrasensitive, selective, and quantitative absorption measurements will be an indispensable aid in trace detection and environmental monitoring, which range from urban pollution to security of industrial sites, from semiconductors processing to medicine and agronomy. In general, spectroscopic methods based on direct absorption offer a quantitative measurement of the absorption coefficient, which is the product of the concentration and the (temperature dependent) integrated cross section of

the transition being observed. In addition, if high spectral resolution is available, selectivity among different coexisting species (even isotopomers) is possible.

We will consider in details two of the most powerful methods of absorption spectroscopy, namely cavity ringdown (CRDS) and intra cavity laser absorption (ICLAS), which are not yet as well known and appreciated as they deserve. This is especially true if we compare with multipass absorption, diode laser modulation spectroscopy or photoacoustic spectroscopy (PAS), described in several papers and reviews. Diode laser modulation and multipass systems only occasionally achieve the same detection limit as routinely reported in most CRDS or ICLAS applications, which vary from  $10^{-7}$  to  $10^{-9}/\text{cm}\sqrt{\text{Hz}}$ . Much lower limits may actually be obtained:  $5 \times 10^{-11}$  for CRDS and  $2 \times 10^{-12}/\text{cm}\sqrt{\text{Hz}}$  for ICLAS. In addition, both these methods quantitatively measure sample absorption with excellent spectral resolution. This is a definite advantage with respect to PAS, where the determination of absorption intensities is inaccurate, depending on the collisional properties of the gas mixture and on the acoustics of the resonance cell. Also, contrary to CRDS and ICLAS, PAS cannot be used with supersonic jets. For completeness, we should also consider other methods which have been most successful for the absorption spectroscopy in collimated molecular beams, such as optothermal detection. However, the domain of application of these methods is limited and we will not try a detailed discussing and comparison here.

Recently, J. Hall *et al.* [1] used a high finesse cavity to obtain very high resolution absorption measurements with a detection limit orders of magnitude lower than any other method ( $10^{-14}/\text{cm}$ ). For now, it appears that this "NICE OHMS" method will be especially suitable for establishing new frequency standards based on saturated molecular transitions. It is not yet clear if it will also be practical in molecular spectroscopy or for trace detection.

Except for a few short comments where appropriate, we will not attempt comparing to other spectroscopic methods. We will rather give a detailed description of CRDS and ICLAS to arrive at an objective and complete comparison. In particular, we hope this will help assessing which method is preferable according to the application of interest. We will cite as much as possible papers where questions of principle have been carefully discussed. On the other hand, of the many experimental papers published, we will cite only a selection which we consider representative examples of specific applications.

**Basic ideas in ICLAS and CRDS.** The Lambert–Beer law may be written, for small absorption, as  $\Delta I/I = -\alpha L$ , where  $\Delta I$  is the light intensity lost along the path  $L$ . In order to detect weak absorption,  $L$  should be made as large as possible and the noise on  $\Delta I/I$  should be minimized. The ratio  $[\Delta I/I]_{\text{noise}}/L$  gives the detection limit, that is, the smallest detectable (noise-equivalent) absorption. Stabilized diode lasers together with modulation techniques allow detecting  $\Delta I/I$  as small as  $10^{-6}$  [2]. A shot noise limit of  $4 \times 10^{-8}/\sqrt{\text{Hz}}$  using differential double beam detection has also been occasionally demonstrated [3], but extreme care has to be taken in avoiding optical feedback to the laser and interference fringes in the spectrum baseline. On the other hand, standard multipass cells permit to increase  $L$  up to 100 m, compatibly with maintaining a reasonable apparatus size.

Coupling together a diode laser and a multipass cell is also a possible solution, but it usually leads to increased feedback and interference effects.

Photons trapped inside an optical cavity for a long time interval  $\Delta t$  interact with a sample filling the cavity over an *equivalent path length*  $L_{\text{eq}} = c\Delta t$ . With ICLAS, this idea was applied back in 1970 by exploiting the 'active' cavity of a multimode laser, where photons are created and maintained by laser amplification [4,5]. More recently, with CRDS [6,7], the same principle has been applied by injecting laser radiation into a 'passive' cavity. While photons live longer inside an active laser cavity (giving a larger  $L_{\text{eq}}$ ), subtle phenomena involving nonlinear coupling among the cavity modes must be understood and controlled. These are due to the very presence of the laser gain medium, thus they are absent in CRDS. This very briefly resumes the basic similarities and differences between these two methods, which we are now going to consider separately in more detail.

### Cavity Ring-Down Spectroscopy

In CRDS, a gas sample is placed inside an optical cavity, usually formed by two high reflectivity dielectric mirrors. The sample absorption is then accurately measured as a variation of the cavity loss rate. This is the inverse of the time constant  $\tau$  of the observed exponential decay (ring-down) of laser radiation after it has been injected into the cavity. An equivalent absorption pathlength may then be defined as  $L_{\text{eq}} = c\tau$  ( $c$  is the speed of light). With good mirrors,  $\tau$  may be as large as 100  $\mu\text{s}$ , corresponding to  $L_{\text{eq}} = 30$  km. Since it is the rate of loss  $dI/dt$  which is measured,  $L_{\text{eq}}$  has only a value of reference for CRDS.

Until recently, pulsed lasers have been used for cavity injection by simple transmission of a small fraction of each laser pulse through one of the mirrors, along the cavity axis. The main advantage of "pulsed-CRDS" is that one can reach any wavelength from the IR (4-5  $\mu\text{m}$  with OPO lasers) to the UV ( $\sim 200$  nm by harmonic generation with pulsed dye lasers). Since CRDS measures the cavity loss rate, in principle it is insensitive to the pulse-to-pulse intensity fluctuations, which make classical absorption measurements with pulsed lasers almost worthless. Even if dielectric mirrors in the UV or in the mid-IR are much worse than in the visible, detection limits in the range  $10^{-5}$ - $10^{-7}$ /cm have been obtained.

Pulsed-CRDS was first demonstrated as a powerful spectroscopic tool by O'Keefe and Deacon [7]. Among other applications, it was employed in the spectroscopy of species seeded in supersonic jets [8]; in the investigation of weak transitions in the gas phase [9-11]; to investigate reaction kinetics by exploiting the method's time resolution [12]; and to detect transient species in flames, reactors or discharges [13-15].

In the last few years, much effort was dedicated to developing new applications of CRDS. In association with a step-scan Fourier transform apparatus, spectral multiplexing was recently demonstrated by Meijer *et al.* [16]. The same group also showed that CRDS may be used for polarization spectroscopy in the presence of a magnetic field [17]. Finally, a major event has been the introduction of CW lasers for cavity injection. In 1996, Meijer and co-workers [18] have shown that the phase-shift method applied in the past to measure mirror reflectivities [19]

may be effective in obtaining "PS-CRDS" spectra with a cw laser. At the same time, another known method of measuring mirror reflectivities [6] was adapted by us to obtain "CW-CRDS" spectra with a detection limit better than  $10^{-10}/\text{cm}$  and MHz resolution [20] even with diode lasers and slit jet samples [21,22]. More recently, in Zare's laboratory a simplified CW-CRDS setup for diode lasers was demonstrated which eliminates the need for an optical isolator [23].

**Parasitic cavity losses and other issues.** One of the frequent objections against CRDS is that high reflectivity mirrors are too delicate, they may get dirty, and in general the cavity quality may be easily spoiled. In fact, depending on the coating materials, dielectric mirrors may be extremely resistant to corrosive agents and to repeated cleaning. Even if dirt over the mirrors will cause troubles of various kinds, this did not impede using CRDS to study species present in discharges, flames or chemical reactors. In fact, in many cases it is possible to protect the mirrors using a small flow of a buffer gas close to their surfaces.

It is also true that broad band losses associated with the sample undesirably add to the intrinsic cavity losses, thus spoiling the detection limit. For example, when measuring the spectrum of  $\text{SiH}_2$  radicals in a  $\text{Ar}+\text{SiH}_4$  discharge [24], we observed a shortening of the ringdown time when starting the discharge, and a slow return to its previous value after turning the discharge off. This effect was due to scattering losses by nanometer-size dust particles produced in the discharge. While this was quite a nuisance in our experiment, the ability to quantitatively measure the presence of dust is extremely interesting for the optimization of semiconductor processing in plasma reactors. In addition, we are not aware of other techniques able to quantitatively measure absorption continua with high sensitivity. We will see that even in CRDS this is not trivial [25].

Spoiling the cavity quality factor cannot be avoided with solid state samples, which usually have sizable surface and bulk losses (reflection and scattering). Until now, we are not aware of any publication on the CRDS absorption spectroscopy of crystals, glasses, or solutions, even if this is certainly possible with reduced performance (similar to that of CRDS in the UV). One of the limitations is that the spectral range of a pair of dielectric mirrors is often too narrow compared to the width of the absorption bands. This can be circumvented by exploiting cavities based on total internal reflection, which might open the way to ringdown measurements in the condensed phase [26].

Additional problems in CRDS have been discussed and solutions proposed in [9,27]. In particular, the broad-band amplified spontaneous emission (ASE) usually present at the output of pulsed dye lasers should be removed for accurate quantitative measurements of transition intensities. Also, regular oscillations in the spectrum baseline may be observed, due to etaloning between external (uncoated) and internal (high reflectivity) surfaces of the supermirrors.

**A closer look at CRDS.** We may now delve into more technical details. Assuming the cavity is formed by two equal mirrors with radius  $R$  facing each other at a distance  $\ell$ , if the condition  $0 \leq (1 - \ell/R)^2 < 1$  is satisfied then the cavity is "stable" [28]. Light injected along the cavity axis will remain collimated as it

travels back and forth between the mirrors and will usually suffer negligible losses due to the finite mirrors size (diffraction losses). Mirror coatings are characterized by their reflectivity  $\mathcal{R}$ , transmittivity  $\mathcal{T}$ , and losses  $\mathcal{L}$ , which include direct absorption by the multilayer dielectric coating but also scattering due to surface irregularities. This is why high reflectivity coatings are usually deposited over hyperpolished substrates. Conservation of incoming energy into the reflected and transmitted beams requires that  $\mathcal{R} + \mathcal{T} + \mathcal{L} = 1$ .

Mirrors with  $\mathcal{T} < 10^{-5}$  and  $\mathcal{L} \sim 10^{-6}$  are available in the visible or near-infrared [29]. When an intense laser pulse, typically  $N_p^1 \sim 10^{15}$  photons, is injected through one such mirror, about  $10^{10}$  photons are transmitted and remain trapped inside the cavity. Sample absorption and surface losses are usually smaller or comparable to mirror transmission, thus most of the injected photons are eventually re-transmitted outside the cavity rather than dissipated. About half of these photons (for a two mirror cavity) may be collected by a photomultiplier or photodiode detector placed outside the cavity. An intense ringdown signal may be obtained, characterized by an exponential decay envelope and a structure periodic with the cavity round-trip time  $t_c$ . This is given by the laser pulse traveling back and forth inside the cavity, partially interfering with itself and possibly distorted by dispersion and absorption [30]. Since ringdown times are usually larger than 100 ns, this fast ( $t_c = 2\ell/c = \text{few ns}$ ) structure is removed by choosing a sufficiently long detector time constant. There are also (avoidable) situations where multimode cavity excitation produces unacceptably large and slow beating patterns which cannot be simply filtered away [31].

A rigorous and general treatment of the cavity response to an incoming optical field has been described elsewhere [30]. Here we will simply write the decay rate as  $\gamma = \tau^{-1} \simeq c(\mathcal{T} + \mathcal{L})/\ell + c\alpha$ , which is obtained directly dividing the losses per pass by the corresponding time  $\ell/c$ . As dielectric mirrors have a slow and smooth wavelength dependence over several tens of nanometers, the 'cavity absorption coefficient'  $\alpha_c = (\mathcal{T} + \mathcal{L})/\ell$  is just a smooth baseline profile for the sample absorption spectrum  $\alpha(\nu)$ . For absorption spectra with narrow resolved lines (small, light molecules), the sample spectrum stands up clearly against this baseline. However, in the case of broad spectral features (e.g. rotationally unresolved spectra of large molecules) or of continuum absorption, the baseline should be separately measured after removing the sample from the cavity [25].

This is indeed a subtle point. The relative alignment of the laser to the cavity and the relative cavity mirror positions should be mechanically stable in time and with respect to changes of pressure in the ringdown cavity. This assures that injection is reproducible, that is, that the same portions of the mirror surfaces interact with the injected photons for each ringdown event. Otherwise, large (1 to 10%) variations of the baseline are easily observed, especially if the mirrors have accumulated some dirt or if their coating is slightly inhomogeneous. Since the optical field inside the cavity can always be decomposed into a superposition of cavity modes possessing different transverse field distributions, inhomogeneity of mirror surfaces translates into different loss rates for modes of different transverse orders. The same is true for spatially inhomogeneous sample absorption.

In practice, to obtain the ringdown time constant and the cavity loss rate ( $\gamma = 1/\tau$ ), one may use a (fast) digital-to-analog converter (D/A) to transfer the decay profile to a computer. Then, after taking the logarithm, a linear least-squares fit can be done in real time [7]. Another simple solution [9] is using two gated integrators with the same window size and different delays  $t_b$  and  $t_a = t_b + \Delta t$  from the beginning of the ringdown signal. By taking the logarithm of the ratio of these two integral values, one obtains  $\Delta t/\tau$  directly. This may be done all by analogic electronics, or numerically after reading the two integral values with a (slow) D/A. Finally, the sample absorption  $\alpha$  (plus the baseline  $\alpha_c$ ) is obtained directly in units of  $1/\text{cm}$  using  $\alpha_{\text{tot}} = \alpha_c + \alpha = 1/c\tau$ . Absorption per unit length is more representative when the sample uniformly fills the cavity. In other circumstances, as with molecular jets, it might be more meaningful to report the absorption per pass  $\alpha\ell$ .

**Cavity modes.** Until now, we skipped over the basic property of optical cavities, which is their acting as narrow frequency filters with transmission peaks regularly spaced in frequency space. This cannot be neglected for a complete understanding of cavity ring down. Even though this topic is treated in advanced optics handbooks, we still need to make some specific remarks here.

A cavity transmission peak manifests the presence of a standing wave (mode) supported by the cavity geometry. In fact, sizable cavity transmission is possible only by the coherent buildup of the incoming optical field into such a standing wave. Each standing wave has an amplitude distribution  $E(x, y, z)_{q,m,n}$  that is constant in time, except for a phase oscillating with an optical frequency  $\nu_{q,m,n}$ , and a global amplitude factor which corresponds to the number of photons populating the mode. The main features of the standing wave are its  $q$  nodal planes orthogonal to the cavity axis  $z$ , and its  $m$  and  $n$  nodal planes which are parallel to the cavity axis and to the  $x$  or  $y$  axes. The mode number  $q$  defines the *longitudinal* mode order, while  $m, n$  define the *transversal* mode order. During cavity injection by an incoming field, several modes may build up different photon populations. After the excitation field is over, these populations decay due to cavity losses, generally different for modes of different transverse order. By Fourier transform, the exponential decay of the field in a mode corresponds to its Lorentzian FWHM spectral width,  $\Delta\nu = 1/\pi\tau$ . In the absence of nonlinear phenomena on the mirror surfaces or in the intracavity medium, each mode evolves and interacts with the external field independently (superposition principle). The buildup of intensity in a mode is proportional to the product of two factors:

- (A) The spectral density of the incoming field at the mode frequency  $\nu_{q,m,n}$ .
- (B) The superposition integral of the incoming field with the standing wave of the mode in a transverse plane (independent of the plane and also of  $q$ ).

For a symmetric linear cavity

$$\nu_{q,m,n} \simeq \frac{c}{2\ell} \left[ q + (m + n + 1) \frac{2}{\pi} \arctan \sqrt{\frac{\ell}{2R - \ell}} \right],$$

which implies that modes of the same transverse order  $(m, n)$  but different values of  $q$ , form a comb with spacing given by the free spectral range  $\text{FSR} = c/2\ell$ . Sometimes, a laser beam is focused onto the cavity in such a way as to maximize overlap with the  $(0, 0)$  modes (simply called *longitudinal or axial modes*) and avoid excitation of higher transverse order modes. This procedure of *mode-matching*, has the effect that the cavity transmission simplifies to a single comb with spacing equal to the FSR. In the case of a confocal cavity ( $R = \ell$ ), the equation above shows that the frequency of a mode with even  $m + n$  becomes degenerate with that of a  $m + n = 0$  mode of larger  $q$ , while an odd mode degenerates with a  $m + n = 1$  mode. Thus, even in absence of mode-matching, the transmission of a confocal cavity is also a simple comb, but with  $\text{FSR}/2$  spacing (and usually alternating transmission intensities). Finally, we note that other degenerate cavity configurations do also exist for rational values of  $R/\ell$  [30].

We may now go back to considering the impulsive excitation of a ringdown cavity in the frequency domain. By (A), injection works if the laser pulse spectrum overlaps at least one of the transmission frequencies of the cavity. This is granted with pulsed dye lasers having a typical linewidth of a few GHz, usually much larger than the cavity FSR. (To be more accurate, we should also consider that the laser pulse spectrum itself has a mode structure given by the laser cavity [32]). In the time domain, this may correspond (but not necessarily) to the laser pulse being shorter or comparable to the cavity round-trip time. The pulse then maintains its identity and shape as it bounces back and forth inside the cavity. In general, several modes (for each of several transverse orders, if no mode-matching is used) are excited with amplitudes and phases such that their beating reproduces the initial pulse profile. In the case of longer pulses, different parts of the pulse come to spatial overlap, with destructive or constructive interference. However, in the time domain it is not obvious to predict if some residual intracavity field will be left at the end of the pulse, to give an observable ringdown. Instead, in the spectral domain, mode excitation can be determined according to the factors (A) and (B) in the case of arbitrarily long pulses. In particular, it should be noted that even a long pulse may have a broad spectrum, since the Fourier transform indetermination relation (i.e.  $\Delta t \Delta \nu > 1/2\pi$ ) only limits its *minimum* bandwidth.

With respect to excitation of several modes, if these also belong to different transverse orders (no mode matching), variations in decay rates with mode order convert into excess noise. This is due to variations in the pattern of transverse mode excitation when tuning the laser. It has also been observed that transverse mode beating may strongly distort the exponential ringdown envelope [31]. As modes of different transverse orders are orthogonal, this last effect should disappear if the cavity output is uniformly detected on the transverse plane.

Mode matching should be the correct approach to avoid this excess noise. Unfortunately, especially with pulsed lasers, it is usually unfeasible to achieve good mode matching. However, the larger transverse size of higher order modes can be exploited to increase their decay rate by using small mirrors or by introducing a diaphragm inside the cavity. Right after injection, transverse mode beatings and



a multi-exponential decay are usually present in the photon decay signal, but in the tail of this decay a clean exponential corresponding to residual excitation of the longitudinal modes alone may be observed. This tail is the only part of the decay signal used for determining the ringdown rate. This is equivalent to having mode matched cavity excitation, but wastes much of the injected light. Even so, in the past this simple solution gave us excellent results using a standard pulsed dye laser, with a detection limit of  $3 \times 10^{-10} / \text{cm}\sqrt{\text{Hz}}$  [9].

The main problem when mode matching a pulsed laser to a cavity, is that there is currently no standard procedure to monitor and minimize excitation of the transverse cavity modes when beam and cavity alignment are adjusted. On the other hand, this is very easy to do with single mode narrow CW lasers, since one can look at the cavity transmission while modulating the laser wavelength. We used this fact for mode matching in CW-CRDS (described below). In fact, after placing mode matching optics in the right place, one still needs substantial cavity mirror adjustment before observing prevalent excitation of the longitudinal modes only. This implies that with pulsed lasers, it is really insufficient to place mode matching optics according to their calculated positions. If a method for mode matching will be devised for pulsed lasers, the award will be that shot noise measurements with pulsed lasers will become possible.

**Factors affecting pulsed-CRDS resolution.** Higher spectral resolution is needed for resolving spectra taken at low pressure or in a supersonic jet. Fourier-transform-limited pulsed OPO lasers are now commercially available with a linewidth on the order of 100 MHz, which is typically smaller than the cavity FSR. In this situation, an effective way of obtaining continuous cavity injection during a laser scan has been proposed [13]. This amounts to recognizing that a non-confocal cavity with no mode-matching gives a high spectral density of 'available' transverse modes of different orders, practically a quasi-continuum of modes. However, this scheme is affected by excess noise produced by excitation of different transverse orders, as discussed above.

Another interesting solution [30] was successfully tested very recently [33]. This consists in using a Fourier-transform limited pulsed laser with close mode matching to a cavity having a mode spacing larger than the laser bandwidth. By tuning the laser wavelength together with the cavity mode, single mode CRDS excitation allowed recording spectra with a resolution much higher than the pulsed laser bandwidth, limited by fluctuations in the stabilized cavity length. Close to single transverse mode excitation also allowed for higher sensitivity to be achieved.

An important factor to consider when measuring narrow transitions is that these should not fall in between two excited cavity modes [34,30]. Otherwise, a negligibly small spectral density of the optical field is present in the cavity at resonance with the spectral line, and the corresponding absorption cannot have a noticeable effect on the ringdown. The case of a laser broader than the transition has also been investigated, and it was shown that the absorption coefficient can still be accurately deduced if the laser mode structure is measured [32]. It is though considerably simpler to have a sufficiently narrow instrumental resolution compared to the transitions of interest, as it is the case with CW-CRDS.

**CW-CRDS.** The PS-CRDS method proposed recently [18], is one of the first schemes proposed for high sensitivity absorption spectroscopy exploiting a high finesse cavity and a CW laser source. The laser beam is amplitude modulated and the phase shift induced by the cavity is measured in transmission by lock-in detection. This phase shift is due to the finite response time of the cavity, so that this scheme is in principle equivalent to the direct measure of the ringdown time. However, multimode cavity excitation is exploited to avoid locking the cavity to the laser. The different phase shifts of different transverse modes and the low cavity throughput likely account for the relatively low sensitivity demonstrated with PS-CRDS.

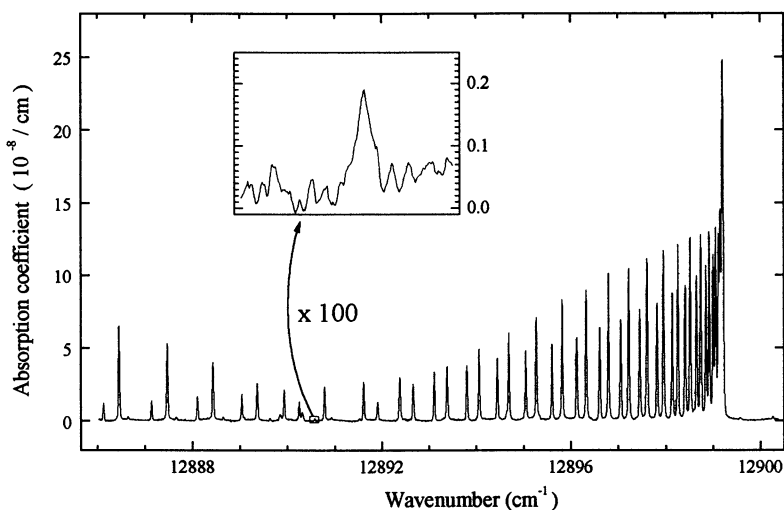


FIG. 1. Diode laser CW-CRDS spectrum of a Doppler limited weak overtone transition  $\text{N}_2\text{O}$  (30 torr). Small features in the baseline are water impurities in the sample.

Another scheme for high resolution CRDS with a CW laser was developed in our laboratory [20]. We exploited the buildup of the intracavity field that occurs when a cavity mode passes through resonance with the laser line, which is easily detected in transmission [35]. An exponential decay with a chirped beating is observed following the buildup, as the frequency difference increases between the incoming laser field and the built-up mode field [36]. To avoid this beating pattern, the laser beam is interrupted when the buildup goes above a given threshold, and digitization of the following pure exponential ringdown is triggered. A steady repetition rate of such buildup-ringdown events is obtained by modulating the cavity length, so that the cavity modes oscillate in frequency space and cross the laser line periodically. By partial mode-matching, we obtained a buildup 10 to 100 times stronger for the longitudinal modes than for the higher transverse modes. Then, the threshold was set in order to select exclusively those stronger buildup events belonging to longitudinal modes, which improved performance by 1 or 2 orders of magnitude.

CW-CRDS is especially attractive after demonstration that excellent performance is obtained even with low power tunable diode lasers (see figure 1) [21,23]. Either external-cavity or distributed feedback (DFB) diodes operating in the range from 1 to 2  $\mu\text{m}$  can now be used to build compact and inexpensive CW-CRDS trace gas detectors.

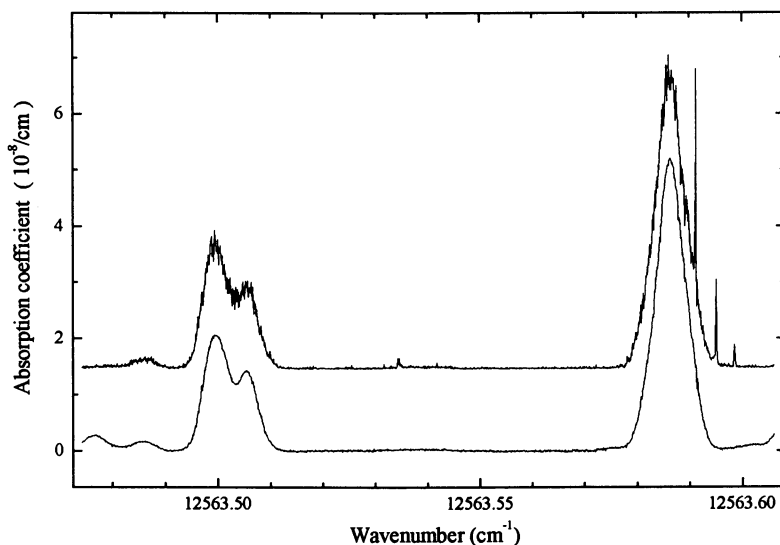


FIG. 2. CW-CRDS and fluorescence spectra (higher) from sub-Doppler rovibronic transitions of  $\text{NO}_2$  seeded in a supersonic slit jet. The narrow fluorescence peaks (a few MHz wide, due to Ti:Sa laser jitter) are from two-photon Doppler-free absorption.

**Power saturation in CRDS.** Until now, absorption by the sample has been assumed to be linear. In typical conditions, one estimates that with pulsed-CRDS, laser pulse attenuation upon injection and poor spectral resolution make unlikely that saturation effects could be observed even in presence of strong electronic molecular transitions. With narrowband Fourier transform limited pulsed lasers, injected energy may produce saturation in the limit of strong molecular or atomic transitions. On the other hand, with CW-CRDS we recently observed saturation of weak molecular electronic transitions. Indeed, in the CW-CRDS buildup process, watts of intracavity power in a single mode may be easily obtained, corresponding to  $\text{KW}/\text{cm}^2$  power densities. The transit time of molecules across the mode usually limits the ultimate spectral resolution of the apparatus to a few hundreds kHz (typically larger than the mode spectral width). In the laboratory of R. Jost and with the collaboration of P. Dupré [22], we used a CW Ti:Sa laser having about 5MHz linewidth (averaged over 1s), which further limited the spectral resolution. In the timescale of the cavity buildup, the laser linewidth was still 1MHz, about 1000 times more than the cavity mode width (a few kHz).

Thus, only about 1/1000 of the laser spectral density would be resonant with the cavity mode at any instant and constructively contribute to the mode buildup. Since the buildup efficiency of our cavity for resonant radiation was more than  $10^4$  we could still measure about 30 W in a single longitudinal mode in correspondence with the beginning of the ringdown signal. This required sweeping the cavity mode across the laser line sufficiently slowly (about 30 Hz cavity length modulation with  $< 0.1\lambda$  amplitude). Strong power broadening and Doppler-free saturation dips were observed in rovibronic transitions of  $\text{NO}_2$  seeded in a supersonic slit jet. Using simultaneous fluorescence detection at 90 degrees with the jet and the cavity axis, we could also observe both single-color double-resonance and Doppler-free two-photon processes (see figure 2).

**Detection limit in CRDS.** As in other spectroscopic techniques, the ultimate detection limit in CRDS is achieved when all sources of noise are made smaller than the intrinsic shot noise of the optical signal. Shot noise originates from the statistical quantum nature of creation and destruction processes ruling the existence of the signal carriers (photons or electrons). The fractional level of shot noise at the detector is equal to  $1/\sqrt{N_e}$ , where  $N_e$  is the number of photoelectrons produced during the integration time considered.

Integrating the detector photocurrent produced during one ringdown event one obtains  $N_e = I(0)\tau/q_e$ , where  $I(0)$  is the current at the beginning of the ringdown and  $q_e$  the electron charge. Correspondingly, the fractional shot noise on the determination of  $\tau$  by an exponential fit of the digitized signal, is approximately [9]  $\delta\tau/\tau = \sqrt{q_e/I(0)\tau}$ , which is also equal to  $\delta\alpha/\alpha_{\text{tot}}$ . If a linear fit of the logarithm of the data is used instead (for simplicity and numerical speed), the standard deviation on  $\tau$  increases by a constant factor which is close enough to unity to be neglected here.

Besides shot noise, electronic noise and digitizer resolution are practical limiting factors. For a digitizer with  $b$  bits and sampling time  $dt$ , the sampling noise is about  $V_f 2^{-b}$ , where  $V_f$  is the digitization range. On the other hand, the number of photoelectrons collected during  $dt$  gives the fractional shot noise for the ringdown signal  $V(t)$  at the digitizer input. This is  $V(t)/\sqrt{I(t)dt/q_e} = V_f \exp(-t/2\tau)/\sqrt{I(0)dt/q_e}$ , where we assumed that the full digitization range is exploited with  $V(0) = V_f$ . It is to be noted that electronic amplification is usually possible without further degrading the fractional shot noise level which is produced at the detector.

As an example, we will consider again our recent observations with a CW-CRDS setup based on a single-mode Ti:Sa laser [22]. The photocurrent of a silicon detector was converted into a voltage signal by a FET OP-AMP with a 25 K $\Omega$  resistor in the feedback loop. No further amplification was needed, and the threshold which triggered interruption of laser beam and data acquisition was set to 5V, so that  $I(0) = 200 \mu\text{A}$ . We used a 12 bits, 1 MHz, A/D PC card, set for a 0–5 volts range. Thus we had a digitization step of 1.2 mV. This was larger than the expected shot noise of 0.14 mV in the (initial) 1  $\mu\text{s}$  sampling intervals of the A/D card. However, the observed electronic noise was even larger (4 mV)

than the A/D resolution. To obtain  $\tau$  in real time for each ringdown event, the PC was programmed to subtract the detector bias, take the logarithm of the digitized decay, and perform a linear fit. In this fit, the 4 mV noise produced a standard deviation on  $\tau$  of  $\sim 0.1\%$ . Since  $|\delta\tau/\tau| = |\delta\alpha_{\text{tot}}/\alpha_{\text{tot}}| = \alpha_{\text{min}}/\alpha_{\text{tot}}$  (the minimum detectable, noise-equivalent absorption coefficient), using  $\tau = 120 \mu\text{s}$  and considering our 50 Hz ringdown sampling rate we obtain the reported value of  $\alpha_{\text{min}} \sim 5 \times 10^{-11}/\text{cm}\sqrt{\text{Hz}}$ . It is important that this same value was also obtained as the noise level of the recorder spectra, indicating that we were limited by electronic noise and not by other effects such as fringes, fluctuations of the laser beam, or changes in the supersonic jet density.

Since it is possible to build better electronics which can deliver the shot noise limited signal to the D/A, a 16 bit resolution would be needed and would allow a 10 times improvement of the detection limit. However, other effects might produce fluctuations of the ringdown time larger than the expected shot noise of 0.01%. On the other hand, we may also play on the cavity modulation, which could be easily increased to 10kHz or more. The faster frequency sweep would reduce the buildup and the ringdown signal level, with a 10 times larger fractional shot noise, which could be handled by a 12 bit digitizer. Faster signal averaging would recover this factor of 10. Incidentally, we note that inexpensive 12 bit digitizers are fully adequate to handle the weaker ringdown signal typically obtained with less intense laser sources, e.g. diode lasers. To conclude, we trust that the shot noise limit for ringdown measurements can be reached with improved optical and electronic designs. This would lead to a 10 times improved detection limit, down to  $10^{-12}/\text{cm}\sqrt{\text{Hz}}$ .

### Intra Cavity Laser Absorption Spectroscopy

In the typical ICLAS spectrograph, a sample cell is placed inside the cavity of a laser with an homogeneously broadened gain medium (e.g. a dye laser), which is operated intermittently in long pulses at a high repetition rate (for example  $\sim 1$  KHz for 1 ms pulses). No narrow band elements are present in the cavity, so that each laser generation pulse starts out with a broad spectrum spanning some  $10^4$  active modes. Absorption lines are detected as dips digging into the laser spectrum as a function of the time  $t_g$  from the beginning of the laser generation. If things are properly done, absorption lines grow according to the Lambert-Beer law with  $L_{\text{eq}} = ct_g$  (up to a saturation time limit). Using an acousto-optic deflector to briefly inject the laser beam into a spectrograph, the spectrum at  $t_g$  is dispersed and recorded as a whole with a CCD array (spectral multiplexing). A single laser generation gives a very noisy spectrum, due to initial random seeding of laser cavity modes by spontaneous emission. However, a smooth ICLAS spectrum can be obtained in a few seconds, after averaging (on the CCD) a few thousands pulses.

The need for a CW laser (dye or solid state) limits ICLAS to the visible and near IR. On the other hand, spectral multiplexing is a very powerful feature, which is also an intrinsic and unavoidable feature of ICLAS. Since laser amplitude fluctuations are the same for all lasing modes, absorption features are

sensitively revealed only by looking at the relative intensities of different spectral elements as simultaneously recorded by the CCD array. For the same reason, broad band cavity losses or absorption features broader than the lasing profile are not detectable and produce only a variation of the laser threshold. This limitation increases when pushing to higher sensitivity (larger  $t_g$ ), due to laser spectral narrowing. Lack of understanding of this fundamental feature has led people to try intracavity absorption measurements using single-mode or narrow band lasers, with poor results.

ICLAS began being used on a regular basis for the spectroscopy of weak transitions around 1975 [37]. A variety of publications demonstrate that this is a polyvalent technique, which was applied to gas and pulsed slit-jet measurements [38–40], trace monitoring in chemical reactors (diamond deposition) [41] or in flames [42], and to chemical kinetics investigations [43].

Recently, by ratioing spectra sampled at two successive generation times during the same laser generation, we were able to obtain absorption spectra without averaging over laser generations (see below and figure 4) [44]. Correlated double sampling (CDS) allows reducing the interaction time with the sample down to a technical limit of a few tens of microseconds. CDS-ICLAS will be especially valuable for the spectroscopy of rare or infrequent events (e.g. double resonance with a low repetition pulsed excitation laser, detection of transient species in shock wave tubes, etc.).

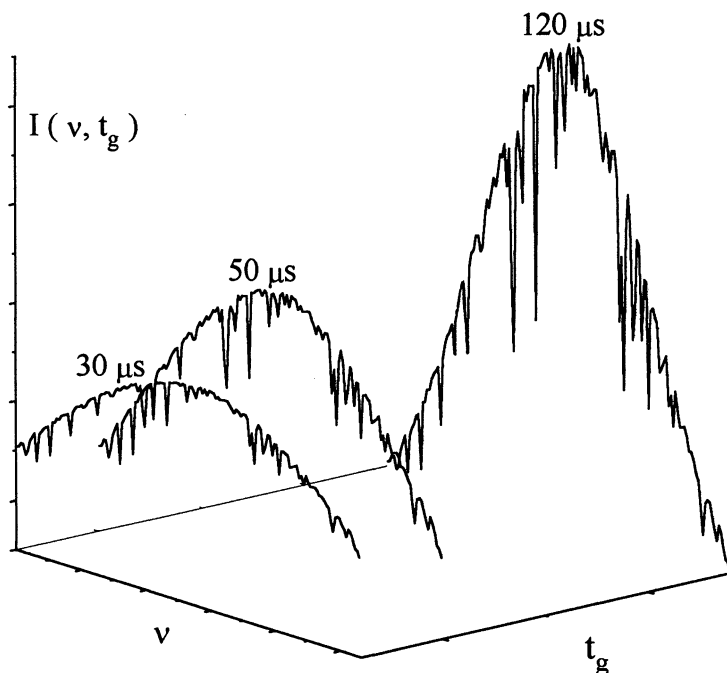


FIG. 3. Temporal evolution of a multimode ICLAS laser spectrum.

**Spectral resolution in ICLAS.** Commercial spectrographs may achieve a resolving power  $\delta\nu/\nu$  of about  $10^5$  ( $0.1\text{ cm}^{-1}$  resolution in the visible), but high order diffraction gratings can be exploited to build custom ICLAS spectrographs with resolving power of up to  $2 \times 10^6$ . This is possible for two reasons. Firstly, the small separation of high diffraction orders is sufficient with a laser emission spectrum at most 200 or  $300\text{ cm}^{-1}$  wide. Secondly, the intensity lost in different active diffraction orders is not a concern since a lot of light is available. Using multipass configurations, compact design of the spectrometer is possible for portable trace detection devices [45], especially for atmospheric measurements where a spectral resolution of  $0.1\text{ cm}^{-1}$  is enough for pressure broadened transitions.

With respect to absorption linewidth, similar problems as in CRDS do exist when the laser mode spacing is approached [40]. If the mode frequencies fluctuate sufficiently during the few seconds needed for averaging, narrow absorption lines are still seen in the average as if there were no cavity modes, convoluted with the spectrograph instrumental function. However, since part of the time these absorption lines fall in between laser modes, there is a net loss of signal and thus sensitivity in addition to the instrumental broadening.

This may be a severe limitation in slit-jet spectroscopy. A preliminary study has shown that it is possible to exploit the high spectral purity of laser modes to go beyond the resolution of the spectrograph [46]. In contrast to the difficulty of obtaining pure excitation of the longitudinal modes in a passive CRDS cavity, a longitudinally pumped CW laser is easily aligned to run with only longitudinal modes. This gives a simple comb in frequency space. In this study, the mode separation was increased by introducing a low finesse etalon inside the laser cavity, which allowed lasing of a subset of regularly spaced modes. Each of these modes could be resolved by the spectrograph to obtain a mode-resolved spectrum. By scanning the etalon thickness, mode resolved spectra of successive interleaved subsets of modes were recorded. The high resolution picture was finally reconstructed by joining these spectra. Finer tuning would also be possible by controlling the cavity length. It is important to realize that, since several laser modes are active at the same time, we still have a multimode laser characterized by the same dynamics and extreme ICLAS sensitivity to narrow band (mode selective) intracavity losses.

**A closer look at ICLAS.** Long generation pulses are usually produced by modulation of the laser pumping the ICLAS gain medium. Due to the fast excited state relaxation of dyes, after the pump beam is switched on, the total output power in the ICLAS laser increases exponentially during a fraction of a microsecond. Then the gain saturates to the point where it exactly compensates the average cavity losses, and a stationary state is reached for the total laser intensity. Due to the broad homogeneous character of the gain profile, losses are compensated in average for most of the modes except those corresponding to narrow absorption lines of the sample. The intensity of these modes will then decrease in time. This situation may be assimilated to that of a multipass cell having lossless mirrors. For a more detailed description see [47] and references therein.

The time evolution of the laser spectrum, averaged over many laser generations, is shown in figure 3 and is well described by the following equation for the number of photons  $M_q$  in the laser mode  $q$ ,

$$M_q(t_g) = M_{\text{tot}} \sqrt{\frac{\gamma t_g}{\pi Q^2}} \exp \left[ - \left( \frac{q - q_0}{Q} \right)^2 \gamma t_g \right] \exp \left[ - \alpha(\nu_q) \left( \frac{\ell_s}{\ell} \right) c t_g \right], \quad (1)$$

which is derived from the laser rate equations. Here,  $\gamma$  is the cavity loss rate and  $\ell_s$  is the sample length which, divided by the laser cavity length  $\ell$ , gives the “filling ratio” of the sample inside the cavity. The first exponential term gives the well-known spectral narrowing of the laser emission profile. This is due to cavity losses which are not completely compensated for modes further away from the center of the gain curve. The rate of spectral narrowing depends on the shape of the gain profile, which is approximated near its top by a parabola  $[(q - q_0)/Q]^2$ . The second exponential represent Lambert–Beer absorption due to the sample, with an equivalent pathlength  $L_{\text{eq}} = c t_g (\ell_s/\ell)$ .

Solid state laser media are characterized by an excited state relaxation slower than the photon lifetime in the cavity. Gain saturation is no more achieved smoothly, but after large relaxation oscillations of the total laser intensity. For these lasers, eq. 1 still approximately holds after including the time dependence of the total intensity in the term  $M_{\text{tot}}$ . Most important, spectral absorption has been found to still follow the Lambert–Beer law [48,49], which confirms that solid state lasers such as Ti:Sa may be used for ICLAS in the near IR.

**Power saturation in ICLAS.** As in pulsed–CRDS, possible saturation of strong molecular or atomic transitions should to be considered according to the specific case. However, for typical outputs of a few milliwatts, the intracavity power may be on the order of a few watts, which is divided among several thousands active laser modes with large mode to mode and pulse to pulse fluctuations (due to the seeding noise, see below). Thus, the weak power content of each laser mode makes saturation of narrow molecular transition quite unlikely, but, if nonlinear phenomena were to be observed in ICLAS, their modeling would be very complex since it should account for the fluctuations and the statistics of the mode intensity distribution.

**Effects limiting ICLAS sensitivity.** In deriving eq. 1, the spontaneous emission term in the laser rate equations had to be neglected. Since the rate of spontaneous emission into the laser mode  $q$  is  $M_q$  times smaller than the rate of stimulated emission, the effect of neglecting this term comes in only at long generation times. It can be shown that due to spontaneous emission the spectral evolution eq. 1 does not proceed indefinitely but reaches a steady state for  $t_g > \tau_{\text{sp}} = M_{q_0}/\gamma$ , where  $M_{q_0}$  is taken at the steady state. Thus, spontaneous emission poses an ultimate limit to absorption growth and to spectral narrowing.

For typical laser parameters,  $\tau_{\text{sp}} \sim 1$  s. However, absorption growth is limited to earlier times due to nonlinear mode coupling, which was also not included in the above equation and is too complex a subject to be discussed here (see



[50] and references therein). In practice, one finds that for a linear cavity laser eq. 1 is an accurate quantitative description if the laser is close to threshold ( $\sim 10\%$ ) and up to generation times not much larger than 1 ms [51]. Carefully dispersion-compensated ring lasers have been found to reduce the effect of mode coupling so that generation times up to 10-100 ms may be reached. Due to spectral narrowing the useful spectral window is only a few  $\text{cm}^{-1}$  at such long generation times, which is usually too strong a limitation in spectroscopic applications. In general, when absolute absorption coefficients are of interest, ICLAS spectra at different generation times should be used to detect possible saturation effects of the absorption growth. A single spectrum recorded at one generation time should never be used to determine absorption intensities, even relative ones.

We already hinted that laser generation starts from photons seeded into the cavity modes by spontaneous emission. After a photon is seeded into a mode, its intensity starts growing exponentially, until the gain becomes saturated. Given the statistical nature of the seeding process, buildup in different modes starts at different times. This produces an exponential distribution of initial mode intensities, characterized by a standard deviation equal to the mean value of photons in each mode (100% noise) [52]. It is evident that with such a noise level all other noise sources are negligible. Even after averaging, seeding noise has been demonstrated to dominate and determine the detection limit in an experiment using a traveling-wave ring dye laser [51].

However, seeding noise is not the fundamental limit for ICLAS, since the mode evolution has a memory of the initial distribution of mode intensities. This is the basis of the CDS scheme: If laser spectra are measured at  $t_g$  and  $t_g + \Delta t$  during *the same generation*, their ratio gives a spectrum which is free of the initial seeding noise and has  $L_{\text{eq}} = c\Delta t$ . As it turns out, extra noise accumulates in the spectrum during the interval  $\Delta t$ . This is shot noise due to the creation (amplification) and destruction (losses) events that affect the photons in each active mode [49,44], which produces a random-walk of the mode intensities. As usual, this statistical noise may still be reduced by averaging.

Simple standing-wave lasers are most often employed in ICLAS. For these, interference fringes constitute a lower practical limit to the smallest detectable absorption. These are due to spatially localized losses (dust particles over the optics or bulk defects in the case of solid state lasers) [53], which may affect with different strength modes (standing waves) having a node or a peak at the loss location. Fringes grow at the same rate as the absorption spectra, so their relative effect is independent of the generation time. The typical situation is that fringe amplitude is on the order of 1% for generation times of about 200 or 300  $\mu\text{s}$ . This is on the same order as the intrinsic noise of the ICLAS spectrum averaged over few tens of seconds. For running wave ring lasers, which are mostly free from such effects, one may work comfortably with  $t_g$  up to 1 ms, before spectral narrowing becomes a limiting factor.

After this short overview of all these factors, we will now consider the detection limit that can be achieved with a linear standing-wave cavity, with a ring cavity, and also by using the CDS scheme. We will assume a 50% sample filling

ratio. In estimating the contribution of the seeding noise, we have to account for the averaging over the number of modes which are integrated in one spectral element (given by the spectrograph instrumental width), and for the averaging over the number of samples collected in 1 s. The laser mode spacing is typically 100 MHz ( $0.003 \text{ cm}^{-1}$ ) and for a custom ICLAS spectrograph the resolution is about  $0.01 \text{ cm}^{-1}$  in the visible. A spectral element will therefore average the contribution of 3 modes. Using a commercial CCD array of 6000 pixels, and allowing about 6 pixels to sample the instrumental function, we can sample 1000 spectral elements at a time, corresponding to a spectral window of  $10 \text{ cm}^{-1}$ . For the standing wave case,  $t_g = 100 \mu\text{s}$  makes for  $10^4$  samples/s and a noise level of  $100\%/\sqrt{3 \times 10^4} \approx 0.6\%$ , corresponding to a detection limit of  $4 \times 10^{-9}/\text{cm}$ . For a ring laser  $t_g = 1 \text{ ms}$  gives  $1 \times 10^{-9}/\text{cm}$ . To account for multiplexing, we divide by the square root of 1000 to obtain normalized detection limits of  $1.5 \times 10^{-10}$  and  $4 \times 10^{-11}/\text{cm}\sqrt{\text{Hz}}$  for the linear and the ring cavity setups, respectively. To conclude, from the CDS spectrum of figure 4, we see that a noise level of  $3 \times 10^{-9}/\text{cm}$  was obtained in a measurement time of  $400 \mu\text{s}$ . Considering the number of spectral elements, the detection limit is  $2 \times 10^{-12}/\text{cm}\sqrt{\text{Hz}}$ .

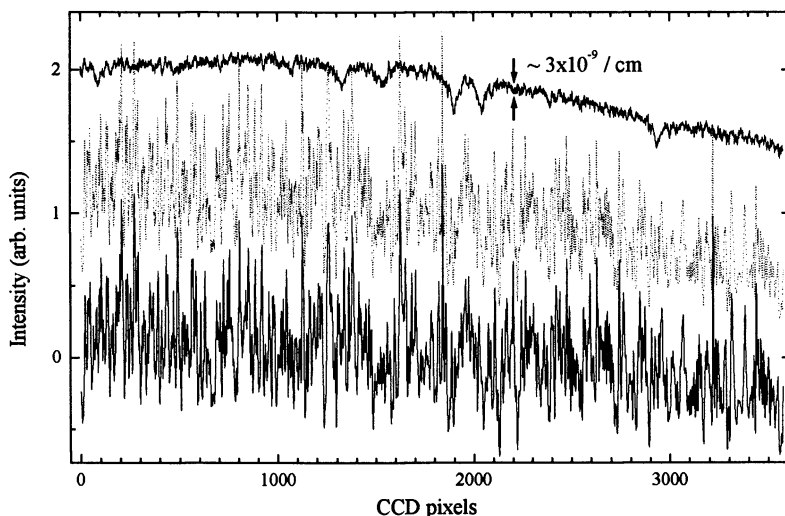


FIG. 4. Single-pulse ICLAS: Two noisy spectra have been recorded at  $t_g$  and  $t_g + 400 \mu\text{s}$  ( $L_{\text{eq}} = 120 \text{ km}$ ) during the same laser generation. Their ratio (above) disposes of the laser seeding noise and reveals weak atmospheric absorption lines.

## Conclusion

Accurate quantitative determination of sample absorption with very high sensitivity classifies both CRDS and ICLAS as powerful spectroscopic techniques. The recent introduction of CW-CRDS, makes it now possible to use CRDS with room temperature diode lasers, already commercially available in the range from

1 to 2  $\mu\text{m}$ , where most molecules possess quite strong low-overtone transitions. It is thus possible to realize compact CRDS devices capable of detecting ppm or ppb trace levels in the gas phase. In the near future, size and cost of ICLAS systems could also be greatly reduced by using diode-pumped solid state lasers. ICLAS has a multiplexing ability which is a definite advantage over CRDS. For example, it could be invaluable for diagnostic applications by giving a real time display of spectral modifications produced by changes in system parameters.

An advantage common to both methods is the small ( $< 1 \text{ cm}^3$ ) sampled volume, which reduces the cost of spectral analysis of isotopically substituted species. This is usually a limitation with multipass cells, where the light beam is folded over a complex path sampling a large effective volume. This also makes both CRDS and ICLAS well adapted to measuring absorption through supersonic slit jets. In trace detection, this feature allows a fast renewal of the sample ( $\sim 1 \text{ s}$ ) and a fast device response.

The choice of a technique is often forced by the spectral range of interest. When using CW-CRDS with diode lasers, the available spectral range is limited from about 630 nm to 2  $\mu\text{m}$ . IR Peltier-cooled diode lasers or new quantum cascade lasers will allow reaching easily longer wavelengths where stronger vibrational transitions will improve performance of trace detection.

By using Ti:Sa or dyes, the spectral range from 500 nm to 1  $\mu\text{m}$  may be accessed both with ICLAS and CW-CRDS. These are bulky systems adapted for spectroscopic applications, which require ion-laser pumping. For ICLAS, a dedicated broad band laser system has to be built, while for CRDS one may use a commercial CW single-mode system. Reaching further down into the IR with ICLAS (1 to 3  $\mu\text{m}$ ) is possible using F-center or IR laser crystals [54], but this still requires testing and further research.

The largest possible spectral extent is obtained with pulsed-CRDS: Nonlinear conversion techniques get to the near UV, and OPO's are available in the IR. Contrary to CW-CRDS, exactly mode matching a pulsed laser to the cavity poses serious problems and as a result a larger noise level is typical. In the UV, CRDS operation has been demonstrated, but with the lower detection limit allowed by the poorer quality of high reflectivity coatings. It appears that mirrors below 2  $\mu\text{m}$  are also of lower quality than in the visible. However, in the UV the limiting factor is unavoidable Rayleigh scattering, while in the IR the problem lies in the dielectric materials employed. We expect that the quality of IR mirror will substantially improve in the future.

Spectral resolution in ICLAS depends on the spectrograph. This can be specifically built to achieve  $0.01 \text{ cm}^{-1}$  in the visible, still maintaining a compact profile (1 m length). We also discussed preliminary work showing how it is possible to achieve even higher resolution using an intracavity etalon to select groups of widely spaced laser modes. On the other hand, in CW-CRDS high spectral resolution is easily obtained with narrow band CW laser sources. These are perhaps more expensive and difficult to operate than a high resolution spectrograph, with the exception of external cavity tunable diode lasers. When pulsed dye lasers are used for CRDS,  $0.04 \text{ cm}^{-1}$  is about the best to be expected, but are now com-

mercially available sophisticated, narrow-band, pulsed OPO systems, with about 100 MHz resolution and broad tunability. Low resolution, compact and rugged commercial OPO's are also very appealing, e.g. for trace detection of volatile organic compounds (VOCs) in the IR. Unfortunately, when closely spaced absorption lines are present from a "contaminant" in the sample (notably, H<sub>2</sub>O), low resolution pulsed sources do not allow discriminating these from the broad VOC absorption profile.

Spectral multiplexing is an intrinsic ICLAS feature. It would be a convenient feature in CRDS too. Indeed, it has been demonstrated that a broad band pulsed laser for cavity injection can be used, by wavelength selecting the ringdown in a step-scan Fourier transform apparatus. While this approach is worth for enhancing the sensitivity of a FT apparatus, a real-time display of the absorption spectrum cannot be obtained. With respect to multiplexing, CRDS remains fundamentally complementary to ICLAS. This is perhaps the most evident difference between the two methods, but it is even deeper than expected at a first sight...

In ICLAS, there is a fundamental limitation in that absorption features broader than the laser emission spectrum cannot be measured. Laser spectral narrowing imposes an inverse relationship between maximum spectral width and detection sensitivity. At a generation time of  $t_g = 100 \mu\text{s}$ , the laser spectral width is down to about  $100 \text{ cm}^{-1}$ , already comparable to the room-temperature width of ro-vibrational band contours in VOCs. For this same reason, ICLAS is not adapted to the spectroscopy in solid or liquid samples, where absorption profiles are usually too broad. Nonetheless, relatively broad but intense (requiring small  $t_g$ ) gas-phase absorption bands have been measured using this technique [55].

Conversely, in CRDS there is no fundamental difficulty in obtaining the baseline-free difference spectrum of the cavity with and without sample. This rather unique ability to measure broad band or even continuum absorption is very interesting for several applications. For example, for detecting dust in discharges or characterizing the infrared continuum atmospheric absorption, which is a long standing problem. Measuring broad absorption features could also find application in the spectroscopy of the condensed phases.

The other side of the medal is that ICLAS is more "robust" and adapted to applications where broad band sample losses larger or close to 1% per pass cannot be avoided. For example, a cell with Brewster windows is normally used for inserting the sample inside the ICLAS laser cavity. This is not advisable in CRDS, since window losses spoil the cavity quality factor. Thus, in the presence of aggressive or 'dirty' samples, CRDS mirrors must be protected, e.g. by flushing a clean buffer gas over their surfaces.

Due to their complementarity, both methods will survive and gain a more relevant place in high sensitivity absorption applications. Interesting and unexplored possibilities still exist in CRDS and ICLAS which await for future developments.

## Acknowledgements

This work would have not been possible without extensive discussion especially with A. A. Kachanov, K. K. Lehmann, and F. Stoeckel.

## Literature Cited

- [1] Hall, J. In *Ohio State University International Symposium on Molecular Spectroscopy*; Miller, T. A., Ed.; Columbus, Ohio, 1996.
- [2] Grosklos, R.; Kersten, P.; Demtröder, W. *Applied Physics B* **1994**, *58*, 137.
- [3] Hobbs, P. C. D. *Appl. Opt.* **1997**, *36*, 903.
- [4] Pakhomycheva, L. A.; Sviridenkov, E. A.; Suchkov, A. F.; Titova, L. V.; Churilov, S. S. *JETP Lett.* **1970**, *12*, 43.
- [5] Peterson, A. C.; Kurilo, M. J.; Braun, W.; Bass, A. M.; Keller, R. A. *J. Opt. Soc. Amer.* **1971**, *61*, 746.
- [6] Anderson, D. Z.; Frisch, J. C.; Masser, C. S. *Appl. Opt.* **1984**, *23*, 1238.
- [7] O'Keefe, A.; Deacon, D. A. G. *Rev. Sci. Instrum.* **1988**, *59*, 2544.
- [8] O'Keefe, A.; Scherer, J. J.; Cooksy, A. L.; Sheeks, R.; Heath, J.; Saykally, R. J. *Chem. Phys. Lett.* **1990**, *172*, 214.
- [9] Romanini, D.; Lehmann, K. K. *J. Chem. Phys.* **1993**, *99*, 6287.
- [10] Scherer, J. J.; Voelkel, D.; Rakestraw, D. J.; Paul, J. B.; Collier, C. P.; Saykally, R. J.; O'Keefe, A. *Chem. Phys. Lett.* **1995**, *245*, 273.
- [11] Pearson, J.; Orr-Ewing, A. J.; Ashfold, M. N. R.; Dixon, R. N. *J. Chem. Soc. Faraday Trans.* **1996**, *92*, 1283.
- [12] Yu, T.; Lin, M. C. *J. Am. Chem. Soc.* **1993**, *115*, 4371.
- [13] Meijer, G.; Boogaarts, M. G. H.; Jongma, R. T.; Parker, D. H.; Wodtke, A. M. *Chem. Phys. Lett.* **1994**, *217*, 112.
- [14] Zalicki, P.; Ma, Y.; Zare, R. N.; Wahl, E. H.; Dadamio, J.; Owano, T. G.; Kruger, C. H. *Chem. Phys. Lett.* **1995**, *234*, 269.
- [15] Kotterer, M.; Conceicao, J.; Maier, J. P. *Chem. Phys. Lett.* **1996**, *259*, 233.
- [16] Engeln, R.; Meijer, G. *Rev. Sci. Instrum.* **1996**, *67*, 2708.
- [17] Engeln, R.; Berden, G.; van den Berg, E.; Meijer, G. *J. Chem. Phys.* **1997**, *107*, 4458.
- [18] Engeln, R. E.; von Helden, G.; Berden, G.; Meijer, G. *Chem. Phys. Lett.* **1996**, *262*, 105.
- [19] Herbelin, J. M.; McKay, J. A.; Kwok, M. A.; Ueunten, R. H.; Urevig, D. S.; Spencer, D. J.; Benard, D. J. *Appl. Opt.* **1980**, *19*, 144.
- [20] Romanini, D.; Kachanov, A. A.; Sadeghi, N.; Stoeckel, F. *Chem. Phys. Lett.* **1997**, *264*, 316.
- [21] Romanini, D.; Kachanov, A. A.; Stoeckel, F. *Chem. Phys. Lett.* **1997**, *270*, 538.
- [22] Romanini, D.; Dupré, P.; Jost, R. *in preparation*.
- [23] Paldus, B. A.; J.S. Harris, J.; Martin, J.; Xie, J.; Zare, R. N. *J. Appl. Phys.* **1997**, *82*, 3199.
- [24] Campargue, A.; Romanini, D.; Sadeghi, N.; Biennier, L. *J. of Physics D.*, accepted.
- [25] Romanini, D.; Kachanov, A. A.; Stoeckel, F. *Chem. Phys. Lett.* **1997**, *270*, 546.
- [26] Pipino, A. C. R.; Hudgens, J. W.; Huie, R. E. *Rev. Sci. Instrum.* **1997**, *68*, 2978.
- [27] Romanini, D.; Lehmann, K. K. *J. Chem. Phys.* **1995**, *102*, 633.
- [28] Yariv, A. *Quantum Electronics*; Third Edition; John Wiley & Sons: New York, NY, 1989.
- [29] Rempe, G.; Thompson, R. J.; Kimble, H. J.; Lalezari, R. *Optics Lett.* **1992**, *17*, 363.

- [30] Lehmann, K. K.; Romanini, D. *J. Chem. Phys.* **1996**, *105*, 10263.
- [31] Martin, J.; Paldus, B. A.; Zalicki, P.; Wahl, E. H.; Owano, T. G.; J. S. Harris, J.; Kruger, C. H.; Zare, R. N. *Chem. Phys. Lett.* **1996**, *258*, 63.
- [32] Hodges, J. T.; Looney, J. P.; van Zee, R. D. *Appl. Opt.* **1996**, *35*, 4112.
- [33] Hodges, J. T.; Looney, J. P.; van Zee, R. D. In *Ohio State University International Symposium on Molecular Spectroscopy*; Miller, T. A., Ed.; Columbus, Ohio, 1998.
- [34] Zalicki, P.; Zare, R. N. *J. Chem. Phys.* **1995**, *102*, 2708.
- [35] Ziyuan Li; Stedman, G. E.; Bilger, H. R. *Optics Comm.* **1993**, *100*, 240.
- [36] Ziyuan Li; Bennet, R. G. T.; Stedman, G. E. *Optics Comm.* **1991**, *86*, 51.
- [37] Antonov, E. N.; Koloshnikov, V. G.; Mironenko, V. R. *Optics Comm.* **1975**, *15*, 99.
- [38] Goldstein, N.; Brack, T. L.; Atkinson, G. H. *Chem. Phys. Lett.* **1985**, *116*, 223.
- [39] Campargue, A.; Chenevier, M.; Stoeckel, F. *Chem. Phys. Lett.* **1991**, *183*, 153.
- [40] Georges, R.; Delon, A.; Bylicki, F.; Jost, R.; Campargue, A.; Charvat, A.; Chenevier, M.; Stoeckel, F. *Chem. Phys.* **1995**, *190*, 207.
- [41] Vetterhofer, J.; Campargue, A.; Chenevier, M.; Stoeckel, F. *Diamond and Related Materials* **1993**, *2*, 481.
- [42] Cheskis, S. *J. Chem. Phys.* **1995**, *102*, 1851.
- [43] Bryukov, M. G.; Kachanov, A. A.; Panov, S. I.; Sarkisov, O. M. *J. Phys. IV (Paris)* **1991**, C7-485.
- [44] Kachanov, A. A.; Romanini, D.; Charvat, A.; Abel, B. In *Ohio State University International Symposium on Molecular Spectroscopy*; Miller, T. A., Ed.; Columbus, Ohio, 1998.
- [45] Kachanov, A. A. *private communication*.
- [46] Kachanov, A. A.; Stoeckel, F.; Charvat, A.; O'Brien, J. J. *Appl. Opt.* **1997**, *36*, 4062.
- [47] Campargue, A.; Stoeckel, F.; Chenevier, M. *Spectrochimica Acta Rev.* **1990**, *13*, 69.
- [48] Kachanov, A.; Charvat, A.; Stoeckel, F. *J. Opt. Soc. Am. B* **1994**, *11*, 2412.
- [49] Romanini, D.; Kachanov, A. A.; Lacot, E.; Stoeckel, F. *Phys. Rev. A* **1996**, *54*, 920.
- [50] Kachanov, A.; Charvat, A.; Stoeckel, F. *J. Opt. Soc. Am. B* **1995**, *12*, 970.
- [51] Kachanov, A. A.; Mironenko, V. R.; Pashkovich, I. K. *Sov. J. Quantum Electron.* **1989**, *19*, 95.
- [52] Mironenko, V. R.; Yudson, V. I. *Sov. Phys. JETP* **1980**, *52*, 594.
- [53] Antonov, E. N.; Antsiferov, P. S.; Kachanov, A. A.; Koloshnikov, V. G. *Optics Comm.* **1982**, *41*, 131.
- [54] French, P. M. W. *Laser Focus World* **1995**, *31*, 93.
- [55] Campargue, A.; Stoeckel, F. *J. Chem. Phys.* **1986**, *85*, 1220.

## Chapter 10

# Fourier Transform and Polarization Dependent Cavity-Ringdown Spectroscopy

Richard Engeln, Giel Berden, and Gerard Meijer

Department of Molecular and Laser Physics, University of Nijmegen,  
Toernooiveld, 6525 ED Nijmegen, The Netherlands

In Fourier transform cavity-ringdown spectroscopy the demonstrated high sensitivity of the cavity-ringdown method is combined with the multiplex advantage of Fourier transform spectroscopy. In polarization dependent cavity-ringdown spectroscopy the advantages of polarization spectroscopy are used to improve the sensitivity and species selectivity of the cavity-ringdown method, as well as to extend the applicability of the cavity-ringdown method to the accurate and absolute measurement of polarization rotation. In this Chapter the operation principle of both techniques is described, and exemplified by measurements on the atmospheric band of molecular oxygen under various experimental conditions, as well as by measurements on transparent solid samples.

Since the first report on cavity-ringdown (CRD) absorption spectroscopy in 1988 by O'Keefe and Deacon [1], it was evident that this technique would hold great promise for measurements of either strong absorptions of species present in trace amounts or for measurements of weak absorptions of abundant species. By now, trace gas detection by means of CRD absorption spectroscopy has been demonstrated via the measurement of OH and CH<sub>3</sub> in flames and discharges [2, 3] and via the detection of trace amounts of atomic mercury vapour and ammonia in ambient air [4], to just name a few. Successful application of CRD for the measurement of absolute oscillator strengths of weak (forbidden) transitions of stable molecules has, for instance, been demonstrated on overtone transitions of HCN in the visible region of the spectrum [5] and on the Herzberg bands of molecular oxygen in the near UV [6, 7]. In Figure 1 a CRD absorption measurement of ambient air around 253.7 nm is shown, to explicitly demonstrate the use of CRD for trace gas detection (atomic mercury, known oscillator strength  $\Rightarrow$  density) and for measuring absolute oscillator strengths (molecular oxygen, known density  $\Rightarrow$  absorption cross section).

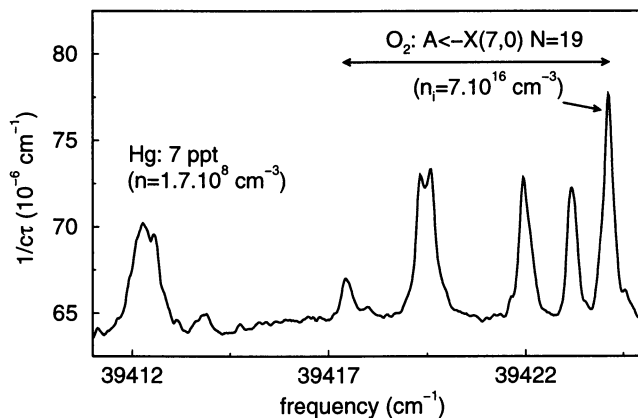


Figure 1: Cavity loss spectrum of ambient air around 253.7 nm measured in a 45 cm long cavity, using mirrors with a reflection coefficient of (only) 99.7 % (Reprinted with permission from [4]. Copyright 1996 American Institute of Physics).

Although CRD absorption spectroscopy is significantly more sensitive than 'conventional' absorption spectroscopy, in general it can not compete with background-free detection techniques like Laser Induced Fluorescence (LIF) or Resonance Enhanced Multi Photon Ionization (REMPI). However, both LIF and REMPI can only be sensitively applied under stringent experimental conditions. In a high pressure medium, for instance, the fluorescence can be quenched and ions are difficult to be detected. Alternatively, the laser excited states can have a low quantum yield for fluorescence and/or ionization. In these situations CRD absorption spectroscopy might be a viable alternative. For instance, the CRD technique has been used to determine predissociation lifetimes of the  $A^2\Sigma^+(v'=1)$  state of the SH radical [8] and to determine the rotational level dependent predissociation of  $OH(A^2\Sigma^+v'=3)$  [9]. In the latter experiment, the CRD absorption spectrum was measured simultaneously with the LIF excitation spectrum, and relative predissociation rates were determined from the ratio of the CRD to the LIF signal [9].

In other experiments, explicit use has been made of the pulsed nature of the CRD detection method, due to which the absorbing species only need to be present in the ringdown cavity for a short period of time. CRD is therefore well suited for absorption measurements in repetitive sources like pulsed molecular beams [10–13] and pulsed discharges [14], as well as for the study of dynamical processes via time-resolved absorption measurements [15]. In view of the limited duty cycle, the pulsed nature of the CRD detection method is actually a drawback when absorption measurements are performed on static samples; in a typical CRD experiment with a 10–50 Hz repetition rate laser and cavities with ring-down times of 1–50  $\mu$ s, one effectively measures only during a small fraction of the time. For this reason, as well as for the reason of compactness, the use of continuous (diode) lasers has



been experimented with in a variety of experimental schemes [16–18]. As in these experiments the spectral resolution is in principle only limited by the width of the longitudinal cavity modes [19], i.e. the spectral resolution can even be better than the band width of the laser, (extremely) high resolution CRD absorption spectroscopy can be performed in these cw-CRD detection schemes.

There is no intrinsic limitation to the spectral region in which CRD can be applied, provided mirrors with a sufficiently high reflectivity, detectors with a sufficiently fast time-response, and tunable (pulsed) light sources are available. The above mentioned detection of ammonia [4] and the detection of CO on the spin-forbidden Cameron band [20] showed the applicability of CRD spectroscopy down to 200 nm. Using a state-of-the-art narrow band tunable infrared laser system, Rakestraw and co-workers reported the first CRD experiment in the IR spectral region out to 3500 nm [21]. Using a free-electron laser, CRD absorption experiments were performed at even longer wavelengths, and the detection of ethylene in the 10–11  $\mu\text{m}$  region was demonstrated [22].

Although not at the focus of attention at first, CRD absorption can also be performed on transparent solid samples. An obvious way to proceed is to place a transparent solid sample, containing for instance a thin film of the material to be studied, at Brewster's angle in the ringdown cavity, thereby minimizing reflection losses. An approach that is experimentally found to be superior is to place the transparent solid sample in the cavity in such a way that all separate cavities are optically stable. Although there will be a significant reflection at each interface, these are not experienced as overall cavity losses; with a 1 mm thick Suprasil quartz window placed in the ringdown cavity, we found the losses per passage through the sample to be below  $3 \times 10^{-4}$  in the visible region of the spectrum, even though the reflection per surface is on the order of 4%. In many circumstances, the optical absorption in the solid will be spectrally rather broad, and the limited tuning range that the high reflectivity mirrors allow for (typically  $\pm 5\%$  of the central wavelength) make it difficult to distinguish the optical absorption from other broad band cavity loss mechanisms. A cavity that can be used over a spectrally broad range would be desired for these measurements [23].

Quantitative information is most readily extracted from the CRD measurements when the line width of the light source can be neglected relative to the width of the absorption line. If this is no longer valid, one can still extract the correct absorption coefficient from the measured transients, provided the spectral intensity distribution of the light source is known [4, 24, 25]. As a consequence, one does not necessarily need a narrow band laser to perform a CRD experiment. One might just as well use a polychromatic light source and extract the spectral information after spectrally dispersing the light exiting the cavity. For this the temporal shape of the ring down transient for a specific frequency (interval) has to be recorded and analyzed. A monochromator with suitable detector or a time-resolved optical multi-channel analyzer could for instance be used. Another possibility is to couple the polychromatic pulsed light exiting the cavity, into a Michelson interferometer. The time dependence of the ring down transient per frequency interval is found after Fourier transformation of the measured time dependence of the (spectrally in-

tegrated) ring down transients, recorded at well-defined interferometer arm length differences. In this so-called Fourier Transform - Cavity-Ringdown (FT-CRD) spectrometer the multiplex advantage of FT-spectrometers is therefore combined with the demonstrated sensitivity of the CRD absorption detection technique [26]. In the first part of this Chapter we detail the operation principle of this FT-CRD spectrometer.

In the second part of this Chapter we demonstrate that use can be made of the polarization state of the light in the cavity to further improve on the sensitivity and species selectivity of the cavity-ringdown absorption detection method. In addition, Polarization Dependent (PD) CRD extends the applicability of the cavity-ringdown method to the accurate measurement of polarization rotation [27]. In PD-CRD the *rate* of polarization rotation is measured which enables the polarization rotation to be measured on an absolute scale. We here demonstrate the use of PD-CRD in a study of the magneto-optic properties of the atmospheric band of molecular oxygen, i.e. we combine the advantages of magnetic rotation spectroscopy with those of the CRD detection method. Magnetic rotation spectroscopy [28, 29], in which magnetic circular dichroism and magnetic circular birefringence are measured, is a zero-background technique that is considerably more sensitive than direct single- or double-beam absorption. The technique is only sensitive for paramagnetic species, which is an advantage in case samples containing several species are studied. The sensitivity of the technique can in principle be increased by multi-passing through the sample as the polarization rotates further with each traversal, but multi-passing was often found to be limited by the deterioration of the degree of polarization with each mirror reflection. In PD-CRD spectroscopy, multi-passing in the ringdown cavity is used as well, but the detection scheme is such that the residual birefringence of the mirrors does not adversely affect the sensitivity of the measurement.

## Fourier Transform Cavity-Ringdown Spectroscopy

In a standard Fourier Transform absorption spectroscopy experiment, one uses a broad band light source in combination with a Michelson interferometer, and one records the intensity  $I(\Delta)$  of the light that passes through the interferometer as a function of the optical path length difference  $\Delta$ , between the two arms of the interferometer. The desired intensity as function of  $\nu$  is obtained by Fourier transformation of  $I(\Delta)$ . To detect the frequency and time dependence of a certain process simultaneously, time-resolved Fourier transform spectroscopy can be performed. In this case one detects the temporal dependence of the spectrally integrated intensity as a function of  $\Delta$ , i.e. one measures  $I(\Delta, t)$ . The time dependence of the intensity at frequency  $\nu$  ( $I(\nu, t)$ ) is obtained after Fourier transformation of  $I(\Delta, t)$ . Various FT spectrometers are equipped with the required hardware and software to move the mirrors of the interferometer in such a way that time-resolved FT-spectroscopy can be performed [30, 31].

In the FT-CRD spectrometer a time-resolved FT-spectroscopic measurement of the broad band light exiting a ringdown cavity is performed [26]. In this case

the measured quantity  $I(\Delta, t)$  is generally not an exponentially decaying function of time. After Fourier transformation of  $I(\Delta, t)$ , the ring down transient per frequency (interval),  $I(\nu, t)$ , is obtained. This can be written as  $I(\nu, t) = I(\nu, 0) \exp(-t/\tau(\nu))$  and  $\tau(\nu)$ , and thereby the absorption coefficient  $\kappa(\nu)$ , can be determined over the complete spectral range covered by the light source.

In a standard CRD experiment, in which a narrow band pulsed laser is used, the absorption information is deduced from the temporal shape of the ring down transient recorded at a certain frequency and is independent of the absolute intensity of the ring down signal. It suffices, therefore, to record normalized ring down transients at each laser frequency. In the FT-CRD spectrometer the absorption information is deduced from the temporal shape of the ring down transient that is now recorded as a function of the path-length difference  $\Delta$  in the interferometer. Also in this case it is sufficient to only record normalized transients. These transients  $I_{norm}(\Delta, t)$ , normalized to have the same maximum value at  $t = 0$  for all values of  $\Delta$ , can be written as

$$I(\Delta, t) = I_{norm}(\Delta, t) \times I(\Delta, 0) \quad (1)$$

The Fourier transform of the left-handed side of this expression yields the required  $I(\nu, t)$ , from which the absorption spectrum can be deduced. According to the convolution theorem of Fourier analysis, the Fourier transform of a product of two functions is identical to the convolution of their individual Fourier transforms. This implies that  $I(\nu, t)$  can also be obtained by taking the convolution of the Fourier transform of the normalized interferograms with the Fourier transform of  $I(\Delta, 0)$ . The latter is nothing else than the spectral intensity distribution of the light at the time it enters the ringdown cavity. So provided the spectral intensity distribution of the light source is known and is constant during the measurements, a measurement of  $I_{norm}(\Delta, t)$ , an intensity independent measurement, suffices to obtain the absorption spectrum. It is noted that also in the standard CRD experiment the spectral intensity distribution has to be known and has to be constant during the measurement to be able to extract accurate absolute absorption values [4, 24, 25].

**Experimental.** The FT-CRD spectrometer shown in Figure 2, consists of a Nd:YAG pumped broadband dye laser, which produces a 5 ns light pulse with an energy of 2 mJ over a spectral width of about  $400 \text{ cm}^{-1}$ . After passing through two pinholes, a light pulse with a spectral energy density of approximately  $1 \mu\text{J}/\text{cm}^{-1}$  is directed toward the ringdown cavity. The ringdown cavity is formed by two highly reflecting plano-concave mirrors, with a radius of curvature of  $-25 \text{ cm}$  and a reflectivity better than 0.999, placed 45 cm apart. No mode matching is performed to allow a near continuum of modes to build up in the cavity [2, 19, 32, 33]. The light that leaks out of the cavity is focused onto a multi-mode fiber and directed to the entrance port of the FT-spectrometer. The multi-exponentially decaying curves are measured at every mirror position  $\Delta$  with a photo multiplier tube, are amplified, and are digitized by means of a fast (10 ns) and deep (10 bits) oscilloscope. About 100 transients recorded at the same mirror position  $\Delta$  are summed

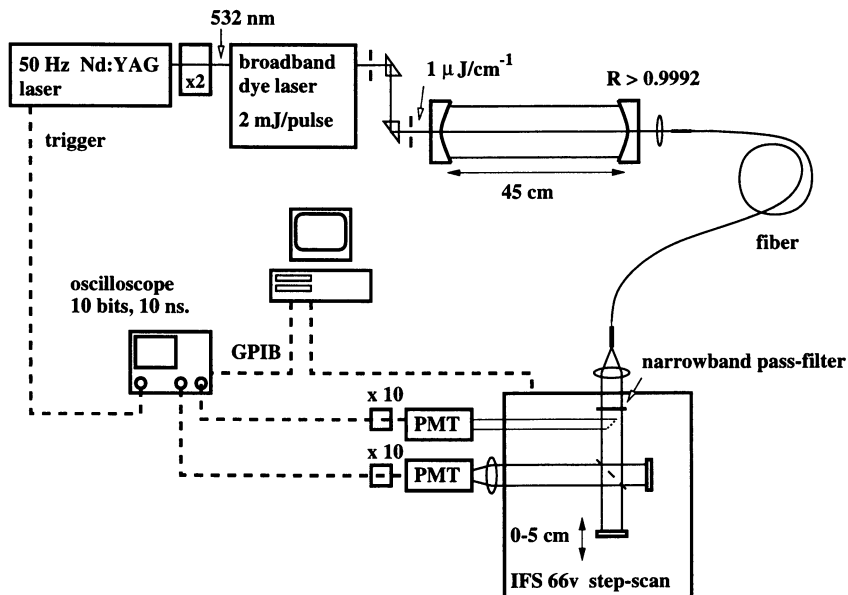


Figure 2: Schematic view of the FT-CRD spectrometer (Reprinted with permission from [26]. Copyright 1996 American Institute of Physics).

in the on-board memory of the oscilloscope to improve the measurement statistics. A PC controls the FT-spectrometer and reads out the averaged ring down transients from the oscilloscope. The data analysis involves the Fourier transformation of the interferograms measured at each time-point, and the determination of the decay time  $\tau$  at each frequency (interval) from the corresponding single exponentially decaying transients. Plotting  $1/c\tau$  versus frequency results in the cavity loss spectrum, i.e. the molecular absorption spectrum superimposed on a baseline, where the latter is determined by the finite mirror reflectivity and the length of the cavity.

In order to illustrate the working principle of the FT-CRD spectrometer, we performed an experiment using a light pulse with a spectral full-width at half-maximum of  $1.1 \text{ cm}^{-1}$ . In Figure 3a and 3c two interferograms are shown, measured at  $t = t_0$  and  $t = t_0 + 2\mu\text{s}$  (as depicted in the insets), after excitation of the ringdown cavity with this light pulse. The cell is filled with molecular oxygen, and the frequency of the laser is centered on the  $^P P_2(9)$  line of the spin-forbidden magnetic dipole  $b^1\Sigma_g^+(v''=0) \leftarrow X^3\Sigma_g^-(v''=0)$  transition. After Fourier transformation of  $I(\Delta, t_0)$ , the spectral intensity distribution of the light pulse at the beginning of the transient is obtained (Figure 3b). This spectral intensity distribution is mainly determined by the pulsed laser, although the molecular absorption that occurs during the first 100 ns can already be recognized. After  $2 \mu\text{s}$  the spectrum as shown in Figure 3d is obtained, in which the oxygen absorption is readily visible. Dividing these two spectra would be equivalent to a two-point CRD measurement. In the

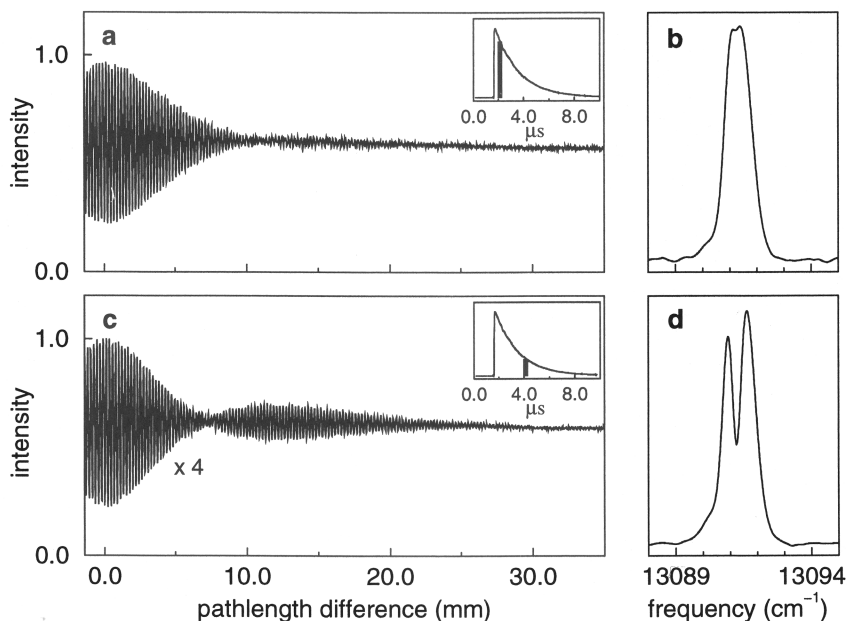


Figure 3: Interferograms, measured with the FT-CRD spectrometer depicted in Figure 2, taken at the beginning of the ring down transient (a) and after  $2 \mu\text{s}$  (c) with their corresponding Fourier transforms (resp. (b) and (d)). Note that the spectral full-width at half-maximum of the light pulse is only  $1.1 \text{ cm}^{-1}$  in this example (Reprinted with permission from [26]. Copyright 1997 American Institute of Physics).

actual experiments many time points are recorded and the frequency dependent absorption coefficient is determined using all these data points. In Figure 4 the FT-CRD spectrum of 15 mbar  $\text{O}_2$  in 1050 mbar  $\text{SF}_6$  is shown, after excitation of the cavity with a light pulse with a spectral FWHM of  $400 \text{ cm}^{-1}$ , centered around 763 nm. The complete vibrational band of molecular oxygen (the oxygen A band) is recorded at once using the multiplex CRD detection scheme. The baseline in the spectrum is again mainly determined by the non-resonant mirror losses, broadband scattering losses and the length of the cavity.

### Polarization Dependent Cavity-Ringdown Spectroscopy

In using a linearly polarized incoming beam in a CRD experiment, one becomes sensitive to rotation of the plane of polarization of the light upon passage through the cavity if a polarization selective optical element is present in front of the detector. With a polarization analyzer that selects radiation polarized parallel to that of the incoming beam placed in front of the light detector, in addition to the 'normal' absorption, rotation of the plane of polarization in the ringdown cavity

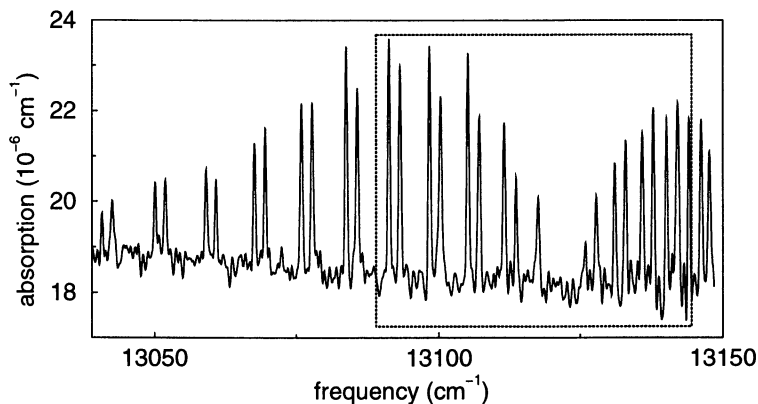


Figure 4: Absorption spectrum of 15 mbar O<sub>2</sub> in 1050 mbar SF<sub>6</sub> around 763 nm recorded with the FT-CRD spectrometer shown in Figure 2 (Reprinted with permission from [26]. Copyright 1997 American Institute of Physics).

will be detected as an apparent absorption, i.e. as a shortening of the ring down time. With the analyzer rotated (almost) 90 degrees [in order to maintain single exponentially decaying transients for either polarization direction, the crossed polarizer configuration has to be avoided [27]] relative to the plane of polarization of the incoming beam, there will still be shortening of the cavity decay time due to absorption but optical rotation will cause a time-dependent *increase* in the detected signal, i.e. it will appear as an apparent lengthening of the ring down time. When both signals are measured simultaneously, one can discriminate between the effects of absorption and optical rotation [27].

There are two different effects that can lead to polarization rotation. First, if there is a preferred direction in the medium, the absorptions can depend on the angle that the plane of polarization of the incoming beam makes with this preferred direction. Such polarization dependent absorptions will lead to an effective rotation of the plane of polarization (dichroism). Second, the plane of polarization can rotate due to dispersion, i.e. due to different velocities for different polarization directions (birefringence). In an external magnetic field molecular oxygen will cause rotation of the plane of polarization due to both magnetic dichroism and due to magnetic birefringence [29, 34]. One distinguishes two experimental configurations, one in which the magnetic field is perpendicular to the propagation direction of the light (Voigt configuration) and one in which the magnetic field is parallel to the propagation direction of the light (Faraday configuration). In the following, the PD-CRD experiment is described in either configuration [27].

**The Voigt Configuration.** In the Voigt configuration a homogeneous magnetic field  $\vec{B}$  is applied perpendicular to the axis of the cavity over a length  $l$ . The plane of polarization of the incoming laser beam makes an angle  $\phi_B$  with the direction of the magnetic field. In the magnetic field we distinguish between ab-

sorptions induced by light that is either polarized parallel or perpendicular to the magnetic field, having absorption coefficients  $\kappa_{\parallel}(\nu)$  and  $\kappa_{\perp}(\nu)$ , respectively. Similarly, a distinction is made between the refractive index for light that is polarized either parallel ( $n_{\parallel}(\nu)$ ) or perpendicular ( $n_{\perp}(\nu)$ ) to the magnetic field. The light exiting the cavity is split into two mutually orthogonal polarization directions by an analyzer which is placed at an angle  $\phi_D$  with respect to the polarizer.

If the time-dependence of the light intensity along two mutually orthogonal polarization directions is measured simultaneously, the difference between the cavity losses measured for either direction is given by [27]

$$\frac{1}{c\tau_{\phi_D}(\nu)} - \frac{1}{c\tau_{\phi_D+90^\circ}(\nu)} = \frac{l \sin(2\phi_D)}{d \sin(2\phi_D)} [\kappa_{\parallel}(\nu) - \kappa_{\perp}(\nu)] \quad (2)$$

and this quantity can be accurately experimentally determined. Compared to 'conventional' CRD absorption spectroscopy there is a gain in intensity due to the factor  $\sin(2\phi_D)$  in the denominator, and there is a sign-difference between absorptions polarized parallel or perpendicular to the external magnetic field. In addition, it is experimentally found that the 'noise' in the spectrum of  $1/c\tau(\nu)$  versus frequency, noise that is probably associated with variations of the mode structure in the cavity, is largely identical for either polarization direction. Therefore the remaining noise in the difference signal is largely reduced.

**The Faraday Configuration.** In the Faraday configuration a homogeneous magnetic field  $\vec{B}$  is applied parallel to the axis of the cavity over a length  $l$ . The linearly polarized incoming laser beam is now to be viewed as the sum of equal amounts of right- and left-circularly polarized light. In the magnetic field we distinguish between absorptions induced by either one of the circularly polarized components, having absorption coefficients  $\kappa_+(\nu)$  and  $\kappa_-(\nu)$ , respectively. Similarly, a distinction is made between the refractive indices  $n_+(\nu)$  and  $n_-(\nu)$  for right- and left-circularly polarized light. If the time-dependence of the light intensity along two mutually orthogonal polarization directions is measured simultaneously, the difference between the values for  $1/c\tau(\nu)$  found for the two directions is solely determined by the dispersion term, and is given by [27]:

$$\frac{1}{c\tau_{\phi_D}(\nu)} - \frac{1}{c\tau_{\phi_D+90^\circ}(\nu)} = \frac{2\omega l}{cd \sin(2\phi_D)} [n_+(\nu) - n_-(\nu)] \quad (3)$$

In this set-up one is therefore selectively sensitive to polarization rotation, a quantity that can not be measured in 'conventional' CRD spectroscopy. Similar to the situation in CRD absorption spectroscopy, where the *rate* of absorption is measured, in PD-CRD spectroscopy the *rate* of optical rotation is measured, and this enables the optical rotation to be put on an absolute scale.

**Experimental.** The experimental set-up for the PD-CRD experiment is schematically shown in Figure 5. Before the light enters the cavity, it passes through a Glan-Thompson (GT) polarizer, to better define the degree of linear polarization

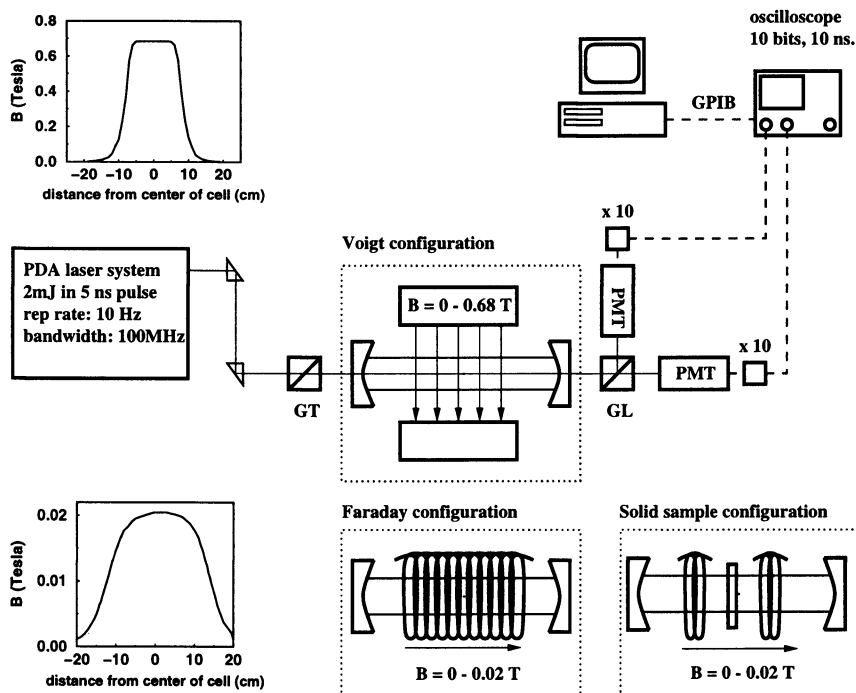


Figure 5: Schematic view of the PD-CRD setup (Reprinted with permission from [27]. Copyright 1997 American Institute of Physics).

of the light. In the Voigt configuration, the polarizer is used to define the angle  $\phi_B$  between the polarization direction of the light and the direction of the magnetic field. The light exiting the cavity is sent through a second polarizer (Glan-Laser, GL), split into its two mutually orthogonally polarized components, and measured with two identical photo multiplier tubes (PMT). The axis of the analyzer can be oriented relative to the polarization direction of the incoming beam to define the angle  $\phi_D$ .

The spin-forbidden  $b^1\Sigma_g^+(v'=2) \leftarrow X^3\Sigma_g^-(v''=0)$  magnetic dipole transition of molecular oxygen around 628 nm (the oxygen  $\gamma$ -band) is used to demonstrate the possibility of selectively measuring either the polarization dependent absorption (Voigt configuration) or the resonant magneto-optical rotation (Faraday configuration). In Figure 6 the PD-CRD spectra of the  $^P P_1(1)$  transition are shown, measured with 400 mbar of  $O_2$  in the cell, and a magnetic field of 0.68 T perpendicular to the cavity axis (Figure 6a and 6b) and with a magnetic field of 0.02 T parallel to the cavity axis (Figure 6c and 6d). In Figure 6a the cavity loss spectra as recorded for two mutually perpendicular polarization directions are shown. In this measurement the angle  $\phi_B$  is set to  $45^\circ$ , and the polarization components that are almost perpendicular (upper trace;  $\phi_D = 95^\circ$ ) and almost parallel (lower trace;  $\phi_D = 5^\circ$ ) to the polarization of the incoming beam are detected. The two spectra



contain information on both the polarization independent and the polarization dependent absorptions. In Figure 6b the difference between the spectra for the mutually orthogonal polarization directions is shown. This difference spectrum shows only the polarization dependent absorptions, as described in Equation 2, taking  $\phi_D = 5^\circ$ . The three individual  $\Delta M$  components in the 0.68 T field are

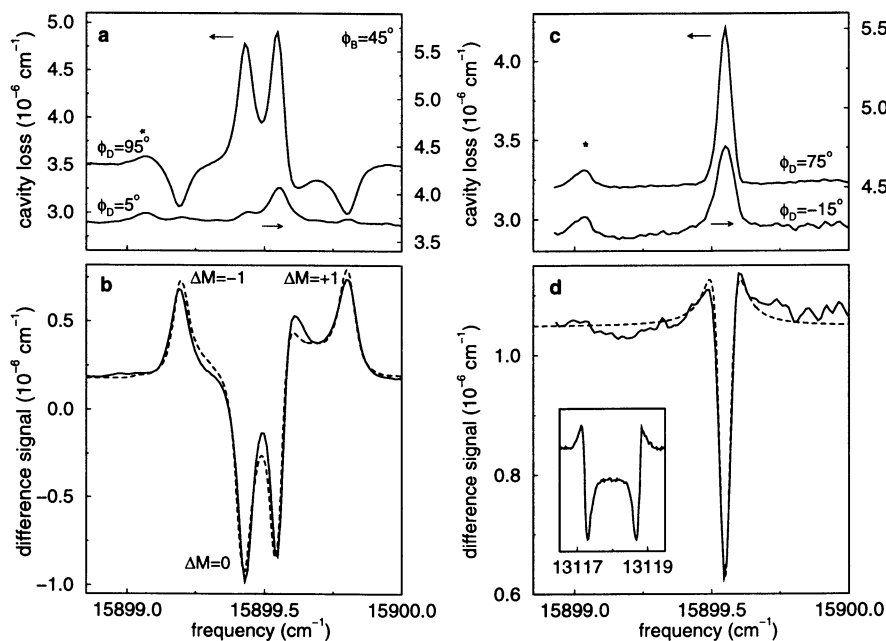


Figure 6: The PD-CRD spectra of the  $P_1(1)$  line of the  $\gamma$ -band of 400 mbar  $^{16}\text{O}_2$  in the Voigt (a,b, at 0.68 T) and the Faraday (c,d at 0.02 T and in the inset the same line of the A-band at 1.5 T) configuration. The line marked with an asterisk is due to water absorption (Reprinted with permission from [27]. Copyright 1997 American Institute of Physics).

indicated as such in the Figure. The additional structure located close to the frequency of the field-free position is due to transitions in the fringe fields of the magnet. As the  $M=0$  component shows a quadratic Zeeman-shift, the  $\Delta M = 0$  transition in the fringe fields causes a sharp peak rather than being smeared out over a wide spectral range, as is the case for the  $\Delta M = \pm 1$  components. Using the calculated Zeeman-shift of the  $\Delta M$  components, the measured strength of the magnetic field along the cavity axis as shown in Figure 5, and the known Doppler and pressure broadening of  $\text{O}_2$  in the room temperature cell, the observed difference spectrum can be quantitatively reproduced, as shown with the dashed line in Figure 6b. The absence of the water absorption peak (indicated with an asterisk) from the difference spectrum explicitly demonstrates the species-selectivity of the

PD-CRD detection scheme. It is seen in Figure 6b that the baseline of the difference spectrum is not exactly zero, implying that there is a difference in lifetime for light polarized in mutually orthogonal directions. This difference is caused by the residual birefringence of the mirrors, which, although causing this offset, hardly influences the detection sensitivity in the PD-CRD scheme [nowadays, dielectrically coated mirrors with extremely low residual birefringence can be produced [35, 36]]. It is important, however, to select mirrors that do not deteriorate the 'purity' of the polarization state of the light inside the cavity upon multiple reflections.

The noise-equivalent absorption detection limit in the difference spectrum in Figure 6b is found to be around  $3 \times 10^{-9} \text{ cm}^{-1}$ , i.e. around  $10^{-3}$  of the overall cavity losses. This is at least a factor three better than in the CRD spectra of the individual polarization components, due to cancellation of systematic 'noise'. Relative to CRD absorption spectra taken with  $\phi_B = 45^\circ$  but without polarization selection in the detection step, there is an additional gain in sensitivity with a factor  $2/\sin(2\phi_D)$ , i.e. a factor 11.5 for  $\phi_D = 5^\circ$ . So apart from the species-selectivity and the advantage of getting a sign-difference between absorptions polarized parallel or perpendicular to the external magnetic field, there is a demonstrated overall gain in sensitivity of more than a factor 30 in PD-CRD spectroscopy compared to 'conventional' CRD absorption spectroscopy for this specific line in molecular oxygen.

In Figure 6c the cavity loss spectra in the Faraday configuration as recorded for two mutually perpendicular polarization directions, i.e. for the polarization components that are almost perpendicular (upper trace;  $\phi_D = 75^\circ$ ) and almost parallel (lower trace;  $\phi_D = -15^\circ$ ) to the plane of polarization of the incoming beam, are shown. The two spectra contain information on both the polarization (in)dependent absorptions, as well as on the optical rotation. In the low magnetic field employed the individual  $\Delta M$  components are no longer resolved. Only the  $M$ -changing transitions can occur in the Faraday configuration. In Figure 6d the difference between the spectra for the mutually orthogonal polarization directions is shown. This spectrum solely shows the optical rotation, as described in Equation 3, taking  $\phi_D = -15^\circ$ . The observed difference spectrum can again be quantitatively reproduced in a simulation (dashed curve) in which the difference of the dispersion curves for the  $\Delta M = +1$  and  $\Delta M = -1$  components, obtained via the Kramers-Kronig relations, is taken to be responsible for the observed signal. In the inset of Figure 6d the PD-CRD measurement of the same rotational transition in the oxygen A-band is shown in a magnetic field of 1.5 T, in which case the individual dispersion curves are completely resolved. The peak intensity of the difference signal corresponds to a polarization rotation of  $1.6 \times 10^{-7} \text{ rad./cm}$ . The absolute value for the difference  $[n_+(\nu) - n_-(\nu)]$  in refractive indices can be determined from this spectrum. From the spectrum a noise-equivalent polarization rotation of around  $10^{-8} \text{ rad./cm}$ , corresponding to an absolute polarization rotation of approximately  $1.5 \times 10^{-5}$  degree per passage through the sample is deduced for the setup depicted in Figure 5.

Apart from studying electro-optic and magneto-optic phenomena on gas phase species, the PD-CRD technique is applicable to the study of optical rotation of

transparent solid samples as well. The polarization rotation per passage as deduced from a PD-CRD measurement on a 2 mm thick BK7 sample is determined as a function of the magnetic field in the Faraday configuration [27]. For this measurement, the coils producing the magnetic field, the first polarizer and the CRD cell with the sample are placed inside a vacuum tank, in order to avoid interferences with ambient air. The difference in cavity loss for the two mutually orthogonal polarization directions is measured as function of the magnetic field at a wavelength of 618.8 nm. The rotation is deduced using Equation 3 and  $\phi_D = -15^\circ$ . From the fit through the data points the Verdet constant of BK7 is determined to be  $5.36 \text{ rad T}^{-1} \text{ m}^{-1}$  ( $= 1.84 \times 10^4 \text{ min of arc T}^{-1} \text{ m}^{-1}$ ), which is in good agreement with values quoted for the Verdet constant of glasses as reported in textbooks. Only magnetic fields up to a few mT could be used, since higher fields caused the transient to significantly deviate from single exponentially decaying functions.

In the Faraday configuration one can alternatively use either right-handed ( $\sigma^+$ ) or left-handed ( $\sigma^-$ ) circularly polarized light to perform a 'conventional' CRD experiment, i.e. without polarization selection in the detection step, to selectively measure  $\kappa_+(\nu)$  or  $\kappa_-(\nu)$  to reach a simplification of complex spectra. Such an experiment is complementary to the PD-CRD experiment, in which the difference in refractive indices is measured. In Figure 7a,b, and d three CRD absorption spectra of molecular oxygen in a magnetic field of 20 Tesla, using different polarization states of the light, are shown. The different spectra are measured using right-circularly (a), left-circularly (b), and linearly (d) polarized light. The spectral region shown is the same as the spectral region indicated in Figure 4 with the dashed box, i.e. the spectral region around the center of the oxygen A-band. The spectra are measured using a tunable pulsed dye laser (line width  $0.07 \text{ cm}^{-1}$ ) and a ringdown cavity of only 3 cm length, filled with 0.5 bar of oxygen, placed inside a Bitter magnet (Berden, G.; Engeln, R.; Christianen, P.; Maan, J.C.; Meijer, G. *J. Chem. Phys.*, submitted). The magnetic field is homogeneous within 1 % over the length of the cavity.

The sum of the spectra measured with right- and left-handed circularly polarized light (Figure 7c) should be identical to the spectrum measured with linearly polarized light, but although all features can be found in both spectra, it is seen that the intensity of strong features which arise *solely* from  $\Delta M = +1$  or  $\Delta M = -1$  transitions are underestimated in the spectrum measured with linearly polarized light. This is an experimental artefact that can be understood by realizing that at such a transition only one of the circularly polarized components can be absorbed, while the other is not affected at all. Since the transient measured at the exit of the cavity is fitted to a single exponential curve, this will result in an overestimate of the decay time, and thus an underestimate of the absorption. A comparable effect occurs when the band width of the light source is larger than the line width of the absorption [4, 24].

Although care has to be taken in the interpretation of the spectra obtained with linearly polarized light, it is evident from the spectra shown, that the polarization states are well-defined inside the cavity, and that the spectra simplify and are distinctly different in going from linearly to circularly polarized light.

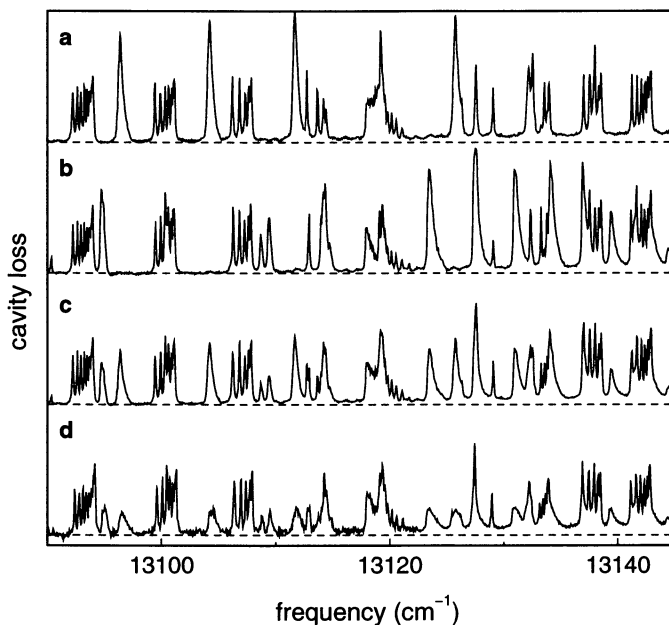


Figure 7: CRD spectra of the  $b^1\Sigma_g^+(v' = 0) \leftarrow X^3\Sigma_g^-(v'' = 0)$  transition of molecular oxygen measured in a magnetic field of 20 T (Faraday setup) for different polarization of the laser light (right-handed (a) and left-handed (b) circularly polarized light, the sum of the spectra shown in (a) and (b) divided by 2 (c), and linearly polarized light (d)). The dashed box in Figure 4 indicates the same spectral region measured in zero magnetic field.

## Summary

Cavity-Ringdown spectroscopy has sufficiently matured by now that implementation of this superior absorption detection method in a variety of existing spectroscopic techniques is to be expected. We here demonstrated the successful combination of CRD spectroscopy with FT absorption spectroscopy to perform multiplex absorption spectroscopy with an improved detection sensitivity. The combination of CRD with polarization spectroscopy is shown to be a sensitive technique for absorption studies of paramagnetic species. In addition, PD-CRD spectroscopy extends the applicability of CRD spectroscopy to the sensitive and absolute measurement of polarization rotation. In magneto- and electro-optics the polarization rotation per pass through a linear cavity adds up, due to the presence of a preferred direction in space. If the laser beam is always made to pass through a sample in the same direction, for instance by using a ring-cavity, the PD-CRD technique is expected to offer unique possibilities for the study of optically active molecules and their complexes in the gas-phase.

## Acknowledgments

The authors like to thank all co-workers who have contributed to the work presented in this chapter, especially R. Jongma, H. Naus, E. van den Berg, G. von Helden, M. Boogaarts, and I. Holleman. This work is part of the research program of the 'Stichting voor Fundamenteel Onderzoek der Materie (FOM)', which is financially supported by the 'Nederlandse Organisatie voor Wetenschappelijk Onderzoek (NWO)', and receives direct support by the NWO via PIONIER-grant # 030-66-89.

## Literature Cited

- [1] O'Keefe, A.; Deacon, D.A.G. *Rev. Sci. Instrum.* **1988**, *59*, 2544.
- [2] Meijer, G.; Boogaarts, M.G.H.; Jongma, R.T.; Parker, D.H.; Wodtke, A.M. *Chem. Phys. Lett.* **1994**, *217*, 112.
- [3] Zalicki, P.; Ma, Y.; Zare, R.N.; Wahl, E.H.; Dadamio, J.R.; Owano, T.G.; Kruger, C.H. *Chem. Phys. Lett.* **1995**, *234*, 269.
- [4] Jongma, R.T.; Boogaarts, M.G.H.; Holleman, I.; Meijer, G. *Rev. Sci. Instrum.* **1995**, *66*, 2821.
- [5] Romanini, D.; Lehmann, K.K. *J. Chem. Phys.* **1993**, *99*, 6287.
- [6] Huestis, D.L.; Copeland, R.A.; Knutsen, K.; Slinger, T.G.; Jongma, R.T.; Boogaarts, M.G.H.; Meijer, G. *Can. J. Phys.* **1994**, *72*, 1109.
- [7] Slinger, T.G.; Huestis, D.L.; Cosby, P.C.; Naus, H.; Meijer, G. *J. Chem. Phys.* **1996**, *105*, 9393.
- [8] Wheeler, M.D.; Orr-Ewing, A.J.; Ashfold, M.N.R.; Ishiwata, T. *Chem. Phys. Lett.* **1997**, *268*, 421.
- [9] Spaanjaars, J.J.L.; ter Meulen, J.J.; Meijer, G. *J. Chem. Phys.* **1997**, *107*, 2242.
- [10] O'Keefe, A.; Scherer, J.J.; Cooksy, A.L.; Sheeks, R.; Heath, J.; Saykally, R.J. *Chem. Phys. Lett.* **1990**, *172*, 214.
- [11] Scherer, J.J.; Paul, J.B.; Collier, C.P.; Saykally, R.J. *J. Chem. Phys.* **1995**, *102*, 5190.
- [12] Boogaarts, M.G.H.; Meijer, G. *J. Chem. Phys.* **1995**, *103*, 5269.
- [13] Paul, J.B.; Scherer, J.J.; Collier, C.P.; Saykally, R.J. *J. Chem. Phys.* **1996**, *104*, 2782.
- [14] Kotterer, M.; Maier, J.P. *Chem. Phys. Lett.* **1997**, *266*, 342.
- [15] Yu, T.; Lin, M.C. *J. Am. Chem. Soc.* **1993**, *115*, 4371.
- [16] Engeln, R.; von Helden G.; Berden, G.; Meijer, G. *Chem. Phys. Lett.* **1996**, *262*, 105.
- [17] Romanini, D.; Kachanov, A.A.; Sadeghi, N.; Stoeckel, F. *Chem. Phys. Lett.* **1997**, *264*, 316.
- [18] Paldus, B.A.; Harris, J.S.; Martin, J.; Xie, J.; Zare, R.N. *J. Appl. Phys.* **1997**, *82*, 3199.
- [19] Lehmann, K.K.; Romanini, D. *J. Chem. Phys.* **1996**, *105*, 10263.

- [20] Jongma, R.T.; Boogaarts, M.G.H.; Meijer, G. *J. Mol. Spectrosc.* **1994**, *165*, 303.
- [21] Scherer, J.J.; Voelkel, D.; Rakestraw, D.J.; Paul, J.B.; Collier, C.P.; Saykally, R.J.; O'Keefe, A. *Chem. Phys. Lett.* **1995**, *245*, 273.
- [22] Engeln, R.; van den Berg, E.; Meijer, G.; Lin, L.; Knippels, G.M.H.; van der Meer, A.F.G. *Chem. Phys. Lett.* **1997**, *269*, 293.
- [23] Pipino, A.C.R.; Hudgens, J.W.; Huie, R.E. *Rev. Sci. Instrum.* **1997**, *68*, 2978.
- [24] Zalicki P.; Zare, R.N. *J. Chem. Phys.* **1995**, *102*, 2708.
- [25] Hodges, J.T.; Looney, J.P.; van Zee, R.D. *Applied Optics* **1996**, *35*, 4112.
- [26] Engeln, R.; Meijer, G. *Rev. Sci. Instrum.* **1996**, *67*, 2708.
- [27] Engeln, R.; Berden, G.; v.d. Berg, E.; Meijer, G. *J. Chem. Phys.* **1997**, *107*, 4458.
- [28] Buckingham, A.D.; Stephens, P.J. *Ann. Rev. Chem.*, **1966**, *17*, 399.
- [29] Brecha, R.J.; Pedrotti, L.M.; Krause, D. *J. Opt. Soc. Am. B*, **1997**, *14*, 1921, and references therein.
- [30] Hartland, G.V.; Xie W.; Dai, H-L. *Rev. Sci. Instrum.* **1992**, *63*, 326.
- [31] Preses, J.M.; Hall, G.E.; Muckerman, J.T.; Sears, T.J.; Weston, Jr. R.E.; Guyot, Ch.; Hanson, J.C.; Flynn, G.W.; Bernstein, H.J. *Rev. Sci. Instrum.* **1995**, *64*, 95.
- [32] Hodges, J.T.; Looney, J.P.; van Zee, R.D. *J. Chem. Phys.* **1996**, *105*, 10278.
- [33] Martin, J.; Paldus, B.A.; Zalicki, P.; Wahl, E.H.; Owana, T.G.; Harris, J.S.; Kruger, C.H.; Zare, R.N. *Chem. Phys. Lett.* **1996**, *258*, 63.
- [34] Takubo, Y.; Muroo, K.; Miwa, S.; Yamamoto, K.; Suzuki, K.; Yamamoto, M. *J. Mol. Spectrosc.* **1996**, *178*, 31.
- [35] Moriwaki, S.; Sakaida, H.; Yuzawa, T.; Mio, N. *Appl. Phys. B*, **1997**, *65*, 347.
- [36] Brandi, F.; Della Valle, F.; De Riva, A.M.; Micossi, P.; Perrone, F.; Rizzo, C.; Ruoso, G.; Zavattini, G. *Appl. Phys. B*, **1997**, *65*, 351.

## Infrared Cavity-Ringdown Laser Absorption Spectroscopy of Transient Species in Pulsed Supersonic Expansions

J. B. Paul, R. A. Provencal, C. Chapo, E. Michael,  
A. Pettersson, and R. J. Saykally

Department of Chemistry, University of California,  
Berkeley, CA 94720-1460

Infrared Cavity Ringdown Laser Absorption Spectroscopy (IRCRLAS) has been developed using simple and reliable Raman-shifted dye lasers. The robust and economical system presented here currently provides continuous spectral coverage to wavelengths exceeding 7  $\mu\text{m}$ , with a sensitivity of 1-2 ppm fractional absorption per pass. Results from the application of this technique to the study of a variety of transient molecules produced in supersonic expansions, including water clusters, carbon clusters, molecular ions, and isolated and solvated small biomolecules will be presented.

Following the pioneering studies made by O'Keefe and coworkers (1,2), cavity ringdown laser absorption spectroscopy (CRLAS) has become quite widely used as a new tool for measurement of trace species in gaseous environments. Presently, the types of trace species probed by CRLAS methods in our laboratory include pure metal clusters, metal silicides, molecular ions, and radicals in flames and plasmas, as described in several recent reviews (3,4). The promise of this new method for ultrasensitive trace gas analysis seems very high.

Scherer *et al.* have successfully extended this technique into the mid-IR (5). This work was carried out with high resolution OPO/OPA laser systems, employing state-of-the-art laser developments. Several IR studies employing CRLAS have followed, including the novel use of a free electron laser as a light source (6,7). At Berkeley, we have recently developed a simple (albeit lower resolution) approach that exploits efficient Raman shifting of a commercial pulsed dye laser as a convenient, reliable, and broadly tunable light source in the vibrational IR. Paul *et al.* (8) have used this system to measure the O-H and O-D stretching vibrations of  $(\text{H}_2\text{O})_n$  and  $(\text{D}_2\text{O})_n$  clusters (9,10), characterizing the O-D motions for the first time. More recently Provencal *et al.* (11) have measured IR-CRLAS spectra of jet cooled carbon clusters, Chapo *et al.* (12) have measured vibrational spectra of nucleotide bases and amino acids complexed with water.

We have acquired several sets of high quality mirrors (Laser Power Optics, Inc.) covering a significant region of the infrared spectrum. The experimentally measured mirror curves are shown in Figure 1, along with the operating range of the laser dyes employed to generate the fundamental radiation. When pumped with the

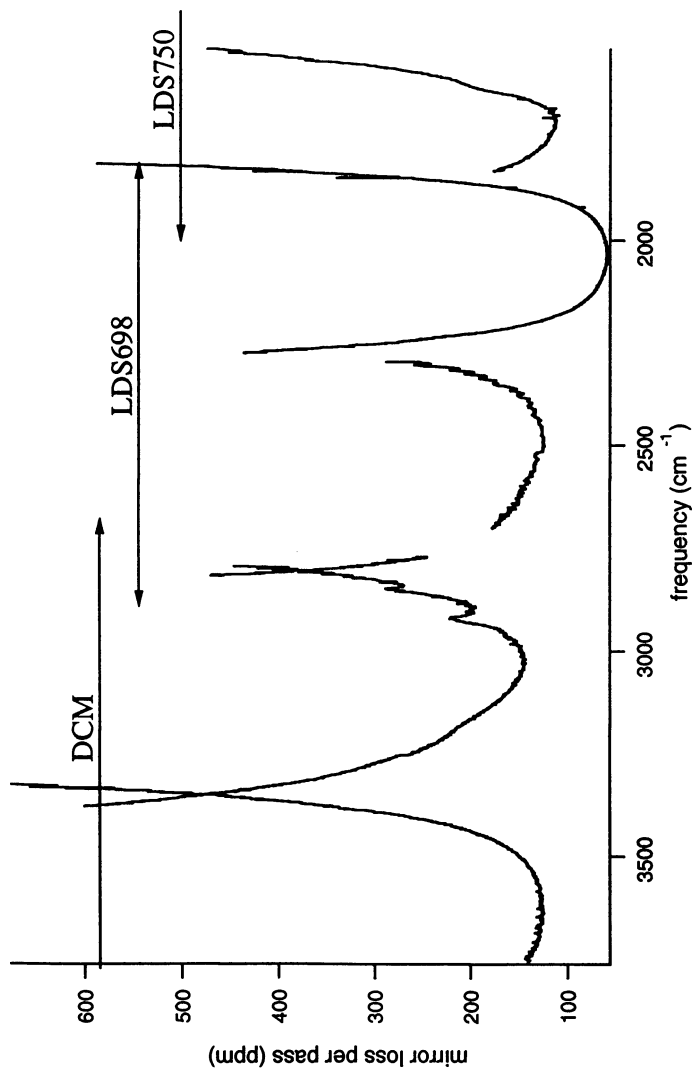


Figure 1. The experimentally measured total intensity loss per mirror is shown for the IR cavity mirrors presently in our possession. Note that these mirrors are all of excellent quality, providing more than adequate reflectivity for use in cavity ringdown experiments. The manufacturer of these optics (Laser Power Optics) indicates that extending our coverage beyond  $10\ \mu\text{m}$  is not a problem in terms of the availability of these mirrors. Also, note the relatively few number of laser dyes needed to cover this fairly large portion of the infrared region ( $>2000\ \text{cm}^{-1}$ ).



second harmonic of a Nd:YAG laser, these dyes are very efficient and have long lifetimes. The relatively few number of dyes needed to cover these regions of the spectrum results in few time consuming dye changes. The Raman shifter consists of a 3.5 m Herriot cell effecting 17 periodically refocused passes through 14 atm of H<sub>2</sub>. A dye-laser output of 30-40 mJ generates 0.5-1 mJ of IR radiation in the third Stokes band, providing a constant frequency shift of the fundamental of 12,465.9 cm<sup>-1</sup>. The ringdown signal is obtained by focusing the light leaving the cavity onto an InSb detector. The detector output is amplified, digitized, and averaged for 20 shots/wavelength. We must caution researchers attempting to use Raman shifting in conjunction with cavity ringdown to carefully filter out additional frequencies produced in the Raman shifter, primarily from rotational Stokes and anti-Stokes lines. These frequencies, spaced roughly 600 cm<sup>-1</sup> to either side of the vibrational fundamental, will not generally be attenuated by the cavity, and can easily damage the fragile detector element.

Additionally, we are developing a novel high resolution version of this IR-CRLAS experiment, which could entirely replace the cumbersome technology of diode lasers, color center lasers, and difference frequency lasers that are currently used for sensitive trace gas analysis. A high power (80 mJ) ultra-narrowband alexandrite laser (40 MHz) will produce tunable pulsed radiation in the 710-800 nm region which will be Raman shifted into the IR. By combining 1st and 2nd order Stokes Scattering in high pressure gas cells containing H<sub>2</sub> and D<sub>2</sub>, we can theoretically cover the entire spectrum (ca. 1000 cm<sup>-1</sup> to UV) quite conveniently. This novel laser source will be used for studies of new species that have eluded characterization thus far. These include important molecular ions (CH<sub>5</sub><sup>+</sup>, H<sub>3</sub>O<sup>+</sup>(H<sub>2</sub>O)<sub>n</sub>, SiH<sub>5</sub><sup>+</sup>), cyclic carbon clusters, and polypeptides.

## Recent Applications

**Water Clusters.** The study of the mid-IR O-H and O-D stretching vibrations in water clusters demonstrates two powerful advantages of IR-CRLAS relative to other spectroscopic methods: the ability to record accurate absorption intensity information over large regions of the spectrum, and the ability to access wavelength regions that have proven difficult for most other techniques. Figure 2 shows the absorption spectrum of water clusters in a supersonic expansion as a function of increasing source backing pressure. The small water clusters appear to grow in sequentially with cluster size as the pressure is raised. From this data, and *ab initio* integrated band intensities, we have estimated the concentrations of water clusters in the expansion, which are given in Figure 3. Additionally, these studies allowed us to assign an absorption feature to an O-H stretching band of the water hexamer for the first time. This feature occurs close in frequency to a band assigned to benzene-(H<sub>2</sub>O)<sub>6</sub> by Zwier et al.(13) Finally, we observed a very broad feature (~400 cm<sup>-1</sup>) that appeared at even higher backing pressures. The contour of this absorption was observed to change from one resembling that of liquid water, to that of amorphous ice as the mean cluster size grew as a function of applied backing pressure. The cluster size range of the clusters contributing to this feature was estimated to be between 1000-5000 water molecules per cluster, which is certainly large enough to exhibit bulk-like behavior. Hence, the similarity of our cluster spectra with that of ice grown in the laboratory by depositing water vapor on a cryogenic substrate (4 - 100 K) is not surprising.

While much of the spectra discussed above has been observed previously using a variety of techniques (14-17), the corresponding spectra of the fully deuterated isotopomers have remained uncharacterized primarily due to limitations in the available light sources. The use of IR-CRLAS greatly reduces the demands placed on

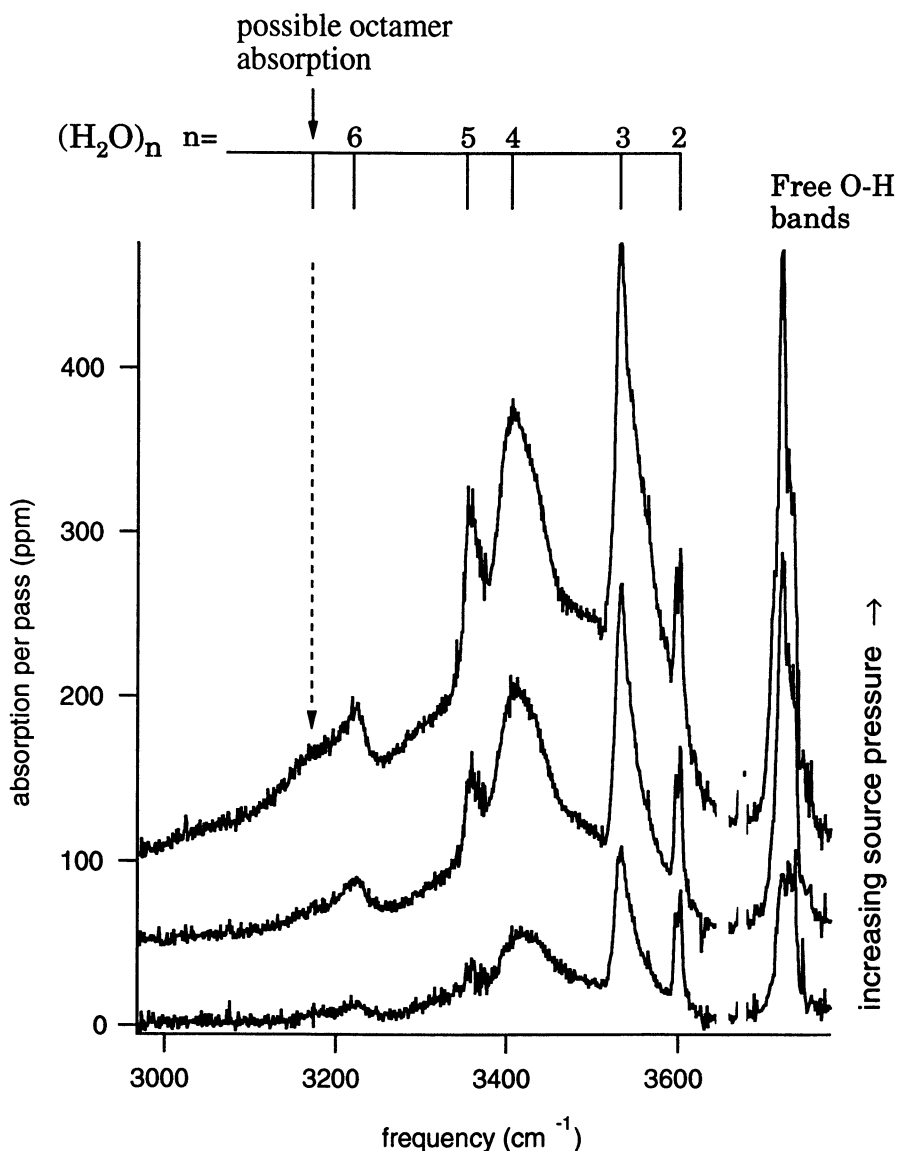


Figure 2. The cavity ringdown absorption spectrum of small jet-cooled water clusters measured in the O-H stretching region. The inherent ability of the ringdown method to accurately measure intensity information across broad regions of the spectrum allows us to quantify changes in the cluster distribution with changes in the expansion conditions. In some cases, such as for the hexamer absorption shown here, this can lead to spectral carrier assignments.

## Density of small water clusters ~1 cm from slit orifice

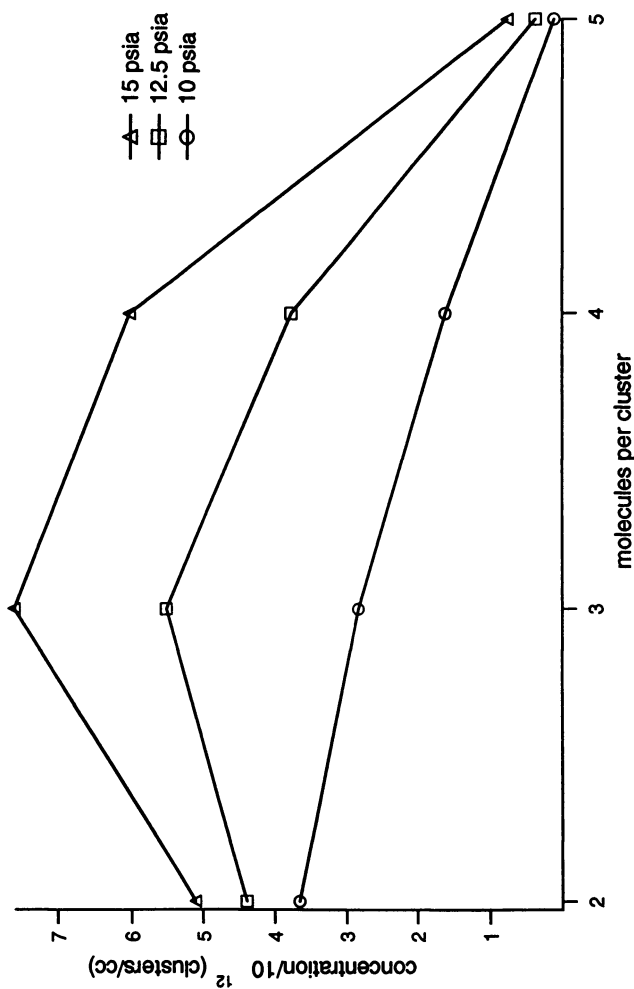


Figure 3. *Ab initio* absorption cross-sections were used along with the measured integrated band intensities to determine the absolute concentrations of water clusters produced in the supersonic expansion. These results show that the trimer is the most abundant species in the expansion under these conditions.

the light source, providing easy access to this spectral region with our Raman-shifted dye laser. The spectrum of D<sub>2</sub>O clusters is shown in Figure 4. While much of these data remain to be analyzed, we have presented a detailed analysis of the hydrogen-bond-acceptor anti-symmetric stretching vibration(10). In Figure 5, a portion of this spectrum is shown, in which a two-fold splitting of the spectral features is clearly observed, which arises from a quantum tunneling motion known as "acceptor tunneling". By assuming an adiabatic between the intra-molecular stretching coordinate excited by the absorption event, and the inter-molecular tunneling coordinate, an improved picture of the tunneling dynamics in both the ground and excited states was established.

**Carbon Clusters and Other Laser Vaporized Species.** Nearly all spectroscopic studies of gaseous carbon clusters thus far have employed diode laser sources to probe the C-C stretching bands(18). The sporadic frequency coverage and slow scanning speed of these laser systems has left much of the spectrum unstudied, leaving at least one important question unanswered. Cyclic carbon clusters, despite predictions indicating that they are energetically favored over linear isomers for clusters with 10 or more atoms(19), have yet to be definitively observed spectroscopically. While carbon cluster ions in this size range have been shown to exist as cyclic isomers(20), their neutral counterparts have thus far eluded detection. Our initial efforts applying IR-CRLAS to this problem are very promising. Figure 6 shows the IR-CRLAS spectrum of the  $\nu_3$  band of C<sub>5</sub>. The frequency bandwidth of the laser employed in these studies was 900 MHz, while the individual absorption features were roughly 80 MHz, as determined by diode laser spectroscopy. This non-Beer's Law application of CRLAS results in a reduction of the measured absorption intensity by a factor of ~15. Even with this drastic reduction in signal strength, the high signal-to-noise ratio displayed in the spectrum reflects the very high sensitivity of CRLAS. This sensitivity combined with the rapid scanning capability and complete frequency coverage are expected to reveal much interesting new information about carbon clusters. The high resolution system described above could then prove crucial for providing unambiguous carrier identification once interesting features are located, as the spectrum of a large cyclic carbon cluster is likely to be unresolved with the 900 MHz resolution of the present laser system. Other systems we intend to study using the laser vaporization source include High Energy Density Materials (HEDMs).

**Ions and Radicals.** We have developed a pulsed discharge slit source capable of producing large quantities of elusive ions and radicals. The design of this source is very similar to that recently published by Nesbitt and coworkers (21). Our early attempts with this source have produced the spectrum shown in Figure 7 of a single rovibrational transition of H<sub>3</sub>O<sup>+</sup>. While we expect the signal strength to greatly improve as we refine the source design, once again the signal strength is considerably reduced due to the fact that the laser bandwidth is over ten times that of the absorption linewidth.

**Gas Phase Biomolecules and Biomolecule-Water Complexes.** We presently have two goals in our studies of biologically relevant molecules. One project involves characterizing the hydrogen bonding interaction between two isolated gas phase nucleotide bases. We have successfully observed spectral features in the N-H stretch region attributable to uracil, thymine, adenine, and cytosine, leaving only guanine unobserved. Absorptions due to clusters of these molecules are expected to shift substantially to lower frequencies. While we have measured many features that could result from clusters, these features are rotationally unresolved, and further congested by neighboring features. This has prohibited their definite assignment.

## Broad scan of water cluster absorption in the O-D stretch region

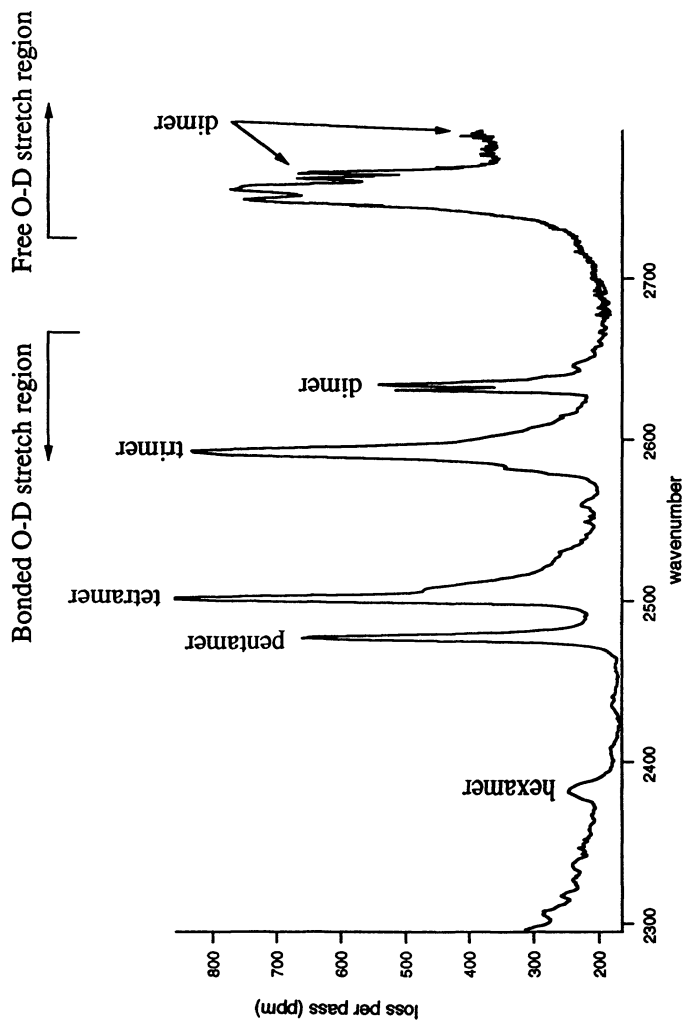


Figure 4. The spectrum of fully-deuterated water clusters in the O-D stretching region. This spectral region has been difficult to cover using previously existing method. As a result, this spectrum has remained unobserved until the present work.

$(D_2O)_2$  acceptor antisymmetric stretch

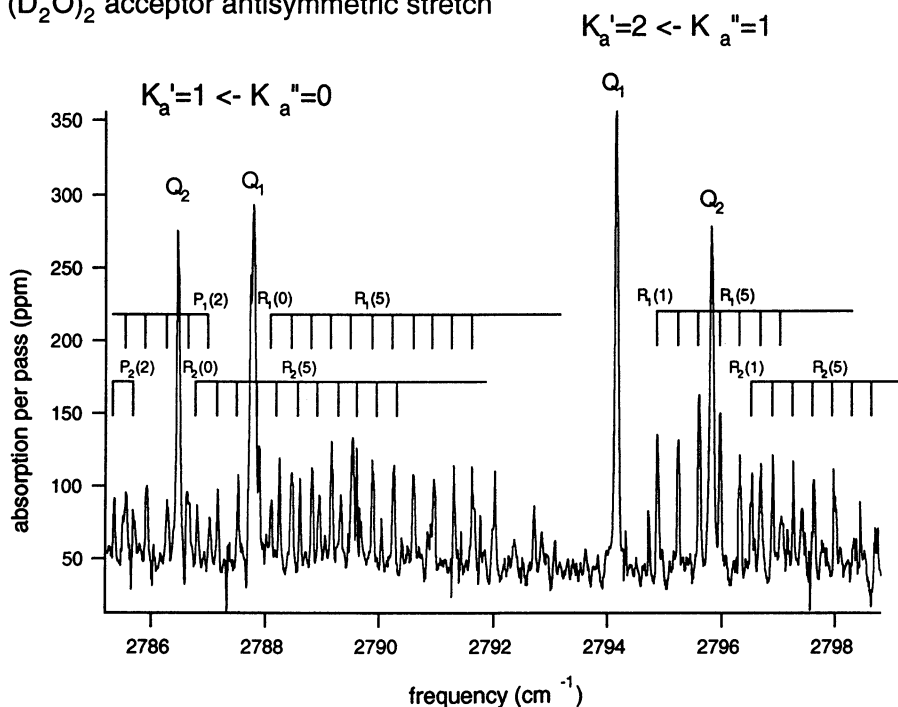


Figure 5. A portion of the  $(D_2O)_2$  acceptor anti-symmetric stretching band is shown. Once again, the ability to record accurate intensity information aided in the assignment of the observed features. In this case, each rovibrational transition is doubled due to a quantum tunneling motion known as "acceptor tunneling." Based on nuclear spin statistics, the intensity ratio of these components is expected to be 2:1, which is observed in the spectrum. This allowed the rigorous assignment of each feature to the appropriate symmetry component to be made, and led to an improved understanding of the tunneling dynamics.

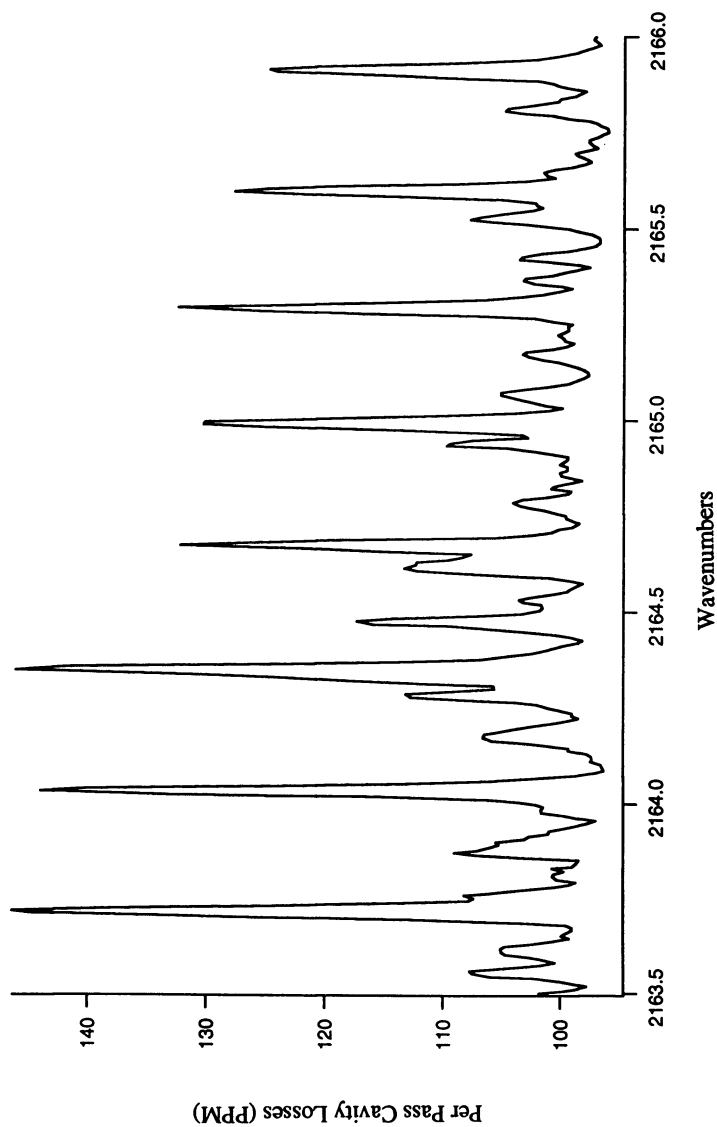


Figure 6. We have applied the IR-CRLAS method to study species produced in laser vaporization sources. Here, we show a portion of the  $\nu_3$  band of  $C_5$  along with several hot-band transitions. While the signal-to-noise ratio of the stronger lines is fairly good ( $\sim 2.5:1$ ), the signal strength is severely reduced because the laser bandwidth (900 MHz) is over a factor of 10 larger than the absorption bandwidth (80 MHz).

500 Torr, 1 Amp pulsed H<sub>2</sub>O/He discharge across 4" slit

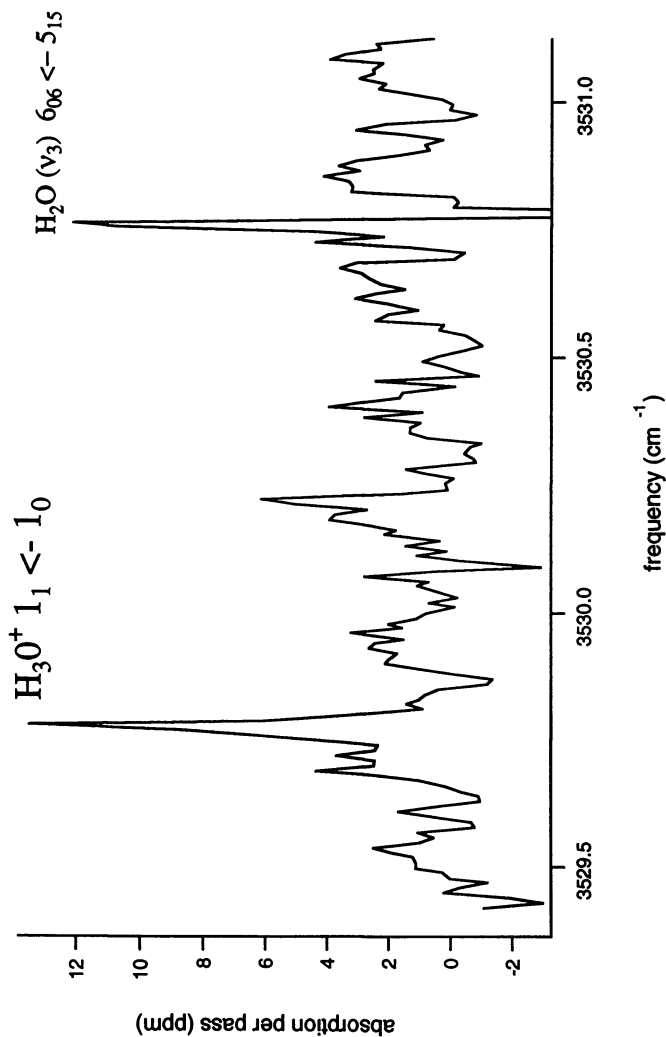


Figure 7. A single rovibrational transition of the H<sub>3</sub>O<sup>+</sup> molecular ion is shown, resulting from a probe of a pulsed slit-discharge source using the ringdown method. Once again, an order of magnitude gain in absorption strength could be obtained using a narrower bandwidth laser source.



We hope that future experiments in the C=O stretch region will further elucidate these systems. In addition, optimizing the clustering conditions in the jet using IR-CRLAS could greatly improve the chances for successfully probing these hydrogen bonds directly using Far-IR spectroscopy, as the extremely high resolution of those systems makes locating new features a difficult and time consuming problem.

A second effort involves studying the interactions of amino acids and proteins with water. Water is thought to play a key role in the folding and secondary structure of proteins, which is currently a very active area of research. We have successfully observed the jet-cooled spectrum of valine, a simple amino acid, as well as complexes of this molecule with water (Figure 8). We are also in the process of studying these systems in the C=O stretch region, as these bands are commonly the most intense transitions, with transition frequencies which are very sensitive to the local environment of the C=O group.

**Acknowledgments.** We wish to thank Dr. Arthur Suits and Prof. Y.T. Lee for loaning to us the Raman shifter used in these studies. This work is supported by grants from AFOSR, NSF, and NASA.

#### Literature Cited.

- (1) O'Keefe, A.; Deacon, D. A. *G. Rev. Sci. Instrum.* **1988**, *59*, 2544-2551.
- (2) O'Keefe, A.; Scherer, J. J.; Cooksy, A. L.; Sheeks, R.; Heath, J.; Saykally, R. J. *Chem. Phys. Lett.* **1990**, *172*, 214-218.
- (3) Scherer, J. J.; Paul, J. B.; O'Keefe, A.; Saykally, R. J. *Chem. Rev.* **1997**, *97*, 25-51.
- (4) Paul, J. B.; Saykally, R. J. *Anal. Chem.* **1997**, *69*, 287-292.
- (5) Scherer, J. J.; Voelkel, D.; Rakestraw, D. J.; Paul, J. B.; Collier, C. P.; Saykally, R. J.; O'Keefe, A. *Chem. Phys. Lett.* **1995**, *245*, 273-280.
- (6) Martin, J.; Paldus, B. A.; Zalicki, P.; Wahl, E. H.; Owano, T. G.; Harris, J. S., Jr.; Kruger, H.; Zare, R. N. *Chem. Phys. Lett.* **1996**, *258*, 63-70.
- (7) Engeln, R.; van den Berg, E.; Meijer, G.; Lin, L.; Knippels, G. M. H.; van der Meer, A. F. G. *Chem. Phys. Lett.* **1997**, *269*, 293-7.
- (8) Paul, J. B.; Collier, C. P.; Scherer, J. J.; O'Keefe, A.; Saykally, R. J. *J. Phys. Chem.* **1997**, *101*, 5211-5214.
- (9) Paul, J. B.; Provencal, R. A.; Chapo, C.; Pettersson, A.; Saykally, R. J. , in preparation.
- (10) Paul, J. B.; Provencal, R. A.; Saykally, R. J. *J. Phys. Chem* **1998**, in press.
- (11) Provencal, R. A.; Paul, J. B.; Saykally, R. J. , unpublished results.
- (12) Chapo, C.; Paul, J. B.; Provencal, R. A.; Saykally, R. J. , unpublished results.
- (13) Pribble, R. N.; Zwier, T. S. *Science* **1994**, *265*, 75.
- (14) Coker, D. F.; Miller, R. E.; Watts, R. O. *J. Chem. Phys.* **1985**, *82*, 3554-3562.
- (15) Huisken, F.; Kaloudis, M.; Kulcke, A. *J. Chem. Phys.* **1996**, *104*, 17-25.
- (16) Vernon, M. F.; Krajnovich, D. J.; Kwok, H. S.; Lisy, J. M.; Shen, Y. R.; Lee, Y. T. *J. Chem. Phys.* **1982**, *77*, 47-57.
- (17) Page, R. H.; Frey, J. G.; Shen, Y. R.; Lee, Y. T. *Chem. Phys. Lett.* **1984**, *106*, 373-376.
- (18) van Orden, A.; Provencal, R. A.; Keutsch, F. N.; Saykally, R. J. *J. Chem. Phys.* **1996**, *105*, 6111.
- (19) Martin, J. M. L.; Francois, J. P.; Gijbels, R.; Almlof, J. *Chem. Phys. Lett.* **1991**, *187*, 367.
- (20) von Helden, G.; Hsu, M. T.; Gotts, N. G.; Bowers, M. T. *J. Phys. Chem.* **1993**, *97*, 8182.
- (21) Anderson, D. T.; Davis, S.; Zwier, T. S.; Nesbitt, D. J. *Chem. Phys. Lett.* **1996**, *258*, 207-212.

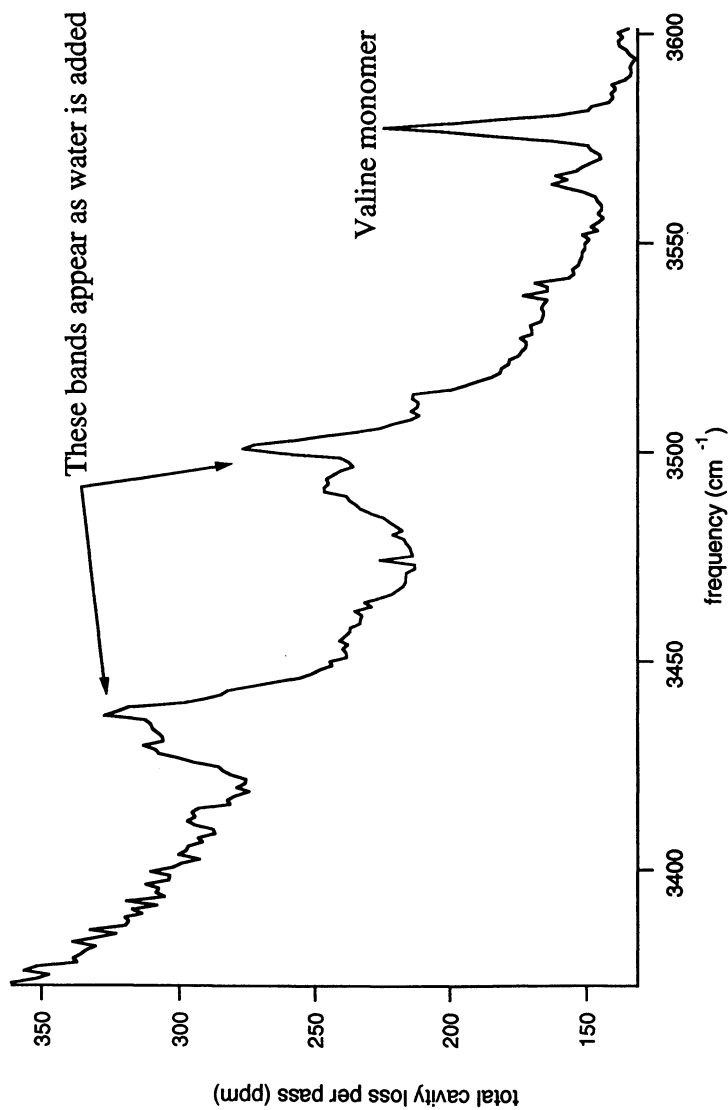


Figure 8. In this Figure, the gas-phase hydration of valine, a small amino acid, is shown. As water vapor is added into the supersonic expansion, the valine monomer O-H stretching fundamental decreases as the two red-shifted bands grow in.

## Chapter 12

# Cavity-Ringdown Laser Absorption Spectroscopy of Polyatomic Radicals in Low Pressure

J. J. Scherer<sup>1</sup>, K. W. Aniolek<sup>2</sup>, and D. J. Rakestraw

Combustion Research Facility, Sandia National Laboratories,  
Livermore, CA 94551

Infrared and visible cavity ringdown laser absorption spectroscopy (CRLAS) was employed for the determination of polyatomic radical concentrations in low pressure methane-air flames. Absorption spectra for the methyl and formyl radicals were analyzed with the aid of CARS temperature measurements of molecular nitrogen, to determine absolute species concentrations as a function of height above the burner surface in flat, laminar, low pressure flames. The concentration profiles obtained were compared with combustion chemistry simulations, and were found to be in agreement under stoichiometric conditions. Under rich flame conditions (equivalence ratio  $\Phi=1.5$ ), significant deviation between experimental and theoretical values was observed for both the methyl and formyl radicals. General issues concerning the capabilities of CRLAS as a combustion diagnostic are addressed, and indicate the feasibility of the approach for the study of other polyatomic species present in flames.

Gas phase spectroscopic techniques have served as a powerful tool for noninvasive combustion chemistry studies. The ability to obtain quantitative spectral information is fundamental to the deduction of species concentrations and temperatures, and several spectroscopies have been developed for such studies. Techniques employed as combustion diagnostics include laser induced fluorescence (LIF), resonant ionization methods (REMPI), coherent anti-stokes Raman spectroscopy (CARS), resonant four-wave mixing (RFWM), photoacoustic spectroscopy (PA), and conventional absorption methods<sup>1</sup>. In many of these techniques, with the exception of the Raman and direct absorption methods, deconvolution of the spectral intensities can be complicated by inter- and

<sup>1</sup>Current address: Los Gatos Research, 67 East Evelyn Avenue, Suite 3, Mountain View, CA 94041

<sup>2</sup>Department of Mechanical Engineering, Drexel University, 32nd and Chestnut Street, Philadelphia, PA 19104

intramolecular dynamics, such as quenching, dephasing, predissociation, and internal conversion. Frequently, complex models are required to deconvolve the experimentally observed spectral intensities to obtain species concentrations and temperatures<sup>2</sup>. Diode laser spectroscopy also offers a potential route to obtaining direct absorption data as presented here using infrared CRLAS. Measurements in combustion environments using diode laser spectroscopy typically have been limited in sensitivity to absorbance in the  $10^{-3}$  to  $10^{-4}$  range due to complications such as accidental etalon interference fringes and infrared luminescence.<sup>3</sup> Recently, two highly sensitive absorption based methods, cavity ringdown laser absorption spectroscopy (CRLAS) and intracavity laser absorption spectroscopy (ICLAS) have been successfully implemented for flames studies.<sup>4,5,6,7,8</sup> Although highly sensitive, the ICLAS studies have been limited to spectral regions (visible) where high resolution cw lasers are available. In contrast, CRLAS has been demonstrated in spectral regions ranging from the ultraviolet<sup>9</sup> to the infrared<sup>10</sup>, due to the ability to utilize widely tunable, pulsed laser sources. This advantage is particularly important in the context of the recent development of optical parametric oscillator-based laser systems, which are capable of achieving narrowband, single mode operation from the near to mid-infrared spectral regions.

In this paper, the application of both visible and infrared CRLAS for the determination of species concentrations of polyatomic radicals in flames is presented. Specifically, the generality and high sensitivity of the technique for quantitative, low pressure laminar flames studies is demonstrated. Absolute species concentration profiles are obtained for both the methyl and formyl radicals using a combination of CRLAS absorption spectra together with nitrogen CARS temperature measurements. The ability to obtain reproducible, spatially resolved (1-D) absorption spectra in methane/air flames is demonstrated in two spectral regions centered around 615 nm and 3.3  $\mu\text{m}$ , respectively. In the 615 nm region, the HCO A-X system is studied, while in the 3.3  $\mu\text{m}$  region, the  $\nu_3$  rovibrational band of the methyl radical is monitored. These data are combined with CARS temperature measurements to obtain absolute radical concentrations as a function of height above the burner surface (HAB). These data demonstrate the routinely achievable technique sensitivity in these two spectral regions, the challenges presented due to spectral congestion in the infrared, and the degree of spatial specificity in CRLAS achievable compared to that which is required for quantitative studies in flames. The experimentally derived concentration profiles for methyl and formyl are directly compared to combustion chemistry simulations under both stoichiometric and rich flame conditions. Collectively, these data demonstrate the suitability of CRLAS for detailed quantitative studies in low pressure combustion environments.

## Experiment

The low pressure flame diagnostics apparatus is shown in Fig. 1, and employs both CARS and CRLAS spectroscopies for flame temperature and species measurements, respectively. Infrared and visible CRLAS and CARS are employed

## CRLAS/CARS experiment

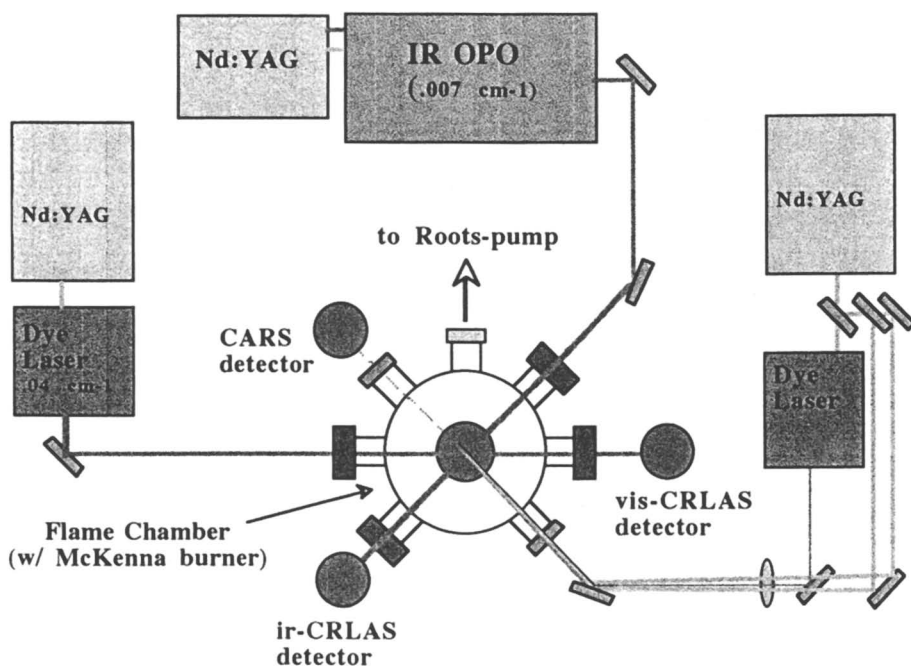


Figure 1. Low pressure flame diagnostics apparatus: Both CARS and infrared and visible CRLAS are employed for the non-invasive study of low pressure flames.

in a fixed, crossed, horizontal geometry while the burner is translated vertically for 1-dimensional height-above-burner (HAB) studies. Although CRLAS data presented later could in principle be used also for the determination of temperatures, the N<sub>2</sub> CARS measurements possess significantly better (as well as 2-dimensional) spatial resolution, and thus enable temperatures to be obtained all the way from the burner surface to regions high in the flame. In both of these regions, CRLAS (polyatomic) radical spectra are typically too weak for temperature studies. Additionally, in the infrared CRLAS work, the limited number of methyl transitions discernible over a reasonable wavelength range is not adequate for precise temperature determination. As will be shown explicitly later, the precise determination of flame temperatures is paramount to extracting good concentration data from the associated CRLAS absorption spectra.

The flame source employed in these studies is a 6 cm water-cooled McKenna plug burner which is located in a pressure controlled vacuum chamber. Source conditions are adjusted to produce flat, laminar flames ranging from 30 to 100 ( $\pm 0.1$ ) Torr. Flow rates for the premixed flames are controlled by calibrated flow meters which possess an accuracy of ca. 4%. Industrial grade (>99% purity) methane, hydrogen, oxygen, and nitrogen are used to generate low pressure flames. As such, fuel impurities (such as acetylene in methane) are readily observed with CRLAS at low HAB levels. The burner assembly is translated vertically with a resolution of .002", while absorption and temperature spectra are typically recorded at 0.5 mm intervals.

### CARS Apparatus

The use of CARS as a reliable diagnostic of flame temperatures has been established in numerous studies and is discussed in detail elsewhere.<sup>1</sup> The accuracy of the CARS derived temperatures in low pressure flames has been experimentally determined to be ca.  $\pm 25$  K. The laser system consists of a seeded Nd:YAG laser which is used for both the CARS pump beam as well as for simultaneous pumping of a .04 cm<sup>-1</sup> bandwidth probe dye laser (Lumonics Hyper-Dye 500). The 532 nm Nd:YAG and 615 nm dye laser beams are combined to achieve an effective probe volume which is ca. 100 microns in diameter and 4 mm in length. The probe region is centered in the burner to avoid the temperature gradients which occur at the flame boundaries. Typically, twenty five rovibrational transitions are scanned at a fixed burner position for each temperature measurement, and these data are then fitted using a routine developed by Palmer<sup>11</sup> These pointwise data are then fit to obtain an analytical expression for the continuous temperature profile, which is used both as input for combustion chemistry simulations as well as for calculation of the species concentrations.

### CRLAS Apparatus

The infrared and visible cavity ringdown systems are also shown in Fig. 1, and are described in detail elsewhere<sup>7,8</sup>, while a complete review of CRLAS theory and

development can be found in a recent publication.<sup>12</sup> Briefly, the infrared ringdown laser system consists of an injection seeded, pulsed Nd:YAG laser which pumps a tunable, single mode optical parametric oscillator (OPO) system (STI Mirage 3000). This laser system produces a ca. 1 mJ pulse of single longitudinal mode infrared light with a pulse duration of ca 3.5 ns (FWHM) at a repetition rate of 10 Hz. The energy at the cavity input mirror typically ranges from 50-100  $\mu$ J/pulse. Both the longitudinal and transverse mode quality of the OPO signal beam are continuously monitored to assure single transverse as well as longitudinal mode quality. For the visible CRLAS measurements of HCO, a Nd:YAG-pumped dye laser system is employed. In both the visible and infrared studies, the laser bandwidth is significantly less than the associated spectral features, which assures quantitative absorption data can be obtained.

The output beams for both the visible and infrared systems are each tailored with two telescopes for injection into the cavity, and the resultant far-field quality of the beams is then optimized beyond the cavity exit mirror before the cavity mirrors are mounted and aligned. Careful beam shaping is required in order to achieve adequate transverse spatial specificity in these low pressure flame studies. The mirrors used in the infrared studies consisted of high reflectivity ( $R_{\max} = 99.98\% @ 3.3 \mu\text{m}$ ) surface coated silicon substrates with a 6 m radius of curvature, while the visible mirror substrates are fused silica with the same curvature and similar maximum reflectivity ( $R_{\max} = 99.99\% @ 630 \text{ nm}$ ). The transmitted light at the output mirror (roughly  $10^{-8}$  of the laser light) is focused into either an InSb detector for the  $3.3 \mu\text{m}$  work or a photomultiplier in the visible work, amplified, and recorded with a digital storage oscilloscope. In the present work, 16-32 decay waveforms are averaged in the scope before being transferred to a computer for calculation of cavity losses. The intensity decay of the trapped light pulse is monitored in time via transmission through the output mirror. For each round trip time interval  $dt$ , the trapped light intensity  $I$  diminishes proportionally to the transmission factor  $T$  of the cavity, according to

$$dI/dt = -ITc/2L, \quad (1)$$

where  $L$  is the mirror spacing, and  $c$  is the speed of light. The subsequent intracavity light intensity as a function of time  $t$  is therefore given by

$$I = I_0 e^{-Tct/2L}. \quad (2)$$

Total cavity losses  $\Gamma$  (per pass) are then obtained as a function of injection laser frequency from the expression

$$\Gamma = 1 - e^{-2L/c\tau}, \quad (3)$$

where  $\tau$  is characteristic decay time of the cavity (the time required for the intracavity light intensity to decay to  $1/e$  of its initial value). Non-resonant intracavity losses are measured as an effective reduced reflectivity, and include

contributions from Mie and Rayleigh scattering, as well as from any alignment fluctuations which result from thermal lensing effects. In the case of flames, it is impossible to quantify the individual contributions from each of these sources of loss with CRLAS alone. However, it is straightforward to simply subtract this total (broadband) loss contribution in the case where individual (narrowband) rovibrational/rovibronic features are measured. Molecular absorption intensities are then easily determined. In these flame studies, baseline losses varied significantly over the full range of burner positions due to a combination of the aforementioned effects, but did not impede the ability to detect targeted species, even under rich flame conditions. Typical baseline losses when off-resonance ranged from 100-500 ppm, depending on the stoichiometry of the flame as well as the probe position. Absorption intensities and temperatures were determined for a full range of HAB values, and subsequently used to extract absolute species concentrations. In the infrared work, hydrogen-oxygen flames were also scanned for a full range of HAB positions, in order to identify spectral interferences from non-carbon containing species, such as H<sub>2</sub>O.

A desirable feature of the CRLAS method is that it is largely insensitive to the absolute value of the initial intracavity light intensity, and therefore is not effected by the large pulse to pulse intensity fluctuations common to pulsed laser systems. Similarly, the fitted decay time is largely insensitive to interference effects which can occur as the narrowband laser light is scanned in wavelength over the free spectral range of the cavity. Although recent studies<sup>13,14</sup> have stressed that transient etalon effects can be observed in the ringdown decay waveform under the condition of coherent cavity excitation, these studies did not identify the subsequent effect on the fitted decay time (and hence calculated cavity losses) for more commonly employed experimental configurations. In experiments where high reflectivity ( $R > 99.95\%$ ) mirrors are employed, oscillations in the decay waveform ascribed to mode competition are typically on timescales much faster than the decay time, and hence are averaged out in the exponential fitting routine. We have found in our narrow linewidth infrared studies where intensity anomalies are routinely observed (where significant coherent excitation of the cavity occurs) as long as the probe laser is narrower than the absorption feature and a measurable decay is observed (i.e. the transmission modulation observed in the ringdown is detectable at the minimum), no absorption intensity anomalies are observed, to within the few ppm noise level typical in flame environments. Even in cases where the cavity is explicitly manipulated to exhibit large transmission contrast (short cavities which are injected with coherent light), we have found that spectral intensities are not affected to within the normal reproducibility (a few %) of experiments wherein no transmission contrast is observed, regardless of whether the absorption feature falls in a transmission minimum or maximum. In the present visible work, mode competition phenomena are not observed in either the decay waveforms or the associated absorption spectra, due to the limited coherence length of the laser with respect to the cavity length.



## Determining Absolute Species Concentrations and Comparison to Theory

The spectral intensities observed are a convolution of the transition moments, species concentrations, temperatures, and linewidths. Absolute radical concentrations were determined using the Beer-Lambert absorption law, which requires the use of temperature corrected absorption cross sections for the associated transitions. Calculation of the cross sections  $\sigma(\nu)$  for different temperatures  $T$  for the associated transitions were obtained using the standard relation

$$\sigma(\nu) = S_{ji}(\nu)g(\nu), \quad (4)$$

where  $S_{ji}$  is the linestrength and  $g(\nu)$  is the lineshape function. In the case of the methyl radical, the temperature corrected linestrengths were calculated from the experimentally determined transition moments  $\mu$  reported by Bethardy and MacDonald<sup>15</sup> via

$$S_{ji} = (8\pi^3/3hc)\nu_{ij} \langle j|\mu|i \rangle^2 \{A_{NK}(1 - \exp(-h\nu/kT)) \times \{s_K g_{NK} \exp(-E_i/kT)/Q_T\}, \quad (5)$$

where  $\nu_{ij}$  is the transition frequency between states  $i$  and  $j$ ,  $\mu$  is the transition dipole moment,  $A_{NK}$  is the Hönl-London factor,  $s_K$  and  $g_{NK}$  are the spin and nuclear degeneracies, respectively,  $E_i$  is the energy of the lower state, and  $Q_T$  is the total internal partition function. For the  $\nu_3$  methyl band, the Herman-Wallis factors, which represent the dipole moment dependence on the vibration-rotation level, are currently not available and therefore are not included. This correction, however, is expected to lead to a correction of less than 10%.<sup>15</sup> The stimulated emission term in Eq. 5 ( $1 - \exp(-h\nu/kT)$ ) leads to a small, non-negligible correction (6%) for the methyl cross sections, while this contribution is negligible for the visible HCO work.

In the present study, Doppler-corrected line center absorption intensities were used for calculation of species concentrations, instead of the more traditional integrated line intensities for several reasons. In the case of the methyl work, this was done to avoid interferences present in the line kernels, while for the formyl radical, the linewidths are dominated by lifetime broadening. Additionally, in calculation of the lineshape functions, no correction is made for the contributions from pressure broadening. Although this correction is expected to be small, it is omitted due to the lack of availability of broadening coefficients for the collision partners present in flames.

The reduction in the absorption cross section which occurs at flame temperatures significantly increases the difficulty associated with obtaining spectra of polyatomic species at elevated temperatures. For example, the  ${}^1R(6,6)$  methyl transition cross section studied here is reduced by a factor of ca. 70 in going from room temperature to a typical flame temperature of 1600 K, with a concomitant increase in the minimum detectable concentration. The explicit inclusion of this

temperature correction is required in order to extract quantitative concentration profiles from the absorption spectra. In cases where the absorption cross section or species concentration vary significantly over the transverse dimension of the ringdown light, the absorption data are compromised. This point is illustrated by comparing the theoretical concentration and associated absorption profiles, using the experimental temperature profile and gas flow rates (as described earlier) as input data for combustion chemistry simulations.

In Fig. 2, the experimental temperature profile is shown together with the temperature corrected cross sections, theoretical number densities, and associated expected absorption intensities for the  ${}^1R(6,6)$  methyl and  $Q(8)$  HCO transitions (a and b, respectively) in a stoichiometric flame for HAB positions ranging from 2 to 12 mm. The theoretical absorption intensities are predicted assuming a single pass absorption path length of 6 cm. The simulations are performed using a modified Miller-Bowman mechanism which includes nitrogen chemistry.<sup>16</sup> Nearly identical results for both methyl and formyl radicals are obtained using other mechanisms, or excluding nitrogen chemistry. Of particular interest in this comparison is the difference between the methyl and formyl radicals in the correlation between their respective absorption and concentration profiles. While the absorption profile closely follows the concentration curve for the formyl radical, noticeable deviation occurs for the methyl transitions. This effect results primarily from the difference in the associated vibrational partition functions, as the rotational vibration partition function scales with temperature similarly for both species. In the methyl case, the predicted absorption maxima at 4.5 mm occurs well before predicted maximum concentration at 6.5 mm, due to the steep temperature gradient which manifests in a comparably steep cross section correction. This behavior is common to all of the methyl transitions monitored in this study, and furthermore highlights some of the limitations imposed on CRLAS for the study of larger polyatomic species or for the study of flames at higher pressure. Larger polyatomic radicals, such as the propargyl radical, exhibit even more pronounced anti-correlation between the absorption intensity and concentration, again, due primarily to the vibrational partition function correction to the absorption cross section. Additionally, in the case of the propargyl radical, the absorption drops off (spatially) at a rate which will significantly hinder the ability to quantify IR-CRLAS data, due to the limited spatial resolution achievable at infrared wavelengths. Similarly, in higher pressure flames, the temperature and concentration gradients are even more severe, and thus will limit the utility of CRLAS for quantitative flame studies of transient polyatomic radicals.

### Formyl Radical

The formyl radical has been extensively studied due to its importance in a wide range of chemical problems, including photochemistry, pollution chemistry, and combustion chemistry. In the present study, we focus on the A-X system, which was first observed by Ramsay et al.<sup>17</sup> in flash photolysis, direct absorption experiments. In the case of flames, the  $3p^2\Pi-X$ , B-X, and A-X systems of HCO

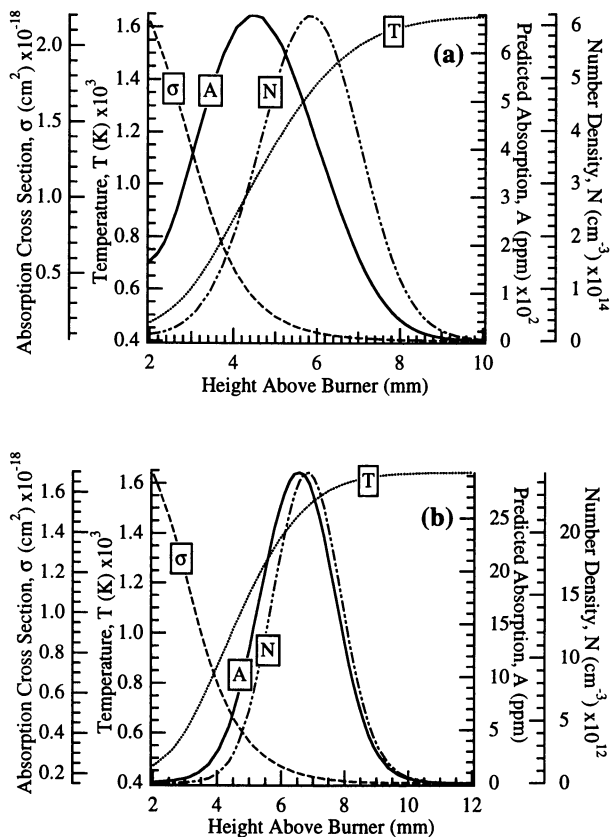


Figure 2. Comparison of the predicted absorption and concentration profiles as a function of height above the burner surface for both methyl (a) and formyl (b) radicals, with corresponding temperature profiles and absorption cross sections.

have been detected in REMPI<sup>18</sup>, LIF<sup>19</sup>, ICLAS<sup>6</sup> and CRLAS<sup>7</sup> experiments, respectively. In the 2+1 REMPI study of Bernstein et al.<sup>19</sup> relative concentration profiles were obtained after a significant correction was made for the nonlinear ionization probe response. Similarly, relative concentration profiles were obtained in the LIF study of the B-X system of Jeffries et al.<sup>20</sup>, but no correction was made for the possible change in the fluorescence quantum yields, due to a lack of information on the B state quenching rates. In both studies, no absolute concentrations were obtained. To address these drawbacks, Cheskis recently obtained the A-X spectrum in an atmospheric pressure flame using ICLAS<sup>6</sup>, but was unable to obtain quantitative information due to the large variation in species concentration over the intracavity laser dimensions. Following this work, Scherer and Rakestraw obtained CRLAS data of HCO in a low pressure flame using this same band system, and were able to obtain peak absolute HCO concentrations from the associated absorption spectra.<sup>7</sup> Recently, Lozovsky et al. have obtained HCO temperature and concentration profiles in a near stoichiometric low pressure flame, again via the A-X system using ICLAS.<sup>20</sup> In these studies, the temperature was obtained with a precision of +/- 200 K. In the present work, we combine more precise CARS temperature measurements with CRLAS spectra to obtain quantitative absolute HCO radical concentration profiles in both stoichiometric and rich ( $\Phi=1.5$ ) CH<sub>4</sub>/N<sub>2</sub>/O<sub>2</sub> flames.

CRLAS spectra of the (09<sup>0</sup>0)-(00<sup>1</sup>0) vibronic band of the A-X system of HCO are shown in Fig. 3, which also includes several lines (labeled \*) which have been assigned to the excited-state (singlet) methylene radical.<sup>20</sup> This spectrum was obtained 7 mm above the burner surface in a stoichiometric CH<sub>4</sub>/O<sub>2</sub>/N<sub>2</sub> flame at a total pressure of 37.5 Torr. The flames were run with slightly less nitrogen than the standard 4:1 ratio of air in order to minimize curvature in the visible region of the flame front. Several scans were obtained at 1 mm increments ranging from 2 to 9 mm above the burner surface and used to construct the associated concentration points. Below ca. 2 mm, no HCO signal is observed. As is evident in Fig. 3, visible CRLAS is capable of attaining sub-ppm (fractional absorption) sensitivity levels in these environments, limited largely by the ability to achieve stable flame operation. This level of sensitivity is comparable to more recent ICLAS results<sup>20</sup>, although the CRLAS data does not display the pronounced baseline variation evidenced in the ICLAS data.

Predissociation in the A-X system has been the focus of numerous studies, and is manifest as a homogeneous line broadening which is strongly dependent on both the upper and lower state rotational and vibrational quantum numbers. This is due to a state selective heterogeneous predissociation which results from a strong Renner-Teller interaction in the excited state. The line broadening associated with different rovibronic transitions of the A-X system has been studied in detail by Vasudev and Zare, who ascribed the N'-dependent linewidths to a Coriolis interaction and K-type resonance between the K'=0 and K'=1,2 levels.<sup>21</sup> This N-dependent line broadening is clearly evident in Fig. 3, with widths ranging from ~0.23 to 0.6 cm<sup>-1</sup> (FWHM). This linewidth is significantly broader than the expected Doppler width of ~0.1 cm<sup>-1</sup>, and moreover complicates the extraction of

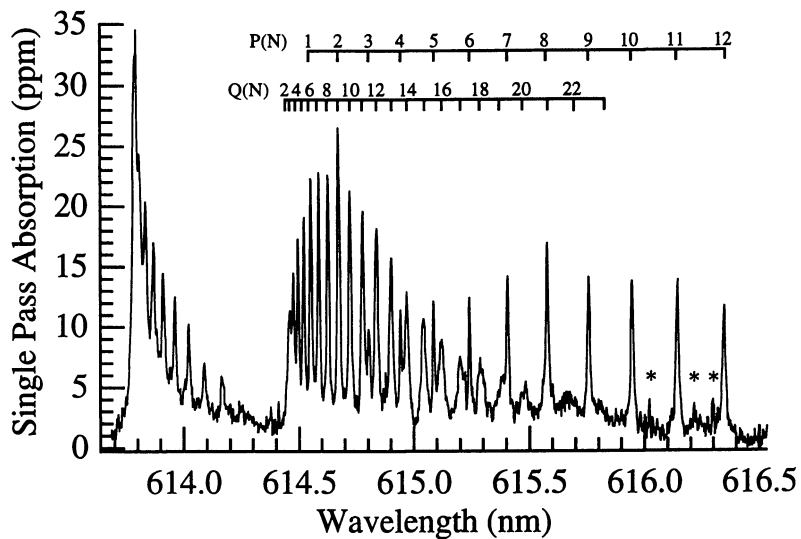


Figure 3. Visible CRLAS spectra of the A-X system of HCO, obtained 6 mm above the burner surface in a methane/air flame.

temperatures from the HCO data alone. Several studies<sup>22,23,24</sup> have focused on determining absorption cross sections for the A-X system including the absorption studies of Baggott et al.,<sup>25</sup> Langford and Moore,<sup>26</sup> and Zhu et al.<sup>27</sup> The CRLAS data together with the cross sections obtained in previous studies allows the absolute number density of HCO in the probe region to be determined. In the studies of Baggott et al.,<sup>25</sup> the cross section for the P/Q bandhead at 614.49 nm was determined to be  $\sigma=2.3(\pm 0.6)\times 10^{-18}$  cm<sup>2</sup>, at an estimated HCO temperature of 300 K. In the recent work of Zhu et al.,<sup>27</sup> the cross section for this same feature was determined to be  $1.2 (\pm 0.3)\times 10^{-18}$  cm<sup>2</sup> at 282 K. Although both of these cross section values possess the highest quoted precision of all studies reported to date, their utility for this high temperature work is limited. This is primarily due to the difference in probe laser linewidth, which in both of these studies is significantly broader than the absorption features. Additionally, values given for the Q bandhead/P-branch region overlap several transitions, which further complicates extrapolation of the cross section. An alternate though less precise value for the cross section in this same band system is obtained from the work of Langford and Moore,<sup>26</sup> who utilized a 20 MHz bandwidth laser to obtain a cross section for the Q(9)/P(2) line of  $3.6 (\pm 1.6) \times 10^{-18}$  cm<sup>2</sup>, again at a temperature of 300 K. In this case, the cross section contains an approximately 20% contribution from the P(2) line, which changes with temperature. For the present studies, we use the ratio of the expected Q(9)/P(2) transition intensities to remove the P(2) contribution, and calculate the Q(8) transition strength based on the expected ratio of the Q(9)/Q(8) linestrengths. By using the Q(8) transition in these flame studies, we remove the difficulty associated with correcting the cross section of the blended lines for each temperature.

Experimental concentration profiles for the HCO radical are shown for both stoichiometric and rich flames in Fig. 4, together with the predicted values obtained as described earlier. In this case, the predicted concentrations are in excellent agreement in the stoichiometric case, while significant deviation from the model occurs under rich flame conditions. For the stoichiometric flame, maximum HCO concentration is predicted to occur at 6.5 mm, with an associated concentration of  $\sim 2.5 \times 10^{13}$  mol. cm<sup>-3</sup>, compared to the 6.2 mm peak value measured here with a concentration of  $1.3(\pm 0.5) \times 10^{13}$  mol. cm<sup>-3</sup>. This difference is almost within the error in these studies, which is primarily due to uncertainties in the previously determined cross section. With the current signal-to-noise ratio, the extrapolated minimal detectable HCO concentration for CRLAS is  $\sim 1 \times 10^{12}$  mol. cm<sup>-3</sup> at 1600 K, with an associated lower limit of  $\sim 7(\pm 0.6)\times 10^{10}$  mol. cm<sup>-3</sup> at 300 K. The relatively large uncertainties in the previously determined cross sections and associated problems with laser linewidth considerations given above highlights the need for more precise HCO cross section measurements. Moreover, in order to fully realize the potential of CRLAS to obtain absolute HCO concentrations in flames, more precise values for the cross sections of this band system are essential. The above deviation of the experimental data from the model predictions under rich conditions is similarly observed for the methyl radical, as demonstrated in the following section.

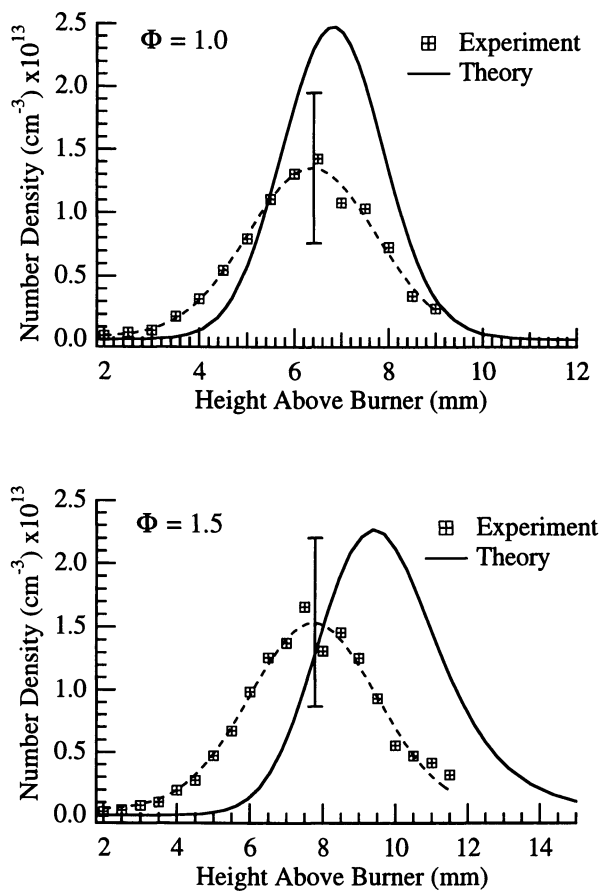


Figure 4. Experimental and predicted HCO concentration profiles for stoichiometric and rich flames.

## Methyl Radical

The methyl radical is an important combustion intermediate,<sup>28</sup> and is central in other processes such as the formation of diamond films during chemical vapor deposition.<sup>29</sup> Numerous studies have established the spectroscopic signature of methyl in the ultraviolet<sup>30</sup> and infrared<sup>31</sup> regions, and these signatures have been utilized for its detection in numerous environments. The ability to determine absolute methyl radical concentrations in some of this work has been made possible by previous studies which have established transition strengths for the associated bands.<sup>15,32,33</sup> In the ultraviolet, these studies include the determination of methyl radical concentrations in flames,<sup>34,35,36</sup> while infrared spectra have been utilized for the study of methyl concentrations in radio frequency discharges,<sup>37</sup> plasmas,<sup>38</sup> and, recently, flames.<sup>8</sup>

Here we describe this recent application of IR-CRLAS for the detection of methyl radical, and again combine the CARS data with the CRLAS data to obtain absolute concentrations as a function of HAB values under the same flame conditions as those given above for the formyl studies. These IR-CRLAS studies constitute the first infrared detection of a polyatomic radical in a flame, and moreover demonstrate the ability to monitor trace species in the spectrally congested mid-infrared. Although mid-infrared transitions of the methyl radical do not possess the high transition strength of the above UV bands, the simplicity associated with monitoring and temperature correcting discrete rovibrational transitions makes them, in some cases, more desirable for the task of quantitative methyl monitoring.

The primary obstacle to monitoring trace species in flames in the infrared is that of spectral interferences and congestion. High spectral congestion can in many cases severely limit the ability to employ sensitive wavelength or frequency modulation infrared absorption techniques, which have demonstrated very high sensitivity in other environments. In cases where spectral assignments can be conclusively made in spite of spectral congestion, infrared spectroscopy possesses the unique ability to monitor many species within a narrow spectral region. Fourier transform infrared spectroscopy has demonstrated this ability in flame studies<sup>39</sup>, but with limited sensitivity ( $>10^{-3}$  fractional absorption). In many cases, this level of sensitivity is not adequate for monitoring trace species at elevated temperatures. For typical methyl concentrations expected in low pressure flames, mid-infrared detection for commonly employed burner dimensions requires a fractional absorption sensitivity significantly better than ca.  $10^{-3}$ . To address the above, IR-CRLAS was employed for flame studies of the methyl radical in the mid-infrared.<sup>39</sup>

IR-CRLAS spectra of the  $\nu_3$  fundamental band system of the methyl radical were obtained in spectral regions centered around  $3150\text{ cm}^{-1}$  and  $3120\text{ cm}^{-1}$ . A total of four rovibrational transitions were unambiguously assigned to the methyl radical, while only two of these features did not exhibit severe interferences. In this spectral region, other methyl transitions were either totally obscured by or appear as



shoulders on the side of stronger absorption features. Representative IR-CRLAS spectra are shown in Fig. 5, which include both the  ${}^{\text{R}}\text{R}(6,6)$  ( $\Delta K\Delta N(N'',K'')$ ) and  ${}^{\text{R}}\text{R}(5,4)$  methyl lines, the latter of which sits on the shoulder of a strong  $\text{H}_2\text{O}$  feature. The lower trace in Fig. 5 is obtained in a stoichiometric hydrogen/oxygen flame at 37.5 Torr and a 6 mm HAB position, while the upper trace is obtained in the rich methane flame at the same pressure with a 4 mm HAB position. Comparison of the spectra obtained in the two flames facilitates identification of non-carbon containing species, and moreover allows spectral interferences to be identified. In addition to methyl, other species identified within this narrow spectral region include  $\text{C}_2\text{H}_2$  (fuel impurity),  $\text{H}_2\text{O}$ ,  $\text{CH}_4$ , and  $\text{CO}_2$ . Notable is the absence of both  $\text{CO}_2$  and  $\text{CH}_3$  in the hydrogen-oxygen scan, as expected. Methyl transitions were confirmed by their frequencies, absolute as well as relative intensities, and HAB absorption profiles.

As is shown in Fig. 5, a significant obstacle in monitoring trace species via their associated infrared signatures is the spectral congestion which occurs in the high temperature, fuel and water abundant environment. Methyl lines employed for the current work were chosen based both on the availability of transition moments as well as the lack of spectral interferences. Over  $100\text{ cm}^{-1}$  was selectively scanned at high resolution in order to identify potential candidates for methyl monitoring. Once potential lines were identified, detailed scans were performed to identify possible contamination due to interferences. Strategies employed for the identification of spectral interferences included scanning hydrogen-oxygen and methane-air flames over a full range of HAB positions, in addition to scanning the unburned fuel (which contains numerous features due to impurities). As shown in Fig. 5, most of the observed features are assignable to  $\text{H}_2\text{O}$ , which is the most abundant product in the flame. In several of the methyl lines observed, interferences precluded their use for quantitative studies. An example is the  ${}^{\text{R}}\text{R}(5,4)$  transition also shown in Fig. 5, which sits on the shoulder of a much stronger spectral feature. This transition, although not suitable for quantitative analysis, exhibits the expected absolute as well as relative intensity for the range of HAB values studied here. Other methyl features observed but similarly not suitable for quantitative studies in methane flames were the  $\text{PQ}(7,7)$  and  $\text{PR}(2,1)$  transitions located at  $3223.98\text{ cm}^{-1}$  and  $3221.75\text{ cm}^{-1}$ , respectively. In the present study, three rovibrational transitions which exhibit minimal spectral interferences were identified, and subsequently combined with CARS temperatures to obtain absolute number densities.

Data obtained at various HAB positions for the  ${}^{\text{R}}\text{R}(6,6)$  transition are shown in Fig. 6, which also displays the routine sensitivity levels achieved in different regions of the flame. In these data, two  $\text{H}_2\text{O}$  transitions are observed to either side of the methyl line, while strong fuel (methane, etc.) transitions are observed within  $0.2\text{ cm}^{-1}$ . Similar absorption profiles were also obtained for the  ${}^{\text{R}}\text{Q}(2,0)$  and  ${}^{\text{R}}\text{R}(4,3)$  lines, although some interference was observed in the former feature at intermediate burner positions. Concentration profiles determined independently from different lines confirmed the assignment to the methyl radical, to within the uncertainty of the associated absorption cross sections. Sensitivity levels achieved in these

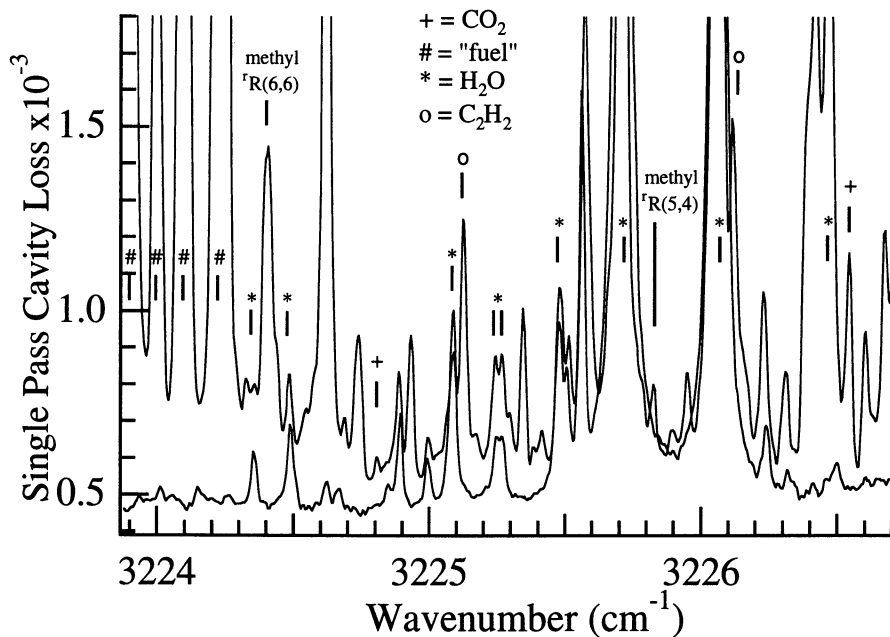


Figure 5. High resolution infrared CRLAS spectra obtained in the 3 micron region in methane/air (upper trace) and hydrogen/oxygen (lower trace) flames.

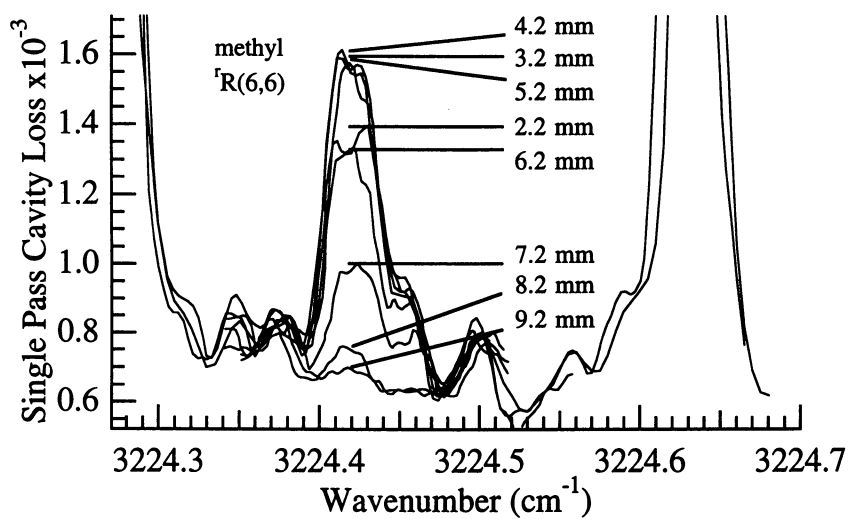


Figure 6. Infrared CRLAS spectra of the  $\text{R}(6,6)$  transition of the  $\nu_3$  fundamental of methyl as a function of height above the burner surface.

studies were approximately 3 ppm fractional absorption per pass, with a concentration detection limit of 10 ppm (mole fraction) for the  $^2R(6,6)$  transition at the concentration maximum @1400K, with a corresponding number density detection limit of  $1.5 (+/-0.3) \times 10^{13}$  mol.  $\text{cm}^{-3}$ .

The experimental concentration profiles are compared to combustion chemistry simulations in Fig. 7, which, again, displays the results for both stoichiometric and rich flame conditions. As observed in the HCO studies, there is excellent agreement between the experimental and theoretical data under stoichiometric conditions, while the model appears to overestimate both the species concentration and position maxima under rich ( $\Phi=1.5$ ) flame conditions. This discrepancy between the experimental and theoretical data under rich flame conditions could be due to several factors, such as the exclusion of chemical mechanisms in the simulations for molecules with more than a single carbon atom. Rich flames present a substantial challenge in this respect, due to the many additional reaction pathways which arise in the presence of excess carbon. The quantitative results obtained in the present work can be used as a benchmark for further theoretical studies and experimental work. In this endeavor, the ability to monitor many species simultaneously should prove invaluable to this effort.

### Spatial Specificity

In CRLAS, as with any optical measurement, it is important to note that the absorption intensity for a given feature will represent an average value over the transverse as well as linear dimension of the probe beam. For this reason, the suitability of CRLAS (as well as for other line-of-sight absorption methods) for laminar flame studies can be greatly reduced as the probe region is made increasingly larger, or as edge effects in the boundary layer of the flame become significant. The data presented here represent an average over the probe beam dimension, which, as highlighted in Fig. 2, is extremely sensitive to temperature gradients and the associated cross section corrections. This is perhaps the greatest weakness of direct absorption methods compared to other techniques such as LIF or DFWM, which have demonstrated spatial resolution of ca. 100  $\mu\text{m}$  in one dimension. In the case of these laminar flame studies, the suitability of CRLAS is effected primarily by the transverse probe dimension. In the visible experiments, the transverse diameter of the probe laser beam was reduced to  $< 1$  mm before injection into the cavity, and the actual multipass probe dimension was experimentally determined by raising the burner and noting the distance required to go from a slightly clipped decay ( $\sim 10\%$  reduction in decay time) to no decay signal at all. Using this approach, we determined the vertical probe dimension in the flame to be  $0.8 \pm 0.2$  mm in the visible work. Typical radical concentrations and differ by only 10-20% over this dimension, and therefore do not significantly effect the precision of the concentration determination. In the infrared, the input beam is similarly tailored to ca. 1.5 mm, with an associated probe dimension of ca. 2 mm, which again, does not significantly degrade the precision of the concentrations obtained from the absorption data. Both of these probe dimensions are close to

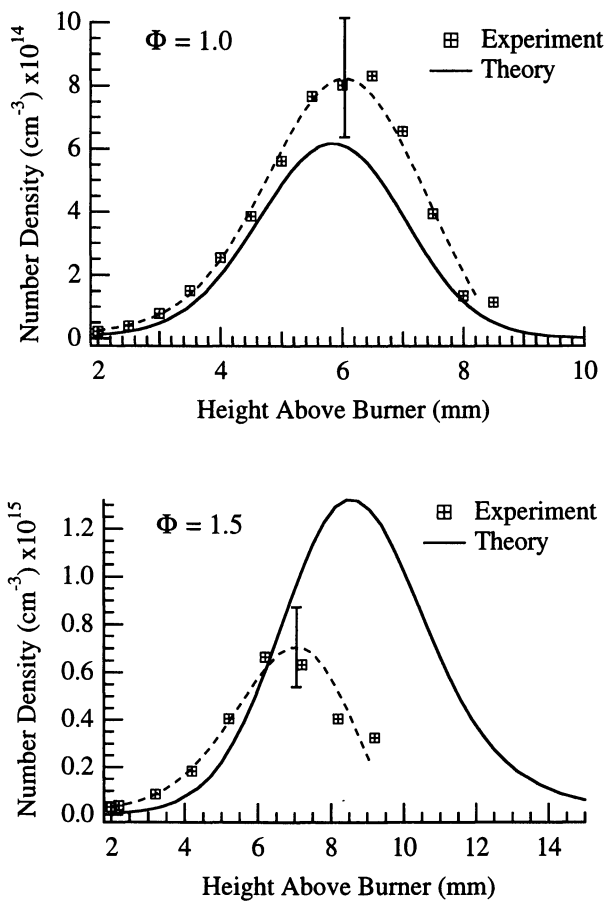


Figure 7. Experimental and predicted methyl radical concentration profiles for stoichiometric ( $\Phi=1.0$ ) and rich ( $\Phi=1.5$ ) flames.

their respective fundamental beam waist diameters. In the case of efficient mode matching, the smallest probe beam diameter will be equal to the fundamental mode beam waist, which increases with the square root of the laser wavelength. For this reason, the precision of the CRLAS-obtained concentrations will degrade with increasing pressure or as one extends further into the infrared. Additionally, the total probe volume across the burner face should be compared with the theoretical transverse mode dimensions (tapering to the beam waist), which changes more appreciably as the cavity geometry is made closer to confocal. In the present studies, the probe beam diameter is essentially constant over the 6 cm burner dimension. Near constant beam waists are achieved by employing mirrors with a radius of curvature much larger than the cavity length. These 37.5 Torr flames were chosen for the present study based on the above spatial considerations, in addition to the difficulty of maintaining a flat, homogeneous flame profile at lower pressures. Although it is anticipated that CRLAS will have further potential applications in other combustion environments, the quantitative value of the data will be compromised at either significantly higher pressures or in cases where the flame symmetry is not suited to line-of-sight measurements.

## Conclusion

Infrared and visible CRLAS were employed for the quantitative study of methyl and formyl radicals in low pressure, laminar, methane-air flames. CARS spectra of molecular nitrogen were combined with the CRLAS measurements to obtain absolute species concentrations as a function of height above the burner surface. The ability to obtain quantitative spectral information in low pressure flames has been demonstrated, with emphasis on the inherent limitations of CRLAS as well as the difficulties associated with performing spectroscopic measurements in flames in the mid-infrared. While the absorption and concentration data are well correlated as a function of HAB values, significant deviation occurs in the case of methyl. This uncorrelated behavior is even more pronounced for other polyatomic radicals important in combustion processes, such as the hydroperoxyl and propargyl radicals. As a result, the ability to extract quantitative concentration information from CRLAS absorption spectra depends on both the species and temperature gradients, which markedly increase with increasing pressure. Although the utility of CRLAS for quantitative concentration determinations will likely be limited to low pressure systems due to such gradients, these studies collectively demonstrate the suitability of CRLAS for the study of polyatomic radicals in low pressure combustion environments.

## Acknowledgments

This work was supported by the U.S. Department of Energy, Office of Basic Energy Sciences, Chemical Sciences Division. We would like to acknowledge J. Volponi for providing the flame simulation results and E. Bochenski for technical assistance.

## Cited References:

- <sup>1</sup> see e.g. A. C. Eckbreth, *Laser Diagnostics for Combustion Temperature and Species*, A. K. Gupta and D. G. Lilley (Eds.), Abacus Press, Tunbridge Wells (1988)
- <sup>2</sup> see e.g. K. Kohse-Höinghaus, *Prog. Energy Combust. Sci.* **20**, 203 (1994).
- <sup>3</sup> see e.g. J.T. McKinnon, E. Abraham, and J.H. Miller, *Combustion Science and Technology* **85**, 391 (1992), R.R. Skaggs, and J.H. Miller, *Combustion and Flame* **100**, 430(1995), D. S. Cline and P. L. Varghese, *Twenty-Third Symposium (International) on Combustion*, The Combustion Institute, Pittsburgh, 1990, pp 1861-1868, and Q. V. Nguyen, B. L. Edgar, R. W. Dibble, and A. Gulati, *Combustion and Flame* **100**, 395 (1995)
- <sup>4</sup> G. Meijer, M.G.H. Boogaarts, R.T. Jongma, D.H. Parker, and A.M. Wodtke, *Chem. Phys. Lett.* **217**, 112 (1994)
- <sup>5</sup> J.J. Scherer, D. Voelkel, and D.J. Rakestraw, *Appl. Phys. B*, **64**, 699 (1997)
- <sup>6</sup> S. Cheskis, *J. Chem. Phys.* **102**, 1851 (1995)
- <sup>7</sup> J.J. Scherer and D.J. Rakestraw, *Chem Phys. Lett.*, **265**, 169 (1997)
- <sup>8</sup> J. J. Scherer, K. W. Aniolek, N. P. Cernansky, and D. J. Rakestraw, *J. Chem Phys.* **107**, 6196 (1997)
- <sup>9</sup> P. Zaliki, Y. Ma, R.N. Zare, E.H. Wahl, J.R. Dadamio, T.G. Owano, and C.H. Kruger *Chem Phys. Lett.*, **234**, 269 (1995)
- <sup>10</sup> J.J. Scherer, D. Voelkel, J.B. Paul, C.P. Collier, D.J. Rakestraw, R. Saykally, and A. O'Keefe, *Chem Phys. Lett.*, **245**, 273 (1995)
- <sup>11</sup> R.E. Palmer, SAND89-8206, Sandia National Laboratories, Livermore. Contact R.L. Farrow, Sandia National Laboratories, MS9057 (email: farrow@ca.sandia.gov) for availability
- <sup>12</sup> J.J. Scherer, J. B. Paul, A. O'Keefe, and R.J. Saykally *Chem. Rev.* **97** (1), 25 (1997)
- <sup>13</sup> J. Martin ;B. A. Paldus;P. Zalicki ;E. H. Wahl; and R.N. Zare, *Chem. Phys. Lett.* **258**, 63 (1996)
- <sup>14</sup> J. T. Hodges ;J.P. Looney ; and R. D. Van Zee, *J. Chem. Phys.* **105**, 10278 (1996)
- <sup>15</sup> G.A. Bethardy and R. G. MacDonald. *J. Chem. Phys.* **103**, 2863 (1995)
- <sup>16</sup> J.Pauwels, J. V. Volpani, and J.A. Miller, *Combust. Sci. and Tech.* **110-111**, 249 (1995)
- <sup>17</sup> D.A. Ramsay, *J. Chem. Phys.* **21**, 1960 (1953)
- <sup>18</sup> J. S. Bernstein, X.-M. Song, and T. A. Cool, *Chem. Phys. Lett.* **145**, 188 (1988)
- <sup>19</sup> J. B. Jeffries, D. R. Crosley, I.J. Wysong, and G.P. Smith, *Twenty-Third Symposium (International) on Combustion/ The Combustion Institute 1990*, p.1847
- <sup>20</sup> V. A. Lozovsky, S. Cheskis, A. Kachanov, and F. Stoekel *J. Chem. Phys.* **20**, 8384 (1997)
- <sup>21</sup> R. Vasudev and R.N. Zare, *J. Chem. Phys.* **72**, 5267 (1982)
- <sup>22</sup> B. Veyret, P. Roussel, and R. Lesclaux, *Chem. Phys. Lett.* **103**, 389 (1989)
- <sup>23</sup> S.A. Mulenko, *Z. Prikl. Spektroskopii* **33**, 35, (1980)
- <sup>24</sup> D. B. Oh, A.C. Stanton, and J. A. Silver, *J. Phys. Chem.* **97**, 2246 (1993)

- 
- <sup>25</sup>J.E. Baggott, H.M. Frey, P.D. Lightfoot, and R. Walsch, *Chem. Phys. Lett.* **132**, 225 (1986)
- <sup>26</sup>A. O. Langford and C. B. Moore, *J. Chem. Phys.* **80**, 4204 (1984)
- <sup>27</sup>L. Zhu, D. Kellis, and C.-F. Ding, *Chem. Phys. Lett.* **257**, 487 (1996)
- <sup>28</sup>see e.g. J.A. Miller, R.J. Kee, and C. K. Westbrook, *Ann. Rev. Phys. Chem.*, **41**, 345 (1990)
- <sup>29</sup>W.Y. Fan, J. Ropcke and P.B. Davies, *J. Vac. Sci. Tech. A.*, **14** 2970 (1996)
- <sup>30</sup>G. Herzberg and J. Shoosmith, *Can. J. Phys.*, **34**, 523, (1956)
- <sup>31</sup>T. Amano, P. F. Bernath, and C. Yamada, Y. Endo, E. Hirota, *J. Chem. Phys.* **77**, 5284 (1982)
- <sup>32</sup>J. Wormhoudt and K. E. McCurdy, *Chem. Phys. Lett.*, **156**, 47, (1989)
- <sup>33</sup>I. Tanarro, M.M. Sanz, C Domingo, D. Bermejo, J. Santos, and J. L. Domenech *J. Phys. Chem.*, **989**, 5862 (1994)
- <sup>34</sup>V. Sick, M.N. Bui-Pham, and R.L. Farrow *Opt. Lett.*, **20**, 2036 (1995)
- <sup>35</sup>R.L. Farrow, M.N. Bui-Pham, and V. Sick, **Paper 623**, *Twenty-Sixth Symposium (International) on Combustion*, The Combustion Institute 1996
- <sup>36</sup>T. Etzkorn, J. Fitzer, S. Muris and J. Wolfrum, *Chem. Phys. Lett.*, **208**, 307 (1993)
- <sup>37</sup>H. Kojima, H. Toyoda, and H. Sugai, *Appl. Phys. Lett.*, **55**, 1292 (1989)
- <sup>38</sup>J. Wormhoudt, *J. Vac. Sci.* **A8(3)**, 1722 (1990)
- <sup>39</sup>L.R. Thorne and C.F. Melius, *Twenty-Third Symposium (International) on Combustion*, The Combustion Institute, Pittsburg (1990) pp 397-403



## Chapter 13

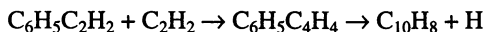
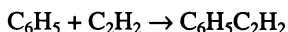
# Kinetic Studies of Aromatic Radical Reactions by Cavity-Ringdown Spectroscopy

J. Park and M. C. Lin

Department of Chemistry, Emory University, Atlanta, GA 30322

The cavity ringdown (CRD) technique has been applied to measure the absolute rate constants of  $C_6H_5$  radical reactions relevant to incipient soot formation. The high sensitivity of the CRD technique allows us to determine reproducibly the absolute values of rate constants to as low as  $10^{-16}$ - $10^{-15}$   $cm^3/molecule \cdot s$ , which is as good as what can be achieved by the laser-induced fluorescence technique for fluorescing species. The absolute rate constants for reactions with NO, O<sub>2</sub>, C<sub>2</sub>H<sub>2</sub>, C<sub>2</sub>H<sub>4</sub>, *i*-C<sub>4</sub>H<sub>10</sub>, (*i*-C<sub>3</sub>H<sub>7</sub>)<sub>2</sub>, cycloalkanes (C<sub>5</sub>H<sub>10</sub> - C<sub>8</sub>H<sub>16</sub>), CCl<sub>4</sub>, HBr and DBr have been determined over the temperature range 297-523 K. The mechanisms involved in these reactions are discussed.

Phenyl radical is an important reactive intermediate in the combustion of small aromatic hydrocarbons (key ingredients of lead-free gasoline) and in the formation of polycyclic aromatic hydrocarbons (PAH's), the building blocks of soot in hydrocarbon combustion reactions (1-5). The reaction of  $C_6H_5$  with C<sub>2</sub>H<sub>2</sub>, for example, has been suggested as the key process leading to the production of naphthalene (C<sub>10</sub>H<sub>8</sub>) (1,4), viz.



The repetition of such a successive addition/cyclization process involving increasingly larger aromatic radicals has been proposed as a possible route to the formation of PAH's which give rise to soot (4).

In order to elucidate of the soot formation mechanism and the aromatic hydrocarbon combustion chemistry, we have carried out a series of studies (5-12) on the kinetics and mechanisms of phenyl radical reactions with a number of combustion species: C<sub>2</sub>H<sub>2</sub>, C<sub>2</sub>H<sub>4</sub>, CH<sub>2</sub>O, NO, O<sub>2</sub>, and alkanes, etc. In addition, organic solvent

molecules, such as cyclopentane, cyclohexane and carbon tetrachloride, which were employed extensively by organic chemists in their studies of phenyl radical kinetics in solution as reference standards using the relative rate methods, have been investigated in this work. In this chapter, we review the application of a novel multipass laser absorption technique first employed by O'Keefe and Deacon (13) who referred to it as the cavity ringdown method, to determine for the first time the absolute rate constants for these  $C_6H_5$  and related  $C_6H_5O$  reactions in the gas phase. Our discussion will focus on the methods of data acquisition and analysis as well as the rate constants obtained for  $C_6H_5$  reactions over the broad range of the molecular reagents investigated.

## Experimental and Results

**A. Apparatus.** The experiment was carried out with the apparatus constructed for the studies of the kinetics of nonfluorescing radical reactions using the cavity ringdown (CRD) technique. This reaction system, including the flow reactor and the data acquisition equipment, is schematically presented in Fig. 1.

All experiments were performed under slow-flow conditions using Ar as the carrier gas. The flow reactor consists of a heatable Pyrex glass tube attached with two pairs of laser windows opposite of each other, permitting the two-split photolysis laser beams to cross at the center of the reactor at a  $30^\circ$  angle. The reactor was vacuum-sealed at the ends with a pair of highly reflective mirrors ( $R = 0.9999$  at 500 nm, radius curvature 6 m), which form a high quality optical cavity, approximately 50 cm in length. The quality of the cavity is such that a pulse of probing dye laser operating at 500 nm with FWHM  $\approx 10$  ns can be lengthened to about 20  $\mu$ s, providing an effective optical path of  $6 \times 10^5$  cm.

Two pulsed lasers were employed, one for the generation of the  $C_6H_5$  radical and the other for its detection. For radical generation, we employed Lambda Physik LPX 100 excimer laser, either at 193 nm (with  $C_6H_5COCH_3$  as the radical precursor) or at 248 nm (with  $C_6H_5NO$  as the precursor). For the probing of the  $C_6H_5$  radical, either a Laser Photonics nitrogen laser or Lambda Physik excimer laser pumped tunable dye laser was used. It has a half-width of about 5 or 10 ns respectively, and pulse energy of 1-2 mJ at 500 nm. As shown in Fig. 1, the probing laser was injected directly into the reactor cavity through one of the mirrors along the axis of the reactor tube. A fraction

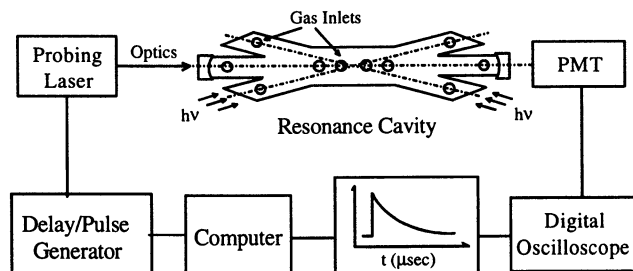


Figure 1. Schematic diagram of the cavity-ring-down absorption apparatus.

of the photon pulse transmitted through the second mirror was filtered and detected with a Hamamatsu photomultiplier tube (PMT). Photoelectric signal from the PMT was amplified with a fast preamplifier (SR445) and acquired and averaged with a multichannel digital oscilloscope (LeCroy 9310 M). The averaged signal was stored in a computer for future data analysis. A pulse-delay generator (SR DG 535) interfaced with the computer was employed to control the firing of the two lasers as well as the triggering of the data acquisition system.

**B. Chemicals.** All chemicals employed in the study, except  $O_2$  and Ar, were obtained from Aldrich. They were purified by trap-to-trap distillation using appropriate slush baths before use.  $O_2$  and the Ar carrier gas, acquired from Specialty Gases (99.995% UHP grade), were used without further purification.

**C. Kinetic Data Acquisition and Analysis.** For kinetic measurements, both  $C_6H_5$  and  $C_6H_5O_2$ , the product of the  $C_6H_5 + O_2$  reaction at low temperatures, have been used as probes. As has been described previously (5), the  $C_6H_5$  radical has distinct absorption features in the 450-530 nm region. We selected one of the strongest absorption peaks which appears at 504.8 nm to monitor  $C_6H_5$  decay rates in its reaction with all reagents except  $O_2$ . For the reaction of  $C_6H_5$  with  $O_2$ , we measured the rates of formation of  $C_6H_5O_2$  (phenylperoxy radical), which is the only product of the reaction formed in the temperature range studied, 297-523 K (11). The  $C_6H_5O_2$  radical has been shown by us in the gas phase and by Alfassi, von Sonntag and coworkers (14) in aqueous solution to have a broad and strong visible absorption peaking at 490 nm. Accordingly, for the kinetics of the  $C_6H_5 + O_2$  reaction, we measured the rise time of the phenyl peroxy radical at 496.4 nm at which no absorption by  $C_6H_5$  occurs.

The CRD method measures the decay times of the injected probing photons in the absence ( $t_c^o$ ) and the presence ( $t_c$ ) of absorbing species. These photon decay times can be related to the concentration of the species at time  $t'$  after its generation by the

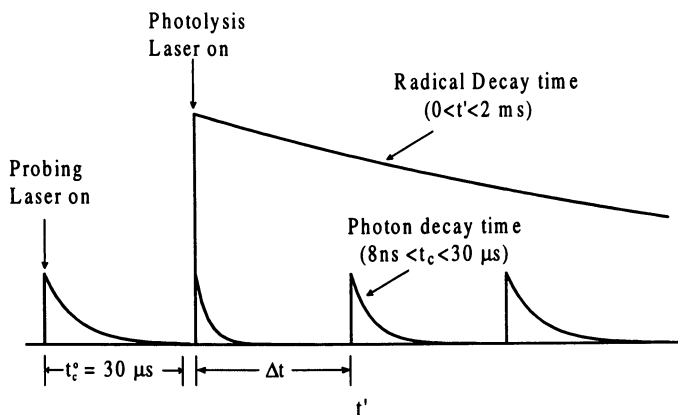


Figure 2. Relationship between photon decay times and radical decay time.

equation (5-12),

$$1/t_c = 1/t_c^o + B[A]_o e^{-k't'} \quad (\text{Ia})$$

or

$$\ln(1/t_c - 1/t_c^o) = C - k't' \quad (\text{Ib})$$

where  $[A]_o$  is the initial concentration of the radical species of interest,  $C_6H_5$ ,  $B$  is a constant which contains experimental parameters such as the cavity length (50 cm), the refractive index of the absorbing medium, etc. (5,6), and  $C = \ln(B[A]_o)$ . Eq. (I) is valid provided that the decay time of the species of interest is much longer than that of photons within the cavity as illustrated in Fig. 2. This condition can be readily met because the chemical decay time, typically in the range of several hundreds of microseconds to tens of milliseconds, can be controlled by the concentration of the molecular reagent.

The slopes of the  $\ln(1/t_c - 1/t_c^o)$  vs.  $t'$  plots as illustrated in Fig. 3 for the reactions of  $C_6H_5$  with cyclohexane yield the pseudo-first-order rate coefficients,  $k'$ , for the decay of  $C_6H_5$  in the presence of known, excess  $c-C_6H_{12}$  concentrations as specified. A standard plot of  $k'$  vs. reagent concentration is shown in Fig. 4, which gives the averaged second-order rate constant  $k''$  from its slope according to the relationship

$$k' = k^o + k_x'' [X] \quad (\text{II})$$

where  $k^o$  is the radical decay constant in the absence of the molecular reactant  $X$  due to the loss of the radical by diffusion away from the probing beam and recombination reactions (e.g.,  $C_6H_5 + NO$  and  $C_6H_5 + C_6H_5$ ):

In the second-order plot illustrated by Fig. 4, we have also included the first-order decay constants obtained by monitoring  $C_6H_5O_2$  formed by the  $C_6H_5 + O_2$  reaction when a small, constant amount of  $O_2$  was added to the system. The advantage of using  $C_6H_5O_2$  as a probe lies in its broad and much larger extinction coefficient than  $C_6H_5$  in the visible region (11). In this case, the rise time of the absorption by the

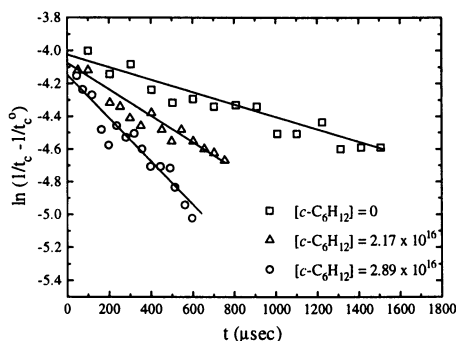


Figure 3. Typical pseudo-first order decay plots for the  $C_6H_5 + c-C_6H_{12}$  reaction under various excess concentrations of  $c-C_6H_{12}$  at 333 K. Concentration units are in molecules/cm<sup>3</sup>.

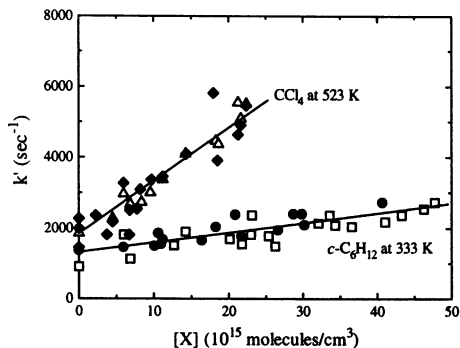


Figure 4.  $k'$  vs.  $[X]$  at 333 K for  $c\text{-C}_6\text{H}_{12}$  and at 523 K for the  $\text{CCl}_4$  reaction. The open symbols obtained by monitoring the decay of  $\text{C}_6\text{H}_5$  (eq. I) and the solid symbols by measuring the formation of  $\text{C}_6\text{H}_5\text{O}_2$  (eq. III).

peroxy radical in the presence of a known, large excess amount of molecular reagent (such as  $c\text{-C}_6\text{H}_{12}$  or  $\text{CCl}_4$  as shown in Fig. 4) was measured and analyzed with the equation (11,12)

$$1/t_c = 1/t_c^o + B[A]_o (1 - e^{-k't'}) \quad (\text{III})$$

where

$$k' = k^o + k_{\text{O}_2}'' [\text{O}_2] + k_x'' [X] \quad (\text{IV})$$

At long reaction time ( $t' \rightarrow \infty$ ) the absorption is expected to reach a plateau value with the photon decay time,  $t_c^\infty$ :

$$1/t_c^\infty = 1/t_c^o + B[A]_o \quad (\text{V})$$

Combining eqs. (III) and (V) and rearranging yield

$$\ln[t_c / (t_c - t_c^\infty)] = C + k't' \quad (\text{VI})$$

where  $C = \ln[t_c^o / (t_c^o - t_c^\infty)]$ , which is independent of the chemical reaction time  $t'$  for each experimental run. With eq. (III), we analyzed the measured photon decay time by nonlinear least-squares regression. Eq. (VI) predicts the existence of a linear relationship between  $\ln[t_c^o / (t_c^o - t_c^\infty)]$  and  $t'$  (12). The plot of  $k'$  vs.  $X$  is shown in Fig. 4. For the examples given,  $\text{C}_6\text{H}_5$  +  $c\text{-C}_6\text{H}_{12}$  and  $\text{CCl}_4$ , the second order rate constants obtained by both probing methods agree closely.

## Result and Discussion

To date, the kinetics of many reactions involving  $\text{C}_6\text{H}_5$  and  $\text{C}_6\text{H}_5\text{O}$  radicals have been studied in this laboratory by the CRD technique. The systems selected in the initial

phase of our investigation lie either in their relevancy to the chemistry of incipient soot formation or in their kinetic implications to numerous other processes studied in solution by the relative rate method; for example,  $C_6H_5$  with  $c-C_5H_{10}$ ,  $c-C_6H_{12}$  and  $CCl_4$ , some of the most common organic solvents as well as reaction standards employed in earlier relative rate studies. Several of these systems are selected for discussion below.

**A.  $C_6H_5 + NO$ .** The association of  $C_6H_5$  with  $NO$  produces nitrosobenzene in a simple manner:



The reaction is very relevant because nitrosobenzene is a convenient thermal and photochemical source of  $C_6H_5$ . The rate constant for reaction (1) is not known although that for the decomposition of  $C_6H_5NO$  has been reported by Choo et al. using the very-low pressure pyrolysis (VLPP) technique (15). This early result, as will be shown later, is not very reliable and the C-N bond energy derived from the VLPP study is too low.

The values of  $k_1$  measured by CRD in the temperature range 298-500 K can be given by:

$$k_1 = 10^{-11.35 \pm 0.06} \exp[+(433 \pm 111)/T] \text{ cm}^3/(\text{molecules} \cdot \text{s})$$

The reaction was found to be independent of pressure in the 20-120 Torr range.

Recently, we have investigated the reverse, decomposition reaction (-1) employing Fourier transform infrared (FTIR) spectrometry under atmospheric pressure in the temperature range 556-648 K with  $k_{-1} = (1.42 \pm 0.13) \times 10^{17} \exp(-27,710 \pm 544)/T) \text{ s}^{-1}$ . A third-law analysis of the forward ( $k_1$ ) and reverse ( $k_{-1}$ ) rate constants gave rise to the 0 K C-N bond energy of  $54.12 \pm 0.50 \text{ kcal/mol}$ . This value agrees quantitatively with the theoretically predicted result, 53.8-55.4 kcal/mol using the G2M method (16). These new values, after a minor thermal correction to 298 K, are higher than the accepted one based on the VLPP result of Choo et al. (15) ( $51 \pm 2 \text{ kcal/mol}$ ) by as much as 4 kcal/mol. The correlation of  $k_1$  and  $k_{-1}$  using the theoretically calculated equilibrium constant is presented in Fig. 5.

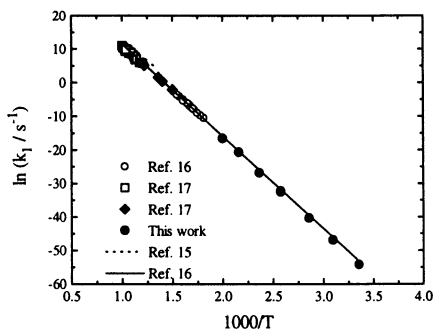
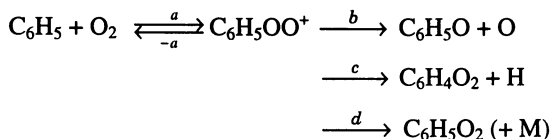


Figure 5. Comparison of the nitrosobenzene decomposition rate after high-pressure-limit correction for data reported in Ref. 17 for  $k_1$  and  $k_{-1}$  by the RRKM theory.

**B.  $C_6H_5 + O_2$ .** The rate constant for the  $C_6H_5 + O_2$  reaction was monitored conveniently by the rise time of the  $C_6H_5O_2$  CRD signal at 496.4 nm (where no absorption by  $C_6H_5$  was shown to occur) analyzed with eqs. (III) and (VI). The second-order rate constant measured under the conditions:  $20 \text{ Torr} \leq P \leq 80 \text{ Torr (Ar)}$  and  $297 \text{ K} \leq T \leq 473 \text{ K}$ , were found to be pressure-independent with a small negative activation energy of 0.32 kcal/mol. The absence of pressure effect and the small negative temperature dependence, as illustrated in Fig. 6(A), are fully consistent with the result of an RRKM calculation based on the following mechanism:



The transition states for steps (b) and (c) could be constructed to account for the data of Frank et al. for the production of O and H atoms (18):  $k_O = 4.3 \times 10^{-11} \exp(-3,080/T)$  and  $k_H = 5.0 \times 10^{-11} \exp(-4,520/T) \text{ cm}^3/\text{molecule}\cdot\text{s}$ . The calculated rate constants for the three product channels are summarized in Figs. 6(A) and 6(B) as functions of pressure and temperature.

The theoretical results quantitatively support our findings that the  $C_6H_5 + O_2$  reaction occurs primarily by the addition/stabilization process producing  $C_6H_5O_2$  at low temperatures ( $T < 1000 \text{ K}$ ). Above 1000 K, the formation of  $C_6H_5O + O$  and  $C_6H_4O_2 + H$  becomes competitive with the  $C_6H_5O_2$  channel. Under combustion conditions (*i.e.*, high T and P), the rate constants for the individual channels are strongly T, P-dependent (11).

**C.  $C_6H_5 + C_2H_2$  and  $C_2H_4$ .** The reactions of  $C_6H_5$  with both  $C_2H_2$  (9) and  $C_2H_4$  (10) were studied by monitoring the decay of  $C_6H_5$  at 504.8 nm. The second order rate constants evaluated with eqs. (I)-(III) for 297-523 K at a constant reaction pressure of 20 Torr Ar for  $C_2H_2$  and  $C_2H_4$  can be represented respectively by

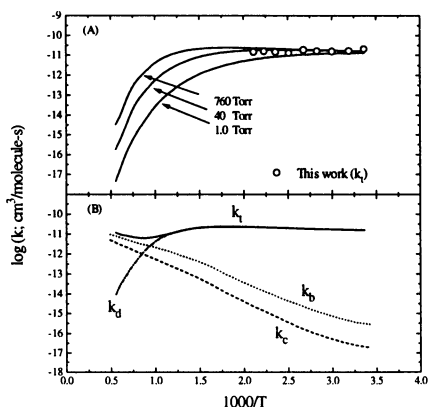


Figure 6. Arrhenius plots for the  $C_6H_5 + O_2$  reaction. (A), experimental data (O) and the RRKM results (curves for different pressures); (B), predicted rate constants for the processes of  $C_6H_5 + O_2 \rightarrow C_6H_5O + O$  ( $k_b$ ),  $C_6H_5 + O_2 \rightarrow C_6H_4O_2 + H$  ( $k_c$ ) and  $C_6H_5 + O_2 \rightarrow C_6H_5O_2$  ( $k_d$ ) at 2 bar pressure:  $k_1 = k_b + k_c + k_d$ .

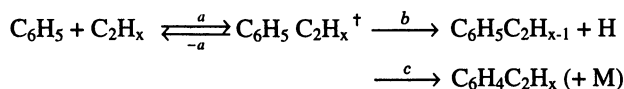
$$k_3 = 10^{-12.43 \pm 0.12} \exp[(-1560 \pm 240)/T]$$

$$k_4 = 10^{-11.92 \pm 0.35} \exp[(-2,250 \pm 630)/T]$$

in units of  $\text{cm}^3/(\text{molecule}\cdot\text{s})$ . These results are summarized in Figs. 7(A) and 7(B) for comparison with those determined by Fahr and Stein (19,20) at low pressures (1-10 mTorr) using a Knudsen cell in the 1000-1300 K temperature range.

For both reactions, Farr and Stein (19,20) employed the recombination reaction of  $\text{C}_6\text{H}_5$  producing biphenyls as a reference reaction. Their results, presented in Figs. 7(A) and 7(B) have been rescaled by using our phenyl recombination rate constant,  $k_r = 10^{-11.92 \pm 0.35} \exp [(-2,250 \pm 630)/T] \text{ cm}^3/(\text{molecule}\cdot\text{s})$  (21).

As is evident from these figures, both their high-temperature (1000-1300 K), low-pressure (1-10 mTorr) data and our low-temperature (297-523 K), high-pressure (20 Torr) results can be quantitatively correlated with the RRKM theory using the following addition/elimination/stabilization mechanism:



where  $x=2$  and 4. Take the  $\text{C}_2\text{H}_2$  ( $x=2$ ) reaction, for example. Under the conditions employed by us, the  $\text{C}_6\text{H}_5 + \text{C}_2\text{H}_2$  reaction produces exclusively  $\text{C}_6\text{H}_5\text{C}_2\text{H}_2$  by the addition/stabilization process. Under the low-pressure, high-temperature conditions used by Fahr and Stein (19,20), the  $\text{C}_6\text{H}_5 + \text{C}_2\text{H}_2$  reaction occurs by the addition/H-atom elimination process yielding  $\text{C}_6\text{H}_5\text{C}_2\text{H}$ , which was measured experimentally with reference to the  $\text{C}_6\text{H}_5$  recombination product,  $\text{C}_{12}\text{H}_{10}$ . Under these separate conditions, the measured rates were controlled by the addition process. We have also calculated the rate constants for the production of  $\text{C}_6\text{H}_5\text{C}_2\text{H}$  and  $\text{C}_6\text{H}_5\text{C}_2\text{H}_2$  under the atmospheric pressure of Ar or  $\text{N}_2$  for the temperature range 300-2000 K:

$$k_{3b} = 9.5 \times 10^{-42} T^{9.33} \exp(-1,713/T)$$

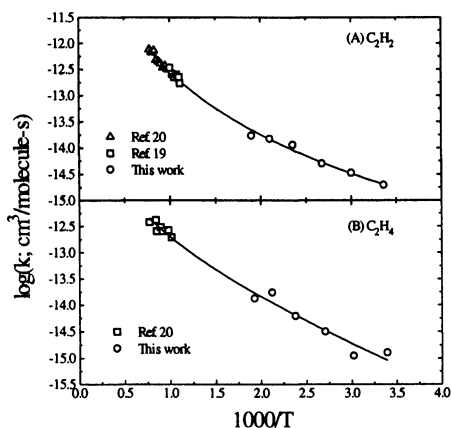


Figure 7. Arrhenius plots for the  $\text{C}_6\text{H}_5 + \text{C}_2\text{H}_2$  (A) and  $\text{C}_2\text{H}_4$  (B). Curves are RRKM values for the total rate constants.



$$k_{3c} = 1.8 \times 10^{-7} T^{-1.65} \exp(-2,711/T)$$

$$k_{3t} = k_{3b} + k_{3c} = 4.1 \times 10^{-18} T^{1.77} \exp(-1,152/T),$$

all given in units of  $\text{cm}^3/(\text{molecule}\cdot\text{s})$ . Under combustion conditions, the production of  $\text{C}_6\text{H}_5\text{C}_2\text{H}$  and  $\text{C}_6\text{H}_5\text{C}_2\text{H}_2$  from  $\text{C}_6\text{H}_5 + \text{C}_2\text{H}_2$  is equally important; both are relevant to the formation of PAH's and soot (9). A similar calculation was made for the  $\text{C}_2\text{H}_4$  reaction as presented in Fig. 7(B).

**D.  $\text{C}_6\text{H}_5 + i\text{-C}_4\text{H}_{10}$  and  $(i\text{-C}_3\text{H}_7)_2$ .** The reactivities of aromatic radicals towards alkanes, particularly with respect to the primary, secondary and tertiary C-H bonds, remain to be characterized. In the first of this series of studies, we investigated the reaction of  $\text{C}_6\text{H}_5$  with  $i\text{-C}_4\text{H}_{10}$  and  $(i\text{-C}_3\text{H}_7)_2$  which contain one and two *t*-C-H bonds, respectively. These data will be compared with those obtained from the reactions with  $\text{C}_2\text{H}_6$  and *neo*- $\text{C}_5\text{H}_{12}$  to sort out the (probably small) contribution from their *p*-C-H bonds.

By monitoring the decay of  $\text{C}_6\text{H}_5$  at 504.8 nm in the presence of varying amounts of the molecular reactants, we obtained reasonable and reproducible second-order rate constants in units of  $\text{cm}^3/(\text{molecule}\cdot\text{s})$  for the isobutane and di-isopropyl reactions in the temperature range 298-500 K:



with

$$k_5 = 10^{-13.30 \pm 0.18} \exp [(-1532 \pm 150)/T] \text{ cm}^3/(\text{molecule}\cdot\text{s}),$$

$$k_6 = 10^{-12.06 \pm 0.15} \exp [(-1007 \pm 124)/T] \text{ cm}^3/(\text{molecule}\cdot\text{s})$$

Their Arrhenius plots are presented in Fig. 8. For reaction (5), Duncan and Trotman-Dickenson(22) reported a relative rate to the recombination of  $\text{C}_6\text{H}_5$ . Combination of their relative rate with our recombination rate constant gave rise to values which are lower by at least an order of magnitude.

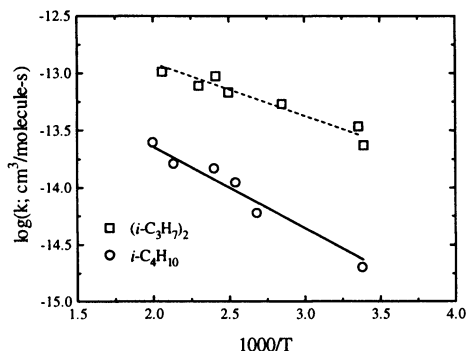


Figure 8. Arrhenius plots for the  $\text{C}_6\text{H}_5 + i\text{-C}_4\text{H}_{10}$  and  $(i\text{-C}_3\text{H}_7)_2$ .

**E.  $C_6H_5$  + cycloalkanes ( $C_5H_{12}$  -  $C_8H_{16}$ ).** As alluded to in the introduction, cycloalkanes, particularly  $c$ - $C_5H_{10}$  and  $c$ - $C_6H_{12}$ , have been employed as solvents and reference standards in the earlier rate studies of  $C_6H_5$  reactions in solution by Bridger and Russell (23,24). The  $C_6H_6$  product formed in the reactions,



offers a convenient standard for reactions involving non-hydrogen-containing reactants such as  $CCl_4$ :



By the well-used relative rate method, the rate constant ratio for the  $c$ - $C_5H_{10}$  reaction, for instance, can be readily determined by the relationship:

$$k_7/k_9 = ([CCl_4][C_6H_6])/([c-C_5H_{10}][C_6H_5Cl]) \quad (VII)$$

where  $[X]$  represents absolute concentration of  $X$  measured in the early stages of the reaction in solution. For  $C_6H_5$ , numerous reactions involving organic compounds have been measured at limited temperatures (298 or 333 K) (23-25). With the  $CCl_4$  or the  $c$ - $C_6H_{12}$  reaction as a reference standard, the absolute rate constant for  $C_6H_5 + O_2$  reported by Bridger and Russell, after the conversion with our  $k_8$  or  $k_9$ , was found to agree reasonably with the result presented in section III-B (12).

The second-order rate constants for reactions (7) and (8) are presented in Fig. 9. Those for the phenyl reactions with  $c$ - $C_7H_{14}$ ,  $k = (8.16 \pm 0.43) \times 10^{-14}$  and  $c$ - $C_8H_{16}$ ,  $k = (8.95 \pm 3.16) \times 10^{-14}$   $cm^3/(molecule \cdot s)$ , both determined at 333 K, are summarized in Table I. An inspection of the reactivities of  $C_6H_5$  toward these cycloalkanes reveals no simple correlation of the absolute rate constant with the numbers of  $s$ -CH bonds available in these molecules. Further studies will be carried out for analogous reactions with  $n$ -alkanes.

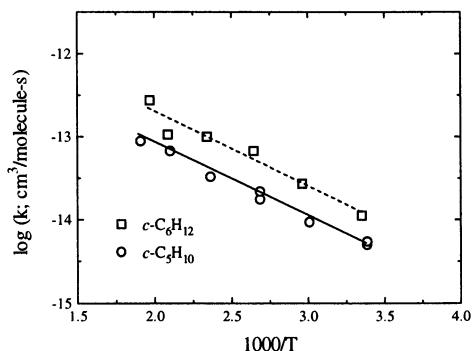


Figure 9. Arrhenius plots for the  $C_6H_5 + c$ - $C_5H_{10}$  and  $c$ - $C_6H_{12}$ .

TABLE I: Absolute Rate Constants for the Reactions of C<sub>6</sub>H<sub>5</sub> Studied by the CRD Method<sup>a</sup>

Reaction	T (K)	A	B	C
C <sub>6</sub> H <sub>5</sub> + NO	298-500	4.47×10 <sup>-12</sup>	0	-433
C <sub>6</sub> H <sub>5</sub> + HBr	297-523	3.98×10 <sup>-11</sup>	0	554
C <sub>6</sub> H <sub>5</sub> + DBr	298-500	4.37×10 <sup>-11</sup>	0	612
C <sub>6</sub> H <sub>5</sub> + C <sub>2</sub> H <sub>2</sub>	297-523	3.72×10 <sup>-13</sup>	0	1,560
→ C <sub>6</sub> H <sub>5</sub> C <sub>2</sub> H+H	300-1500	9.50×10 <sup>-42</sup>	0	1,713 <sup>b</sup>
→ C <sub>6</sub> H <sub>5</sub> C <sub>2</sub> H <sub>2</sub>	300-1500	1.80×10 <sup>-7</sup>	-1.63	2,711 <sup>b</sup>
C <sub>6</sub> H <sub>5</sub> + C <sub>2</sub> H <sub>4</sub>	297-523	1.20×10 <sup>-12</sup>	0	2,250
→ C <sub>6</sub> H <sub>5</sub> C <sub>2</sub> H <sub>3</sub> +H	300-2000	1.20×10 <sup>-22</sup>	3.50	4,200 <sup>b</sup>
→ C <sub>6</sub> H <sub>5</sub> C <sub>2</sub> H <sub>4</sub>	300-2000	1.50×10 <sup>-17</sup>	-9.30	6,640 <sup>b</sup>
C <sub>6</sub> H <sub>5</sub> + O <sub>2</sub>	298-473	1.00×10 <sup>-11</sup>	0	-161
C <sub>6</sub> H <sub>5</sub> + <i>c</i> -C <sub>3</sub> H <sub>10</sub>	297-523	4.47×10 <sup>-12</sup>	0	2,039
C <sub>6</sub> H <sub>5</sub> + <i>c</i> -C <sub>6</sub> H <sub>12</sub>	297-523	7.94×10 <sup>-12</sup>	0	1,913
C <sub>6</sub> H <sub>5</sub> + <i>c</i> -C <sub>7</sub> H <sub>14</sub>	333	8.20×10 <sup>-14</sup>		
C <sub>6</sub> H <sub>5</sub> + <i>c</i> -C <sub>8</sub> H <sub>16</sub>	333	9.00×10 <sup>-14</sup>		
C <sub>6</sub> H <sub>5</sub> + CCl <sub>4</sub>	297-523	2.00×10 <sup>-12</sup>	0	1,379
C <sub>6</sub> H <sub>5</sub> + <i>i</i> -C <sub>4</sub> H <sub>10</sub>	295-501	5.01×10 <sup>-13</sup>	0	1,532
C <sub>6</sub> H <sub>5</sub> + ( <i>i</i> -C <sub>3</sub> H <sub>7</sub> ) <sub>2</sub>	295-487	8.71×10 <sup>-13</sup>	0	1,007

a. Rate constants are given by  $k = AT^B \exp(-C/T)$  in units of cm<sup>3</sup>/molecule·s.

b. 1 atm pressure (Ar).

**F. C<sub>6</sub>H<sub>5</sub> + CCl<sub>4</sub>.** The relevancy of this reaction lies in its extensive use as a reference standard in solution for the kinetics of C<sub>6</sub>H<sub>5</sub> reactions with many organic compounds as alluded to above. In our investigation by CRD, the absolute rate constant of reaction (9) could be quantitatively determined by monitoring the rise of C<sub>6</sub>H<sub>5</sub>O<sub>2</sub> at 496.4 nm when a small constant concentration of O<sub>2</sub> was added to the flowing mixture as described above. The second-order plot for one of the C<sub>6</sub>H<sub>5</sub> + CCl<sub>4</sub> reaction data sets obtained at 523 K is illustrated in Fig. 4. The Arrhenius plot for  $k_9$  is shown in Fig. 10 in comparison to the sparse condensed phase data determined by the relative rate method (12). The reaction was found to have a small activation energy of 2.7 kcal/mol.

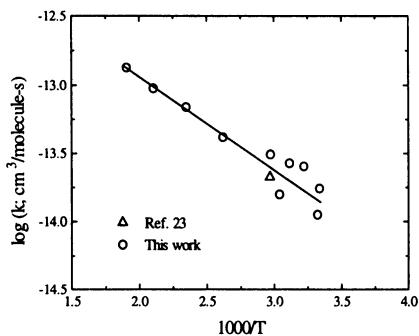


Figure 10. Arrhenius plot for the C<sub>6</sub>H<sub>5</sub> + CCl<sub>4</sub> reaction.

**G. C<sub>6</sub>H<sub>5</sub> + HBr/DBr.** Although these two reactions have no direct relevance to soot formation chemistry, their absolute rate constants are valuable for correlation with existing detailed kinetic data obtained by Gutman (26), Wine(27) and coworkers for alkyl radical reactions with HBr and DBr, which exhibit large negative activation energies from -0.4 kcal/mol for CH<sub>3</sub> to -1.9 kcal/mol for *t*-C<sub>4</sub>H<sub>9</sub> (26,27). Significantly, for the more reactive H atom, the activation energy was determined to be +0.94 kcal/mol (28).

The second-order rate constants determined for the two phenyl reactions



by direct monitoring of C<sub>6</sub>H<sub>5</sub> decay at 504.8 nm are summarized in Fig. 11. A least-squares analysis of these data gave

$$k_{11} = 10^{-10.40 \pm 0.24} \exp [(-554 \pm 208)/T] \text{ cm}^3/(\text{molecule}\cdot\text{s}),$$

$$k_{12} = 10^{-10.36 \pm 0.17} \exp [(-612 \pm 151)/T] \text{ cm}^3/(\text{molecule}\cdot\text{s}),$$

for the temperature ranges 297-523 K and 297-500 K, respectively. The positive, rather than negative, activation energies of the two reactions are most revealing. Aromatic rings are known to be electron-withdrawing, instead of electron-donating as in the case of alkyl radicals. For this reason, we attempted to correlate the activation energies for reactions of HBr and DBr with H, CH<sub>3</sub>, C<sub>2</sub>H<sub>5</sub>, C<sub>3</sub>H<sub>7</sub>, *t*-C<sub>4</sub>H<sub>9</sub> and C<sub>6</sub>H<sub>5</sub> with Taft's σ\* (polar coefficient) obtained by studies on the hydrolysis of α-substituted esters (29).

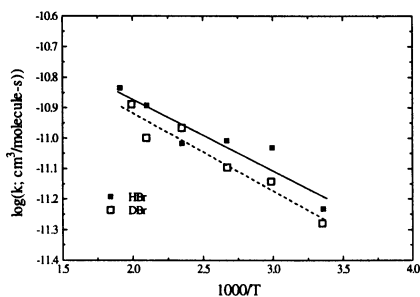


Figure 11. Arrhenius plots for C<sub>6</sub>H<sub>5</sub> + HBr and DBr.

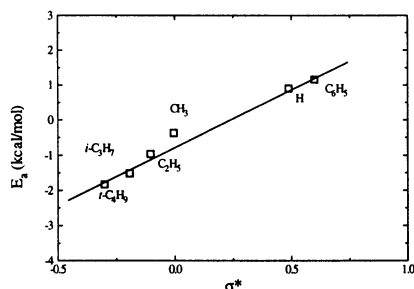


Figure 12. The correlation of the measured activation energies for the R + HBr → RH + Br reaction with Taft's σ\* (polar) values as summarized in ref. 29.

The correlation results summarized in Fig. 12 reveal the existence of a strong correlation for both isotopic reactants. The fact that the more reactive radicals, H and C<sub>6</sub>H<sub>5</sub>, have positive activation energies in their reactions with HBr, contrary to those of the less reactive alkyl radicals, strongly suggests the importance of the polar interaction R<sup>-</sup> - H<sup>+</sup> Br<sup>-</sup> in promoting the metathetical processes, R + HBr → RH + Br.

### Concluding Remarks

In this series of studies on the kinetics of C<sub>6</sub>H<sub>5</sub> radical reactions, we have utilized the new type of multipass laser absorption technique, CRD, first employed by O'Keefe and Deacon, for kinetic applications. The technique appears to be as sensitive as the laser-induced fluorescence method, enabling us to measure absolute rate constants to as low as 10<sup>-16</sup>-10<sup>-15</sup> cm<sup>3</sup>/(molecule·s).

For C<sub>6</sub>H<sub>5</sub> radical reactions, both direct detection using its well-resolved absorption bands in the 400-500 nm region and indirect probing following the growth of C<sub>6</sub>H<sub>5</sub>O<sub>2</sub> absorption continuum between 400-550 nm (when a small amount of O<sub>2</sub> is present) provide very convenient diagnostics for its kinetic measurements. The Arrhenius parameters of all phenyl radical reactions studied to date are summarized in Table I. Extension of these studies to other aromatic radicals and molecular reagents is currently underway.

The versatility of the CRD method for kinetic applications has recently been further demonstrated for C<sub>2</sub>H<sub>5</sub> + O<sub>2</sub> by Atkinson and Hudgens (30) and for C<sub>2</sub>H<sub>3</sub>O + O<sub>2</sub> by Zhu and Johnston (31). Earlier we had also extended the studies to the reactions of NO with NH<sub>2</sub> (32) and C<sub>6</sub>H<sub>5</sub>O (33). In addition, the employment of the probing wavelength to the IR and near-IR regions of the spectrum using diode lasers is a natural trend as has already been witnessed in this symposium.

**Acknowledgment.** The authors gratefully acknowledge the support of this work by the Division of Chemical Sciences, Office of Energy Sciences, DOE under contract No. DE-FG02-97ER14784.

### References

- (1) Glassman, I. *Combustion*, 2nd ed., Academic Press, NY, 1986.
- (2) Brezinsky, K. *Prog. Energ. Combust. Sci.* **1986**, *12*, 1
- (3) Bittner, J.D.; Howard, J.B.; Palmer, H.B. Proc. NATO Workshop, NATOASI Set. VI, Mater. Sci. Lahaye, J.; Prado, G., Eds.; Plenum Press, NY, 1983, vol. 7, pp. 95-125.
- (4) Frenklach, M.; Clary, D.W.; Gardiner, W.C. Jr.; Stein, S.E. *22nd Symp. (Int.) Combust. [Proc.]*, **1988**, *20*, 887.
- (5) Yu, T.; Lin, M.C. *J. Am. Chem. Soc.* **1993**, *115*, 4371.
- (6) Lin M.C.; Yu, T. *Int. J. Chem. Kinet.* **1993**, *25*, 875.
- (7) Yu, T.; Lin, M.C. *Int. J. Chem. Kinet.* **1994**, *26*, 771.
- (8) Yu, T.; Lin, M.C. *J. Phys. Chem.* **1994**, *98*, 2105.
- (9) Yu, T.; Lin, M.C.; Melius, C.F. *Int. J. Chem. Kinet.*, **1994**, *26*, 1095.
- (10) Yu, T.; Lin, M.C. *Combust. Flame*, **1995**, *100*, 169.
- (11) Yu T.; Lin, M.C. *J. Am. Chem. Soc.*, **1994**, *116*, 9571.

- (12) Yu, T.; Lin, M.C. *J. Phys. Chem.*, **1995**, *99*, 8599.
- (13) O'Keefe, A.; Deacon, D. A. G. *Rev. Sci. Instrum.* **1988**, *59*, 2544.
- (14) (A) Mertens, R.; von Sonntag, C., *Angew. Chem. Int. Ed.*, **1994**, *33*, 1262; (B) Khaikin, G. I.; Alfassi, Z. B.; Neta, P. *J. Phys. Chem.* **1995**, *99*, 11447 and 16722.
- (15) Choo, K.-L.; Golden, D. M.; Benson, S. W. *Int. J. Chem. Kinet.* **1975**, *7*, 713.
- (16) Park, J.; Dyakov, I.; Mebel, A. M.; Lin, M. C. *J. Phys. Chem. A* **1997**, *101*, 6043.
- (17) Horn, C.; Frank, P.; Trauter, R. S.; Schaug, J.; Grotheer, H.-H.; Just, Th. *26th Symp. (int.) Combust., [Proc.]*, **1996**, 575.
- (18) Frank, P.; Herzler, J.; Just, Th.; Wahl, C. *25th Symp. (Int.) Combust. [Proc.]*, **1994**, 833.
- (19) Fahr, A.; Mallard W.G.; Stein, S.E. *21st Symp. (Int.) Combust. [Proc.]*, **1986**, *21*, 825.
- (20) Fahr, A.; Stein, S.E. *22nd Symp. (Int.) Combust. [Proc.]* **1988**, *22*, 1023.
- (21) Park, J.; Lin, M. C. *J. Phys. Chem. A* **1997**, *101*, 14.
- (22) Duncan, H. T.; Trotman-Dickenson, A. F. *J. Chem. Soc.* **1962**, 4672.
- (23) Bridger, R.F.; Russell, G.A. *J. Am. Chem. Soc.* **1963**, *85*, 3754.
- (24) Russell, G.A.; Bridger, R.F. *J. Am. Chem. Soc.* **1963**, *85*, 3765.
- (25) Pryor, W.A.; Echols, J.T., Jr.; Smith, K.J. *J. Am. Chem. Soc.* **1966**, *88*, 1189.
- (26) (A) Russell, J. J.; Seetula, J. A.; Gutman, D.; Nava, D. F. *J. Am. Chem. Soc.* **1988**, *110*, 3084; (B) Russell, J. J.; Seetula, J. A.; Gutman, D.; Nava D. F. *J. Am. Chem. Soc.* **1988**, *110*, 3092.
- (27) (A) Nicovich, J. M.; van Dijk, C. A.; Kruetter, K. D.; Wine, P. H. *J. Phys. Chem.* **1991**, *95*, 9890; (B) Nicovich, J. M.; Wine, P. H. *Int. J. Chem. Kinet.* **1990**, *22*, 379; (C) Nicovich, J. M.; Kruetter, K. D.; van Dijk, C. A.; Wine, P. H. *J. Phys. Chem.* **1992**, *96*, 2518;
- (28) Seakins, P. W.; Pilling, M. J.; Niiranen, J.T.; Gutman, D.; Krasnoperov, L. N. *J. Phys. Chem.* **1992**, *96*, 9848.
- (29) Laidler, K. J. *Chemical Kinetics*, 2nd ed., McGraw Hill, 1965, p. 251.
- (30) Atkinson, D. B.; Hudgens, J. W. *J. Phys. Chem. A*, **1997**, *101*, 3901.
- (31) Zhu, L.; Johnston, G. *J. Phys. Chem.*, **1995**, *99*, 15114.
- (32) Diau, E. W. G.; Yu, T.; Wagner, M. A. G.; Lin, M. C. *H. Phys. Chem.* **1994**, *98*, 4043.
- (33) Yu. T; Mebel, A. M.; Lin, M. C. *J. Phys. Org. Chem.* **1995**, *8*, 47.

## Chapter 14

# Cavity-Ringdown Methods for Studying Intramolecular and Intermolecular Dynamics

Fredrick C. Hagemeister, Caleb A. Arrington, Brent J. Giles<sup>1</sup>,  
Bobby Quimpo, Limin Zhang, and Timothy S. Zwier<sup>2</sup>

Department of Chemistry, Purdue University,  
West Lafayette, IN 47907-1393

Cavity ring-down spectroscopy (CRDS) is used in two quite different contexts which demonstrate the power and versatility of the method for answering spectroscopic and dynamical questions about isolated molecules and their molecular clusters. In the first example, CRDS is used to record the direct absorption spectrum of the spin-forbidden  ${}^3\Delta_u \leftarrow {}^1\Sigma_g^+$  transition in diacetylene ( $C_4H_2$ ). The upper state of this transition is thought to be responsible for the efficient photochemistry of diacetylene. An estimate of the integrated absorption cross section for the transition leads to a prediction for the intrinsic phosphorescence lifetime of the upper state of about 1 sec. In the second example, CRDS is combined with laser-induced fluorescence spectroscopy to determine relative single-vibronic level fluorescence quantum yields of jet-cooled tropolone and tropolone- $(H_2O)_n$  clusters with  $n=1-4$  in its  $S_1$  state. The complexation of a single water molecule to tropolone is seen to increase the fluorescence quantum yield of tropolone by a factor of  $8.0 \pm 1.0$ .

Many interesting problems in electronic spectroscopy are those which seek to answer a question of dynamical importance involving such processes as intramolecular vibrational redistribution (IVR), intersystem crossing, internal conversion, photoisomerization, photo-dissociation, and excited state photochemical reactivity.

This paper presents an overview of two areas in which cavity ringdown methods have been used to address questions of dynamical interest regarding: (i) the photo-chemically reactive states of diacetylene, and (ii) solvent effects on the

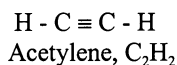
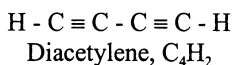
<sup>1</sup>Current address: Department of Chemistry, Mercer University, Macon, GA 31207

<sup>2</sup>Permanent address: Department of Chemical Physics, University of Science and Technology of China, Hefei 230026, China

photophysics of tropolone. The work on diacetylene uses cavity ringdown absorption spectroscopy to detect a spin-forbidden singlet-triplet transition whose upper state is responsible for diacetylene's photochemistry, which our group is currently exploring(1-6). The second study utilizes simultaneous laser-induced fluorescence (LIF) and CRDS measurements to record relative single vibronic level fluorescence quantum yields in jet-cooled tropolone (TrOH) and TrOH-(H<sub>2</sub>O)<sub>n</sub> clusters.

## I. Singlet-triplet spectroscopy of Diacetylene

**A. Introduction.** Diacetylene is the first member of the poly-yne with an obvious and strong linkage with its smaller precursor acetylene.



Diacetylene plays a role in such diverse settings as planetary atmospheres(5) and sooting flames (7). It is the largest hydrocarbon which has been positively identified in the atmosphere of Titan, one of the moons of Saturn (5). Its role in Titan's atmosphere is similar to that of ozone in Earth's atmosphere. Its ultraviolet absorptions (which begin at about 2300 Å), partially shield the lower atmosphere from such radiation. At the same time, its efficient photochemical reactivity makes it an obvious potential precursor to even larger hydrocarbons in Titan's atmosphere, which could contribute to the visible-absorbing haze which surrounds Titan (8,9).

Our group at Purdue has sought to determine the photochemical reactivity of C<sub>4</sub>H<sub>2</sub> using a scheme in which the laser-excited C<sub>4</sub>H<sub>2</sub> reacts for only 20 μsec prior to probing of the products by VUV photoionization/time-of-flight mass spectroscopy (1-4,6). This scheme enables one to look at the first reaction steps free from interference from the polymerization which complicates bulb studies (10) of diacetylene.

One of the unusual features of diacetylene's photochemistry is that it is dominated in the ultraviolet by reactions from metastable triplet states rather than free radical processes (Figure 1) (10). In our experiment, following excitation to the <sup>1</sup>Δ<sub>u</sub> state of C<sub>4</sub>H<sub>2</sub>, intersystem crossing to the triplet manifold occurs (Figure 1), whether directly or by way of the lower-energy <sup>1</sup>Σ<sub>u</sub><sup>+</sup> state (not shown). Vibrational deactivation within the triplet manifold proceeds in parallel with reaction. The lowest two triplet states of C<sub>4</sub>H<sub>2</sub>, of <sup>3</sup>Σ<sub>u</sub><sup>+</sup> and <sup>3</sup>Δ<sub>u</sub> symmetry in the linear configuration, are thought to be responsible for the observed reactions of metastable diacetylene (C<sub>4</sub>H<sub>2</sub><sup>\*</sup>) (10).

Our studies of C<sub>4</sub>H<sub>2</sub><sup>\*</sup> have shown it to have a rich chemistry -- reacting with all unsaturated hydrocarbons to which it has been exposed. Among the major products of the reaction of C<sub>4</sub>H<sub>2</sub><sup>\*</sup> with alkenes (ethylene and propylene) and alkynes (acetylene, diacetylene, propyne) are poly-yne, enyne, and cumulene products. A particularly exciting development is the recent discovery that the reaction of metastable diacetylene with 1,3-butadiene produces benzene and



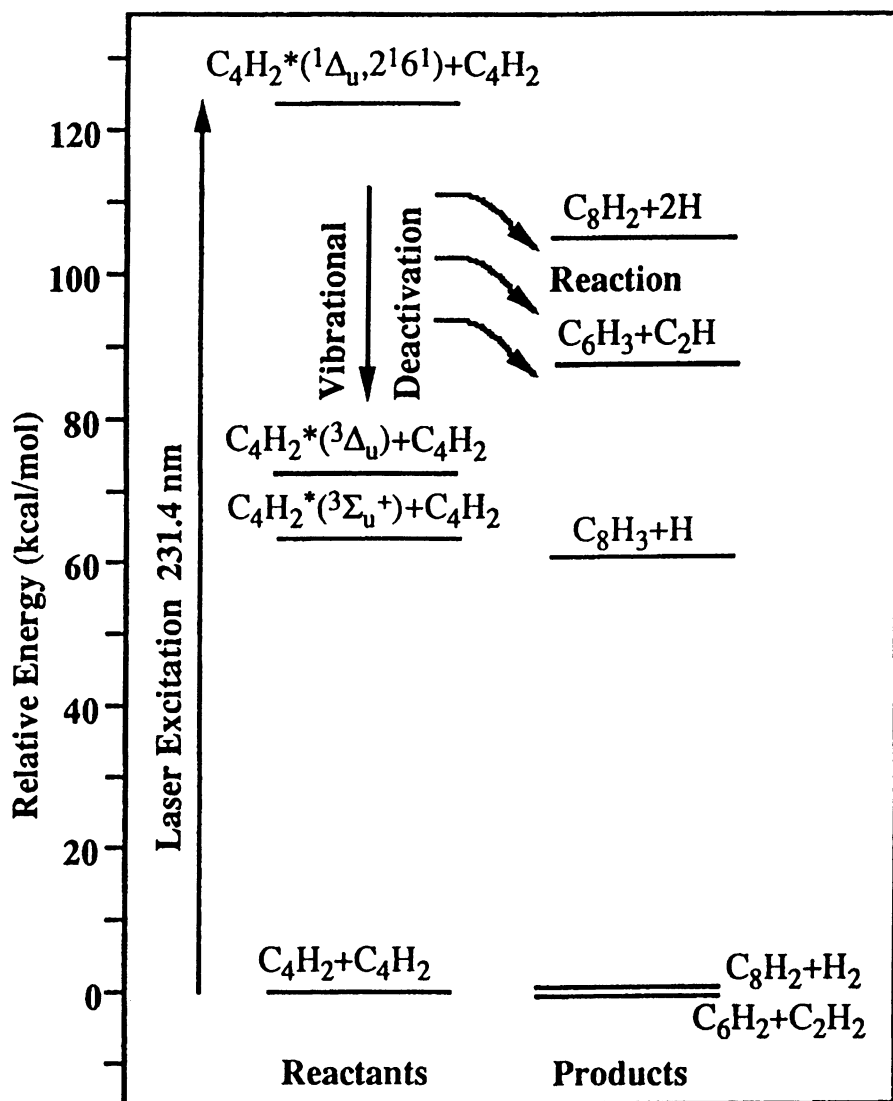
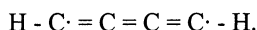


Figure 1. Energy level diagram for diacetylene and its metastable state reactions with ground state  $C_4H_2$  to form products.

phenylacetylene as primary products (6). This may have implications for ring-forming reactions in flames, where aromatics lead to soot formation.

While this chemistry is interesting, there are still serious deficiencies in our understanding of the triplet states of  $C_4H_2$  themselves. This need forms the motivation for the study of the singlet-triplet spectroscopy of diacetylene using CRDS methods.

The only previous experimental data on the triplet states of  $C_4H_2$  is from Michael Allan, (11) who has recorded the electron energy loss spectrum (EELS) of  $C_4H_2$ , assigning the state observed near 3 eV to the  $T_2 \ ^3\Delta_u$  state. At the resolution of EELS, only a long progression with a spacing of  $2100\text{ cm}^{-1}$  is identified and subsequently assigned to the  $C\equiv C$  stretch. This progression appears because the excited state is best pictured (12,13) as a biradical cumulene with all  $C=C$  double bonds:



**B. Experimental.** The cavity ringdown cell used in the present study (see Figure 2) consists of a meter long stainless steel cell with mirrors on both ends that serve as both the ringdown cavity and cell windows. The mirrors have reflectivities of 99.8% centered at 370 nm. Home-built mounts support the mirrors, incorporating flexible bellows to allow for alignment.

An excimer-pumped dye laser was used as the radiation source. Its output was sent through mode-matching optics and on to the ringdown cell. The signal was detected by a photomultiplier tube (PMT) connected to the second mirror mount on axis. The PMT output was sent to a digital scope for signal averaging and on to a computer for fitting and storage of the exponential decay constant.

Since diacetylene cannot be handled as a liquid above  $-20^\circ\text{C}$ , it is synthesized using standard procedures (14) and then immediately prepared for storage as a dilute gas-phase mixture of about 5% in helium (15). To record the CRD spectra with an adequate signal-to-noise ratio, sufficient diacetylene was trapped in a cold finger so that, upon pumping away the helium, warming back to room temperature produced a pressure of about 200 torr of pure  $C_4H_2$ . In the gas phase, the sample was stable over the timescale of a day.

**C. Results and Discussion.** Figure 3 shows the overview CRD scan of  $C_4H_2$  spanning the wavelength range from 387 to 343 nm. The spectrum spans about  $3500\text{ cm}^{-1}$ , encompassing two members of the  $C\equiv C$  stretch progression with frequency  $2030\text{ cm}^{-1}$ . The triplet-state  $C\equiv C$  stretch frequency is about  $160\text{ cm}^{-1}$  less than in the ground state ( $2189\text{ cm}^{-1}$ ), consistent with the decrease in  $C\equiv C$  bond order calculated for the triplet states (12).

The increased resolution of the CRD spectrum over that in the EEL spectrum reveals a number of vibrational bands associated with the low-frequency bends of  $C_4H_2$ . The length of this progression suggests that the excited state is bent away from linear. However, the spacing of the main transitions in Figure 3 is highly irregular, showing a decrease in spacing from 500 to 347 to 306 to  $287\text{ cm}^{-1}$ .

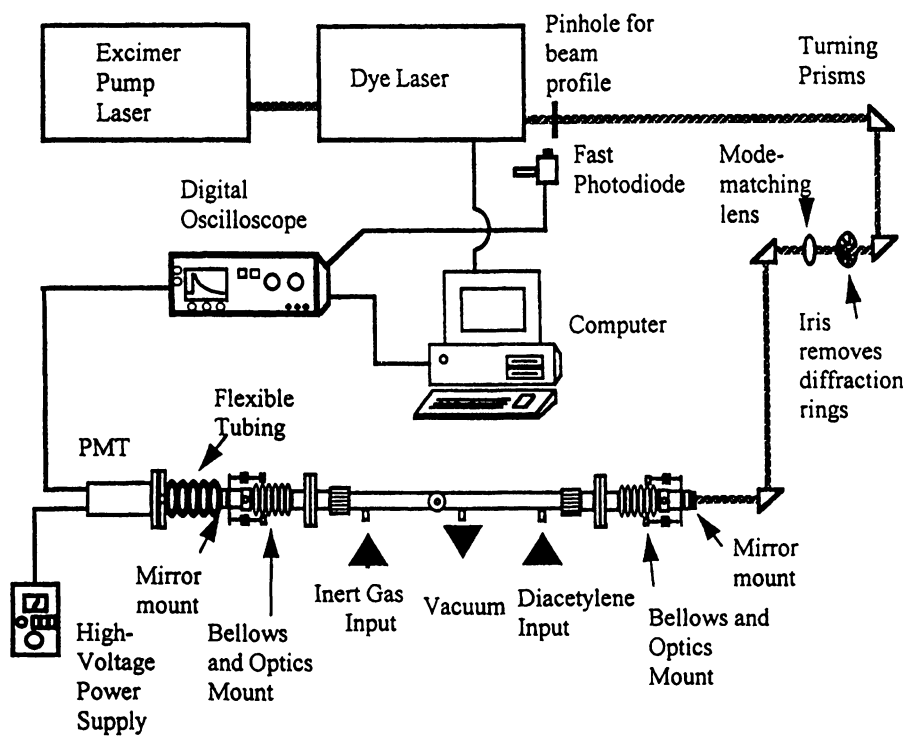


Figure 2. Experimental apparatus used in the singlet-triplet cavity ringdown spectroscopy of  $C_4H_2$ .

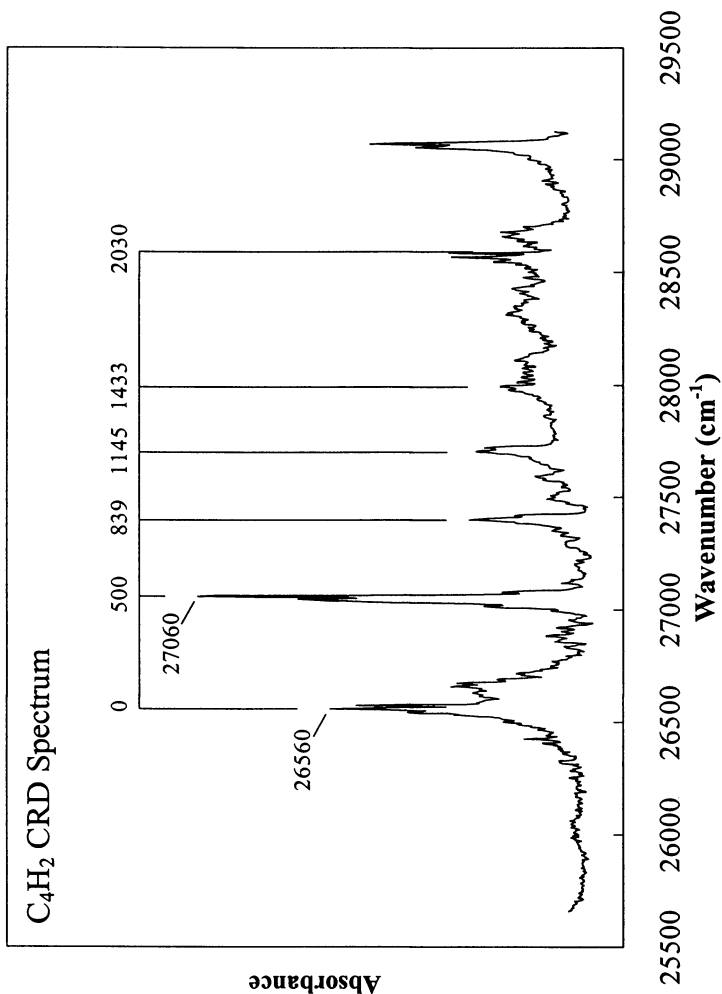


Figure 3. Overview CRD scan of the  ${}^3\Delta_0 \leftarrow {}^1\Sigma_g^+$  transition in C<sub>4</sub>H<sub>2</sub> from 387 to 343 nm.

We do not have a firm assignment of this structure yet. Here we simply set out the possible sources of the unusual spacing observe.

First, the irregular vibrational structure could result from Renner-Teller coupling in the  ${}^3\Delta_u$  state. To better understand the excited states of  $C_4H_2$ , Jordan (16) has performed *ab initio* calculations on the low-lying excited states at several levels of theory up to the CASPT2(g2) method using an atomic natural orbital (ANO) basis set (17). The details of these calculations will be presented elsewhere (16). The one-dimensional potential energy curves in Figure 4 show the calculated adiabatic and vertical excitation energies from the ground state to the lowest triplet states. The upper state of the observed transition is tentatively assigned as the lower member of the  ${}^3\Delta_u$  Renner-Teller couple (the  $T_2$  state) with symmetry  ${}^3A_u$  in the *trans* configuration or  ${}^3A_2$  in the *cis* configuration. Since the  $\pi_g$  bending modes of  $C_4H_2$  are Renner-Teller active, their spacing could be modulated by the Renner-Teller coupling.

A second possibility is presented by the small energy difference between the *cis* and *trans* conformer minima calculated for the  $T_2$  state. The *trans* minimum is calculated to be only  $160\text{ cm}^{-1}$  lower in energy than the *cis* minimum in the CASPT2(g2) ANO calculations (16), in striking contrast to the *cis/trans* energy difference in the corresponding triplet states of  $C_2H_2$ , which is almost 50 times larger. Because of this close proximity, it is conceivable that the observed transition in  $C_4H_2$  could carry Franck-Condon (FC) intensity to both *cis* and *trans* minima, with the observed spectrum being a composite of both.

Finally, the irregular spacing could be caused in part by a low barrier between *cis* and *trans* minima. The 1D curves of Figure 4 show the vertical excitation energy, which is calculated to be 1.1 eV above the *cis* and *trans* minima. However, the true *cis/trans* isomerization transition state probably involves motion of a single hydrogen atom along a C-H bending coordinate and is almost certainly much lower in energy. As shown in Figure 5, this transition state is best pictured on a two-dimensional potential energy surface in which the two axes are the symmetric and antisymmetric CH bends of ground state  $C_4H_2$  which lead to the *cis* and *trans* minima in the excited state, respectively. The *cis/trans* isomerization transition states are located between each set of *cis* and *trans* wells. If the barrier is low enough, as the bending levels approach the top of the barrier, tunneling between *cis* and *trans* wells would produce an unusual spacing of the energy levels, as observed. Jordan and coworkers are currently calculating *cis/trans* isomerization transition state energy to provide further insight to this possibility.

One of the most important results to arise from the CRD spectrum is the absolute cross section it provides for the singlet-triplet transition. The peak absorption cross section for the transition at  $27060\text{ cm}^{-1}$  is

$$\sigma_{\text{peak}} = 2.7 \times 10^{-5} \text{ atm}^{-1}\text{cm}^{-1}.$$

This is about  $3 \times 10^6$  times smaller than the corresponding strongest transition in the  ${}^1\Delta_u \leftarrow {}^1\Sigma_g^+$  transition ( $80\text{ atm}^{-1}\text{cm}^{-1}$ ) of  $C_4H_2$  (10).

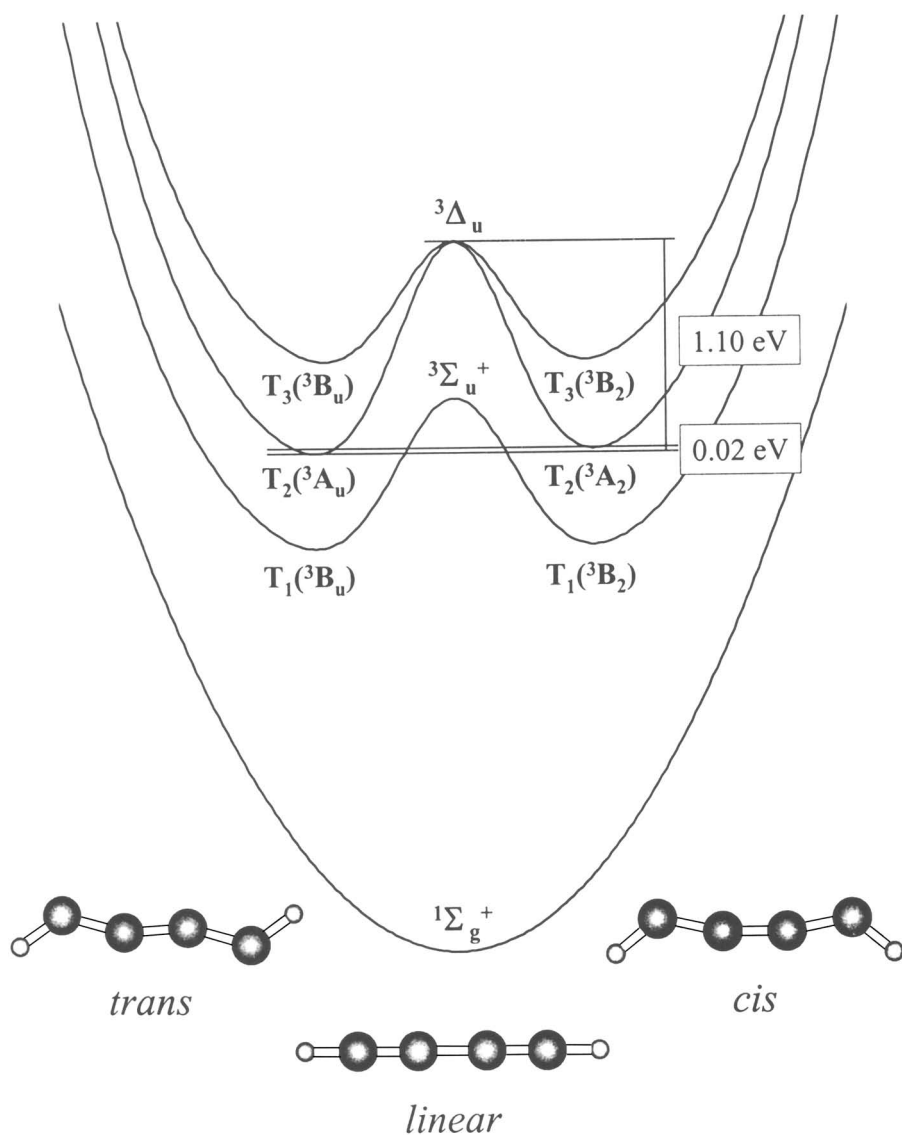


Figure 4. One dimensional potential energy curves for diacetylene along the *trans*-linear-*cis* isomerization coordinate.

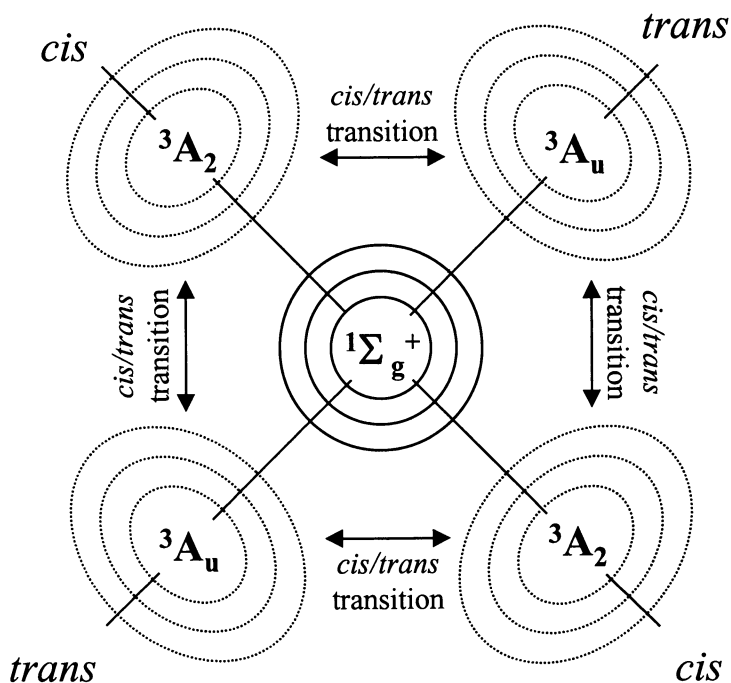


Figure 5. Two dimensional potential energy surfaces along the *cis* and *trans* bending coordinates with the ground state well pictured using solid curves. The double-minimum wells of the triplet-state *cis* and *trans* conformers are depicted with dotted curves.

From the absorption cross section one can extract the intrinsic phosphorescence lifetime  $\tau_{\text{ph}}$  of the triplet state using equation (1) (18).

$$\sigma_{\text{int}} = (\lambda^2/8\pi\tau_{\text{ph}}) \quad (1)$$

The total integrated intensity of the transitions built off one member of the C $\equiv$ C stretch progression is determined from the spectrum to be about seven times the integrated intensity of the 27060 cm<sup>-1</sup> transition. Since we haven't recorded the spectrum over the entire electronic transition, the total integrated absorption cross section is estimated by comparing the observed region of the CRDS spectrum (Figure 3) to Allan's EELS spectrum. Estimating that the region we have studied comprises about 1/5 of the total integrated absorption cross section leads to an intrinsic phosphorescence lifetime for the triplet state of about 1.5 sec. This provides an upper bound for the true triplet state lifetime, which may be reduced by intersystem crossing to the ground state.

Zwier and Allen (5) have recently modeled the role of metastable diacetylene in the formation of complex hydrocarbons in Titan's atmosphere using 1 msec as the triplet state lifetime for C<sub>4</sub>H<sub>2</sub>\*. This value was chosen because it represents a lower limit on metastable acetylene's lifetime obtained in electric deflection studies (19). Even with the underestimated phosphorescence lifetime, C<sub>4</sub>H<sub>2</sub>\* was predicted as the leading pathway to larger hydrocarbon formation at an altitude of 100 km in Titan's atmosphere. With the new upper bound for  $\tau_{\text{ph}}$ , that domination is extended to altitudes of 200 km and above, suggesting that C<sub>4</sub>H<sub>2</sub>\* could be an important source of large hydrocarbons in Titan's atmosphere.

## II. Tropolone and Tropolone·(H<sub>2</sub>O)<sub>n</sub> Clusters

**A. Introduction.** Tropolone (TrOH) is a seven-membered pseudo-aromatic molecule noted for its hydrogen-atom tunneling in a symmetric double minimum potential well, as shown in Figure 6. Several groups have studied tropolone, its derivatives, and various tropolone clusters in recent years in order to learn about its spectroscopy and H-atom tunneling dynamics (20-31). Its easily-reached S<sub>1</sub>←S<sub>0</sub> transition (370 nm), reasonable fluorescence quantum yield, and low S<sub>1</sub>-state H-atom tunneling barrier produces S<sub>1</sub> tunneling splittings which are easily observed and probed on a single vibronic level basis. H-atom motion is coupled to the heavy atom motions in TrOH, leading to significant vibrationally mode-specific effects on the tunneling splittings. For instance, vibrations such as  $\nu_{13}$  and  $\nu_{14}$  which have significant C-O/C=O in plane wagging character, have unusually large tunneling splittings (>30 cm<sup>-1</sup>), while several other modes effectively suppress the tunneling (<1 cm<sup>-1</sup>) (22,28,32).

Our group has studied the effects of substitution on the ring and of complexation by solvent on the mode-specific tunneling using the methods of laser-induced fluorescence, UV-UV hole-burning spectroscopy, and fluorescence-dip infrared spectroscopy (FDIRS) (33-39). In symmetric derivatives, the electronic spectroscopy has provided insight to substituent effects on tunneling via the low-



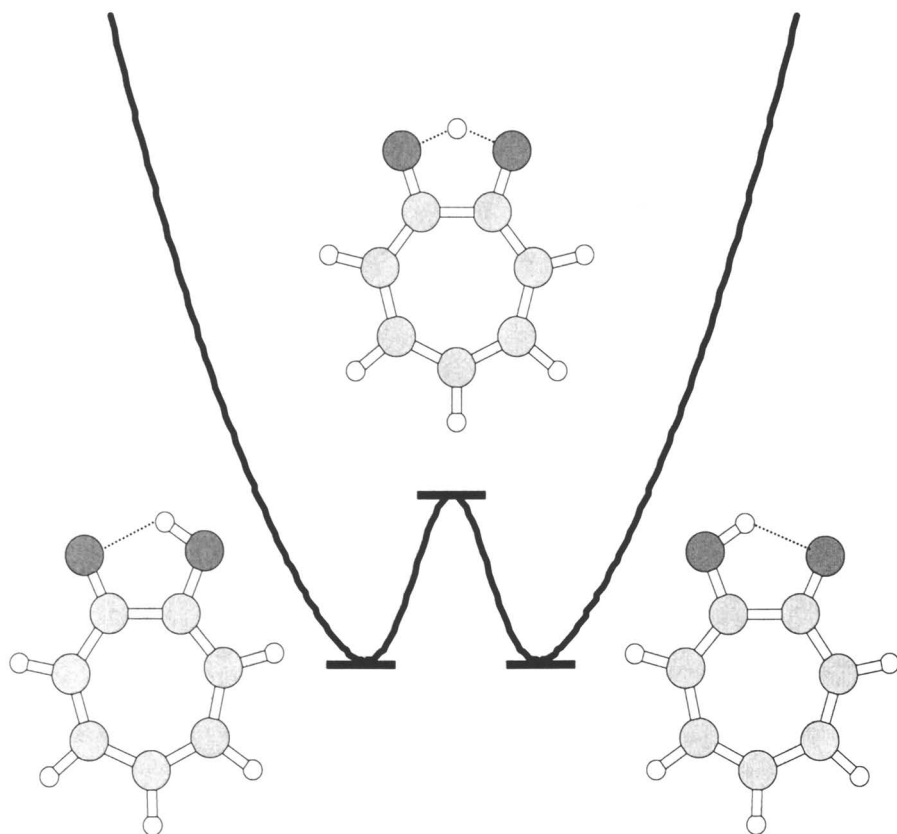


Figure 6. Schematic experimental diagram of the apparatus used for simultaneous CRDS and LIF measurements of jet-cooled molecules and clusters.

frequency heavy-atom vibrations in  $S_1$ , while the FDIR experiments have probed the effects of OH stretch excitation in  $S_0$ . In asymmetric derivatives, the magnitude of the induced asymmetry relative to the tunneling splitting leads to partial or complete quenching the H-atom tunneling in  $S_0$  and/or  $S_1$  (33,37-39). Similar quenching is observed when even a single water molecule is complexed to TrOH (35,40,41).

One important aspect of the spectroscopy and dynamics of TrOH and  $\text{TrOH-(solvent)}_n$  clusters which has not been studied previously is the photophysics of the  $S_1$  state. In the TrOH monomer, one wonders whether there will be any correlation between the magnitude of the tunneling splitting of a given vibronic level and the coupling to dark background states. One could imagine, for instance, that the different shapes of the tunneling wave functions in the region of the barrier could produce different couplings to triplet or ground state levels. In the same way, complexing hydrogen-bonding solvents such as water to tropolone could also influence its non-radiative coupling in significant ways. In bulk solution, hydrogen-bonding solvents are observed to have a large, but hard-to-predict effect on the fluorescence quantum yields of aldehydes, ketones, alcohols, and heteroaromatics, sometimes increasing and sometimes decreasing the quantum yields by more than an order-of-magnitude (42). What is missing from such data is any knowledge of the vibronic state dependence of the quantum yields, or of the effects of binding one or more solvent molecules to the solute TrOH at single, well-defined binding sites. These can be provided by gas-phase cluster studies.

In order to explore such questions, we have modified our laser-induced fluorescence apparatus (37) in order that LIF and CRD scans of jet-cooled molecules and clusters can be recorded simultaneously. From such measurements, relative single vibronic-level fluorescence quantum yields for tropolone and tropolone- $(\text{H}_2\text{O})_n$  clusters with  $n=1-4$  have been obtained and are reported here.

**B. Experimental.** The schematic diagram for the experimental apparatus used in these studies is shown in Figure 7. The output from an excimer-pumped dye laser is sent through optics consisting of a 0.55 mm pinhole, an iris to remove the fringes, and a focusing lens to offset the divergence induced by transmission through the first mirror. The light then enters the one meter ringdown cavity where it crosses the pulsed supersonic free jet expansion about 1 cm downstream from the nozzle orifice. The ringdown is detected with a photomultiplier tube positioned behind the back mirror while the unfiltered fluorescence is detected simultaneously at  $90^\circ$  from the light path by a second photomultiplier tube. The PMT outputs are then sent to a digital scope and on to a computer for processing and storage.

The data acquisition software analyzes the ringdown signal from the scope by removing approximately the first 50 ns in which amplified spontaneous emission from the dye laser may corrupt the ringdown. The remaining portion is fit to an exponential function, and the two fit constants, the pre-exponential constant,  $I_0$ , and the decay constant,  $b$ , are used as measures of the laser power in the ringdown cavity and the absorption coefficient, respectively. The error of the fit is also recorded for quality assurance. Simultaneous with the absorption

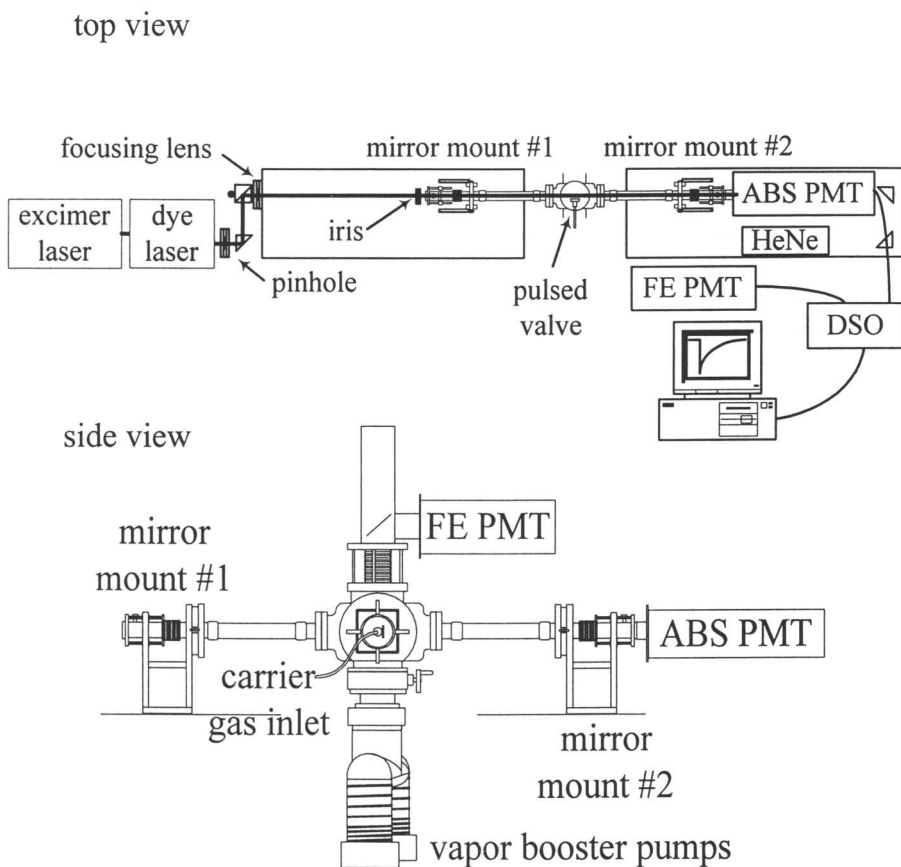


Figure 7. Symmetric double-minimum potential well for the hydrogen-atom transfer in TrOH monomer.

measurement, the fluorescence signal is integrated over the ringdown time scale and recorded.

Since the absorption and fluorescence signals are measured simultaneously, the data can be used to determine the relative fluorescence quantum yields,  $\Phi_{F,rel}$ , on a single vibronic level basis. Quantitatively, the relative fluorescence quantum yield is calculated by dividing each fluorescence peak's integrated area into its absorption counterpart, and comparing the result to the analogous ratio obtained at the TrOH monomer  $a_1$  origin, which we set arbitrarily to a value of 1.00. While it would be preferable to measure absolute fluorescence quantum yields, the imprecise knowledge of the fluorescence collection efficiency across the region of the expansion subtended by the laser has to this point restricted us to relative yields.

TrOH vapor is entrained in the expansion by resistively heating a sample holder containing the solid sample located just prior to the pulsed valve. TrOH-(solvent)<sub>n</sub> clusters are formed by mixing a metered flow of the room temperature liquid with the main flow of helium used as buffer gas. Typical solvent concentrations in the expansion are 0.2-1.0%.

**C. Results and Discussion.** Figure 8 presents an overview CRDS/LIF scan of the first 700 wavenumbers above the TrOH  $\tilde{A}^1B_2 - \tilde{X}^1A_1$  electronic origin. The tunneling doublet at the origin dominates both the LIF and CRD scans. The progression in even overtones of the out-of-plane O-O wag ( $26^\mu$ ) shows its striking decrease in tunneling splitting along the progression. The small intensity of these transitions relative to the origin is in marked contrast to the spectra shown in previous work using single-pass excitation (22,32), in which saturation effects markedly increase the relative intensities of these bands. A significant advantage of the CRDS/LIF method is that the ring-down cavity produces LIF scans with similar signal-to-noise to single-pass experiments, but without the saturation effects that invariably creep into the latter studies.

Figure 9 presents the relative SVL fluorescence quantum yields,  $\Phi_{F,rel}$ , of TrOH monomer within the first 1000  $\text{cm}^{-1}$  of the  $S_1 \leftarrow S_0$  origin. The yields were determined through averaging replicate scans, with attached error bars representing one standard deviation in the yields from the individual scans. Table I summarizes the observations for the key transitions in TrOH. While a detailed analysis of this data is outside the scope of this chapter, several general features of the data are worth summarizing.

First, the relative SVL fluorescence quantum yields show a general fall-off with increasing energy above the origin, dropping to values well below 0.1 of its value at the origin by about 750  $\text{cm}^{-1}$  excess energy. This fall-off is an expected consequence of the increasing density of background states with increasing energy. The fact that the drop-off occurs already in the first 750  $\text{cm}^{-1}$  would seem to reflect either (i) the large density of states resulting from the presence of several low-frequency out-of-plane vibrations in  $S_1$  TrOH, or (ii) the threshold for a new non-radiative channel may occur in this region. We will return to this latter point shortly.

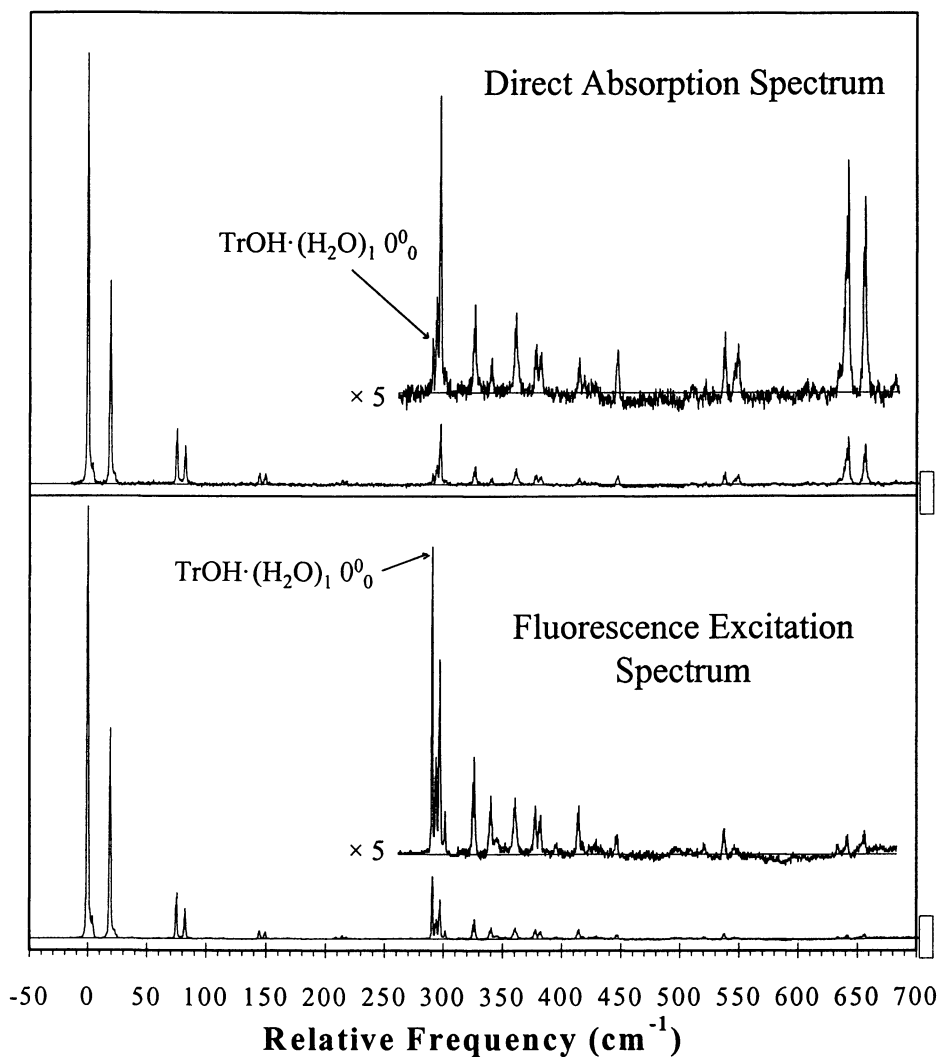


Figure 8. CRDS (upper) and LIF (lower) spectra of the first 700  $\text{cm}^{-1}$  of the  $S_1 \leftarrow S_0$  transition in tropolone.

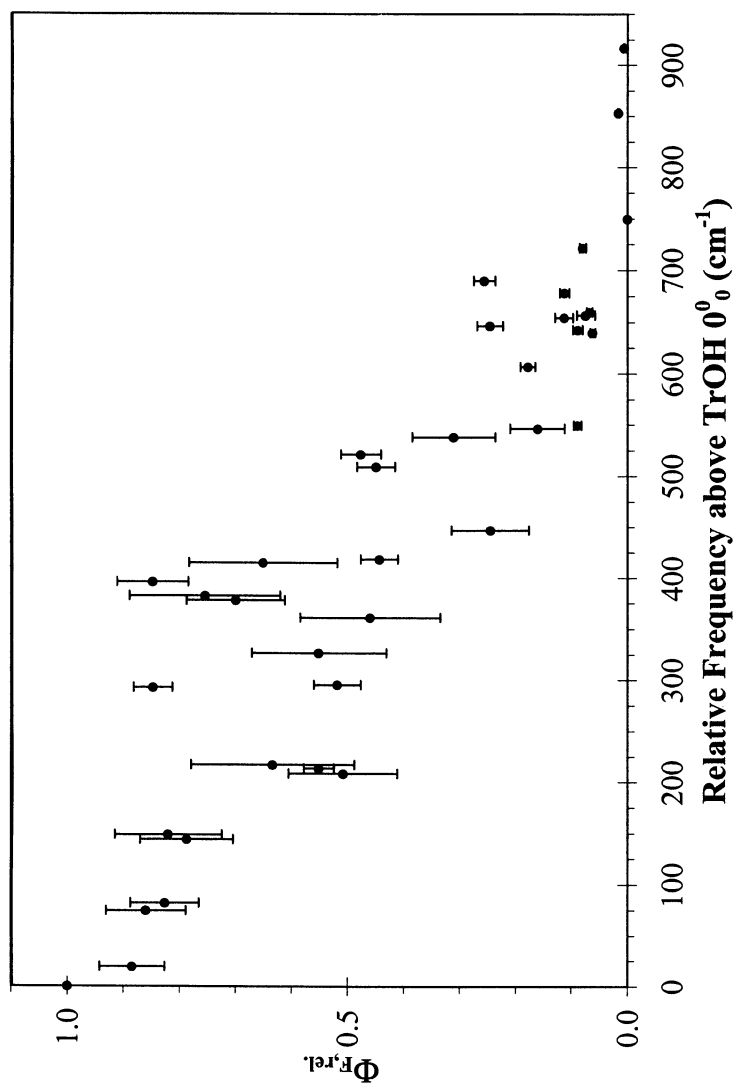


Figure 9. Relative, single vibronic level fluorescence quantum yields of TrOH  $S_1$ - $S_0$  transitions. The error bars on the measurements represent one standard deviation on an average of three to six independent determinations.

Table I. Single vibronic level relative fluorescence quantum yields for TrOH monomer.

<i>Assignment</i> ( <i>ref. 30, 32</i> )	<i>Relative Frequency</i> ( <i>Tunneling Splitting</i> ) ( <i>cm<sup>-1</sup></i> )	$\Phi_{F,rel}$
$0^0_0$	0 (19)	$1.00 \pm 0.00$
$H^1_1$	19	$0.89 \pm 0.06$
$26^2_0$	75 (7)	$0.87 \pm 0.07$
$26^2_0H^1_1$	82	$0.84 \pm 0.06$
$26^4_0$	144 (5)	$0.81 \pm 0.10$
$26^4_0H^1_1$	149	$0.83 \pm 0.10$
$25^1_026^1_0$	208(<1)	$0.51 \pm 0.10$
$26^6_0$	214 (3)	$0.55 \pm 0.03$
$26^6_0H^1_1$	217	$0.63 \pm 0.15$
$25^1_026^3_0$	293(<1)	$0.86 \pm 0.04$
$14^1_0$	296 (30)	$0.53 \pm 0.05$
$14^1_0H^1_1$	326	$0.58 \pm 0.14$
??	361	$0.48 \pm 0.14$
$14^1_026^2_0$	378 (4)	$0.71 \pm 0.09$
$14^1_026^2_0H^1_1$	382	$0.77 \pm 0.13$
??	396	$0.90 \pm 0.07$
$13^1_0$	415 (32)	$0.67 \pm 0.15$
??	418	$0.47 \pm 0.03$
$13^1_0H^1_1$	447 (32)	$0.25 \pm 0.08$
$11^1_0$	509 (12)	$0.45 \pm 0.03$
$11^1_0H^1_1$	521	$0.48 \pm 0.04$
$19^2_0$	538 (8)	$0.31 \pm 0.07$
$19^2_0H^1_1$	546	$0.16 \pm 0.05$
$14^2_0$	607 (27)	$0.17 \pm 0.01$
$14^2_0H^1_1$	634	$0.62 \pm 0.12$
$12^1_0$	642 (4)	$0.09 \pm 0.01$
$12^1_0H^1_1$	646	$0.07 \pm 0.02$

Second, while there do appear to be modest mode-specific effects in the fluorescence quantum yields, these seem to be dictated more by accidental resonances with a sparse manifold of background states rather than by systematic mode-specific causes. There is no obvious correlation in the fluorescence quantum yields with the magnitude of the tunneling splitting for a given level (Table I), suggesting that the H-atom tunneling coordinate is only weakly coupled to the non-radiative pathway(s). The type of vibration excited, whether in-plane or out-of-plane, also appears to have little systematic effect on  $\Phi_{F,rel}$ . Finally, the fluorescence quantum yields of the tunneling doublet associated with a given vibronic level sometimes favor the lower ( $a_1$ ) over the upper ( $b_2$ ) tunneling level, but other times favor the reverse (Table I).

Much more dramatic effects on  $\Phi_{F,rel}$  are observed following complexation of one or more water molecules to TrOH (Table II). Even a cursory look at Figure 8 shows that the fluorescence quantum yield of the TrOH-(H<sub>2</sub>O)<sub>1</sub> origin is much *greater* than that of the TrOH monomer levels around it. Quantitatively, the TrOH(H<sub>2</sub>O)<sub>1</sub> origin has a fluorescence quantum yield  $8.0 \pm 1.0$  times that of the TrOH monomer origin. Furthermore, by operating under higher water flow conditions than those in Figure 8, transitions due to the clusters with  $n=2-4$  have been identified using the assignments of previous fluorescence and resonant multiphoton ionization studies (40,41) of TrOH(H<sub>2</sub>O)<sub>n</sub> clusters as a guide. The relative fluorescence quantum yields of these clusters are  $9.1 \pm 1.8$  for  $n=2$ ,  $10.1 \pm 0.5$  for  $n=3$ , and  $6.2 \pm 1.0$  for  $n=4$ . Thus, the dramatic increase in fluorescence quantum yield is accomplished almost entirely by a single water molecule, with only small further increases accompanying addition of the second and third water molecules.

The knowledge that H-bonding a single water molecule to TrOH increases its fluorescence quantum yield by such a large factor raises two inter-related questions. First, what non-radiative process is responsible for reducing the fluorescence quantum yield in TrOH monomer? Second, why is the efficiency of this process reduced when water H-bonds to TrOH? Of course, the SVL fluorescence quantum yields do not themselves determine the nature of the non-radiative process in operation, whether it be intersystem crossing, internal conversion, or some photochemical process. However, the large body of literature (43,44) on the photophysics and photochemistry of ketones, aldehydes, and heteroaromatics can be used to guide the discussion.

Tropolone, with its carbonyl oxygen lone pairs and pseudo-aromatic  $\pi$  cloud, shares with many other aromatic ketones, aldehydes, and nitrogen heterocycles the close proximity of ( $n,\pi^*$ ) and ( $\pi,\pi^*$ ) excited states. As illustrated in Figure 10a), in most ketones and aldehydes, the lowest energy  $^1(n,\pi^*)$  state is slightly lower in energy than the lowest  $^1(\pi,\pi^*)$  state. However, the rotational band contour analysis of the  $\tilde{A}^1B_2 \leftarrow \tilde{X}^1A_1$  transition in TrOH by Alves and Hollas (26) determined that the  $S_1 \leftarrow S_0$  transition in TrOH is a  $\pi \rightarrow \pi^*$  transition with in-plane transition moment. As these authors note, the apparent inversion of the order of the  $^1(n,\pi^*)$  and  $^1(\pi,\pi^*)$  states probably arises because TrOH has an *intramolecular*



Table II. Relative Fluorescence Quantum Yields of Tropolone and Selected Clusters at Their  $S_1$ - $S_0$  Origins.

<i>Species</i>	$\Phi_{F,rel}$
TrOH	1.0
TrOH·(H <sub>2</sub> O) <sub>1</sub>	8.0 ± 1.0
TrOH·(H <sub>2</sub> O) <sub>2</sub>	9.1 ± 1.8
TrOH·(H <sub>2</sub> O) <sub>3</sub>	10.1 ± 0.5
TrOH·(H <sub>2</sub> O) <sub>4</sub>	6.2 ± 1.0

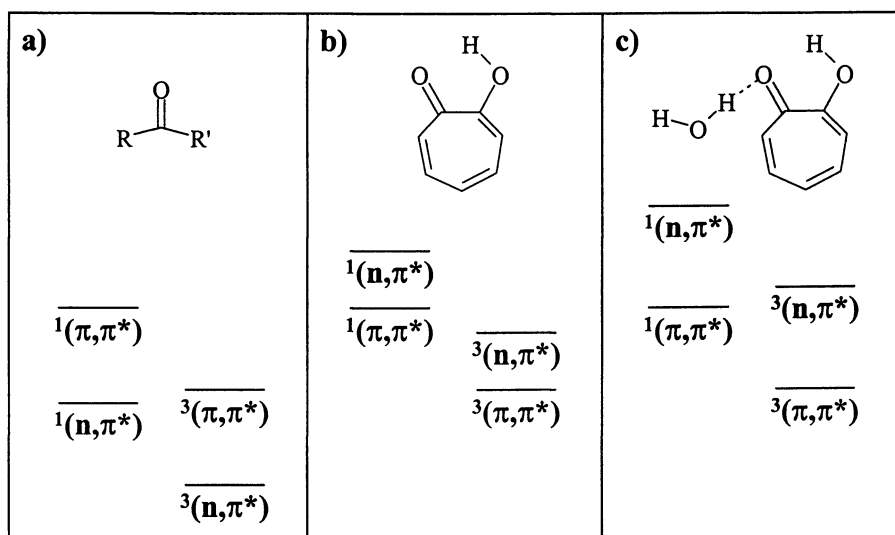


Figure 10. a) Energy level ordering typically found in aromatic ketones and aldehydes. b) Expected shift in the  $(n,\pi^*)$  states in TrOH due to its intramolecular H-bond. c) Additional shift in the  $(n,\pi^*)$  states anticipated for the TrOH·(H<sub>2</sub>O)<sub>n</sub> clusters in which the carbonyl oxygen acts as acceptor for a H-bond from water. See text for details.

H-bond to the carbonyl oxygen which shifts the ( $n,\pi^*$ ) states to higher energy relative to the ( $\pi,\pi^*$ ) states (Figure 10b). The blue-shift of  $n\rightarrow\pi^*$  transitions relative to  $\pi\rightarrow\pi^*$  transitions due to *intermolecular* H-bonds is a general characteristic of molecules with non-bonding pairs which can serve as acceptor sites for hydrogen bonds. First explained by Brealey and Kasha (45) in 1955, the  $n\rightarrow\pi^*$  blue-shift in the presence of H-bonding solvents occurs because the oxygen lone pairs serve as acceptor for H-bond(s) from the solvent. These H-bonds are weakened following  $n\rightarrow\pi^*$  excitation because the removal of one of the lone pair electrons greatly weakens the H-bond to the remaining non-bonding electron in the excited state, thereby shifting the electronic transition of the (solute + solvent) system to the blue. In TrOH, the intramolecular H-bond could produce a similar blue-shift in the ( $n,\pi^*$ ) states relative to the ( $\pi,\pi^*$ ) states.

According to El-Sayed's selection rules for spin-orbit coupling (44,46), the  $^1(\pi,\pi^*)$   $S_1$  state of TrOH will be strongly coupled to  $^3(n,\pi^*)$  states if they are in close proximity. Since the  $^3(n,\pi^*)$  state(s), like the  $^1(n,\pi^*)$  states, will be raised in energy by the intramolecular H-bond, they may well be in close proximity to the  $S_1$  state, and be responsible for reducing the fluorescence quantum yield in TrOH, as observed. Furthermore, it is plausible that the fast drop-off in  $\Phi_{F,rel}$  with increasing energy above the  $S_1$  origin is also caused by the close proximity of these  $^3(n,\pi^*)$  states, whose density of states will rise quickly with increasing energy.

The discussion in the preceding paragraphs also provides a basis for understanding the dramatic increase in fluorescence quantum yield when one or more water molecules bind to TrOH. Previous computational studies of the TrOH( $H_2O$ ) complex have identified two isomers with similar binding energies: (i) an 'exterior' isomer in which the water molecule donates a H-bond to the back side of the intramolecularly H-bonded carbonyl group on TrOH (called the 'exterior' isomer) and (ii) a 'ring' isomer in which the water molecule acts simultaneously as donor to the carbonyl oxygen and acceptor from the OH group of TrOH (35). While the spectroscopic data is not completely unambiguous, the balance of evidence points to structure (i) as that observed experimentally, i.e., that in which the water H-bonds to one of the lone pairs of the carbonyl oxygen (35,40).

We surmise, therefore, that the unusual increase in fluorescence quantum yield when the water molecule donates a H-bond to TrOH is due to an additional shift of the  $^3(n,\pi^*)$  states blue relative to the fluorescing  $^1(\pi,\pi^*)$  state. If this additional shift moves the  $^3(n,\pi^*)$  state(s) above the  $^1(\pi,\pi^*)$  state (Figure 10c), only the  $^3(\pi,\pi^*)$  state would remain below it, and  $^1(\pi,\pi^*) \rightarrow ^3(\pi,\pi^*)$  coupling is typically far smaller than  $^1(\pi,\pi^*) \rightarrow ^3(n,\pi^*)$  coupling (44,46).

The factor of eight increase in fluorescence quantum yield is all the more remarkable because, without the shifts in electronic states, complexation would greatly increase the density of background states due to the several low-frequency intermolecular vibrations accompanying cluster formation. This increased density of background triplet states would decrease the fluorescence quantum yield, not increase it as observed.

The structures of the  $\text{TrOH}(\text{H}_2\text{O})_n$  clusters with  $n=2-4$  is not known experimentally, though infrared spectra for the  $n=2,3$  structures are available.<sup>41</sup> Yanez and co-workers have recently calculated several isomeric structures for the  $\text{TrOH}(\text{H}_2\text{O})_2$  cluster (47). As with  $\text{TrOH}(\text{H}_2\text{O})$ , two structures are within 0.5 kcal/mol of one another, an 'exterior' isomer in which the water dimer interacts only with the back end of the carbonyl oxygen, and a 'ring' isomer in which a water dimer bridges between the  $\text{TrOH}$  OH and carbonyl oxygens. For the purposes of the present discussion, the important point is that both structures retain a strong H-bond with the carbonyl oxygen as acceptor, consistent with the fluorescence quantum yield being similar to that in  $\text{TrOH}(\text{H}_2\text{O})$ .

The decrease in fluorescence quantum yield at  $n=4$  is suggestive of some change in the interaction with the carbonyl oxygen. Based on the structures formed in pure  $(\text{H}_2\text{O})_n$  clusters, it seems plausible that  $\text{TrOH}(\text{H}_2\text{O})_4$  could contain a cyclic  $(\text{H}_2\text{O})_4$  sub-cluster. The strength of the interaction with the carbonyl oxygen could be changed upon formation of the cycle, leading to the observed decrease in  $\Phi_F$ . However, this hypothesis will need to be tested further by experiment and theory.

### III. Conclusion

In this chapter, the methods of cavity ringdown spectroscopy have been brought to bear on two systems in which the dynamical implications of the work are primary importance. In the first example, CRDS is used to directly probe the triplet excited state thought to be responsible for the efficient photochemistry of diacetylene. In the second case, the techniques of CRD and LIF are combined in a single experiment to determine relative single vibronic level fluorescence quantum yields for jet-cooled tropolone and tropolone- $(\text{H}_2\text{O})_n$  clusters with  $n=1-4$ . Studies of spectroscopy and photophysics of ketones and aldehydes in solution have identified the key role played by H-bonding solvents in moving the  $(n,\pi^*)$  states relative to the  $(\pi,\pi^*)$  states (45). Under jet-cooled conditions, complexation of a single water molecule to  $\text{TrOH}$  increases its fluorescence quantum yield by almost an order-of-magnitude, confirming that H-bond donation to the carbonyl oxygen plays a key role in controlling the photophysics of this molecule.

### IV. Acknowledgment

We gratefully acknowledge the NASA Planetary Atmospheres program, the Department of Energy Basic Energy Sciences, and the Petroleum Fund, administered by the American Chemical Society for their support of various aspects of this work. We also acknowledge K.D. Jordan for carrying out the *ab initio* calculations on the triplet states of  $\text{C}_4\text{H}_2$  and M. Yanez for communicating his results on  $\text{TrOH}(\text{H}_2\text{O})_2$  clusters prior to publication.

## References

1. Bandy, R. E.; Lakshminarayan, C.; Frost, R. K.; Zwier, T. S. *Science* **1992**, *258*, 1630-1633.
2. Bandy, R. E.; Lakshminarayan, C.; Frost, R. K.; Zwier, T. S. *J. Chem. Phys.* **1993**, *98*, 5362-5374.
3. Frost, R. K.; Arrington, C. A.; Ramos, C.; Zwier, T. S. *J. Am. Chem. Soc.* **1996**, *118*, 4451-4461.
4. Frost, R. K.; Zavarin, G.; Zwier, T. S. *J. Phys. Chem.* **1996**, *99*, 9408-9415.
5. Zwier, T. S.; Allen, M. *Icarus* **1996**, *123*, 578-583.
6. Arrington, C. A.; Ramos, C.; Zwier, T. S. (manuscript in preparation).
7. Warnatz, J.; Maas, U.; Dibble, R. W. *Formation of Hydrocarbons and Soot*; Warnatz, J.; Maas, U.; Dibble, R. W., Ed.; Springer-Verlag: Berlin, 1996, pp. 237ff.
8. Toon, O. B.; McKay, C. P.; Griffith, C. A.; Turco, R. P. *Icarus* **1992**, *95*, 24-53.
9. Toublanc, D.; Parisot, J. P.; Brillet, J.; Gautier, D.; Raulin, F.; McKay, C. P. *Icarus* **1995**, *113*, 2-26.
10. Glicker, S.; Okabe, H. *J. Phys. Chem.* **1987**, *91*, 437.
11. Allan, M. *J. Chem. Phys.* **1984**, *80*, 6020.
12. Karpfen, A.; Schuster, P. *Can. J. Chem.* **1985**, *63*, 809-15.
13. Arrington, C. A.; Giles, B. G.; Hagemeister, F.; Zwier, T. S. (in preparation).
14. Armitage, J. B.; Jones, E. R. H.; Whiting, M. C. *J. Chem. Soc.* **1952**, 2014.
15. Bandy, R. E.; Lakshminarayan, C.; Zwier, T. S. *J. Phys. Chem.* **1992**, *96*, 5337-5343.
16. Jordan, K. D. (unpublished results) .
17. Andersson, K.; Blomberg, M. R. A.; Fülischer, M. P.; Karlström, G.; Lindh, R.; Malmqvist, P.-A.; Neogrady, P.; Olsen, J.; Roos, B. O.; Sadlej, A. J.; Schütz, M.; Seijo, L.; Serrano-Andres, L.; Siegbahn, P. E. M.; Widmark, P.-O. *Molcas Version 4*.
18. Bernath, P. F. *Spectra of Atoms and Molecules*; Oxford University Press: New York, 1995.
19. Lisy, J. M.; Klemperer, W. M. *J. Chem. Phys.* **1980**, *72*, 3880-3883.
20. Redington, R. L.; Bock, C. W. *J. Phys. Chem.* **1991**, *95*, 10284-94.
21. Redington, R. L. *J. Chem. Phys.* **1990**, *92*, 6447-55.
22. Redington, R. L.; Chen, Y.; Scherer, G. J.; Field, R. W. *J. Chem. Phys.* **1988**, *88*, 627-33.
23. Redington, R. L.; Redington, T. E. *J. Mol. Spec.* **1979**, *78*, 229-47.
24. Tomioka, Y.; Ito, M.; Mikami, N. *J. Phys. Chem.* **1983**, *87*, 4401-05.
25. Rossetti, R.; Brus, L. E. *J. Chem. Phys.* **1980**, *73*, 1546-50.
26. Alves, A. C. P.; Hollas, J. M. *Mol. Phys.* **1972**, *23*, 927-45.
27. Alves, A. C. P.; Hollas, J. M. *Mol. Phys.* **1973**, *25*, 1305.
28. Alves, A. C. P.; Hollas, J. M.; Musa, H.; Ridley, T. *J. Mol. Spec.* **1985**, *109*, 99-122.
29. Sekiya, H.; Sasaki, K.; Nishimura, Y.; Li, Z.-H.; Mori, A.; Takeshita, H. *Chem. Phys. Lett.* **1990**, *173*, 285-90.
30. Sekiya, H.; Nagashima, Y.; Nishimura, Y. *J. Chem. Phys.* **1990**, *92*, 5761-69.

31. Sekiya, H.; Nagashima, Y.; Tsuji, T.; Nishimura, Y.; Mori, A.; Takeshita, H. *J. Phys. Chem.* **1991**, *95*, 10311-17.
32. Sekiya, H.; Nagashima, Y.; Nishimura, Y. *Bull. Chem. Soc. Jpn.* **1989**, *62*, 3229-31.
33. Ensminger, F. A.; Plassard, J.; Zwier, T. S.; Hardinger, S. *J. Chem. Phys.* **1993**, *99*, 8341-44.
34. Frost, R. K.; Hagemeister, F. C.; Arrington, C. A.; Zwier, T. S. *J. Chem. Phys.* **1996**, *105*, 2595-604.
35. Frost, R. K.; Hagemeister, F. C.; Arrington, C. A.; Schleppenbach, D.; Zwier, T. S.; Jordan, K. D. *J. Chem. Phys.* **1996**, *105*, 2605-17.
36. Frost, R. K.; Hagemeister, F.; Arrington, C.; Schleppenbach, D.; Laurence, G.; Zwier, T. S. *J. Phys. Chem.* **1996**, *100*, 16835-16842.
37. Ensminger, F. A.; Plassard, J.; Zwier, T. S.; Hardinger, S. *J. Chem. Phys.* **1995**, *102*, 5246-5259.
38. Ensminger, F. A.; Plassard, J.; Zwier, T. S. *J. Phys. Chem.* **1993**, *97*, 4344-4353.
39. Nash, J. J.; Zwier, T. S. *J. Chem. Phys.* **1995**, *102*, 5260-70.
40. Sekiya, H.; Hamabe, H.; Ujita, H.; Nakano, N.; Nishimura, Y. *Chem. Phys. Lett.* **1996**, *255*, 437-444.
41. Mitzusuka, A.; Fujii, A.; Ebata, T.; Mikami, N. *J. Chem. Phys.* **1996**, *105*, 2618-2627.
42. Mataga, N.; Kubota, T. *Fluorescence yields in hydrogen bonded complexes*; Mataga, N.; Kubota, T., Ed.; Marcel Dekker: New York, 1970, pp 351-356.
43. Lim, E. C. *Vibronic Interactions and Luminescence in Aromatic Molecules with Nonbonding Electrons*; Lim, E. C., Ed.; Academic Press: New York, 1977; Vol. 3, pp 305-337.
44. Klessinger, M.; Michl, J. *Emission -- Fluorescence of Organic Molecules*; Klessinger, M.; Michl, J., Ed.; VCH Publishers: New York, 1995, pp 260-271.
45. Brealey, G. J.; Kasha, M. *J. Am. Chem. Soc.* **1955**, *77*, 4462-4468.
46. El-Sayed, M. A. *J. Chem. Phys.* **1963**, *38*, 2834-2838.
47. Yanez, M. (personal communication).

## Chapter 15

# Using FM Methods with Molecules in a High Finesse Cavity: A Demonstrated Path to $<10^{-12}$ Absorption Sensitivity

Jun Ye<sup>1</sup>, Long-Sheng Ma<sup>2</sup>, and John L. Hall<sup>3</sup>

University of Colorado and National Institute of Standards and Technology,  
Boulder, CO 80309-0440

This paper represents an effort by the authors, as developers of ultra-sensitive optical absorption techniques, to make these ideas and strategies available to the wider community, especially to those colleagues in whatever field who have real scientific problems which could be advanced if only they had available a higher level of absorption sensitivity. We have a few such scientific and/or applications areas in mind ourselves and, indeed, most of this work has been motivated by one of them: the dream of having a general method to produce a high performance frequency reference basically anywhere in the visible/near ir domain. For this, molecular overtones recommend themselves because of their generous spectral coverage, but it is only with the development of these ultrasensitive absorption measurement techniques that this application has been heading for fruition.

### High Sensitivity is Interesting for ...

There are many, many interesting applications for spectroscopic techniques, and there tends to be a general explosion of applicability when the sensitivity gets into today's ppT ( $10^{-12}$ ) domain. We can note just a few to give a flavor.

**Atmospheric detection of trace materials.** An "easy" application of laser spectroscopy is to explosion-hazard assessment. Spectroscopically at least, it is easy since the ir fundamental bands of ubiquitous gases such as  $\text{CH}_4$  are very strong. Of course, making reliable and appropriate laser equipment can be a serious challenge here, since the natural laser of choice, the tunable semiconductor laser has not yet been well-perfected in the 3.0-3.2  $\mu\text{m}$  range. Some systems have been built using the 3.39  $\mu\text{m}$  HeNe laser, but we suppose that future systems will in fact use the well-developed diode lasers at 1.55  $\mu\text{m}$  as the source, even though the absorption strength on the C-H stretch overtone

<sup>1</sup>Current address: Quantum Optics Group, CalTech, Pasadena, CA 91125

<sup>2</sup>Permanent address: Physics Department, East China Normal University, Shanghai, China

<sup>3</sup>Staff member: Quantum Physics Division, National Institute of Standards and Technology

may be 100-fold diminished from that of the fundamental. The point is that the explosion limits are in the percent range, so adequate sensitivity need not be a big problem.

Pollution sensing is a next opportunity, more demanding since many materials are hazardous in concentrations at even the ppm ( $10^{-6}$ ) level. Taken with the complexity of molecular spectra and strong broadening by atmospheric pressure, these applications begin to be more "interesting" for the instrument designer.

A new spectroscopic industry is health-testing via identifying specific metabolism-related gas emissions in exhaled human breath. For example, an active asthma patient exhales pentanes (1) and highly energetic molecules such as  $\text{H}_2\text{O}_2$  (2). Ethane and pentanes (3) are widely found in human breath, appear in juvenile cases of vitamin E deficiency (4), and are believed to originate from the peroxidization of lipid cells by free-radicals within the body. Indeed, some studies consider such emissions as possible early markers for cancer (5). Some confusion arises due to lack of chemical specificity of present tests (6).

**Molecular spectroscopy / overtones and combination bands.** Of course we collectively operate a huge industry to study the spectra of molecules. Current interests include a priori calculation of actual energies of overtone bands. Combination bands in particular are of interest, since they may give some insight into the really fundamental questions of molecular interactions and a first glimpse into a deeper understanding of chemical reaction pathways. Specific interesting spectroscopic questions here relate to large-amplitude coherent molecular vibrations, perhaps laser-induced, and the associated questions of atom exchange, symmetry effects, etc. As users of molecular overtones for frequency standards work (7), mentioned earlier, our sure destiny is to provide some precise molecular overtone parameters for the scientific community.

**Fundamental tests.** An important, albeit perhaps not urgent, fundamental application is setting better limits on the symmetrization postulate. For example some recent studies (8) showed that even levels of the  $\text{O}_2$  antisymmetric ground state are not occupied, with a sensitivity  $\sim 5 \times 10^{-7}$ . The sensitivity limit was associated with the relatively low absorption strength of the "forbidden" 760 nm band, and the simple direct absorption methods utilized for these first studies. With a high finesse cavity to enhance the absorption, probably 3 or more orders of magnitude will be added to the evidence that molecules are not to be found in the symmetry-forbidden states.

An even more speculative concern is for possible discrepancies between different quantum clocks, based on potentially different response of their internal "clock mechanism" to changes in: a) gravitational potential; b) epoch after the Big Bang; c) putative difference in interactions based on Baryon/Lepton ratio, "new physics" etc. This is the quantum clock-builder's playground!

## Optical Heterodyne Detection

**What is optical heterodyne detection ?** In the photo-detection process, we know that photons absorbed give rise to electron-hole pairs in the semiconductor. Ideally a very high fraction,  $\eta$ , of these are separated before recombination, and are separately routed to the device terminals by internally-generated or externally-imposed bias fields. So the expected signal current from this process is easily written as  $i = \eta e P / h\nu$ , where  $i$  is the external current,  $P$  the detected light power,  $e$  the electron charge and  $h\nu$  is the

photon energy. Silicon and InGaAs detectors with a value of quantum efficiency  $\eta > 0.9$  are available at reasonable cost commercially. Before considering the noise of the process, we note that the optical power will generally have a time-dependent term if the applied laser field is the sum from two sources, ie  $P(t) = A I = A \epsilon_0 (E_1(t) + E_2(t))^2$ . Here  $A$  is the effective area of the laser intensity  $I$ , and we will neglect important interference details by assuming the two contributing fields to be mutually mode-matched. With  $E_1(t) = E_1 \cos(\omega_1 t)$  and similarly for  $E_2$  and  $\omega_2$ , when the difference of the two applied frequencies is within the detector system's response bandwidth, we expect a detected photocurrent of the form  $i(t) = (i_1 + 2 \sqrt{i_1 i_2} \sin(\omega_1 - \omega_2)t + i_2)$ . We refer to this cross term at the difference frequency as the *heterodyne* response. If we had chosen to think of the field  $E_2$  as somehow different, for example it was a weak field being produced by a molecular sample, one can see one of the advantages of the heterodyne approach: the scale of the beat current can be increased as we like by increasing the size of  $E_1$ , which is referred to as the "Local Oscillator" field, following the practice in radio-frequency engineering. It is fundamental that the  $S/N$  is not degraded by use of a larger LO power. Some technical remarks below return to this subject.

**How does heterodyne detection reach the limits of fundamental noise ?** Any real physical photodetector will offer some output noise even in total darkness. If we attempt direct detection of a weak signal, the incident POWER will need to be sufficient to give a photodetected current which can mask the detector's noise. Consider the heterodyne case: now the signal-bearing light power is represented by the cross-term between the Local Oscillator field and the weak signal field. It is only this PRODUCT which needs to be adequately large to mask the detector noise. So by merely using a stronger Local Oscillator (LO) field, we can overcome some appreciable noise, typically produced by the amplifier circuit which converts the photocurrent into output voltage.

Of course, this Local Oscillator power can carry laser intensity noise to the detector as well. Any non-fundamental noise imposed on this intensity will be directly converted into an unwelcome output noise. But typically this noise, which we may call "technical noise" to identify its origin, is concentrated at lower frequencies. Everyone has heard some discussion about "1/f" noise sources. Even though technical noise seldom has such a pure spectrum, it does carry a spectral density which is concentrated mainly at power-line harmonics and other low frequencies associated with laboratory vibrations. Various noise processes in semiconductor devices are also restricted to low audio frequencies and below. So an important idea in achieving low noise performance is to place the information-carrying heterodyne signal at a frequency sufficiently high that a negligible level of technical noise is carried by the LO field. Before illustrating noise levels of actual lasers, it is useful to be quantitative about this heterodyne idea.

**What are the physics limits ?** Even in the absence of noise of technical origin, one can observe a fluctuating component of photocurrent when the input light level appears to be ideally steady. Some years ago a radio-engineering explanation of this residual noise would note that the current in the photodiode is actually carried by discrete charged particles, mainly the electrons in view of their higher mobility, and one would associate an irreducible SHOT-NOISE with their fluctuation. A standard formulation would provide the result

$$i_n^2 = 2 e i_{dc} B . \quad (1)$$



Here  $B$  is the bandwidth within which the fluctuating current  $i_n$  is observed, and  $i_{dc}$  is the average photocurrent. While this is indeed the correct answer, there are two important remarks. Firstly, we do not expect to see shot-noise fluctuation currents in some current carried in a simple wire or resistor: this current is carried by a swarm of coordinated charges, something like a slowly-moving “Jello” cloud of electrons. The effective number is huge, while the effective velocity is very small. So the number fluctuations are negligible. Secondly, an entire industry has grown up recently in physics in which the radiation field is “squeezed” to provide sub-shot-noise levels of fluctuation. Surely this would have been a frustrating business if the electron graininess were the real source of the current fluctuation: one simply could not have seen a sub-shot-noise current fluctuation below the limit of Eq. 1. In fact, the “real” source of the fluctuation is that the quantized radiation field interacts with matter in a discrete way. The field can be carrying Poissonian statistics, such as light from a thermal source or a laser far above threshold, or it may have sub-Poissonian levels of fluctuation, providing a more regular rate of photo-electron generation and so an anomalously low fluctuation level for the photocurrent. One should think of the electron as “jumping” when the field commands it: this means that “squeezing”-like processes can only be observed when the photodetection quantum efficiency is high. But here our task is just to be able to approach the standard shot-noise level in our spectroscopy. Of course, if the quantum efficiency of the detector we choose is seriously low, we will be measuring a lower current, and it will therefore have a higher relative fluctuation than was fixed by any fundamental limit.

**Shotnoise limit: the highest possible sensitivity in direct absorption.** The fluctuating current noise, shot-noise calculated above, will set the fundamental sensitivity limit for straight absorption spectroscopy. Taking the  $S/N$  as 1, the molecular absorption needs to be equivalent to the shot-noise in the measurement bandwidth. This gives  $i_{dc} \cdot \alpha L = \sqrt{i_n^2} = \sqrt{2 e i_{dc} B}$ , so we obtain the minimum detectable absorption as

$$(\alpha L)_{\min} = \sqrt{\frac{2eB}{i_{dc}}} \quad (2)$$

To make this concrete, according to Eq. 2 we should be able to detect an integrated absorption of  $1.8 \times 10^{-8}$  with a shot-noise-limited photo current of 1 mA, using a 1 Hz measurement bandwidth. Compared with experience, this feels optimistic.

**What are the real (technical) limits ?** Of course, it is easy to observe that actual lasers display vastly more noise than any fundamental shot-noise limit. We dismiss immediately the silly causes such as inadequate smoothing of power-supply potentials, even though these are basically always an issue in an actual lab experiment. Laboratory vibrations modify the laser’s alignment and so record their presence on the output power. High voltage discharge lasers often have a few deciBels increased noise due to fluctuation of the resistance of the high-voltage ballast resistor (which should be wirewound, not carbon composition, to avoid this degradation.)

A modern trend is the use of a pump laser, such as a diode laser, to provide laser pumping for some more stable, but tunable, laser for our spectroscopy. A typical

example is pumping a Ti:Sapphire laser with an Ar<sup>+</sup> ion laser. A new possibility is to pump the Ti:Sapph with a diode-pumped solid state laser, for example laser-diode-pumped Nd:YVO<sub>4</sub> which is frequency-doubled into the green (9). Such lasers - at the 5 W level ! - are available from two US firms at present. We show data measured with our JILA-designed ring Ti:Sapphire laser pumped by the "Millennium" laser.(10) The photodetected current was amplified by a transimpedance amplifier of 85 kohms with an ac-coupled 43 ohms series resistor in the rf output. Thus the 3.47 V dc level corresponds to a 40.8 μA dc photocurrent. (All three traces were taken at the same DC level.) The calculated rms shot-noise voltage level produced by the amplifier is 0.307 μV, yielding across the 50 ohm input of the spectrum analyzer some 50/(50+43) of this, or 0.165 μV. This represents -122 dBm noise power in a 1 Hz bandwidth. Since the measurement bandwidth was actually 1 kHz, our calculated shot-noise output should be 30 dB higher, viz -92 dBm. In fact, this is the observed value at high frequencies: see Fig. 1. The trace labeled "shot-noise" was taken with illumination by a flashlight, so the noise increase at lower frequencies (<20 kHz) shows some deficiencies of our detector/amplifier system. The trace labeled "Millennia" shows that the diode-pumped solid state laser approach (10) can produce a low level of light noise, only a little above the shot-noise level of our measured ~100 μW of light. However, since the laser output is actually 5 W, some 50,000-fold (+47 dB) larger, this laser's output is in fact far from being "shot-noise-limited." Still, it is one of the quietest pump lasers we have seen.

The 5 W pump light brought our Ti:Sapph laser to 200 mW output at 780 nm, and the noise of a 100 μW sample of this light is also displayed. The broad bump around 150 kHz is the "relaxation oscillation" associated with energy exchange between excited Cr<sup>3+</sup> ions and photons in the laser cavity. The width of the zero-frequency feature shows the 1 kHz resolution level utilized for the spectral analysis. **So the message is: Do the detection at frequencies high enough that the excess noise has basically disappeared.**

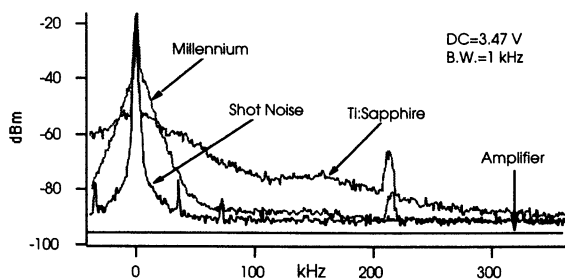


Figure 1. Intensity noise of JILA-designed Ti:Sapphire ring laser pumped by a commercial diode-pumped Nd:YLF solid-state laser system (Spectra-Physics "Millennium" (10)). Comparison curves are shot-noise from the same light level provided by flashlight, and actual intensity noise of green output of the DPSS Millennium system. Detected light power was about 100 μW.

## Sensitivity Enhancement by an Optical cavity

With the aim on further enhancing the detection sensitivity of the optical heterodyne spectroscopy discussed in section II, here we present another sensitivity-boosting technique, namely cavity absorption-enhancement spectroscopy where an external resonator is used to contain both the sample gas and the light field to enhance the light-matter interaction.

It was realized in the early days of laser development that a laser cavity can be used to greatly enhance the absorption detection sensitivity.(11) Basically the advantage comes from the multipass effect and the delicate balance between the laser gain and intracavity absorption.(12, 13) However, it is now often preferred to separate the absorber from the laser in order to extend the experimental flexibility and to have better controlled working parameters. Enhancement of absorption sensitivity has been accomplished by using long multipass absorption cells.(14) Kastler suggested a Fabry-Perot cavity could be used because its transmission is sensitive to small variations of its inside absorption.(15) For high-resolution, Cerez *et al* (16) first applied this external cavity technique to saturated absorption spectroscopy. Ma and Hall (17) were able to use an external resonator combined with the optical heterodyne spectroscopy to achieve excellent signal-to-noise ratios. The use of an external cavity for the detection of molecular overtone transitions was also demonstrated later.(18) In linear-absorption experiments, an enhancement cavity has been used most extensively in the context of ring-down spectroscopy.(19) (See below for further discussions)

The advantages of using an external optical resonator are manifold. First of all, the light travels many times through the intracavity absorber so that the effective absorption length is increased by the factor of  $(2 \cdot \text{Finesse}/\pi)$ . This directly increases the detection sensitivity. Secondly, the cavity builds up its intracavity power. This allows the use of low-power lasers for the input, even for the weak transitions which require large intensities to saturate. It also reduces the output power level that needs to be handled by a photodetector. In addition, the geometrical self-cleaning and matching of the two counter-propagating waves inside the cavity are important both for eliminating pointing-direction-related noises and for obtaining narrow and unshifted resonance lines, as explained by Hall and Bordé.(20) Furthermore, a stable cavity can be used to pre-stabilize the laser frequency when it is locked on a cavity resonance, thereby reducing the detection noise.

Figure 2 shows a standing wave optical resonator. The input coupling mirror has a power transmission coefficient of  $T_{in}$  and loss of  $L_{in}$ , while for the output coupler they are  $T_{out}$  and  $L_{out}$ , respectively. The total empty cavity loss is  $L_{cav} = T_{in} + T_{out} + L_{in} + L_{out}$ . We denote the optical input power as  $P_{in}$ , the cavity-reflected power as  $P_r$ , and the cavity-transmitted power as  $P_t$ . The cavity finesse ( $F$ ) is simply

$$F = \frac{2\pi}{L_{cav}} \quad (3)$$

The (resonant-) cavity reflection efficiency ( $R_{cav}$ ), transmission efficiency ( $T_{cav}$ ), and intracavity build-up power can be expressed as

$$\frac{P_r}{P_{in}} = R_{cav} = (L_{in} + L_{out} + T_{out} - T_{in})^2 \left( \frac{1}{L_{cav}} \right)^2,$$

$$\frac{P_t}{P_{in}} = T_{cav} = 4T_{in}T_{out} \left( \frac{1}{L_{cav}} \right)^2,$$

$$\frac{P_c}{P_{in}} = 4T_{in} \left( \frac{1}{L_{cav}} \right)^2.$$
(4)

Figure 2 also shows the enhancement of absorption contrast by the cavity. The cavity length is  $L$  and it is filled with a weakly-absorbing gas sample with an absorption coefficient of  $\alpha$  per unit length. By weakly-absorbing we mean the cavity round trip loss due to the sample is small:  $1 - \exp(-2\alpha L) \approx 2\alpha L \ll 1$ . In a direct absorption measurement with a plain gas cell of length  $L$ , the output power is:  $P_{out} = P_{in} \cdot e^{-\alpha L} \approx P_{in} (1 - \alpha L)$ . Therefore the absorption signal is  $P_{in} \cdot \alpha L$ , while the shot-noise is determined by the overall output power  $P_{out} \approx P_{in}$ , in the weak absorption limit. Following Eq. 2, the noise-equivalent minimum absorption sensitivity for a cell is thus:

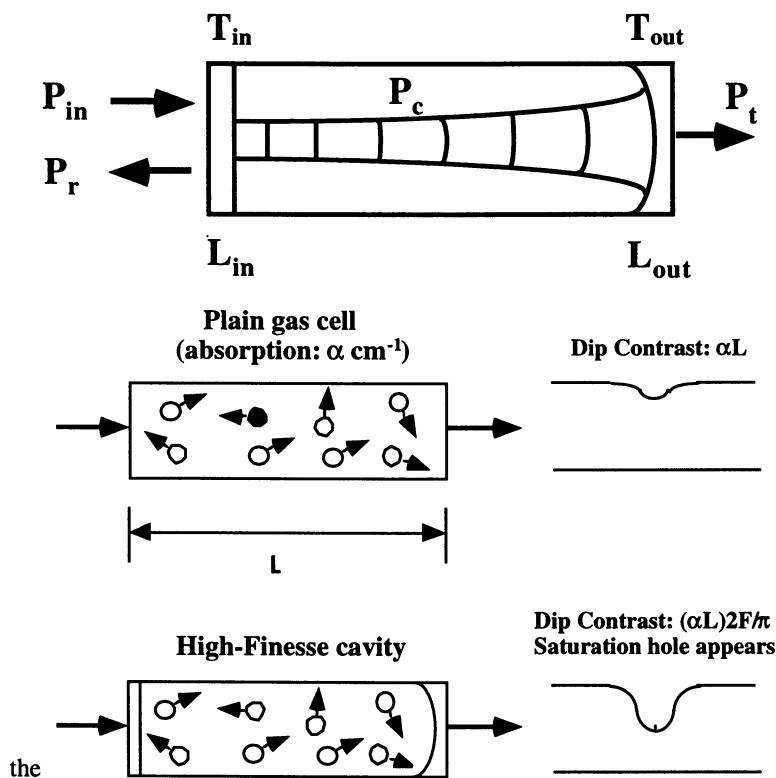


Fig. 2. Notations used for the build-up cavity. Also shown is the comparison of absorption contrast between a plain gas cell and a high-finesse cavity.

$$(\alpha L)_{\min} \approx \sqrt{\frac{2B \cdot h\nu}{\eta P_{in}}} \quad (5)$$

When the sample is placed inside a cavity, the transmitted power is modified from Eq. (4)

$$\frac{P_t}{P_{in}} = 4T_{in}T_{out} \left( \frac{1}{L_{cav} + 2\alpha L} \right)^2 \approx \frac{4T_{in}T_{out}}{L_{cav}^2} \left( 1 - 2\frac{2\alpha L}{L_{cav}} \right) \quad (6)$$

The detected signal contrast in the cavity transmission is therefore enhanced,

$$\frac{\delta P_t}{P_t} = 2\frac{2\alpha L}{L_{cav}} = \frac{2F}{\pi} \cdot (\alpha L) \quad (7)$$

The associated minimum detectable absorption is hence reduced by the cavity enhancement factor of  $(2 \cdot \text{Finesse}/\pi)$ , leading to

$$(\alpha L)_{\min} = \frac{\pi}{2F} \cdot \left( \frac{2Bh\nu}{\eta P_t} \right)^{1/2} = \frac{\pi}{2F} \cdot \left( \frac{2Bh\nu}{\eta T_{cav} P_{in}} \right)^{1/2} \quad (8)$$

The mirror parameters can be pre-designed to maximize the resonant cavity transmission  $T_{cav}$ , by taking into consideration of the intracavity gas absorption. It is clear from Eq. (4) that the intracavity circulating power can be much larger than the input power. For very weak transitions this power buildup is essential to have an appreciable level of saturation to resolve sub-Doppler resonances. The strong light field drives phase-coherently the molecular dipole moments. The radiation from these prepared dipole moments is essentially the signal we want to detect. However, the strong background of the un-absorbed incoming light sets the detection shot-noise level. With the buildup cavity approach, one has a strong field for sample preparation, but it appears reduced after the sample has been prepared and the LO field is detected. When the cavity is tuned onto a molecular line, a major part (determined by the cavity efficiency) of the molecular signal will leak out of the cavity to reach a detector, while a similar (or smaller) portion of the input power will be transmitted by the cavity and reach the same detector to set the shot noise limit. The large intracavity buildup power, however, will remain trapped inside, after having prepared the phase-coherent molecular dipole moments. This result, although explained here from a different but more fundamental perspective, is intrinsically the same manifestation of the cavity enhancement effect, as discussed in the previous paragraphs.

From the technical side, the advantage of the cavity is also clear when the laser source has a relatively large amplitude noise. Then, to approach shot-noise limited detection, the optimum intensity range tends to be pushed to a lower value. Fortunately with the buildup cavity, the detector does not have to receive the large intensity. This effect is similar to the result of polarization spectroscopy<sup>21</sup> or interference filtering. Usually a reasonable power level of cavity transmission can be easily found to operate in the shot noise limited regime.

### Weak Absorption can be Measured By Field-Decay (Time Domain)

According to the above-described principles, it is clear we should use heterodyne methods to measure an interesting optical electric field, and we should organize the measurement to produce a time-dependent signal with its principal Fourier frequencies high enough to avoid most of the laser's excess or technical noise. A natural method for doing this in a transient regime is to look at the light reflected from an optical cavity while the laser frequency is being scanned through the resonance. Such a signal is presented in Fig 3. In this case the frequency scan was basically linear so that the measured beat frequency increased with time.

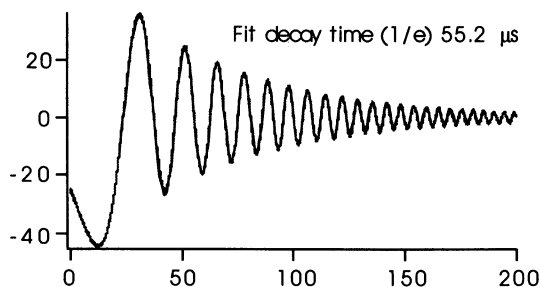


Figure 3. Cavity beating-decay, in reflection (optical heterodyne detection), with fit. We are viewing laser light reflected by a resonant cavity, after the cavity was excited when the laser swept through its resonance. As the laser continued to sweep, the beat frequency between cavity-stored light and the currently-applied field continued to increase: a small quadratic time term improved fit.

What is beating here? What optical fields are mixing in the photodetector to produce this time-dependent wave? One is the continuously-supplied exciting (and frequency-sweeping) field, serving here as our LO for the heterodyne detection. This incident field is mainly just reflected from the cavity's input mirror to reach the detector via a beam-splitter or 3-port optical isolator. It is beating with the leakage field from the cavity, which is still ringing with the energy that entered as the laser passed through its resonance. So we are measuring the cavity's optical electric *field* decay and, of course, this field-decay transient will persist 2-fold longer than a power transient. Evidently, being able to measure the waveform longer in time can be translated into lower required bandwidth, and consequently lower noise.

**The Limitations of Cavity Ring-Down Spectroscopy.** We can estimate the S/N performance ideally obtained in cavity ring-down spectroscopy (CRDS) from a shot-noise limitation. From the above arguments we would like to choose a really high finesse, as then the ringing time is extended and the effective bandwidth and noise can be reduced, in a square-root fashion. There is also a linear win in the depletion of the internal cavity energy by the extra passes, but unless we can measure the cavity field and the molecule-emitted field separately there will be no big advantage of a super-high finesse.

Unfortunately no research group has even approximated the associated theoretical sensitivity level using CRDS. Why? The reason is associated with the obviously-inconvenient expedient of conventional ringdown spectroscopy: the cavity+sample ringdown decay is obtained at a different time-epoch from the cavity-alone reference decay. Even if we have no non-fundamental noise in the measurement of the decays, there could easily be a serious time interval for laser re-tuning to an absorption-free wavelength. An even worse alternative would be to evacuate the sample cavity. It

clearly is unreasonable to expect the cavity's losses to remain constant - at the ~ppm level characteristic of a typical shot-noise limit. The mirrors are evolving in time, and the longer the time separation of the two measurements, the more likely it is that the difference in two ring-down curves will be contaminated by systematic effects, in addition to any molecular absorption.

In fact, in our experience, even larger changes of apparent cavity finesse can easily be produced by changes in the input mode-coupling. We suppose the cavity field is then excited in a variety of its spatial eigenmodes, each of which has a slightly different round-trip phase-shift. The combined field thus can decay with spurious mode-beating phenomena, particularly if we make the recommended heterodyne measurement with the reflected excitation field. It is in principle also possible for figure defects of the cavity mirrors (and scattering) to lead to an evolving spatial distribution of the energy stored within the cavity, which would impact the heterodyne efficiency of the detection process in a time-dependent manner, thus additionally confusing the ringdown picture.

We have also observed that it is difficult to use averaging on these wiggling curves: any phase defects and one finds the decay time is artificially reduced. Even the laser phase noise would enter in this way: one needs a laser coherence time much longer than the cavity ringing time in order that successive traces can be amplitude-summed. This means that to use a simple summation, the laser linewidth would need to be considerably less than that of the cavity: If we *were* in this situation, it would be preferable to use the FM methods to be discussed momentarily.

**Separating the cavity field from the molecular contribution.** It is provocative to think of the molecules also as sources of optical electric fields. They are immersed in a traveling field, say for example the one-direction traveling wave within the ring-down cavity. This field interacts with the molecule's electron cloud, leading to an oscillating dipole moment driven by the applied field. Of course these oscillating charges also radiate a field, each atom radiating in its preferred dipolar pattern. Summed together, there is a coherent molecular contribution only in the forward direction, and it carries the same spatial mode as the drive field. Importantly, its radiation phase is opposed to the drive field. One may usefully return to this molecular response as leading to a "darkness wave" emitted in anti-phase to the driving field. (This phase relationship ensures the attenuation of the wave as represented by the Beer's law.) So at some distance  $L$  downstream, for small absorption we have the applied field, say normalized to unity, and the radiated field is  $-\alpha L/2$ , both oscillating with the same frequency. The downstream power will be  $(1 - \alpha L/2)^2 = 1 - \alpha L$ , as one expects. We are doing optical heterodyne detection with a zero beat frequency!

To emphasize the physical reality of this molecule-emitted darkness wave, we consider the case where there has been a step change of the frequency of the applied field. Now the dipole radiation field and the applied field will experience temporal phase reversals, since the dipole can only continue oscillating at its natural frequency, while the applied frequency is now different. One sees a Free-Induction Decay Transient, known first in NMR. Figure 4 shows data from a 1980 JILA experiment (22) exciting HF molecular dipoles with a color center laser at  $\sim 2.6 \mu\text{m}$  wavelength. As indicated, the laser contained an intra-cavity Pockels cell which allowed its frequency to be stepped to a new value in a very short time. This new field propagates through the absorption cell basically without further interaction with the originally-resonant

molecules, and serves as the LO field for heterodyne detection of the HF-emitted darkness field. Related work was done in the mid-70's at JILA and by Brewer's IBM group (23).

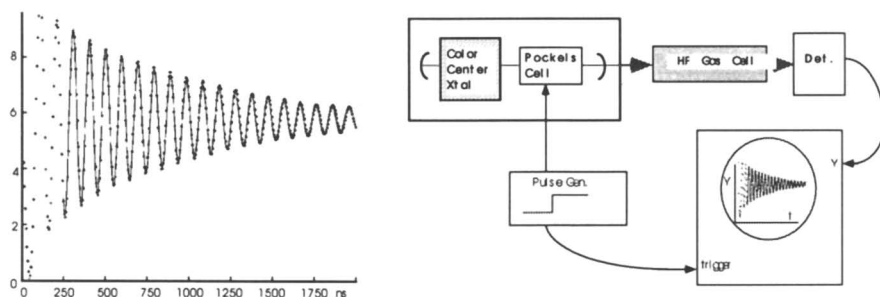


Figure 4: Free-Induction Decay of HF molecules. The laser frequency finds a particular molecular velocity which Doppler shifts the laser into resonance. These molecules become partially saturated and their dipoles continue to emit coherently even when the exciting frequency is abruptly switched away from this (velocity) group, leading to a decay beat wave at the frequency by which the laser jumped.

**Cavity-enhanced coherent transient spectroscopy.** Consider the Free Induction Decay of HF molecules shown in Fig. 4. In view of the low pressure broadening ( $\sim 10$  mTorr), the laser is able to interact mainly with only a narrow velocity range of molecules. These develop a significant dipole moment, leading to radiation in the forward direction which, incidentally, accounts on a microscopic basis for the absorption indicated in Beer's law. When the laser frequency is jumped to a new value, the radiation from this coherent dipole moment overlaps in the forward direction with the exciting laser, now at a new frequency, and so we observe the beat frequency current in the photo-detected laser power. The observed decay envelope is then that of the dipoles' electric field, and contains contributions due to collisional and laser frequency broadening during preparation of the dipole moment, and damping due to transit effects and collisions during the free-precession decay. As noted earlier, if we tried to average this waveform, laser phase noise after the switching would also degrade the ringing time. Because the recorded waveform has many extrema in a decay time, we obtain many samples of the decaying amplitude, i.e. there is amplitude information, to a greater or lesser degree, in all the recorded points. When the frequency is sufficiently stable (or predictable) it seems beneficial to fit all these data. The oscillating signal makes it sure we will be aware of any residual electronic effect that makes for a baseline decay following some optical power transient reaching the photodetector system. Basically we have come to (Molecular) Ring-down Spectroscopy, with heterodyne detection!

**Details of intracavity molecular spectroscopy: collision effects.** To enhance the contrast, these molecules would be contained within a low-loss buildup resonator, which also would have an exponential decay. While this seems like an extra concern, there are some interesting factors to note. First, as indicated earlier, the circulating field inside the resonator is much stronger than the input field, say 300-fold. Thus in its response, the molecule offers a 300-fold larger electric field for us to detect, for the same time-averaged power on the detector, and hence the same shot-noise level. Secondly,



the observed combined decaying field is simply the sum of two fields with two decay rates and can be separated by varying the gas pressure. The clearest case comes up when the gas pressure is high enough that the molecular absorption is pressure-broadened to match the full Doppler width. This will usually occur for pressures higher than  $\sim 30$  Torr. In this domain the absorption is now homogeneously broadened, with each molecule changing its velocity often enough to participate in the absorption process. The saturation intensity has been increased by the linewidth ratio squared, so very high finesse and power buildup could be used even for strongly-interacting molecules. Now it is the molecules which have a very short dipole coherence decay time, and they may add but little ( $\sim$ few ns) to the long ringing time obtained with modern mirrors and reasonably long cell lengths. For the remainder of the cavity ring-down transient they merely serve as a nearly-equilibrated source of cavity damping: this is the usual model for CRDS. For pressures well below this range the behavior will be much more complicated for cavity ring-down spectroscopy, due to partial resolution of the Doppler profile into many velocity packets, and transition saturation effects. So quantitative absorption studies will need to take additional physics into account, and the ringing decay may reflect in part coherent storage in both the cavity field and the molecular dipoles, ie. the cavity ringdown waveform at short times will potentially need a significant correction due to the dipole coherent contribution.

This leads us to the next discussion of a good way to coherently observe the molecular signal in the forward beam - which contains all the information - the NICE-OHMS method (24). This acronym means Noise-Immune, Cavity-Enhanced Optical Heterodyne Molecular Spectroscopy!

### **Weak Absorption Measured By Field-Phase (Phase Domain)**

In the previous section the advantage of an enhancement cavity is explored in the time domain. Complementarily, the signal leaking out of the cavity can also be investigated using phase sensitive detection methods. The field phase of the light beam, associated in its form with the cavity resonant structure, is inevitably perturbed by the molecular radiation which leads to additional phase shifts. It is indeed the goal of this section to bring the phase-sensitive optical heterodyne spectroscopy into the signal recovery process using an enhancement-cavity. The fundamental advantage of this approach lies in the characteristic property of FM spectroscopy: the simultaneous observation and subtraction of the signal and background optical phases in a continuous fashion. Basically one makes temporally-local comparisons of the between on-resonance and off-resonance cases.

As one contemplates on how to probe the external cavity signal with the FM technique, the first modulation approach comes to mind is simply to lock the laser frequency tightly on the corresponding cavity resonance and then modulate the cavity mode around the desired molecular resonance while monitoring the cavity transmission. Essentially this approach is a simple lock-in derivative-lineshape recovery process. In order for this method to be successful, it is important to have a super-tight frequency lock loop between the laser and the cavity since any laser frequency noise relative to the cavity will be converted to amplitude noise in detection. (Such an ideal shot-noise-limited frequency lock has not yet been demonstrated.) A piezo-electric transducer mounted on one of the cavity mirrors can be used to modulate the cavity length and the

laser will track this modulation. The modulation frequency is usually limited to the audio range due to the mechanical resonance and roll-off of the PZT and mirror assembly. Depending upon the laser (amplitude) noise spectral distribution, the attainable modulation frequency may be too low to reach the shot-noise-limited spectral region. The intrinsic lineshape would also be modified (broadened) by this modulation process. However, attractive results have already been obtained in our experiment. Our solid-state Nd:YAG laser is locked onto our high-finesse (100,000) cavity with  $\sim 1$  milliHertz relative linewidth. A cavity-dither (at 500 Hz) and lock-in detection yields a detection sensitivity of  $3 \times 10^{-11}$  ( $6.4 \times 10^{-13}$ /cm) at 1-s averaging. This is already much better than typical ring-down results.

**Principle of NICE-OHMS.** To be tuned more towards the true spirit of FM spectroscopy (and enjoy its noise-reduction advantages), one needs to increase the phase-modulation frequency of the probing field, usually to be much larger than the resonance linewidth under study. Besides the laser-cavity locking issue, we are then faced with another obstacle, namely the cavity bandwidth limit. What is needed is a way to have the FM sidebands at a high frequency to get low amplitude noise, while the cavity accepts the sidebands in exactly the same manner as it accepts the carrier so as to reduce the FM to AM noise conversion. This can be accomplished by frequency modulating the input laser beam at exactly the splitting frequency of the cavity free-spectral-range (FSR). We then detect and demodulate the cavity-transmitted light at the modulation frequency. The small residual frequency variations of the laser will still lead to some amplitude fluctuations and small optical phase shifts of the transmitted carrier, but they

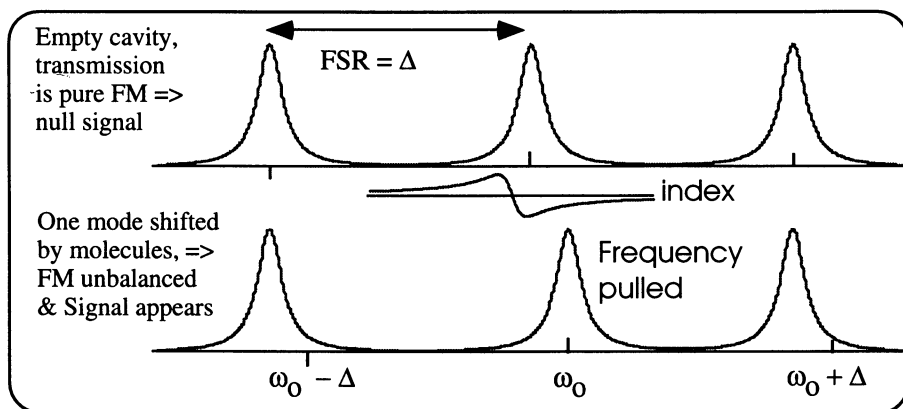


Fig 5. Basic principle of Noise-Immune Cavity-Enhanced Optical Heterodyne Molecular Spectroscopy. FM symmetry is upset when molecular dispersion shifts a cavity resonance and the laser carrier locked to it. This makes sidebands slightly detuned from their resonances, leading to phase shifts in transmitted light.

will also lead to exactly the same amplitude fluctuations and phase shifts of the sidebands which are transmitted on adjacent or nearby cavity axial orders. So the transmitted light still accurately represents an FM spectral triplet, with minimal AM conversion due to the relative laser/cavity frequency jitter. Thus the noise level can approach the intrinsic AM noise level of the laser at the FSR frequency, typically a few hundred MHz or a few GHz.

Figure 5 shows the case where the central component is used to detect the intracavity molecular resonance. Initially all the FM components are lined up with their respective cavity modes. The central cavity mode will then be frequency pulled due to the additional phase shift by the molecular dispersion. The detector viewing the transmitted light will thus generate a dispersion signal in the rf beat after the phase sensitive demodulation. We can refer to this technique as (laser frequency-) Noise-Immune Cavity-Enhanced Optical Heterodyne Molecular Spectroscopy ("NICE-OHMS"). This modulation and detection scheme enables profitable use of very high cavity finesse without any noise penalty.

**Noise immune properties.** To have a convincing demonstration of the noise-immune nature of this detection, we deliberately set the laser/cavity lock to be loose and even oscillating, then we compare the recovered signal-to-noise ratios (S/N) before and after the lock was sabotaged. The result is shown in Figure 6 for the  $C_2HD$  ( $\nu_2 + 3\nu_3$ ) P(5) transition at  $1.064 \mu m$  (7). The signals were recovered in two channels. The first one had the cavity length dithered at a low audio frequency and used a lock-in for demodulation of the direct cavity transmission (DC). The second was from the high frequency channel of NICE-OHMS. Signal lineshapes follow modulation-broadened derivatives of absorption (DC) (25) and dispersion (NICE-OHMS) (26). The DC dither-detection of the intracavity molecular absorption (upper row) is shown to be critically dependent upon the performance of the laser/cavity lock. (A fast, strong laser/cavity frequency-lock servo was used for the graphs in the left column, while a slow and noisy servo was used for those in the right column.) However, increased laser frequency noise (relative to the cavity) yields little effect in our FM detection (bottom row).

These results were obtained in the general experimental schematic shown in Figure 7. One may use two electro-optic phase modulators to impose two sets of FM side bands on the laser beam. The modulation at a low frequency  $\delta$  is detected in the cavity

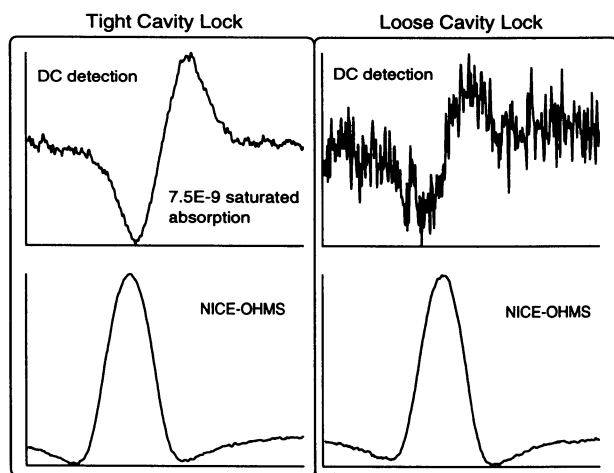


Figure 6. Demonstration of the noise-immune property of NICE-OHMS. The  $C_2HD$  ( $\nu_2 + 3\nu_3$ ) P(5) resonance signal is recovered by both cavity-dither lock-in (DC) detection and NICE-OHMS technique, under conditions of a tight laser/cavity lock (left column) and a substantially deteriorated lock (right column).

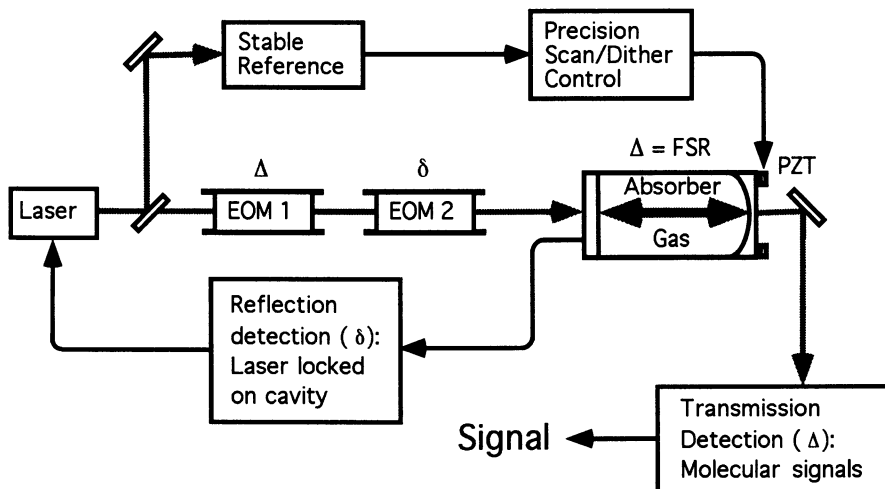


Figure 7 General experimental schematic for the NICE-OHMS spectrometer. For our cavity  $\Delta \approx 324$  Mhz, while  $\delta = 4$  Mhz provides an adequate servo bandwidth ( $\sim 300$  kHz).

reflection signal to produce the cavity dispersion locking error for stabilizing the laser onto the cavity. Although the requirement of the laser/cavity locking is much more relaxed for NICE-OHMS than in the simple DC detection, the laser linewidth still needs to be narrowed so that a stable optical power is effectively coupled into the cavity. The sidebands at the high modulation frequency  $\Delta = \text{FSR}$  are used to probe the intracavity molecular resonances and are detected in cavity transmission. Adequate optical isolation between the photodiode scatter and the cavity is provided by an AOM.

An important technical issue is that the recovered lineshape is influenced by a residual AM (RAM) associated with FM at the cavity FSR frequency. With an active control loop we are able to eliminate the RAM (27) and obtain a lineshape matching perfectly to a theoretical model, resulting in a flat and nearly shot-noise limited background for the fit residual throughout the entire tuning range of the resonance. A frequency offset locking loop is implemented to permit a precision sweep of the laser frequency relative to a stable reference for the study of the resonance lineshape and width. During the scan, the cavity FSR will change slightly. To maintain the noise-immune property, we actively track the sideband frequency to the cavity FSR value.

**Sensitivity statement for NICE-OHMS.** Although NICE-OHMS does not bring in any extra technical noise from the laser frequency jitter relative to the cavity, it still requires carefully-maintained optical isolation throughout the beam layout to achieve the shot-noise limited performance. Compared with Equation (8), for the ideal case of homodyne detection, the heterodyne FM suffers a factor of  $\sim 4$  loss in sensitivity for fixed total optical power. This is due in part to the power reduction implied in converting some of the main carrier to sidebands and in part to the down-conversion of shot noise from two additional spectral windows by the two sidebands. However, being able to achieve the shot-noise limit, the NICE-OHMS sensitivity is simply,

$$(\alpha L)_{\min} = \frac{\pi}{2 \cdot \text{Finesse}} \left( \frac{2Bh\nu}{\eta P_t} \right)^{1/2} \frac{\sqrt{2}}{J_0(\beta)J_1(\beta)}. \quad (9)$$

Here  $J_0$  ( $J_1$ ) is the zero (first) order Bessel function and  $\beta$  is the modulation index (at  $\Delta$ ).

A numerical example is given here for the NICE-OHMS sensitivity using our experimental parameters. Suppose  $\beta = 0.5$  and the photodiode responsivity  $\eta' = 0.85$  Amps/Watt. ( $\eta' = (e/h\nu)\eta$ ). Also assume the total detected power  $P_t = 5$  mW and the detection bandwidth =  $1/2\pi$  Hz, corresponding to a 1s time constant. Then for a plain single-pass cell, the noise-equivalent integrated absorption is:  $(\alpha L)_{\min} = 2.2 \times 10^{-8}$ . Under the same conditions, using NICE-OHMS and a cavity with a finesse of 100,000 improves the sensitivity to:  $(\alpha L)_{\min} = 3.5 \times 10^{-13}$ .

**NICE-OHMS method: the highest sensitivity.** Figure 8 shows the experimental sensitivity we have achieved using 1.8 mTorr of  $C_2HD$  gas. The cavity finesse is 100,000 and the intracavity buildup power is  $\sim 300$  W, giving a saturation parameter of  $\sim 1.75$  and a saturation peak contrast of 13.2%. The single-pass (46.9 cm long cavity) linear absorption is about  $3 \times 10^{-8}$ . Therefore the absolute level of saturated absorption by the intracavity molecules is  $4 \times 10^{-9}$ . This is verified by the DC detection of the cavity transmission, shown in the top graph of the figure. The calibration process involves measurement of cavity finesse, on-resonance transmission, and reflection dip contrast, from which we calculate the residual round-trip cavity losses. With the laser locked tightly onto the cavity with a relative linewidth of  $\sim 1$  milliHertz, the simple cavity-dither and lock-in detection of the transmission yields a S/N (amplitude / rms noise)

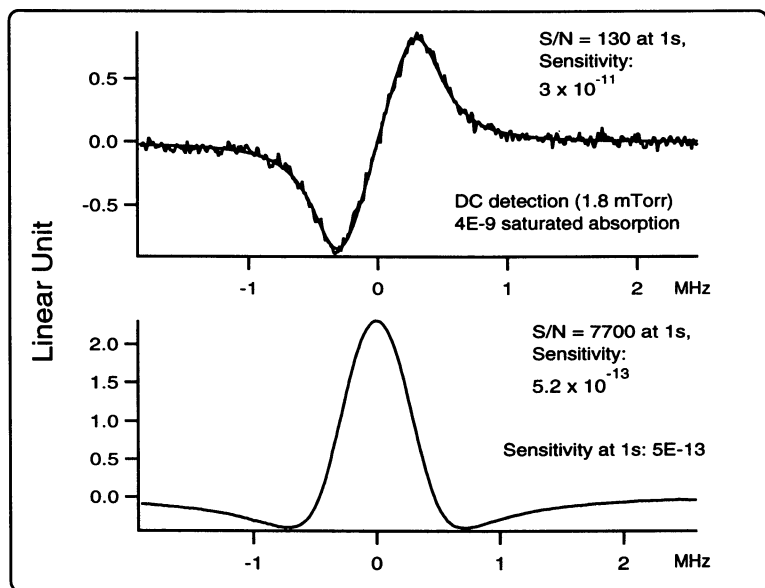


Figure 8. Sensitivity measurement of the NICE-OHMS technique. The upper graph shows the level of the saturated absorption while the lower graph shows the corresponding S/N obtained via NICE-OHMS. The noise-equivalent detection sensitivities (normalized to 1s time constant) are  $3 \times 10^{-11}$  for DC (cavity dither detection) and  $5.2 \times 10^{-13}$  for NICE-OHMS.

noise) of 130 at 1-s averaging. This corresponds to a detection sensitivity of  $3 \times 10^{-11}$  at 1 s. The corresponding S/N from the NICE-OHMS detection is 7700 with a 1 s time constant, as shown in the bottom graph of the figure. This translates into a noise-equivalent detection sensitivity of  $5.2 \times 10^{-13}$  ( $1 \times 10^{-14}$  / cm) at 1 s averaging, about 1.5 times worse than the shot noise limit calculated previously. The NICE-OHMS result is  $\sim 60$  times better than the straightforward dither detection, basically because of its higher modulation frequency (319 MHz FM sideband frequency compared with 500 Hz dither frequency) and its insensitivity towards the laser frequency noise.

### Ultrasensitive measurement of other transitions: HCCH, HCCD, CO<sub>2</sub>

To give an indication of the extreme expansion of our spectroscopic possibilities when the detection sensitivity has increased by 5 orders of magnitude by the use of the NICE-OHMS method, we naturally seek other weak transitions within the tuning range of the Nd:YAG laser at 1.064  $\mu\text{m}$ . We have measured two such additional lines, namely  $^{12}\text{C}_2\text{H}_2$  ( $2\nu_1 + \nu_2 + \nu_3$ ) R(12) (28) and  $^{12}\text{C}^{16}\text{O}_2$  ( $2\nu_1 + 3\nu_3$ ) R(6), (29) with their respective ro-vibronic dipole moment of 50  $\mu\text{Debye}$  and 6  $\mu\text{Debye}$ . (1 Debye =  $3.33564 \times 10^{-30}$  C · m) They are both weaker than the  $\text{C}_2\text{HD}$  ( $\nu_2 + 3\nu_3$ ) P(5) transition, which has a transition dipole moment of  $\sim 70$   $\mu\text{Debye}$ .

Using the same gas pressure, optical power, and cavity dither amplitude, we compare the saturated absorption signals of  $\text{CO}_2$ ,  $\text{C}_2\text{HD}$  and  $\text{C}_2\text{H}_2$  in Figure 9.

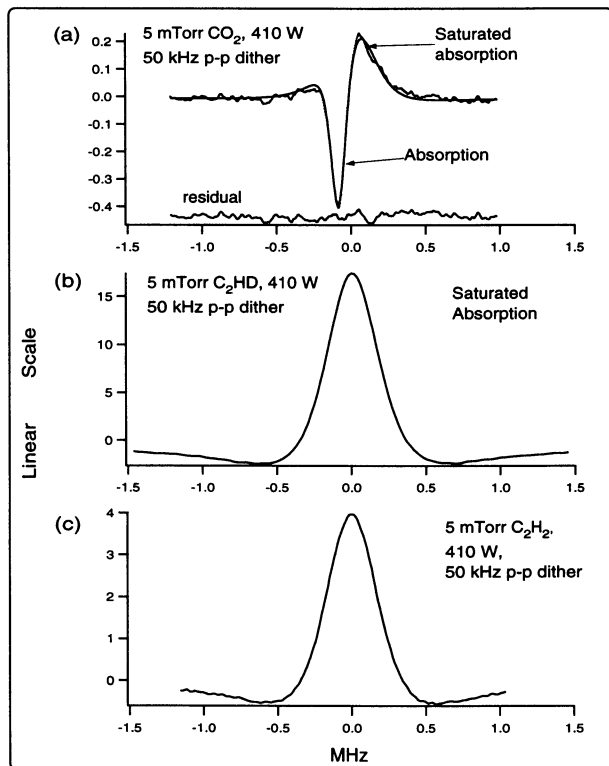


Figure 9. Lineshape comparison among the resonances of three molecules. (a)  $\text{CO}_2$ , (b)  $\text{C}_2\text{HD}$ , and (c)  $\text{C}_2\text{H}_2$ , all data taken under the same experimental conditions. The negative-going  $\text{CO}_2$  resonance has a zero-pressure extrapolated line-width of  $\sim 100$  kHz, half the value of the transit-time broadening. These aspects lead us tentatively to identify this feature as arising from two-photon absorption.

The  $C_2H_2$  transition is recovered with an excellent signal-to-noise ratio, as shown in Figure 9(c). The signal size is about 1/4 of that for  $C_2HD$ , using the same gas pressure and optical power. It provides another frequency reference for the Nd:YAG laser, besides  $C_2HD$ . The center frequency of the resonance is 281,612,403.278 (.025) MHz, i.e., it is 17708.458 (.014) MHz red of a frequency doubled Nd:YAG laser locked on the  $a_{10}$  hyperfine-structure component of the R(56) 32-0  $I_2$  transition.(30) The pressure broadening rate of 34(1) MHz/Torr (FWHM) is similar to that of  $C_2HD$ .(7) For the  $CO_2$  transition, however, the saturated absorption signal is much weaker than the  $C_2HD$  line, by more than a factor of 350. This  $CO_2$  resonance involves two quanta of symmetric stretch and three quanta of antisymmetric stretch of the C-O bond.(29) The bending mode ( $\nu_2$ ) is not excited. The life time of the excited vibrational state is estimated to be  $\sim 2$  ms, mainly due to the IR fluorescence on the vibrational transition  $(2, 0^0, 3) \rightarrow (2, 0^0, 2)$ . The relevant molecular constants are ( $cm^{-1}$ ):  $B' = 0.39021894$ ,  $D' = 1.33373 \times 10^{-7}$  for the ground state, and  $B'' = 0.38234$ ,  $D'' = 1.71$  for the excited state with the band origin at 9388.990.(31)

Under exactly the same experimental conditions (except for the change of sample gas), the recovered lineshape associated with the  $^{12}C^{16}O_2$  ( $2\nu_1 + 3\nu_3$ ) R(6) transition is vastly different from either  $C_2HD$  or  $C_2H_2$ , as indicated in Figure 9.

### Laser Stabilization by NICE-OHMS

In the work of optical frequency metrology, the NICE-OHMS technique can provide us with thousands of weak molecular lines as high quality visible frequency/wavelength references. The narrow linewidths associated with these molecular transitions are invaluable, as they facilitate better definitions of the linecenters to ensure long-term stabilities. Using the NICE-OHMS method, the high signal-to-noise ratio of the resonance information helps to reach the desired short-term stability in reduced averaging time, permitting more effective intercomparisons among various frequency standards. With the narrower linewidth - but lower S/N - of the  $C_2HD$  overtone transition, we have currently achieved a level of stability similar to that of the  $I_2$  system (30). However, the long natural lifetime of overtone transitions provides the opportunity for optical selection of slow molecules to produce a much narrower linewidth (currently by 13 times) than the room temperature transit time limit. (Slow molecules are the ones preferentially responding when the power and pressure are very low.) The narrower line should further improve the long term stability and reproducibility.

A very effective representation of the frequency noise in the time domain is by the Allan variance.(32) In calculating the Allan variance one simply compares adjacent frequency measurements and then averages this difference over the whole data set. The time interval between the adjacent measurements is basically the averaging time for the frequency noise. The Allan variance permits one to separate and isolate different noise processes based on their time scales. In the short-time domain, the Allan variance typically displays a slope of  $\tau^{-1/2}$ , where  $\tau$  is the averaging time. This is because the main contribution to the fast noise originates from white noise, ideally, the shot noise. One thus sees from this argument that the level of this short-term variance is fixed by the ratio between the frequency discrimination linewidth and its S/N. Figure 10 also shows the calculated Allan variance from the beat record of the two stabilized lasers.

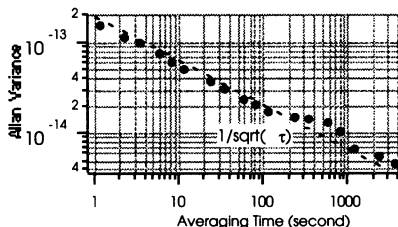
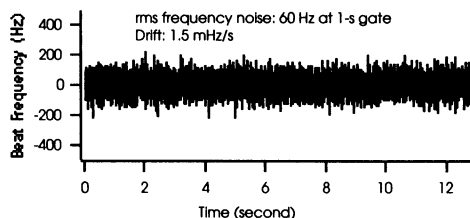


Figure 10a. Stability of beat between  $I_2$  stabilized and HCCD-stabilized lasers. The improving ultrasensitive detection of a weak overtone resonance of molecular HCCD permits progressively better results on the laser stabilization. The heterodyne reference laser is stabilized on an  $I_2$  transition at 532 nm using modulation transfer spectroscopy. This reference laser has a stability  $\sim 5 \times 10^{-14}$  at 1 s, from beating experiments with two  $I_2$ -stabilized systems. See Fig 10b.

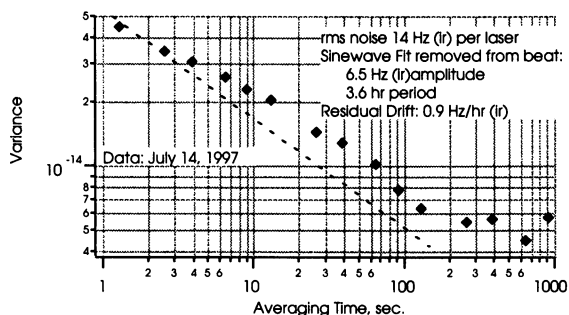


Figure 10b. Beat Stability between two  $I_2$ -stabilized lasers, using R(56) 32-0 transition,  $a_{10}$  hyperfine component and modulation transfer spectroscopy. We note that the molecular absorption is nearly a million-fold stronger than that of the HCCD used for Fig 10a, above, but the short-term stabilization results differ by a mere factor of 4!

The variances are normalized to the optical carrier frequency, i.e., 282 THz (1.064  $\mu\text{m}$ ). The Allan variance of  $\sigma_y = 2 \times 10^{-13}/\sqrt{\tau}$  improves to  $6 \times 10^{-15}$  at a longer integration time ( $> 1000$  s), a promising indicator for an ultrastable frequency reference.

This amazing frequency stability being achieved with the extremely weak reference transition is a direct result of our spectrometer's ultra-high detection sensitivity. Notice that the  $C_2HD$ -stabilized system shows only 2 - 4 times more noise than the  $I_2$  system, a remarkable success considering the green  $I_2$  transition strength is almost a million times stronger than the P(5) line of the  $C_2HD$  ( $\nu_2 + 3 \nu_3$ ) overtone band. The short-term frequency stabilities of the optical sources are comparable to or better than the state of the art microwave standards. However, the optical reproducibility and accuracy are not yet comparable, lagging by 1 or more decades. The urgent task is therefore to vastly reduce the systematic influences on the optical transition line-centers.

Our NICE-OHMS spectrometer naturally provides laser frequency discrimination information by both the cavity resonance and the molecular transition. It is thus an ideal system for achieving simultaneously good short- and long-term frequency stabilizations. The laser frequency basically tracks the cavity resonance on the level of a few millihertz with a fast servo loop. The vibration noise and the long-term drift of the cavity can be reduced - basically eliminated - by stabilizing to the intracavity molecular transition.

The NICE-OHMS signal is intrinsically dispersive when the molecular resonance is probed by the carrier of the FM triplet. However, in practice we found it necessary to dither the cavity length and make a 2-nd derivative signal recovery of the rf balanced



mixer signal output, in order to obtain a “discriminator” lineshape with adequate baseline stability. In part this can suppress the baseline offset problem associated with the imperfect FM modulation at the FSR frequency. However, to achieve the best stabilization results, it is crucial that the FM has a zero (or at worst a small constant) residual AM so that the pure FM dispersion signal lineshape is not contaminated by the absorptive phase component. We used active control of the modulator in our setup.(27)

To summarize, we checked the quality of this overtone-stabilized laser at 1.064  $\mu\text{m}$  against a frequency-doubled Nd:YAG /  $\text{I}_2$  reference system via optical heterodyne beat. (The 532 nm-stabilized laser has a stability  $\sim 5 \times 10^{-14}$  at 1 s, from beating experiments with two  $\text{I}_2$ -stabilized systems: see Fig 10b.) In Figure 10a the counted beat frequency vs. time shows a drift  $\sim 5$  Hz/h and a 60 Hz frequency noise at 1-s counter gate time, in direct agreement with the S/N available at 1.064  $\mu\text{m}$ .

### General Concluding Advice/remarks on attaining the highest sensitivity

It is clear that some dramatic progress in optical detection sensitivity is possible if we can learn well how to separate the molecular signal from the cavity's stored field, and perform the detection at a frequency where there is no non-fundamental noise to bother us. Basically we have to determine the cavity's response simultaneously for the on-resonance and off-resonance cases, so they can be subtracted to reveal the molecular absorption of interest. We have explained how the FM method of NICE-OHMS works to implement this signal isolation and subtraction continuously and simultaneously in real time, and we have illustrated the unprecedented sensitivity level of  $5.2 \times 10^{-13}$  integrated absorption. Still, we feel there may be some repetitive transient heterodyne detection scheme which will also satisfy our design principles for good sensitivity, ideally with lowered technical requirements for the laser system. However even if this dream is not immediately realizable, it is in fact rather straightforward to perform the laser stabilization and modulations at the level required for NICE-OHMS. One must see there is a vast difference between doing the laser stabilization for the first time and doing it again: we are ready to work with the interested community to help this sensitivity be more widely available to interested spectroscopists. Some technical “how-to-do-it” workshop(s) and publications are foreseen for the near future.

### Acknowledgments

We wish to acknowledge the funding support from the National Institute of Standards and Technology, the U.S. Office of Naval Research, the U.S. Air Force Office of Scientific Research, and the National Science Foundation. We thank Professor Kevin Lehmann for useful comments on this manuscript.

### Literature Cited

- 1 Olopade, C.O., Zakkar, M., Swedler, W.I., Rubinstein, I. “Exhaled pentane levels in acute asthma,” *Chest* **1997** (Apr) *111*(4), 862-5.
- 2 Dohlman, A.W., Black, H.R., Royall, J.A. “Expired breath hydrogen peroxide is a marker of acute airway inflammation in pediatric patients with asthma,” *Am Rev Respir Dis* **1993** (Oct) *148*(4 Pt 1), 955-60.

- 3 Kneepkens, C.M., Lepage, G., Roy, C.C. "The potential of the hydrocarbon breath test as a measure of lipid peroxidation," *Free Radic Biol Med* **1994** (Aug) *17*(2), 127-60; erratum appears in *Free Radic Biol Med* **1994** (Dec) *17*(6),609.
- 4 Refat, M., Moore, T.J., Kazui, M., Risby, T.H., Perman, J.A., Schwarz, K.B., "Utility of breath ethane as a noninvasive biomarker of vitamin E status in children," *Pediatr Res* **1991** (Nov) *30*(5), 396-403.
- 5 Hietanen, E., Bartsch, H., Bereziat, J.C., Camus, A.M., McClinton, S., Eremin, O., Davidson, L., Boyle, P. "Diet and oxidative stress in breast, colon and prostate cancer patients: a case-control study," *Eur J Clin Nutr* **1994** (Aug) *48*(8), 575-86.
- 6 Cailleux, A., Allain, P. "Is pentane a normal constituent of human breath?" *Free Radic Res Commun* **1993**, *18*(6), 323-7.
- 7 Ye, Jun, Ma, Long-Sheng, Hall, John L., "Ultrastable Optical Frequency Reference at 1.064  $\mu\text{m}$  Using a  $\text{C}_2\text{HD}$  molecular Overtone Transition," *IEEE Trans. Instrum. & Meas.***1997**, *36* (2), 178-182; Ye, J., Ph.D dissertation, University of Colorado at Boulder (1997).
- 8 de Angelis, M., Gagliardi, G., Gianfrani, L., Tino, G. M., "Test of the Symmetrization Postulate for Spin-0 Particles," *Phys. Rev. Lett.* **1996**, *76*, 2840-2843.
- 9 "Millenium," produced by Spectra Physics, Mountain View CA. See Ref 10.
- 10 The use of brand names is only for technical communication and does not represent an endorsement, nor does it imply that other equipment would be less suitable.
- 11 Hänsch, T. W., Schawlow, A. L., Toschek, P. E., *IEEE J. Quan. Electron.* **1972**, *QE-8*, 802-804.
- 12 Kimble, H. J., *IEEE J. Quan. Electron.* **1980**, *QE-16*, 455-461.
- 13 Harris, T. D., in "Ultrasensitive Laser Spectroscopy"; Klinger, D. S. Ed.; Academic Press, New York (1983) pp 343. ff.
- 14 Altmann, J., Baumgart, R., Weitkamp, C., *Appl. Opt.* **1981**, *20*, 995-9.
- 15 Kastler, A., *Appl. Opt.* **1962**, *1*, 17.
- 16 Cerez, P., Brillet, A., Man-Pichot, C. N., Felder, R, *IEEE Trans. Instrum. & Meas.***1980**, *29*, 352-7.
- 17 Ma, L.-S., Hall, J. L., *IEEE J. Quan. Electron.* **1990**, *QE-26*, 2006-2012.
- 18 De Labacherie, M., Nakagawa, K., Ohtsu, M., *Opt. Lett.* **1994**, *19*, 840-842.
- 19 O'Keefe, A., Deacon, D. A. G., *Rev. Sci. Instrum.* **1988**, *59*, 2544-51; For more recent advances, see else-where in these proceedings.
- 20 Hall, J. L., Bordé, C. J., *Appl. Phys. Lett.* **1976**, *29*, 788-90.
- 21 Wieman, C. E., Hänsch, T. W., *Phys. Rev. Lett.* **1976**, *36*, 1170-3.
- 22 Baer, T. M., Hall, J. L. in *Abstracts of Papers, Atomic Physics 1980*, MIT, Cambridge MA; also see Dubé, P., Levenson, M. D., Hall, J. L., "Free Induction decay in molecular iodine measured with an extended-cavity laser," *Opt. Lett.* **1997**, *22*, 184-6.
- 23 See Brewer, R. G. and Genack, A. Z., *Phys. Rev.* **1978**, *A17*, 1463-73.
- 24 In addition to the following discussion, additional information is contained in Ref. 7.
- 25 Wahlquist, H., "Modulation broadening of unsaturated Lorentzian lines," *J. Chem. Phys.* **1961**, *35*, 1708.
- 26 Smith, R. L., "Practical solutions of the lock-in detection problem for Lorentz and dispersion resonance signals," *J. Opt. Soc. Am.* **1971**, *61*, 1015-22.
- 27 Hall, J. L., Ye, J., Ma, L.-S., Vogel, K., Dinneen, T., "Optical Frequency Standards: Progress & Application" in *Laser Spectroscopy XIII*; Wang, Y. Z., Ed., World Scientific, Singapore, **1998**, 75-80.
- 28 Nakagawa, K., Katsuda, T., Shelkovnikov, A. S., De Labacherie, M., Ohtsu, M., "Highly sensitive detection of molecular absorption using a high finesse optical cavity," *Opt. Commun.* **1994**, *107*, 369-372.
- 29 Fritschel, P., Weiss, R., "Frequency match of the Nd:YAG laser at 1.064  $\mu\text{m}$  with a line in  $\text{CO}_2$ ," *Appl. Opt.* **1992**, *31*, 1910-1912.
- 30 Eickhoff, M. L., Hall, J. L. "Optical frequency standard at 532 nm," *IEEE Trans. Instrum. & Meas.* **1995**, *44*, 155-158; also Jungner, P., Swartz, S., Eickhoff, M. E., Ye, J., Hall, J. L., Waltman, S., *IEEE Trans. Instrum. & Meas.* **1995**, *44*, 151-4.
- 31 Rothman, L. S. and Young, L. D. G. "Infrared energy levels and intensities of carbon dioxide – II," *J. Quant. Spectrosc. Radiat. Transfer* **1981**, *25*, 505-524.
- 32 Allan, D. W., "Statistics of Atomic Frequency Standards," *Proc. IEEE* **1966**, *54*, 221-30.

# Author Index

- Aniolek, K. W., 174  
Arrington, Caleb A., 210  
Berden, Giel, 146  
Busch, Kenneth W., 7, 20, 34  
Busch, Marianna A., 7, 20, 34  
Chapo, C., 162  
Engeln, Richard, 146  
Giles, Brent J., 210  
Hagemeister, Fredrick C., 210  
Hall, John L., 233  
Hennequin, Aurélie, 20, 34  
Hodges, Joseph T., 93  
Lehmann, Kevin K., 106  
Lin, M. C., 196  
Looney, J. Patrick, 93  
Ma, Long-Sheng, 233  
Meijer, Gerard, 146  
Michael, E., 162  
O'Keefe, A., 71  
Paldus, B. A., 1, 49  
Park, J., 196  
Paul, J. B., 71, 162  
Pettersson, A., 162  
Provencal, R. A., 162  
Quimpo, Bobby, 210  
Rakestraw, D. J., 174  
Romanini, Daniele, 125  
Saykally, R. J., 71, 162  
Scherer, J. J., 71, 174  
van Zee, Roger D., 93  
Ye, Jun, 233  
Zare, R. N., 1, 49  
Zhang, Limin, 210  
Zwier, Timothy S., 210

# Subject Index

## A

- Absorption measurements, statistical uncertainties, 98, 100
- Absorption sensitivity. *See* High absorption sensitivity
- Absorption spectroscopies
  - Beer–Lambert law, 49
  - definition, 49
  - historical overview, 1–5
  - laser spectroscopy, 50
  - mean absorption signal, 50
  - minimum detectable absorption loss per shot (MDAL<sub>shot</sub>), 50
  - minimum detectable fractional signal per shot (MDFS<sub>shot</sub>), 50
  - sensitivity expressions, 50
- See also* Cavity-ringdown spectroscopy (CRDS); Continuous-wave cavity-ringdown spectroscopy (CW–CRDS); Fourier transform cavity-ringdown spectroscopy (FT–CRDS); Laser absorption spectroscopy; Linear absorption spectroscopy; Polarization dependent cavity-ringdown spectroscopy (PD–CRDS); Pulsed cavity-ringdown spectroscopy (P–CRDS); Ultrasensitive laser absorption spectroscopies
- Airy lineshape, resonance peaks in RDS transfer function, 59
- Airy's formula
  - Lorentzian approximation, 95
  - transmission of Fabry–Perot cavity, 37
- Aromatic radical reactions, kinetic studies
  - absolute rate constants for the reactions of C<sub>6</sub>H<sub>5</sub> studied by CRD method, 206*t*
  - aromatic hydrocarbon combustion chemistry, 196–197
  - C<sub>6</sub>H<sub>5</sub> radical generation, 197
  - cavity-ringdown (CRD) method, 197–198
  - elucidating soot formation mechanism, 196–197
  - experimental apparatus, 197–198
  - experimental chemicals, 198
  - first-order decay constants for C<sub>6</sub>H<sub>5</sub>O<sub>2</sub> formation, 199, 200*f*
  - kinetic data acquisition and analysis, 198–200
  - nitrosobenzene formation from C<sub>6</sub>H<sub>5</sub> and NO, 201
  - reaction between C<sub>6</sub>H<sub>5</sub> and O<sub>2</sub>, 202
  - reaction of C<sub>6</sub>H<sub>5</sub> with C<sub>2</sub>H<sub>2</sub> and C<sub>2</sub>H<sub>4</sub>, 202–204

- reaction of C<sub>6</sub>H<sub>5</sub> with carbon tetrachloride, 206
- reaction of C<sub>6</sub>H<sub>5</sub> with cycloalkanes (C<sub>5</sub>H<sub>10</sub> to C<sub>8</sub>H<sub>16</sub>), 205
- reaction of C<sub>6</sub>H<sub>5</sub> with HBr/DBr, 207–208
- reaction of C<sub>6</sub>H<sub>5</sub> with *i*-C<sub>4</sub>H<sub>10</sub> and (*i*-C<sub>3</sub>H<sub>7</sub>)<sub>2</sub>, 204
- reactive intermediates in formation of polycyclic aromatic hydrocarbons (PAHs), 196
- relationship between photon decay and radical decay times, 198*f*
- schematic diagram of cavity-ringdown absorption apparatus, 197*f*
- typical pseudo-first order decay plots for C<sub>6</sub>H<sub>5</sub> with cyclohexane, 199*f*
- versatility of cavity-ringdown (CRD) method, 208
- Atmosphere, detection of trace materials, 233–234

## B

- Balmer (1825-1898), specific series of hydrogen lines, 4
- Basov (1922-), maser invention, 5
- Beer–Lambert law
  - in absorption spectroscopy, 8–9, 49
  - ringdown time when law valid, 93–94, 93–95, 104
- Biomolecules (gas phase) and biomolecule–water complexes
  - gas-phase hydration of amino acid valine, 173*f*
  - infrared cavity-ringdown laser absorption spectroscopy (IRCRLAS), 167, 172
- Bloembergen (1920-), devising laser spectroscopy, 5
- Bohr (1885-1962), atomic theory, 4
- Bunsen (1811-1899), flame and spark spectra with Kirchhoff, 3–4

## C

- Carbon clusters
  - infrared cavity-ringdown laser absorption spectroscopy (IRCRLAS), 167
  - spectrum of ν<sub>3</sub> band of C<sub>5</sub>, 170*f*
- CARS. *See* Coherent anti-stokes Raman spectroscopy (CARS); Polyatomic radicals at low pressure

- Cavities. *See* Optical cavities
- Cavity field  
with Gaussian absorber, 119  
with Lorentzian absorber, 113–118
- Cavity Lossmeter, commercial mirror testing instruments, 73–74
- Cavity mirrors  
cavity-ringdown spectroscopy (CRDS), 14–15  
schematic representation of mirror reflectivity for multi-layer dielectric mirror, 15*f*
- Cavity-ringdown laser absorption spectroscopy (CRLAS). *See* Polyatomic radicals at low pressure
- Cavity-ringdown signals, field-based derivation, 94–97
- Cavity-ringdown spectroscopy (CRDS)  
advantages of approach, 56  
advantages of pulsed–CRDS, 127  
alternative techniques, 9  
analog-to-digital conversion, 15–16  
applications for gas-phase absorption measurements, 8–9  
basic considerations, 10–13  
basic experimental setup, 13*f*  
basic ideas, 126–127  
Beer–Lambert law, 8–9  
cavity loss spectrum of ambient air, 146, 147*f*  
cavity mirrors, 14–15  
cavity modes, 130–132  
cavity response decay rate, 129  
comparison of various absorption spectroscopies, 56*t*  
continuous wave CRDS (CW–CRDS), 66–68, 133–134  
detection limit, 135–136  
detection limit comparisons, 126  
development of pulsed cavity ringdown, 73–74  
diode laser CW–CRDS spectrum of Doppler limited weak overtone transition  $N_2O$ , 133*f*  
dynamic range, 17  
events leading to birth of linear absorption spectroscopy, 1–5  
expense of pulsed laser source, 18  
experimental considerations, 16–17  
experimental history, 61–68  
experimental implementation, 13–16  
extraction of quantitative information, 148–149  
factors affecting pulsed–CRDS resolution, 132  
fluorescence spectra from sub-Doppler rovibronic transitions of  $NO_2$  seeded in supersonic slit jet, 134*f*  
fractional absorption per pass, 16  
future prospects, 17–18  
general theory of operation, 74–75  
high resolution CRDS with a CW laser, 133–134
- Kirchhoff's law, 11  
laser alignment and mirror positions, 129  
linear optical resonator, 57*f*  
longitudinal and transversal mode orders, 130–131  
long-path approaches, 9  
loss calculations for cavity, 11–12  
measurements in repetitive sources like pulsed molecular beams and pulsed discharges, 147–148  
measurements of reaction products, 77, 80  
measuring trace components in gas-phase samples by absorption spectroscopy, 7  
mirror coating characterization, 128–129  
mirror reflectometers, precursors to CRDS, 61–63  
mode formation and, 46–47  
mode matching, 131–132  
mode structure of linear optical resonator, 57*f*  
name origin, 10  
original driving forces, 71–73  
overview, 58–68  
parasitic cavity losses, 128  
phase-shift CRDS method, 127–128  
ping-pong model simplistic view, 58–59  
potential problems in real-world environments, 17–18  
power saturation, 134–135  
probing laser vaporization supersonic gas expansion, 83–89  
pulsed–CRDS, 56, 63–66  
ringdown cavity (RDC) transfer functions  
more sophisticated view, 59–60  
required mirror characteristics, 14  
ring gyroscopes and interferometers, 71–73  
schematic diagram of 11-layer dielectric mirror, 14*f*  
schematic diagram of ringdown cavity, 10*f*  
schematic representation of mirror reflectivity for multi-layer dielectric mirror, 15*f*  
schematic representation of ringdown pattern, 11*f*  
sensitivity, 16–17, 60  
solid transparent samples, 148  
stability diagram for optical resonator, 57*f*  
static cell absorption measurements, 75–77  
theory, 58–60  
time domain, 119–123  
trace species detection, 77  
ultra-sensitive absorption measurements, 7  
*See also* Fourier transform cavity-ringdown spectroscopy (FT–CRDS); History of cavity-ringdown spectroscopy (CRDS); Polarization dependent cavity-ringdown spectroscopy (PD–CRDS); Pulsed cavity-ringdown spectroscopy (P–CRDS); Supersonic application
- Cavity stability

- application of matrix optics to, 28, 30–31  
 criteria, 26–31  
 g-parameters, 27  
 graphical determination, 27–28, 29f  
 ray parameters after successive reflections in cavity, 30f  
 ray parameters after successive reflections in unstable cavity, 31f  
 resonator circle diagrams for three cavities, 29f  
 stability diagram,  $g_2$  versus  $g_1$  plot, 28f  
 stable cavities, 26–27  
 transverse ray displacement versus number of round-trips in cavity, 30f  
 unstable cavities, 26
- Coherent anti-stokes Raman spectroscopy (CARS)  
 combustion diagnostics technique, 174–175  
 spectroscopic technique, 5  
*See also* Polymeric radicals in low pressure Compton (1982-1962), photons behaving like particles, 5
- Concave-concave optical cavities, 21  
 Concentric, two-mirror cavities, 32f  
 Condon (1902-1974), ideas of quantum mechanics, 5  
 Confocal, two-mirror cavities, 32f  
 Continuous-wave cavity-ringdown spectroscopy (CW-CRDS)  
 detection limit, 135–136  
 diode laser CW-CRDS spectrum of Doppler limited weak overtone transition  $N_2O$ , 133f  
 experimental history, 66–68  
 fluorescence spectra from sub-Doppler rovibronic transitions of  $NO_2$  seeded in supersonic slit jet, 134f  
 high resolution with CW laser, 133–134  
 laser sources, 67  
 phase shift method, 133  
 Pound-Drever-Hall electronic locking technique, 67  
 power saturation, 134–135  
 spectral range, 142  
 ultimate sensitivity, 68  
 use of edge-emitting laser diodes (LDs), 67
- Copernicus (1473-1543), telescopes for star observation, 1–2
- Copper dimer. *See* Supersonic application  
 Copper trimer. *See* Supersonic application
- CRDS. *See* Cavity-ringdown spectroscopy (CRDS)
- D**
- Daguerre (1789-1851), creation of photographic film, 4  
 da Vinci (1452-1519), vision and stereoscopic function of human eyes, 1–2
- deBroglie (1892-1987), ideas of quantum mechanics, 5
- Decay-time reflectometer  
 experimental setup, 62f  
*See also* Mirror reflectometers
- Deuterated water clusters. *See* Water clusters
- Diacetylene  
 absolute cross section for singlet-triplet transition, 216, 219  
 electron energy loss spectrum (EELS), 213  
 energy level diagram for diacetylene and metastable state reactions with ground state  $C_4H_2$  to form products, 212f  
 experimental apparatus for singlet-triplet cavity ringdown spectroscopy, 213, 214f  
 increased resolution of CRD over EEL spectrum, 213, 216  
 one dimensional potential energy curves along *trans*-linear-*cis* isomerization coordinate, 216, 217f  
 overview CRD scan spanning wavelength range 387 to 343 nm, 213, 215f  
 possibilities for irregular vibrational structure, 216  
 role of metastable diacetylene modeled for complex hydrocarbon formation, 219  
 singlet-triplet spectroscopy, 211–219  
 two dimensional potential energy surfaces along *cis* and *trans* bending coordinates, 216, 218f  
 unusual features of photochemistry, 211–213
- Differential absorption lidar (DIAL), long-path spectroscopic method, 9
- Diffraction integrals, study of light behavior, 21–22
- Dirac (1902-1984), ideas of quantum mechanics, 5
- Dispersion  
 absorption coefficient, 110  
 calculated time dependent intensity of short light pulse after 10,000 reflections, 122f  
 calculating cavity resonant frequencies in presence of molecular resonance, 110–111  
 cavity field with Gaussian absorber, 119  
 cavity field with Lorentzian absorber, 113–118  
 effect on mode matched ringdown cavity, 108–113  
 free space, on-resonance, and off-resonance for cavity round trip time and dephasing time equal, 116, 117f, 118f  
 index of refraction calculation, 110  
 Kramers-Kronig relationships, 110  
 normalized dispersion curve for line with negligible Lorentzian component, 119, 120f  
 normalized free induction decay amplitude produced by cavity propagation of  $\delta$  function, 116f  
 normalized free induction decay amplitude produced by cavity propagation of  $\delta$

- function with optical resonance midway between modes, 116, 117*f*  
 normalized free induction decay amplitude produced by free space propagation of  $\delta$  function, 115*f*  
 output of ringdown cavity (RDC) excitation as Green's function, 109  
 proposed experimental design for detection of time resolved CRDS, 121*f*  
 ringdown cavity excited with pulse much shorter than dephasing time, 113, 114  
 sample resonance exactly half-way between cavity modes, 114–115  
 spacing between cavity modes small that  $\chi(\omega)$  change negligible between modes, 112–113  
 time domain CRDS, 119–123  
 Dolland (1706-1761), acromatic lens invention, 2  
 Doppler profile, best fit for  ${}^9\text{P}(9)$  transition of  ${}^{16}\text{O}_2$  A-band using short cavity, 103*f*, 104  
 Dynamics, intramolecular and intermolecular. *See* Intramolecular and intermolecular dynamics
- E**
- Eigenvectors and eigenvalues  
 identity matrix, 25  
 optical cavities, 24–26
- F**
- Fabry–Perot cavity  
 finesse, 38  
 free spectral range, 37  
 full width at half maximum, 37–38  
 mode formation in optical cavities, 35–38  
 practical considerations, 38  
 propagation of incident wave, 36*f*  
 properties, 37–38  
 transmission of, 35–37, 38*f*  
 two-mirror, 32*f*  
 Fabry–Perot resonator, derivation of ringdown signals, 94–95  
 Faraday (1791-1867), leading to electromagnetic theory, 2  
 Faraday configuration  
 absorption spectra of molecular oxygen in 20 Tesla magnetic field, 158, 159*f*  
 cavity loss spectra, 156*f*, 157  
 homogeneous magnetic field parallel to axis of cavity, 154  
 PD–CRDS spectra of  ${}^9\text{P}_1(1)$  line of  $\gamma$ -band of 400 mbar  ${}^{16}\text{O}_2$ , 156*f*  
 polarization dependent cavity-ringdown spectroscopy (PD–CRDS), 153  
 right- or left-handed circularly polarized light, 158  
 Fermi (1901-1954), ideas of quantum mechanics, 5  
 Finesse, Fabry–Perot cavity, 38  
 FM spectroscopies. *See* Frequency modulation (FM) spectroscopies  
 Formyl radical  
 cavity-ringdown laser absorption spectroscopy (CRLAS), 181–186  
 experimental concentration profiles for HCO radical in stoichiometric and rich flames, 185, 186*f*  
 predicted absorption and concentration profiles as function of height above burner surface (HAB), 182  
 state selective heterogeneous predissociation, 183  
 visible CRLAS spectra of A–X system of HCO, 183, 184*f*  
*See also* Polyatomic radicals at low pressure  
 Fourier transform cavity-ringdown spectroscopy (FT–CRDS)  
 absorption spectrum of 15 mbar  $\text{O}_2$  in 1050 mbar  $\text{SF}_6$ , 153*f*  
 experimental conditions, 150–152  
 interferograms by FT–CRD spectrometer, 152*f*  
 schematic view of spectrometer, 151*f*  
 standard experiment, 149–150  
 time-resolved measurement, 149–150  
 Franklin (1706-1790), electricity positive and negative, 2  
 Fraunhofer (1787-1826), first objective prism, 3  
 Fraunhofer lines, flaws of devised standards, 4  
 Free spectral range, Fabry–Perot cavity, 37  
 Frequency modulation (FM) spectroscopies  
 comparison of various absorption spectroscopies, 56*t*  
 experimental setup, 53*f*  
 ultrasensitive spectroscopy, 52, 54  
*See also* High absorption sensitivity  
 Full width at half maximum, Fabry–Perot cavity, 37–38  
 Fundamental tests, symmetrization postulate application for laser spectroscopy, 234
- G**
- g-parameters, cavity stability criteria, 27  
 Galatry line shape model, 103*f*, 104  
 Gas phase biomolecules and biomolecule–water complexes  
 gas-phase hydration of amino acid valine, 173*f*

infrared cavity-ringdown laser absorption spectroscopy (IRCRLAS), 167, 172  
 Gaussian absorber in cavity field, 119  
 Gaussian excitation, comparison of short and long cavity properties to pulsed excitation, 99*f*  
 Gibbs' phenomenon, abrupt cut-off of high frequency components of FID, 115–116  
 Glass  
   clear lead glass for lenses, 2  
   discovery by Phoenicians, 1  
 Goudsmit (1902-1978), ideas of quantum mechanics, 5  
 Green's function, output of ringdown cavity (RDC), 109

## H

Heisenberg (1901-1976), ideas of quantum mechanics, 5  
 Hemispherical, two-mirror cavities, 32*f*  
 Hermite–Gaussian waves  
   beam profiles for first four Hermitian polynomials, 43*f*  
   cavity resonance frequencies, 42–45  
   rectangular symmetry, 40–41  
   schematic representation of cross-sectional intensity patterns, 44*f*  
 Herzberg (1904-), electronic structure and internal motions of molecules, 5  
 Heterodyne detection. *See* Optical heterodyne detection  
 High absorption sensitivity  
   advantages of external optical resonator, 238  
   atmospheric detection of trace materials, 233–234  
   fundamental tests on symmetrization postulate, 234  
   intracavity build-up power, 238–239  
   minimum absorption sensitivity calculation, 239–240  
   minimum detectable absorption calculation, 240  
   mirror parameters pre-designed for maximum resonant-cavity transmission, 240  
   molecular spectroscopy overtones and combination bands, 234  
   notations used for build-up cavity, 239*f*  
   optical heterodyne detection, 234–237  
   resonant-cavity reflection efficiency,  $R_{\text{cav}}$ , 238–239  
   sensitivity enhancement by optical cavity, 238–240  
   standing wave optical resonator, 239*f*  
   transmission efficiency,  $T_{\text{cav}}$ , 238–239  
   weak absorption by field-decay (time domain), 241–244

weak absorption by field-phase (phase domain), 244–249  
*See also* Noise-immune, cavity-enhanced optical heterodyne molecular spectroscopy (NICE–OHMS); Optical heterodyne detection  
 High finesse cavity. *See* High absorption sensitivity  
 History of cavity-ringdown spectroscopy (CRDS)  
   continuous wave CRDS, 66–68  
   events leading to birth of linear absorption spectroscopy, 1–5  
   experimental history, 61–68  
   mirror reflectometers, 61–63  
   name origin, 10  
   pulsed CRDS, 63–66  
 Hooke (1635-1703), first microscopes, 2  
 Hund (1896-1997), ideas of quantum mechanics, 5

## I

ICLAS. *See* Intracavity laser absorption spectroscopy (ICLAS)  
 Infrared cavity-ringdown laser absorption spectroscopy (IRCRLAS)  
   absorption spectrum of water clusters in supersonic expansion, 164, 165*f*  
   carbon clusters, 167, 170*f*  
   determining absolute concentrations of water clusters, 164, 166*f*  
   experimentally measured mirror curves, 162, 163*f*  
   gas phase biomolecules and biomolecule-water complexes, 167, 172, 173*f*  
   ions and radicals, 167, 171*f*  
   IRCRLAS spectrum of the  $\nu_3$  band of  $C_5$ , 167, 170*f*  
   jet-cooled spectrum of amino acid valine, 172, 173*f*  
   novel high resolution version, 164  
   operating range of laser dyes, 162, 163*f*, 164  
   single rovibrational transition of  $H_3O^+$ , 167, 171*f*  
   spectrum of  $D_2O$  clusters, 167, 168*f*  
   two-fold splitting in  $D_2O$  from quantum tunneling motion, 167, 169*f*  
   water clusters, 164, 167  
 Intracavity laser absorption spectroscopy (ICLAS), alternative technique for detection of gaseous species, 9  
 Interferometers, driving force for CRDS, 71–73  
 Intracavity laser absorption spectroscopy (ICLAS)



- absorption line growth by Lambert–Beer law, 136
- basic ideas, 126–127
- comparison of various absorption spectroscopies, 56*t*
- correlated double sampling, 137
- description, 136
- detection limit comparisons, 126
- different multimode lasers, 55
- disadvantages, 55
- effects limiting sensitivity, 139–141
- experimental setup, 53*f*
- long generation pulse production, 138
- power saturation, 139
- primary advantage, 55
- robust and adaptable, 143
- single-pulse ICLAS, 141*f*
- spectral multiplexing, 143
- spectral resolution, 138, 142–143
- temporal evolution of multimode ICLAS laser spectrum, 137*f*
- time evolution of laser spectrum, 137*f*, 139
- ultrasensitive spectroscopy, 54–55
- Intramolecular and intermolecular dynamics diacetylene by CRDS, 211–219
- simultaneous laser-induced fluorescence (LIF) and CRDS on tropolone and tropolone–(H<sub>2</sub>O)<sub>n</sub> clusters, 219–230
- See also* Diacetylene; Tropolone and tropolone–(H<sub>2</sub>O)<sub>n</sub> clusters
- ionic species, gas phase, cavity ringdown technique, 77, 80, 82*f*
- Ions and radicals
- infrared cavity-ringdown laser absorption spectroscopy (IRCRLAS), 167
- single rovibrational transition of H<sub>3</sub>O<sup>+</sup>, 171*f*
- K**
- Kepler (1571-1630), telescope improvement, 2
- Kinetic studies. *See* Aromatic radical reactions, kinetic studies
- Kirchhoff (1824-1887)
- founder of spectral analysis, 3–4
- general law for emission and absorption spectra relationship, 3
- Kirchhoff's law, cavity-ringdown spectroscopy (CRDS), 11
- Kramers–Kronig relationships, real and imaginary components of  $\chi$ , 110
- L**
- Laguerre–Gaussian waves
- cavity resonance frequencies, 45
- cylindrical symmetry, 41–42
- schematic representation of cross-sectional intensity patterns, 44*f*
- Lamb (1913-), father of saturation spectroscopy, 5
- Lambert–Beer law, basic ideas in ICLAS and CRDS, 126–127
- Langley (1834-1906), bolometer invention, 4
- Laser absorption spectroscopy
- advantages, 50
- ultrasensitive spectroscopies, 51–58
- See also* Ultrasensitive laser absorption spectroscopies
- Laser-induced fluorescence (LIF)
- alternative technique for detection of gaseous species, 9
- background-free detection technique, 147
- combustion diagnostics technique, 174–175
- See also* Tropolone and tropolone–(H<sub>2</sub>O)<sub>n</sub> clusters
- Laser-induced photofragmentation/photoionization, alternative technique for detection of gaseous species, 9
- Leeuwenhoek (1632-1723), first microscopes, 2
- Light detection and ranging (LIDAR), technique to reduce scattering loss, 51–52
- Linear absorption spectroscopy
- 17th century: age of Newton, 2
- 18th century: age of infrared and ultraviolet enlightenment, 2–3
- 19th century: Fraunhofer, Kirchhoff, and birth of spectroscopy, 3–4
- before 16th century: Egypt to Italy, 1–2
- early 20th century spectroscopy, 4–5
- first description of emission spectrum, 3
- historical overview, 1–5
- Longitudinal modes
- long-cavity limit, 99
- mode formation in optical cavities, 39
- short-cavity limit, 97–98
- Long path differential absorption spectroscopy (LPAS)
- comparison of various absorption spectroscopies, 56*t*
- ultrasensitive laser spectroscopy, 51–52
- Long-radius, two-mirror cavities, 32*f*
- Lorentzian absorber in cavity field, 113–118
- Lossmeter (Cavity), commercial mirror testing instruments, 73–74
- Lyman (1874-1954), concave reflection grating of fluorite optics, 4
- specific series of hydrogen lines, 4
- M**
- Matrix optics
- application to cavity stability, 28, 30–31

- generalized optical system, 22*f*  
 optical cavities, 21–24  
 ray propagating through homogeneous medium, 23*f*  
 sign convention, 22
- Maxwell (1831–1879), electromagnetic theory formulation, 2
- Mean absorption signal ( $S_{\text{mean}}$ ), sensitivity measure in absorption spectroscopies, 50
- Methyl radical  
 cavity-ringdown laser absorption spectroscopy (CRLAS), 187–191  
 experimental and predicted concentration profiles for stoichiometric and rich flames, 191, 192*f*  
 high resolution infrared (IR) CRLAS spectra in methane/air and hydrogen/oxygen flames, 189*f*  
 IRCRLAS spectra of  $\nu_3$  transition of  $\nu_3$  fundamental of methyl as function of height above burner surface (HAB), 188, 190*f*, 191  
 predicted absorption and concentration profiles as function of HAB, 182  
 spectral congestion obstacle in monitoring trace species, 188, 189*f*  
 spectral interferences and congestion, 187  
*See also* Polyatomic radicals at low pressure
- Millikan (1868–1953), reduction of ultraviolet limit, 4
- Minimum detectable absorption loss per shot ( $\text{MDAL}_{\text{shot}}$ ), sensitivity measure in absorption spectroscopies, 50
- Minimum detectable fractional signal per shot ( $\text{MDFS}_{\text{shot}}$ ), sensitivity measure in absorption spectroscopies, 50
- Mirror coatings, characterization, 129
- Mirror reflectometers  
 experimental setups, 62*f*  
 precursors of CRDS, 61–63
- Mode formation and cavity-ringdown spectroscopy  
 mode spacing in typical cavity, 47  
 pulse duration longer than relaxation time of absorbing species, 46–47  
 relaxation time of absorbing species greater than pulse duration, 47
- Mode formation in optical cavities  
 Airy's formula, 37  
 cavity resonance frequencies, 42–45  
 Fabry–Perot cavity, 35–38  
 longitudinal modes, 39  
 mode classifications, 35  
 mode formation and cavity-ringdown spectroscopy, 46–47  
 mode spacing, 45–46  
 properties of Fabry–Perot cavity, 37–38  
 quantitative aspects of transverse modes, 39–40  
 role in cavity-ringdown spectroscopy, 34–35  
 transmission of Fabry–Perot cavity, 35–37, 38*f*  
 transverse electromagnetic (TEM) modes, 40–42  
 transverse modes, 39–42
- Mode matching, cavity modes, 130–132
- Mode spacing  
 mode formation in optical cavities, 45–46  
 in typical cavity, 47
- Molecular spectroscopy, overtones and combination bands an application for laser spectroscopy, 234
- Multipass absorption spectroscopy  
 comparing detection limits with cavity ringdown (CRDS) and intra cavity laser absorption (ICLAS), 126  
 comparison of various absorption spectroscopies, 56*t*  
 experimental setup, 53*f*  
 ultrasensitive laser spectroscopy, 52
- ## N
- Newton (1642–1727), first modern spectrometer, 2
- Nitrogen dioxide,  $\text{NO}_2$   
 absorption spectra in d.c. discharge of air, 81*f*  
 cavity ringdown spectra, 79*f*
- Noise-immune, cavity-enhanced optical heterodyne molecular spectroscopy (NICE-OHMS)  
 beat stability between two  $\text{I}_2$ -stabilized lasers, 251*f*  
 demonstration of noise-immune property, 246*f*  
 general advice on attaining highest sensitivity, 252  
 general experimental schematic, 247*f*  
 HCCH transition recovery with excellent signal-to-noise ratio, 249*f*, 250  
 laser stabilization, 250–252  
 lineshape comparisons among resonances for  $\text{CO}_2$ , HCCD, and HCCH, 249*f*  
 method for highest sensitivity, 248–249  
 noise immune properties, 246–247  
 principle, 245–246  
 sensitivity measurement of technique, 248*f*  
 sensitivity statement, 247–248  
 stability of beat between  $\text{I}_2$ -stabilized and HCCD-stabilized lasers, 251*f*  
 ultrasensitive measurement of transitions in HCCH, HCCD, and  $\text{CO}_2$ , 249–250

weak absorption by field-phase (phase domain), 244–249

*See also* High absorption sensitivity; Optical heterodyne detection

## O

Open-path Fourier-transform spectroscopy, long-path spectroscopic method, 9

Optical cavities

cavity resonator, 20–21

criteria for cavity stability, 26–31

eigenvectors and eigenvalues, 24–26

matrix optics, 21–24

optical arrangements, 21*f*

two-mirror cavities, 31–33

*See also* Mode formation in optical cavities

Optical heterodyne detection

cavity beating-decay in reflection, 241*f*

cavity-enhanced coherent transient spectroscopy, 243

description, 234–235

details of intracavity molecular spectroscopy, collision effects, 243–244

free inductive decay of HF molecules, 243*f*

intensity noise of JILA-designed Ti:Sapphire ring laser, 237*f*

limitations of cavity-ringdown spectroscopy, 241–242

physics limits, 235–236

reaching limits of fundamental noise, 235

real technical limits, 236–237

separating cavity field from molecular contribution, 242–243

shotnoise limit, highest possible sensitivity in direct absorption, 236

weak absorption by field-decay (time domain), 241–244

weak absorption by field-phase (phase domain), 244–249

*See also* High absorption sensitivity; Noise-immune, cavity-enhanced optical heterodyne molecular spectroscopy (NICE-OHMS)

Optical parametric oscillator (OPO), light generation in short cavities, 102–104

Oxygen, molecular, cavity ringdown spectrum, 76*f*

## P

Particle picture of CRDS, controversy among researchers, 107–108

Paschen (1865–1947), specific series of hydrogen lines, 4

Pauli (1900–1958), ideas of quantum mechanics, 5

Phase shift CRDS method

continuous wave laser, 133–134

development of CRDS, 72

Phase-shift reflectometer

experimental setup, 62*f*

*See also* Mirror reflectometers

Phenyl radicals. *See* Aromatic radical reactions, kinetic studies

Photoacoustic spectroscopy (PAS)

alternative technique for detection of gaseous species, 9

combustion diagnostics technique, 174–175

comparing detection limits with cavity ringdown (CRDS) and intra cavity laser absorption (ICLAS), 126

Photon bullet model, short duration pulses, 34–35

Ping-pong model, simplistic view of pulsed CRDS, 58–59

Planck (1858–1947), quantized energy states, 4

Plano-concave, optical cavities, 21

Plano-plano, optical cavities, 21

Pockels cell shutter

development of CRDS, 72

switching time relative to cavity decay time, 72–73

Polarization dependent cavity ringdown spectroscopy (PD-CRDS)

applicable to optical rotation of transparent solid sample study, 157–158

cavity loss spectra in Faraday configuration, 157

description, 152–153

effects leading to polarization rotation, 153

experimental, 154–159

extending applicability of CRDS, 159

Faraday configuration, 154

noise-equivalent absorption detection limit in the difference spectrum, 157

PD-CRDS spectra of  $^{31}\text{P}_1(1)$  line of  $\gamma$ -band of 400 mbar  $^{16}\text{O}_2$  in Voigt and Faraday configuration, 156*f*

right- or left-handed circularly polarized light in Faraday configuration, 158

schematic view of PD-CRDS setup, 155*f*

sum of spectra with right- or left-handed circularly polarized light, 158, 159*f*

three absorption spectra of molecular oxygen in 20 Tesla magnetic field, 158, 159*f*

Voigt configuration, 153–154

Polyatomic radicals at low pressure apparatus for coherent anti-stokes Raman spectroscopy (CARS), 177

CARS, 174–175

cavity-ringdown laser absorption spectroscopy (CRLAS), 175

combustion diagnostics techniques, 174–175  
 contributions from Mie and Rayleigh scattering, 178–179  
 CRLAS apparatus, 177–179  
 CRLAS/CARS experiment, 176f  
 CRLAS method insensitive to absolute value of initial intracavity light intensity, 179  
 determining absolute species concentrations and comparison to theory, 180–181  
 experimental, 175, 177  
 formyl radical, 181–186  
 intracavity laser absorption spectroscopy (ICLAS), 175  
 low pressure flame diagnostics apparatus, 176f  
 methyl radical, 187–191  
 spatial specificity, 191, 193  
 tailoring output beams for visible and infrared systems, 178  
 temperature corrected linestrength calculations, 180  
 total cavity losses calculations, 178  
*See also* Formyl radical; Methyl radical  
 Prokharov (1916-), maser invention, 5  
 Ptolemy of Alexandria (A.D. 130), early founder of optics and astronomy, 1  
 Pulsed cavity-ringdown spectroscopy (P-CRDS)  
 experimental history, 63–66  
 first application, 63  
 frequency domain model of pulsed CRDS for Dirac delta function comb and Airy function comb, 58f  
 ping-pong model of pulsed CRDS, 58f  
*See also* Cavity-ringdown spectroscopy (CRDS)  
 Pulsed laser, photon bullet model, 34–35  
 Pulse reshaping  
 general phenomenon in CRDS when pulse coherence time is shorter than dephasing time, 119–123  
*See also* Dispersion and CRDS

## Q

Quantitative absorption measurements  
 conventional CRDS measurements, 101  
 line profile of  ${}^P P(9)$  transition of  ${}^{16}\text{O}_2$  A-band, 103f  
 line shape models, 104  
 long-cavity limit, 100  
 measurements using short cavities, 102–104  
 ringdown signal and rovibronic line profile of  ${}^R R(9)$  transition of  ${}^{16}\text{O}_2$  A-band, 101f  
 short-cavity limit, 100  
 typical ringdown signal and residuals from weighted-least-squares fit, 102, 103f

Quantum mechanics, theory development, 4–5

## R

Radical reactions. *See* Aromatic radical reactions, kinetic studies  
 Radicals and ions  
 infrared cavity-ringdown laser absorption spectroscopy (IRCRLAS), 167  
 single rovibrational transition of  $\text{H}_3\text{O}^+$ , 171f  
*See also* Formyl radicals; Methyl radicals  
 Raman (1888-1971), discovery of Raman effect, 5  
 Range, dynamic, cavity-ringdown spectroscopy (CRDS), 17  
 Radiometric dual-path absorption spectroscopy, comparison of various absorption spectroscopies, 56t  
 RDS transfer functions, more sophisticated view of CRDS, 59–60  
 Reflectometry. *See* Mirror reflectometers  
 Resonance, concept of, 20–21  
 (2+2)Resonance-enhanced multiphoton ionization (REMPI)  
 alternative technique for detection of gaseous species, 9  
 background-free detection technique, 147  
 combustion diagnostics technique, 174–175  
 Resonant four-wave mixing (RFWM), combustion diagnostics technique, 174–175  
 Ringdown time, exponential intensity decay, 93–94  
 Ring gyroscopes  
 development at HeNe laser wavelength, 71  
 driving force for CRDS, 71–73  
 Rowland (1848-1901), dry gelatin photographic plates, 4  
 Rutherford (1871-1937), alpha particle scattering, 5  
 Rydberg (1854-1919), mathematical formula for hydrogen lines, 4

## S

Schawlow (1921-), devising laser spectroscopy, 5  
 Schrödinger (1887-1961), ideas of quantum mechanics, 5  
 Scientific societies, formation in Europe, 2  
 Semi-confocal, two-mirror cavities, 32f  
 Sensitivity  
 cavity-ringdown spectroscopy (CRDS), 16–17  
*See also* High absorption sensitivity  
 Shuttered laser injection of optical cavity, development of CRDS, 72  
 Spectral studies, historical overview, 1–5

Spectroscopies. *See* Absorption spectroscopies  
 Spot size, two-mirror cavities, 31, 33  
 Stable cavities, cavity stability criteria, 26–27  
 Static cell absorption measurements  
 cavity ringdown approach, 75–77  
 cavity ringdown spectrum of molecular oxygen, 76*f*  
 overtone transitions of water, 78*f*  
 Statistical uncertainties  
 CRDS-based absorption measurements, 98, 100  
 minimum measurable absorption coefficient, 98  
 Stokes (1819–1903), quartz transparent in ultraviolet, 4  
 Supersonic application  
 absorption spectrum of copper trimer, 83, 84*f*  
 cavity ringdown technique, 83–89  
 compilation of atomic and molecular species studied to date, 89*t*, 90*t*  
 high resolution spectrum of Cu trimer (Cu<sub>3</sub>), 85, 88*f*  
 resolved spectrum of Cu<sub>2</sub> B–X transition, 85, 86*f*  
 resolved spectrum of Cu<sub>2</sub> C–X transition, 85, 87*f*  
 vibronic bands and assignments for Cu<sub>3</sub>, 85*t*  
 Supersonic expansions. *See* Infrared cavity-ringdown laser absorption spectroscopy

## T

Talbot (1800–1877), creation of photographic film, 4  
 Teller (1908–), ideas of quantum mechanics, 5  
 Tesla (1856–1943), leading to electromagnetic theory, 2  
 Theoretical model of CRDS  
 cavity excitation, 95–97  
 comparison of short and long cavity properties to pulsed Gaussian excitation, 99*t*  
 controversy among researchers, 107–108  
 CRDS signals, 97–98  
 excitation field, 94  
 excitation illustration of ringdown cavity by transform-limited Gaussian pulse, 96*f*  
 Fabry–Perot resonator ringdown cavity, 94–95  
 field-based derivation of cavity-ringdown signals, 94–97  
 pulsed cavity-ringdown technique, 74–75, 76*f*  
 signal power levels and energy transmitted by cavity, 98  
 underpinnings of method, 107–108  
 Thermal lensing measurements, alternative technique for detection of gaseous species, 9

Thomson (1856–1940), electron discovery, 5  
 Time-resolved CRDS  
 advantages or disadvantages, 122–123  
 calculated time dependent intensity of short light pulse after 10,000 reflections, 122*f*  
 experimental apparatus, 121*f*  
 possibilities of, 119–123  
 Townes (1915–), maser invention, 5  
 Trace species detection  
 cavity ringdown technique, 77  
 nitrogen dioxide, NO<sub>2</sub>, 77, 79*f*  
 Transverse electromagnetic (TEM) modes  
 cylindrical symmetry, 41–42  
 Hermite polynomials for Hermite–Gaussian waves, 40–41  
 Laguerre polynomials for Laguerre–Gaussian waves, 40–42  
 rectangular symmetry, 40–41  
 Transverse modes  
 mode formation in optical cavities, 39–42  
 quantitative aspects, 39–40  
 signal calculation for excited, 97  
 transverse electromagnetic (TEM) modes, 40–42  
 Tropolone and tropolone–(H<sub>2</sub>O)<sub>n</sub> clusters  
 complexation of one or more water molecules to tropolone (TrOH), 227  
 data acquisition software analysis of ringdown signal, 221–223  
 decrease in fluorescence quantum yield for cluster of four waters, 230  
 energy level ordering typical for aromatic ketones and aldehydes, 228*f*  
 increasing fluorescence quantum yield by hydrogen bonding, 227–230  
 overview CRDS/LIF scan of first 700 cm<sup>-1</sup> of S<sub>1</sub>WS<sub>0</sub> transition, 223, 224*f*  
 relative fluorescence quantum yields of tropolone and selected clusters, 228*t*  
 relative single vibronic level (SVL) fluorescence quantum yields, 223, 225*f*, 227  
 schematic diagram of apparatus for simultaneous CRDS and LIF measurements, 221, 222*f*  
 seven-membered pseudo-aromatic molecule noted for hydrogen-atom tunneling, 219  
 single vibronic level relative fluorescence quantum yields for tropolone monomer, 226*t*  
 additional shift in (n,π\*) states anticipated for TrOH–(H<sub>2</sub>O)<sub>n</sub> clusters with carbonyl carbon as acceptor for H-bond, 228*f*  
 expected shift in (n, π\*) states in TrOH due to intramolecular H-bond, 228*f*  
 studying effects of substitution on ring, 219, 221  
 symmetric double-minimum potential well for hydrogen-atom transfer, 220*f*

Tunable diode laser absorption spectroscopy (TDLAS), long-path spectroscopic method, 9

Two-mirror cavities  
spot size, 31, 33  
various mirror combinations, 32*f*

## U

Ultrasensitive laser absorption spectroscopies  
cavity-ringdown spectroscopy (CRDS), 56–58  
comparison of various absorption spectroscopies, 56*t*  
frequency modulation (FM) spectroscopies, 52, 54  
intracavity laser absorption spectroscopy (ICLAS), 54–55  
long path differential absorption spectroscopy (LPAS), 51–52  
multipass absorption spectroscopy, 52  
ratiometric dual-path absorption spectroscopy, 51  
Unstable cavity  
cavity stability criteria, 26  
ray parameters after successive reflections in unstable cavity, 31*t*

## V

Voigt configuration  
homogeneous magnetic field perpendicular to axis of cavity, 153–154

PD-CRDS spectra of  ${}^{\text{P}}\text{P}_i(1)$  line of  $\gamma$ -band of 400 mbar  ${}^{16}\text{O}_3$ , 156*f*  
polarization dependent cavity-ringdown spectroscopy (PD-CRDS), 153

## W

Water, overtone transitions, 78*f*  
Water clusters  
absorption spectrum in supersonic expansion, 164, 165*f*  
determining absolute water cluster concentrations, 164, 166*f*  
infrared cavity-ringdown laser absorption spectroscopy (IRCRLAS), 164, 167  
spectrum of fully-deuterated  $\text{D}_2\text{O}$  clusters, 167, 168*f*  
two-fold splitting of spectral features from quantum tunneling motion, 167, 169*f*  
Wheatstone (1802-1875), leading to electromagnetic theory, 2

## Z

Zeeman (1865-1943), magnetic splitting of spectral lines, 4